Towards An improved Understanding of Geodynamic Processes Along the Pacific Coast of Central North America

by

Maryam Yousefi

A thesis submitted to the Faculty of Earth and Environmental Sciences
in partial fulfillment of the requirements for the degree of

Doctor of Philosophy

at the

UNIVERSITY OF OTTAWA

August 2020

To my beloved parents, Touran and Ali

Abstract

The Pacific Coast of Central North America is a geodynamically complex region which has been subject to various geophysical processes. The isostatic response of the Earth to the advance and retreat of ice sheets and glaciers, called glacial isostatic adjustment (GIA), is known to be important on millennial timescales in this area. The other dominant geodynamic process at play along this coastline is that associated with two active plate boundaries. The work presented in this thesis aims to better isolate the signals associated with different geodynamic processes that are observed simultaneously by a variety of data types in order to arrive at a better understanding of these processes. The principal aim of this thesis is to develop an improved GIA model for western North America.

In Chapter 2, I quantify the significance of the GIA signal (and its associated uncertainty) by constraining its two fundamental components- the Earth rheology and history of past ice loading- using relative sea-level (RSL) observations. Due to the possible influence of non-GIA processes on the RSL observations, a careful approach was taken in order to confirm that parameter inferences are robust. The results obtained from a 1D (spherically-symmetric) Earth modelling analysis of two- and three-layer mantle viscosity models suggest that there are significant variations in the inferred viscosity structure from north to south. The data-model misfits (and also sensitivity to the ice model) are largest in northern parts of the study area which were once located close to the ice margin. The optimal parameter sets are then used to estimate the GIA contribution to present-day crustal movement and future RSL change. My results suggest that GIA contributes significantly to present-day vertical motion; mostly at those parts of the coastline experiencing forebulge subsidence.

The data-model misfits evident in Chapter 2 motivated me to improve the applied Earth model by incorporating, in Chapter 3, lateral variations in viscosity structure., and this work is presented in Chapter 3. Three different approaches are used to construct 3D realizations of the Earth structure. For the first approach, lateral variations in sub-lithosphere viscosity are calculated using four different global seismic tomography models and are used with two models of lateral variations in lithosphere thickness. The other two approaches incorporate regional structure into the Earth model by, in one case, inserting a regional seismic model into two of the

global seismic models and, in the other case, by explicitly incorporating the subducting slab, the overlying mantle wedge, and the plate boundary interface. Neither of these approaches reveal any clear preference over the 1D models. However, the two different approaches used to determine 3D Earth structure give us insight to the spread (and thus uncertainty) of modelled RSL values and are a necessary step towards trying other approaches.

In Chapter 4, I apply late Holocene RSL observations (over the past 4 kyr) and GPS data (over the past few decades) to infer the associated vertical land motion (VLM) rates along the Pacific coastline of North America. I model and remove the signals associated with 20^{th}-century glacier mass loss and ground water depletion, so that the residual VLM rates are expected to represent the signal due to the Cascadia earthquake cycle. The residual rates compare well with those predicted using a recent locking model of Cascadia subduction, which is encouraging given that the model was developed using only horizontal land motion observations. Performing a sensitivity test on locking model parameters suggest that the residual VLM rates are able to provide useful constraints on key subduction model parameters such as the (near-trench) locking state.

Acknowledgements

First and foremost, I would like to acknowledge my supervisor, Professor Glenn Milne for his patience and continuous support throughout my PhD program. I am very grateful to have had the opportunity to work with Glenn who helped me to develop my research skills and to become the researcher that I am today.

I would like to thank the group members and my co-authors for their help and support: Ryan Love, Alan Bartholet, François Lapointe and Joseph Kuchar. I am also very thankful to Konstantin Latychev who has spent a generous time to answer my frequent questions. I want to acknowledge Lev Tarasov, Kelin Wang, and Shaoyang Li for their collaborations in my research projects.

I thank my dissertation committee for providing valuable feedback: Professors Thomas James, Giorgio Ranalli, Pascal Audet, and Claire Perry.

Many thanks to all the admin staff in the department of Earth and Environmental Sciences for helping me with admin problems: Lisa, Audrey, Caroline(s), and Hélène.

I am very grateful for the remote support and encouragement that I have received from my parents, Touran and Ali, my brother, Sina, and all my friends in Iran and across the World.

Finally, I thank my beloved husband, Mehdi, for his endless emotional support. Mehdi's love has been the primary heat source that warmed my soul to get relaxed and recover more quickly from the stress built over these years.

Table of Contents

List of Figures

List of Tables

1

Introduction

1.1 General Overview

The dynamics of the Earth system is defined through the processes operating between and within its different components, such as the solid Earth, oceans, cryosphere, continental hydrosphere and atmosphere. Our understanding of the Earth system requires consideration of the broad temporal and spatial scales of these processes. Interactions between different system components and the solid Earth is key to understanding a variety of solid Earth deformation (geodynamic) processes. The response of the solid Earth to these applied forcings is reflected in various geophysical and geological data types, including 3D crustal motion, sea-level variations and change in the Earth's gravity field. Numerous studies have applied different observations at regional and global scales to infer more accurate knowledge about the driving forces and solid Earth response. One typical issue is that geodynamic signals resulting from different processes can occur simultaneously, in time and space, and so the signals overprint each other in the available data sets. Separating these signals to unravel the underlying processes is a challenge in areas that are geodynamically complex.

The pacific coast of North America is affected by various geodynamic processes that operate simultaneously. There is an active convergent plate boundary along this coastline, known as the Cascadia subduction zone, extending over ~1000 km from southwestern British Columbia to northern California (Figure 1.1). Over a broad range of timescales, subduction-related processes cause different types of Earth deformation and motion of the solid surface, from the formation of the Pacific Coastal Mountain Ranges and the Cascade Range over geological timescales to active and rapid crustal movements due to the Cascadia earthquakes. From northern California southwards, the plate boundary setting changes from a convergent to a transform margin (Figure 1.1). The tectonic activity in this area is mainly characterized by the strike-slip motion along the San Andreas fault system that results in local zones of crustal compression and extension as well as large earthquake ruptures.

In addition to tectonic processes, the Pacific coast of North America experiences a considerable geodynamic signal associated with glacial isostatic adjustment (GIA), driven by the repeated advance and retreat of ice sheets in North America during the Quaternary. The isostatic response of the Earth to the glaciation-deglaciation process is complex and involves several components which will be discussed in section 1.2. In plain words, to provide the general idea, imagine that all of Canada and parts of the northern US were covered by ice sheets with regional maximum ice thicknesses of more than 3000 m when the ice was at its greatest extent (at ~21,000 years ago, or 21 ka, Figure 1.2). The weight of such extensive ice imposes a load on the Earth's surface that bends the lithosphere and causes the mantle to flow. During the deglaciation phase, a large volume of meltwater fluxes into the oceans and the surface of the Earth experiences an unloading on the continent but a loading over most of the oceans.

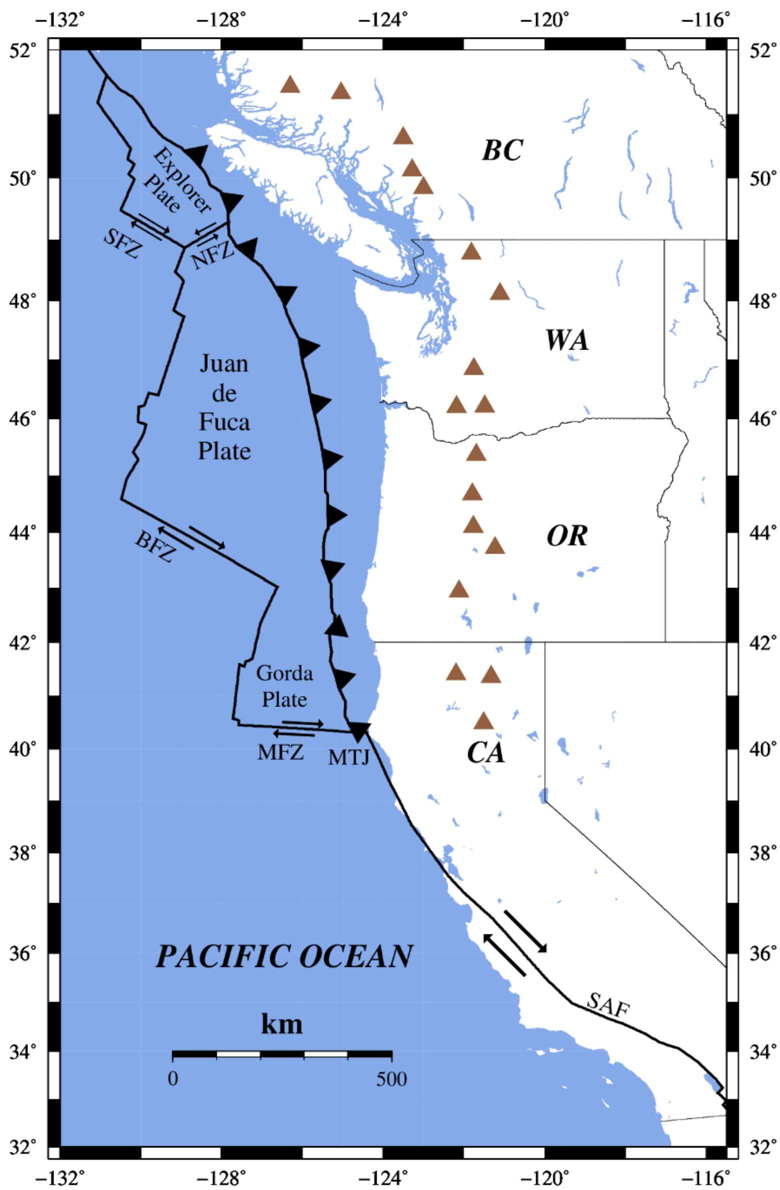

Figure 1.1. Map showing the study area considered in this thesis. Thick black lines show plate boundaries, with the triangles indicating subduction of the Juan de Fuca, Explorer and Gorda plates beneath the North American plate. The brown triangles indicate the major volcanoes of the Cascade Range. MTJ represents the Mendocino Triple Junction; SFZ, BFZ, MFZ, and NFZ represent the Sovanco, Blanco and Mendocino fracture zones, and Nootka fault zone, respectively; SAF is the abbreviation for the San Andreas Fault. US states – Washington (WA), Oregon (OR) and California (CA) – and the Canadian province British Columbia (BC) are indicated along with their geographic boundaries (thin black lines).

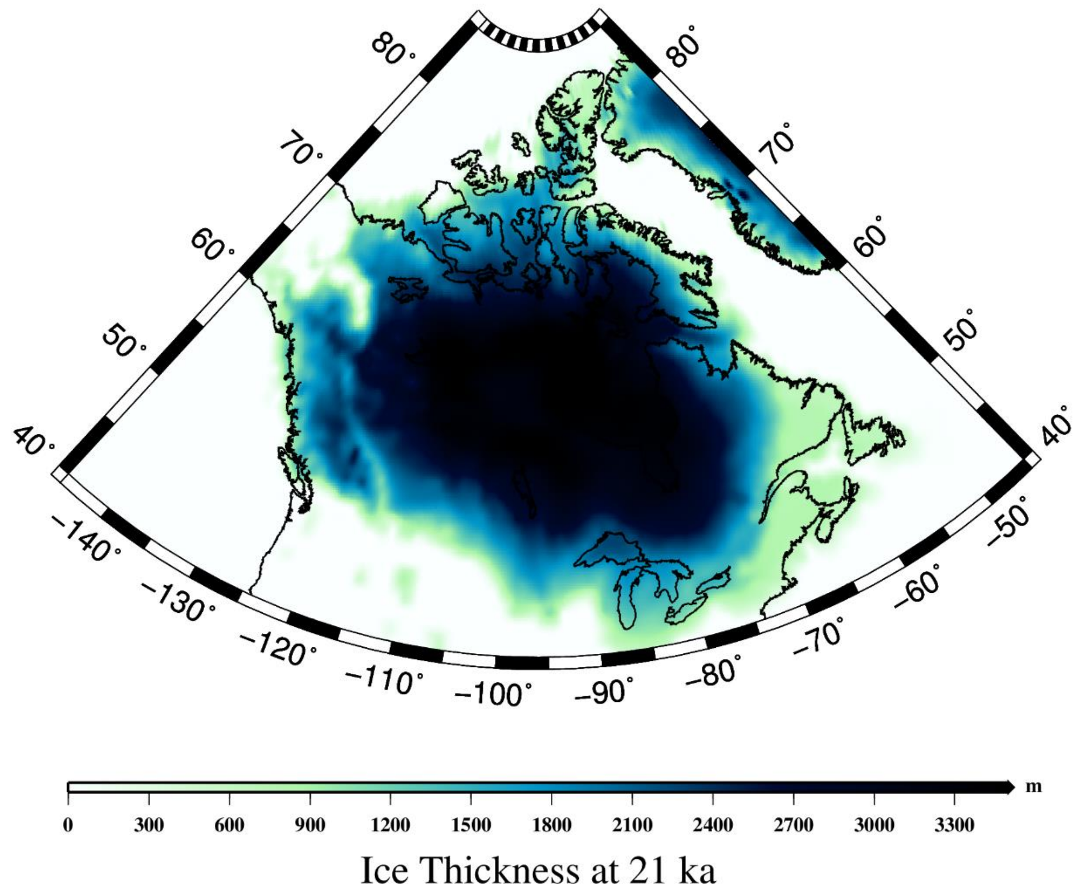

Figure 1.2. A model of ice thickness at 21 ka during the last glacial maximum. The model shown in this plot is from the work of Tarasov et al. (2012).

Although the deglaciation of the ice began around 20 ka and most of the continent was free of ice by ~10 ka, there remains a considerable GIA signal at present in the region indicated in Figure 1.1 that is comparable in magnitude to signals from other geodynamic processes. For example, contemporary uplift rates exceeding 10 mm/yr have been detected in areas near the centers of past ice sheets, such as Hudson Bay located close to the center of Laurentian ice sheet (Sella et al, 2007). In addition to a GIA signal associated with the melting of the ancient North American ice sheets, there also exists a more spatially confined contemporary signal in the northern parts of the coastline shown in Figure 1.1 associated with mountain-glacier mass loss in southwestern Canada and northwestern US during the twentieth century.

In addition to the influence of tectonics and melting ice sheets and glaciers, the hydrological cycle can also produce significant local effects on geophysical observables. The recharge and discharge of groundwater reservoirs occurs naturally and its seasonal variability can produce solid Earth deformation and surface motion. Observations of crustal motion have also been used to identify signals that are not associated with the natural hydrological cycle but originate from the time that human beings began large-scale farming and water management practices. In some populated areas, such as central and southern California, there has been a persistent groundwater extraction during the twentieth century in order to satisfy the water demand in domestic, industrial and, more importantly, agricultural sectors. This excessive groundwater depletion produces a contemporary Earth deformation signal.

The combined effects of the above-mentioned processes over different time scales are reflected in observations acquired from the west coast of North America. These observations are, therefore, commonly used in different research disciplines to model and constrain various processes and model parameters. In turn, these models are used to make predictions of natural hazards: for example GIA models are used to make projections of sea-level change at regional and global scales (Love et al., 2016) and tectonic plate locking models (Li et al., 2018; see section 1.3) provide information that can be used to help predict major subduction-related earthquakes. The important applications of these models emphasise the need to find methods to better isolate the signals of interest in the available data sets and thus more robust estimates of key model parameters. The research presented in this thesis aims to better isolate the signals associated with the processes described above to arrive at a better understanding of these processes and Earth properties beneath the Pacific coast of North America. The primary focus of this thesis is the development of an improved

GIA model for the region defined in Figure 1.1. Section 1.2 provides some additional background to this research field.

1.2 Glacial Isostatic Adjustment

Since the onset of Pleistocene glaciation in the northern hemisphere (around 3 Ma), there has been a quasi-periodic advance and retreat of ice sheets in North America and Eurasia with dominant periods of ~40 and ~100 kyr (e.g., Shackleton and Opdyke 1973). During the most recent glacial cycle which began around 115 ka, ice sheets developed and evolved in North America, reaching a maximum extent at the last Glacial Maximum (LGM) around 21 ka. Three major ice sheets experienced growth and decay during the last glacial cycle in North America: Laurentian, Cordilleran and Innuitian ice sheets. The advance and retreat of these ice sheets along with other ice sheets around the world (notably Eurasian and Antarctic) introduced a global-scale ice-water mass redistribution. The glaciation phase with a relatively slow increase in ice volume lasted ~90 kyr and caused a global sea-level minimum of ~130 m at the LGM (Lambeck et al., 2014). The deglaciation phase, in comparison, occurred more rapidly over a shorter period (~10 kyr) and an equivalent amount of water consumed for the ice expansion was delivered back to the oceans. The ice/water mass transfer between the oceans and continents during glaciation-deglaciation phases applies a considerable load on the Earth's surface that deforms the Earth and its gravity field and thus changes sea-level. A relevant question at this point would be, how we do know all this about such an ancient phenomenon? In short, our knowledge originates from observations, particularly those spanning longer (millennial) timescales.

1.2.1 GIA observables

The response of the Earth to the glaciation-deglaciation process is manifest through a wide range of observables, the primary ones being sea-level change and present-day variations in 3D land motion and gravity. There are various types of observations that constrain the GIA signal over different time scales, including the radial and tangential crustal motion observed using satellite-based methods (e.g. GPS), vertical land motion from land levelling profiles, (relative) sea-level change measured using tide gauges, and land-based and satellite-based gravity measurements. Since the amplitude of GIA decays over millennia following a given loading or unloading event, the contemporary observations capture only a 'snap shot' of this millennial-scale signal.

The dataset that best captures the millennial-scale GIA signal is paleo reconstructions of relative sea level (RSL) from geological records (RSL is the height of the ocean surface relative to the ocean floor; Figure 1.3) (e.g., Milne and Shennan, 2013). Paleo RSL markers consist of a broad range of evidence, such as archaeological artifacts, macrofossils (e.g., corals and mangroves), microfossils (e.g., foraminifera, diatoms, and pollen), biological remnants (e.g., tree stumps), and geomorphological markers (e.g., tidal notches and raised beaches) (see e.g., Khan et al., 2015; Shennan et al., 2015). Some of these markers indicate only the upper limits or lower limits of RSL (known as limiting data points), while some others can provide a more accurate estimation of RSL (known as sea-level index points). Whether a given indicator results in a limiting datum or a sea-level index point, to be useful for constraining the GIA process it should come with the following information: a location, an age, its present elevation, and an indicative meaning which is a quantitative relationship between the sea-level range over which the indicator existed (referred to as the indicative range) and the contemporary tidal reference level. Paleo RSL reconstructions based on geological records have significantly improved our understanding of the GIA process, and they play a central role in the research presented here (Milne and Shennan, 2013).

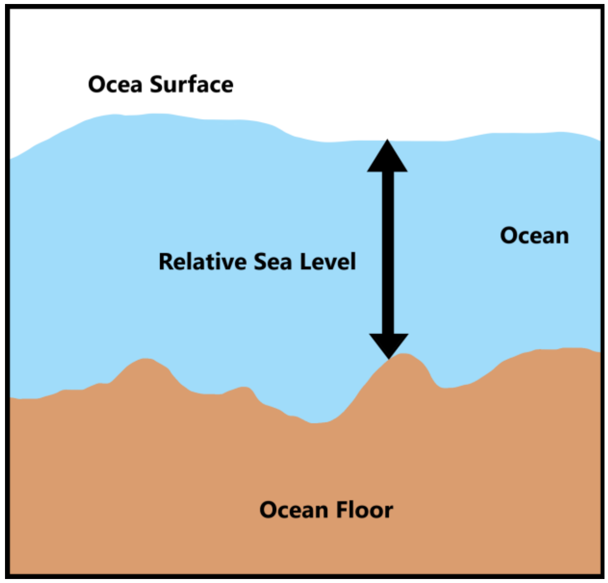

Figure 1.3. A schematic diagram representing relative sea level. Note that topography of the ocean surface has been exaggerated.

1.2.2 GIA mechanism

In this section the influence of GIA on solid Earth deformation, gravity change and sea level variation is discussed. As an ice sheet grows thicker, the underlying regions are depressed and push mantle material away to form the so called "peripheral forebulges" (Figure 1.4). As the Earth experiences subsidence beneath an ice sheet and uplift in the forebulges, the associated internal (solid Earth) mass redistribution perturbs the gravitational potential. Any perturbation in the gravitational potential causes a sea-level variation. This is because the surface of the ocean conforms to a hypothetical surface with a constant gravitational potential, in the absence of ocean and atmosphere circulation. This "equipotential surface" of the Earth's gravity field is known as the geoid. Another mechanism during glaciation that influences the geoid is associated with the mass transfer from the oceans to the continents required to ‘grow’ an ice sheet. In this case, the gravitational changes are produced by the surface mass transfer rather than the resulting Earth deformation.

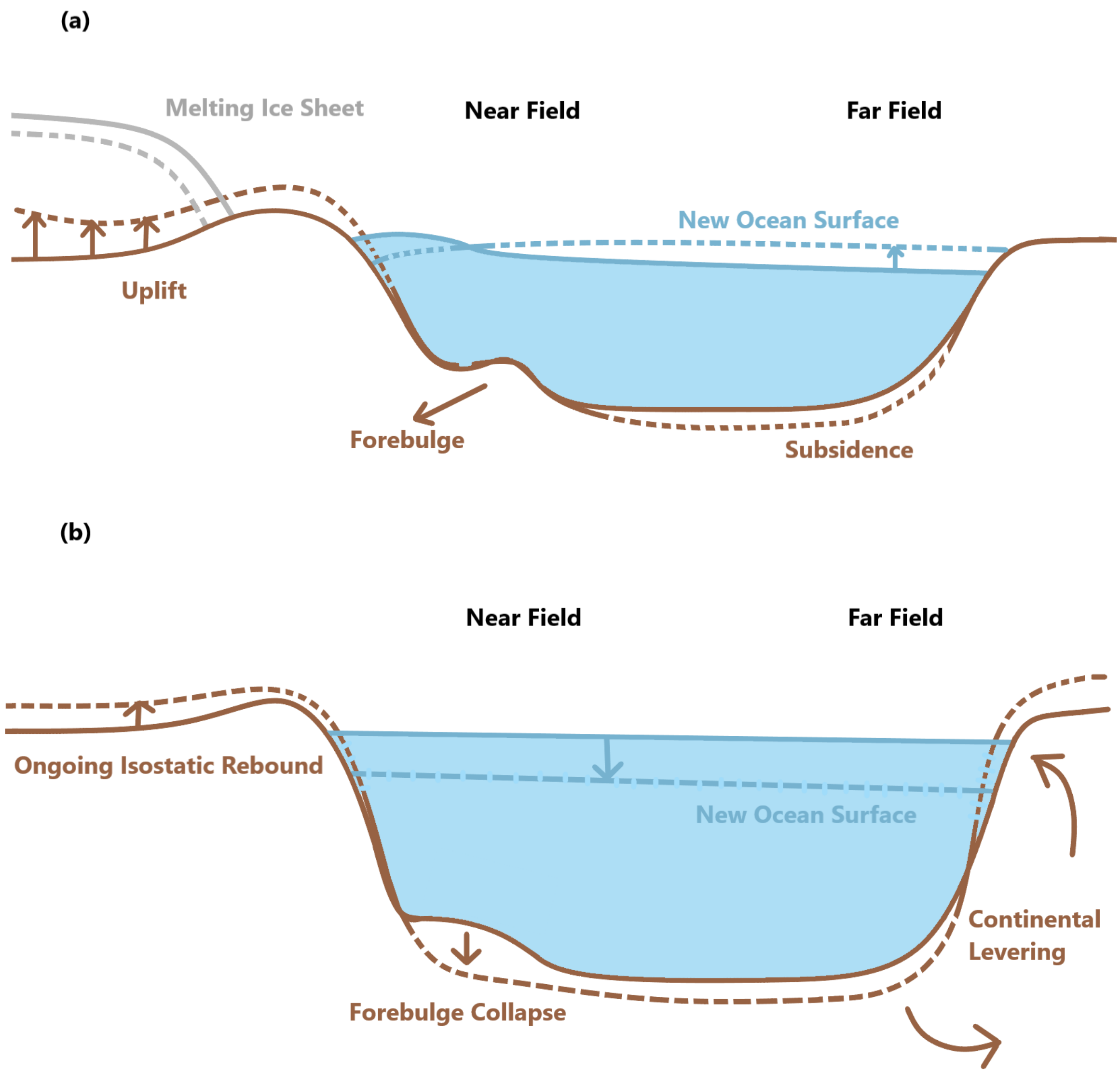

Figure 1.4. A schematic diagram representing the influence of GIA on solid Earth deformation and RSL change during (a) early deglaciation and (b) after disappearance of an ice sheet. Solid and dashed lines indicate the original and new states, respectively. Adapted from Whitehouse (2018).

When an ice sheet decreases in size during deglaciation, the Earth isostatically adjusts to the overlying ice load to reach an equilibrium state. This adjustment process involves mantle return-flow that causes uplift in previously glaciated areas and subsidence of the forebulges. Similar to the glaciation phase, the deformation of the solid Earth results in change of the Earth's gravity field and sea level, but of an opposite sign due to the process described above being reversed. The gravitational attraction of the melting ice decreases significantly, and accordingly, so do the regional geoid heights (e.g. note the raised sea surface indicated by the blue shading in Figure 1.4a). In addition to the mass redistribution (on and inside the Earth) affecting gravity and sea level, the transfer of a large volume of meltwater into the oceans causes a globally uniform shift in sea level, referred to as the barystatic sea-level change. The net effect of these relative sea-level changes is to induce a second load (in addition to the ice), which is applied in ocean areas. In most areas of the ocean, the ocean loading is spatially variable and positive during a deglaciation as illustrated in Figure 1.4. Close to the continental margins, this ocean loading acts like a lever that pushes the continental margins upward and causes subsidence over the ocean basin (hence the term "continental levering", Lambeck and Nakada, 1990). The subsidence of the ocean floor arising from forebulge collapse and continental levering expands the capacity of the ocean basins and so ocean water is redistributed from areas located far from the melting ice sheets to the sinking areas of ocean floor peripheral to the margins of ancient ice sheets or far-field continental shelves (explaining the fall of the ocean surface after the ice has melted (Figure 1.4b). This process is referred to as ocean syphoning (Mitrovica and Milne, 2002).

Figure 1.4 depicts a simplified view of the mechanisms involved in the GIA process. One important GIA feedback mechanism is associated with Earth rotation. Any rotating object has a natural tendency to spin around its axis of maximum moment of inertia, also referred to as its axis of figure. Since GIA is a global process, it results in changes in the Earth's moment of inertia causing the orientation of the "instantaneous spin axis" (indicating the north and south geographic pole positions) to change. This 'wandering' of the spin axis (known as True Polar Wander) has been tracked by the

International Latitude Service. GIA is responsible for a significant, or even dominant, component of the observed (secular) True Polar Wander during the 20th century (e.g., Sabadini et al., 1982). During the glacial cycles, the Earth adjusts its rotation vector to align with the changing moment of inertia configuration and this, in turn, changes the shape and gravity field of the Earth, and thus sea level.

1.2.3 GIA modelling

The first attempts at GIA modelling date back to the early-mid 19th century when some evidence of ice-induced deformed Earth was first discovered. However, it was not until the late 20th century that a sufficient theoretical foundation was laid to enable the development of contemporary GIA modelling. During the past few decades, there have been theoretical and model developments to better simulate different aspects of the complex GIA mechanisms discussed in section 1.2.2. There has also been considerable progress in methods to measure and develop the relevant observational data bases that are required to test and tune the models and thus enable key model components to be better determined. The amplitude of the GIA signal reflected in the observations, particularly the RSL observations, is governed by two primary components: the magnitude of the ice loading applied and the material properties of the Earth's interior. For this reason, the two most common aims of GIA modelling are to constrain: (1) the ice evolution history, i.e., which locations were covered by the ice sheets and what were the changes in ice thickness through time; and (2) the rheology of the Earth, i.e. the material properties of the Earth that determine how the Earth deforms in response to a given loading (induced stress).

The majority of GIA modelling studies have taken a forward modelling approach in which the Earth rheology and/or ice loading history are varied in seeking to reproduce the observables (Figure 1.5) (e.g., Whitehouse, 2018). A core component of the forward model is the so-called "sea-level equation" which is discussed in section

1.2.3.3. In essence, solving this equation gives the sea-level change – which is both a load component and an observable – for an assumed ice history and Earth rheology. GIA model outputs generally include temporal and spatial evolution of RSL, and/or present-day rates of crustal motion, and/or present rates of gravity change. An optimal solution of the forward modelling is determined by comparing the model outputs with their corresponding observations. Each model parameter set that gives the minimum data-model misfit value is chosen as the best-fitting model. However, one issue that usually arises in forward modelling is the non-uniqueness of the solution which results in having more than one set of ice and Earth model inputs that can fit the data equally well. This property as well as model limitations/assumptions and uncertainty in the observations can lead to substantial differences in model parameter estimates.

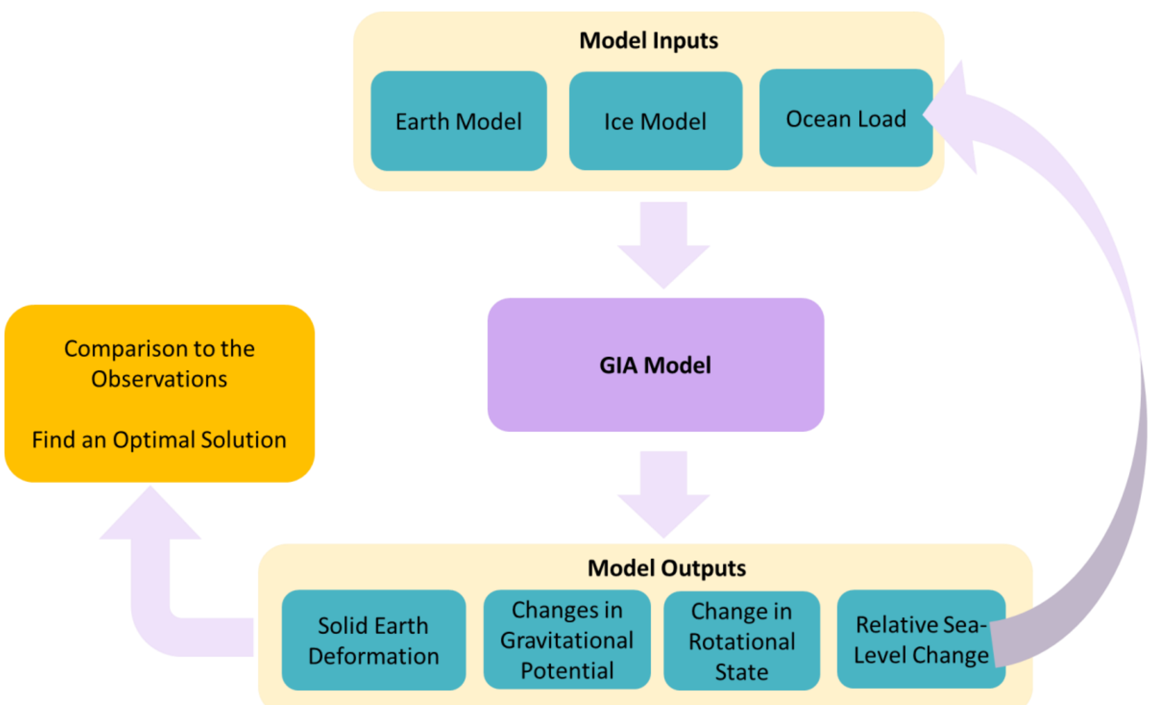

Figure 1.5. The main components of a GIA model. The sea-level equation, a key component of the GIA model that computes the redistribution of water in the ocean basins, is solved in an iterative manner, as the ocean load is both an input to and output of the model (see eqn 1.11 in section 1.2.3.3).

1.2.3.1 Input Earth Model

In GIA modelling, the Earth component has been most often simulated as a spherically symmetric self-gravitating Earth model that behaves as a Maxwell visco-elastic material (e.g., Peltier, 1974). In this model the Earth is comprised of multiple spherical layers that simulate a spring and dashpot connected in series, with each layer giving an immediate elastic response followed by a time-dependent viscous relaxation that decays through time for a given loading change (Ranalli, 1995). The outermost layer of the spherical Earth model is assumed to have a very high viscosity so that it acts as an elastic material over GIA timescales to simulate the lithosphere. A depth-dependent viscosity profile is assigned to the Earth model, from the base of the lithosphere to the core-mantle boundary, which consists of several layers with different viscosity values. The average viscosity of the lower parts of the mantle is usually greater than the average of the shallower parts by ~1-2 orders of magnitude.

The model outputs produced by a spherically symmetric Earth with a linear Maxwell rheology have generally provided reasonable fits to the observations. However, in many studies, the data-model misfits are, at least partly, attributed to these assumptions made in constructing the Earth model. For example, some recent studies and laboratory experiments suggest that non-linear rheology models or a combination of both linear and non-linear rheology, more accurately represent the deformational response of the Earth (e.g., Karato, 2008; Wu et al., 2008; van der Wal et al., 2010; van der Wal et al., 2013). The assumption of spherical symmetry in Earth properties is also one that has been questioned in the recent literature. An increasing number of studies are making progress in developing more realistic Earth models that accommodate lateral heterogeneity in Earth structure to try and better fit the observational constraints (e.g., Steffen and Kaufmann, 2005; Wu et al., 2013; Kuchar et al., 2019).

1.2.3.2 Input Ice Model

The Late-Pleistocene ice sheet reconstructions have been traditionally built upon various types of (dated) geomorphological evidence that mark the extent of the ice, e.g., ice-deposited materials, at different times during its evolution (e.g., Shennan, 2007). One major limitation of this approach is that the deposits containing the records of ice sheet changes prior to the LGM have been mostly destroyed by the regrowth of ice during the most recent glacial phase. Therefore, constraints on ice evolution following the LGM are much more abundant than those for the pre-LGM evolution. One of the most commonly used constraints on the time distribution of ice extent is radiocarbon dating of organic material in glacial deposits. The radiocarbon dates should be calibrated for the spatial and temporal variations in radiocarbon production rate to represent the actual ages of the organic material (Stuiver & Suess, 1966; Törnqvist et al., 2015). We note that all the dates indicated throughout this study are calibrated and presented in calendar years.

Over the past few decades, several studies have published or compiled the radiocarbon dates used to reconstruct the deglaciation of the North American ice sheets (e.g., Dyke et al., 2003; Dyke, 2004; Dalton et al., 2020). The northern regions of our study area, including southwestern British Columbia and northwestern Washington State, was a part of the southwestern extent of the Cordilleran ice sheet. The glaciation history in this region is complex and consists of several advances and retreats during the last glacial cycle. A detailed review of the available constraints on ice margin chronology in this area can be found in Gowan 2007 (e.g., see their Table 3.2).

An important development towards improving reconstructions of the ice evolution history has been the application of numerical ice models that, in addition to the glacial geology observations, incorporate data and constraints from ice physics as well as regional climate change (temperature and precipitation) (e.g., Tarasov and Peltier, 2004; Tarasov et al., 2012). The study by Tarasov et al. (2012) applied a large set of different observational constraints to calibrate the model parameters. More than 50000 model runs were performed to ensure robust parameter inferences and quantify model uncertainty for the reconstructed deglacial history of the North American ice complex. A high-variance subset of these model reconstructions is used in this thesis.

1.2.3.3 The Sea Level Equation

The physical model that is the basis of modern GIA studies is built upon the work of Farrell and Clark (1976) who developed the underlying theory and were the first to accurately calculate sea-level change associated with Earth glaciation. This theory, which is encapsulated in the so-called "sea-level equation", is applied in all contemporary GIA modelling. In their development and first application of the sea-level equation, Farrell and Clark assumed a non-rotating Earth with fixed shorelines. In their theory, the change in relative sea-level change (ΔSL) is attributed to the change in geoid height (ΔG) and variation in the height of sea floor (ΔR):

$$\Delta SL(\theta,\lambda,t) = \Delta G(\theta,\lambda,t) - \Delta R(\theta,\lambda,t) \tag{1.1}$$

where, θ and λ are the colatitude and east longitude in a spherical coordinate system. The sea-surface height changes can be separated into a spatially-varying component ($\Delta\mathcal{G}$) and a spatially uniform shift ($E(t)$), accordingly:

$$\Delta SL(\theta,\lambda,t) = \big(\Delta\mathcal{G}(\theta,\lambda,t) + E(t)\big) - \Delta R(\theta,\lambda,t) \tag{1.2}$$

$E(t)$ is a time-dependant spatially uniform shift that comprises two components: the barystatic sea-level change (E^{B}) and the ocean syphoning (E^{s}), as defined in section 1.2.2. This spatially-uniform term ensures ice-ocean water mass conservation, i.e., the mass lost/gained by the ice sheets is gained/lost by the oceans (Farrell and Clark, 1976). At each time (t_j) the spatially uniform shift of the sea-surface height associated with barystatic sea-level change can be calculated as:

$$\mathrm{E}^B(t_j) = -\frac{V_I}{A_0}\frac{\rho_I}{\rho_W} = -\frac{1}{A_0}\frac{\rho_I}{\rho_W}\iint_\Omega \Delta I(\theta', \lambda', t_j) d\Omega \quad (1.3)$$

A_0 is the ocean area at time step j; ρ_W and ρ_W are the density of the ocean and ice, respectively; V_I is the change in ice volume at time step j; $d\Omega$ is the spherical polar differential element ($\sin\theta' \, d\theta' d\lambda'$); and $\Delta I(\theta', \lambda', t_j)$ is the change in ice thickness at time step j. An expression for the sea-level change associated with ocean syphoning can be obtained by averaging the sea-level over the ocean area:

$$\mathrm{E}^S(t_j) = -\frac{1}{A_0}\langle \Delta\mathcal{G}(\theta, \lambda, t) - \Delta R(\theta, \lambda, t)\rangle_O \quad (1.4)$$

The symbol $\langle \, \rangle_O$ denotes the spatial integration over the ocean area. $\Delta\mathcal{G}$, the spatially-variable component of geoid height change, is determined to first order by dividing the perturbation to the gravitational potential by the gravitational acceleration ($\frac{\Delta\Phi}{g}$). The radial displacement (ΔR) and the perturbation to the gravitational field ($\Delta\Phi$) can be obtained by convolving a given surface mass load, $L(\theta, \lambda, t)$, with the associated Green's functions:

$$\Delta R(\theta, \lambda, t) = \int_{t'} \iint_\Omega L(\theta', \lambda', t') \, GF_R(\psi, t - t') \, a^2 \, d\Omega \, dt' \quad (1.5)$$

$$\Delta\Phi(\theta, \lambda, t) = \int_{t'} \iint_\Omega L(\theta', \lambda', t') \, GF_\Phi(\psi, t - t') \, a^2 \, d\Omega \, dt' \quad (1.6)$$

a is the model Earth's radius;.ψ is the angular distance between the point load (θ', λ') and the observer (θ, λ) and is derived by: $\cos\psi = \cos\theta\cos\theta' + \sin\theta\sin\theta'\cos(\lambda - \lambda')$. $L(\theta', \lambda', t')$ is the surface load model and is defined as a combination of the ocean load and the ice load:

$$L(\theta', \lambda', t') = \rho_W \Delta S(\theta', \lambda', t') + \rho_I \Delta I(\theta', \lambda', t') \quad (1.7)$$

GF_R and GF_Φ are the Green's functions associated with the radial displacement and gravity perturbations. For a linear Maxwell rheology, the green's functions are formulated as follows:

$$GF_R(\psi,t) = \frac{a}{M_E}\sum_{n=0}^{\infty}\left(h_n^V(t) + h_n^E\ \delta(t)\right) P_n(\cos\psi) \tag{1.8}$$

$$GF_\Phi(\psi,t) = \frac{ag}{M_E}\sum_{n=0}^{\infty}\left(\delta(t) + k_n^E\ \delta(t) + k_n^V(t)\right) P_n(\cos\psi) \tag{1.9}$$

where: M_E is mass of the Earth; g is the Earth's surface gravitational acceleration; a is the model Earth's radius; $\delta(t)$ is the Dirac delta function or unit impulse function; P_n is the n^{th} Legendre polynomial. h_n and k_n are the surface load Love numbers associated with the radial deformation and the perturbation to the gravitational field, respectively. The corresponding superscripts V and E represent the contributions from viscous (time dependant) and elastic components of deformation. The Love numbers are dependent on the physical properties of the Earth, such as density and viscosity of the mantle.

A general basic form of the sea-level equation is derived by substituting eqns (1.3)-(1.6) into eqn (1.2):

$$\Delta SL(\theta,\lambda,t) = \int_{t'}\iint_{\Omega} L(\theta',\lambda',t')\left(\frac{GF_\Phi(\psi,t-t')}{g} - GF_R(\psi,t-t')\right)a^2 d\Omega -$$

$$\frac{1}{A_0}\frac{\rho_I}{\rho_W}\iint_{\Omega}\Delta I_j d\Omega - \frac{1}{A_0}\langle\int_{t'}\iint_{\Omega} L(\theta',\lambda',t')\left(\frac{GF_\Phi(\psi,t-t')}{g} - GF_R(\psi,t-t')\right)a^2 d\Omega\rangle_O \tag{1.10}$$

By using the * symbol to represent spatial and temporal convolution, the traditional sea-level equation first presented by Farrell and Clark (1976) appears as:

$$\Delta SL(\theta,\lambda,t) = L*\frac{GF_\Phi}{g} - L*GF_R - \frac{1}{A_0}\frac{\rho_I V_I}{\rho_W} - \frac{1}{A_0}\langle L*\frac{GF_\Phi}{g} - L*GF_R\rangle_O \tag{1.11}$$

Considering the surface load definition that includes the ocean load ($\rho_W\Delta SL(\theta,\lambda,t)$), eqn (1.11) is an integral equation; that means it is a function of itself and so is generally solved in an iterative manner.

Since the seminal work of Farrell and Clark, subsequent studies have extended their theory to include Earth rotation (e.g., Han and Wahr 1989; Milne and Mitrovica, 1998) as well as lateral shoreline migration (e.g. Mitrovica and Milne, 2003 and references therein). The version of the sea-level equation that can accommodate lateral shoreline migration is usually referred to as the "generalized" sea-level equation. This is the version that is used in the research presented in this thesis.

1.3 The Cascadia Subduction Zone

The Cascadia subduction zone is a major tectonic feature within our study area and results in deformation and land motion recorded in the data sets described above and considered in this thesis. It extends about 14,000 km from the southern coast of British Columbia to northern California and marks the convergence between the continental North American plate and three young (4-9 Myr) oceanic plates: Juan de Fuca, Explorer and Gorda (Figure 1.1). These plates subduct beneath the western margin of the North American plate and have a similar fate to their ancient predecessor – the "Farallon" plate – which has been descending for ~150 Myr and separated from the rest of the plate at ~20-30 Ma (Severinghaus and Atwater, 1990; Wilson, 2002, Crameri et al., 2018).

Rupture of the plate interface in this subduction zone is capable of generating a devastating earthquake that would threaten several major population centers. The most recent Cascadia megathrust event occurred on the 26th of January 1700 CE with a moment magnitude of ~9, determined from historical records of a tsunami in Japan (Satake et al., 2003). In the absence of modern instrumental measurements, analyzing the geological records of coastal marshes and marine turbidites suggests that the Cascadia megathrust events have a recurrence interval of ~200-600 years (Adams, 1990; Atwater and Hemphill-Haley, 1997; Leonards et al., 2010; Goldfinger et al., 2012). Considering the recurrence interval and the fact that 300 years has passed since the last major event, there has been extensive research focused on modelling different aspects of Cascadia subduction zone to estimate the hazard associated with a future rupture event.

The cyclic great earthquakes occurring along the Cascadia margin consist of several stages of deformation over different timescales: a sudden coseismic rupture, continuing slip of the fault (termed as afterslip), postseismic relaxation of the stressed mantle, and relocking of the fault and interseismic strain accumulation (Wang et al., 2012). At the time of coseismic rupture, coastal areas experience an abrupt subsidence while inland areas experience uplift (e.g., Atwater, 1987; Dragert et al., 1994). Afterslip along the megathrust interface can continue from a few months to few years, while postseismic relaxation of the material surrounding the rupture zone can take years to decades to dissipate. During the interseismic phase, which has the longest duration, stress builds up as a result of the locked (or partially locked) plate interface until the occurrence of the next rupture. Accordingly, the coastal regions that previously subsided during the coseismic phase gradually uplift and move landward (Wang et al., 2012, Wang et al., 2013). Several studies suggest that the strain accumulated during the interseismic period is not fully recovered during coseismic slip and so a long-term permanent deformation is produced that is reflected in the uplifted shoreline platforms observed in this area (e.g., Kelsey et al., 1994). Note that due to the lack of observations relating to the afterslip and postseismic phases, their amplitude and characteristic timescales are poorly constrained (Leonard et al., 2010).

Most studies have focused on the coseismic and interseismic stages because the modern era of geodetic and seismic observations has provided important information regarding the current late stage of interseismic deformation. For example, geodetic observations of crustal motion have detected the occurrence of some periodic seismic tremors and aseismic slips, termed as episodic tremors and slips (ETS) (see, e.g., Rogers and Dragert, 2003). The observations of teleseismic waves help to explain the mechanism involved in the periodic occurrence of ETS and their correlation with the downdip extent of the fault locking zone. Some recent studies suggest that there are low-permeability materials within the plate interface shear zone that trap fluid released from the subducting slab and cause an increase in fluid pressure, weakening the plate interface and triggering the ETS (e.g., Audet and Kim, 2016; Audet and Schaeffer, 2018). During slip, the low-permeability seal is breached allowing migration of fluids and reduction of fluid pressure. The cycle is repeated as the low-permeability seal is re-established and fluid pressure re-accumulates (Gosselin et al., 2020). The potential influence of the ETS on megathrust earthquake potential and their mutual correlation is an active area of research.

The pattern of deformation during each earthquake stage is highly dependent on the physical properties of the subduction zone interface. A common approach to constrain subduction models is to use geodetic or geophysical data, such as observed crustal motions, seismic imaging, heat flow measurements, etc. One of the primary observations is the horizontal component of motion which has been widely applied to investigate various features of the Cascadia subduction system (e.g., Dragert et al., 1994; Wang et al., 2003; McCaffrey et al., 2007; Li et al., 2018). Some specific features that are of interest to hazard assessment studies are the current along-strike degree of locking, and the depth range of the stick-slip fault behaviour which indicates the fault areas capable of producing large earthquakes (referred to as the "seismogenic zone"). In order to have a robust estimate of these key subduction parameters, the observations should not be contaminated by non-tectonic processes.

Another important constraint in understanding the subduction process along the Cascadia margin comes from seismic tomography. Seismic tomography techniques have provided a powerful tool that enables the determination of 3D seismic velocity structure (Figure 1.6). These variations reflect the influence of compositional and thermal variations on rock properties within the imaged volume and thus highlight its different features and dynamics (e.g., Bostock et al., 2002; , Hawley et al., 2019). For example, the subducting slab is colder relative to the surrounding mantle and is imaged as a zone of higher velocity (large blue oblique zone in Figure 1.6). As the oceanic slab sinks, the increasing pressure and temperature cause it to dehydrate and transform into eclogite. The release of water into the overlying mantle (the so-called "mantle wedge") changes the composition and properties of this region. The resulting information about the heterogeneity in the mantle can be applied to better understand various geophysical processes. Of particular relevance here is the use of these tomographic models to determine viscosity structure as input to the new generation of 3D GIA Earth models (section 1.2.3.1).

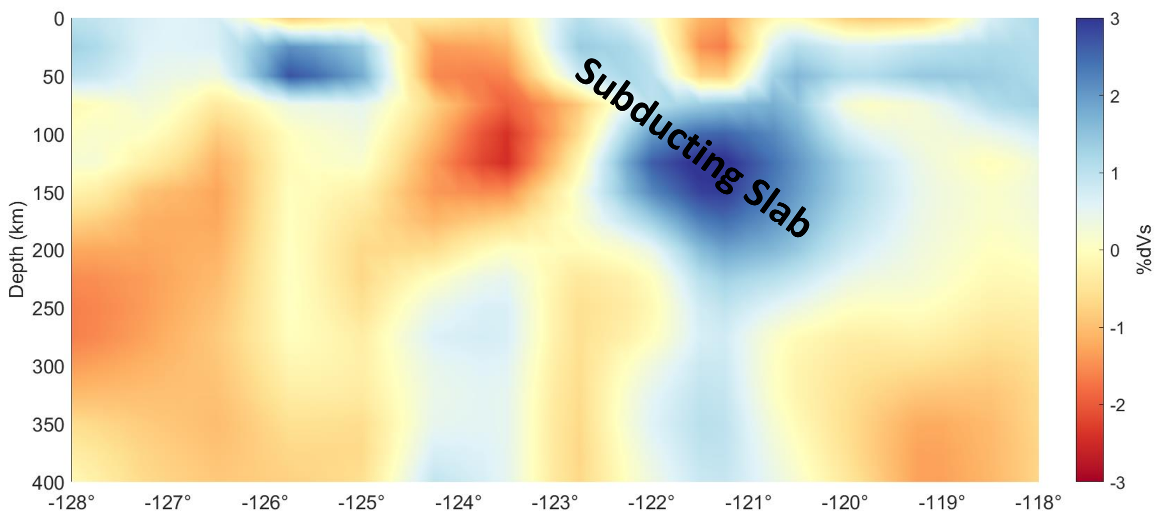

Figure 1.6. Seismic velocity model in central Washington State (The model is adopted from Hawley et al., 2019)

1.4 Contributions and Outline of Thesis

The general aim of my thesis is to use different data types obtained along the Pacific coast of North America to advance our understanding of the underlying geodynamic processes. The main focus of my research is improving estimates of the GIA signal and to better constrain its key components, i.e., the Earth structure as well as the ice loading history.

In Chapter 2, I modelled the contribution from GIA to RSL changes and land motion. As the first step, I used a large parameter space, more than 20000 combinations of Earth and ice models, to search for an optimal one-dimensional (spherically symmetric) Earth viscosity model that provides the minimum data-model misfit. The GIA model parameters were constrained by a state-of-the-art (at the time of publication), Late Glacial/Holocene RSL dataset. Considering the potential contribution from a tectonic signal, the influence of this process was removed from the database, where possible, using estimates based on last interglacial shoreline elevations. Using the results of this model calibration, I generated model output of present-day land motion and RSL change at the locations of GPS and tide-gauge stations with the associated model uncertainty. Considering the significant contribution of GIA to these observables, this model output can be used by colleagues seeking to use these data to interpret other signals. I also generated model output of RSL change at the end of the 21st century and show that GIA contributes significantly – as much as 28% of the total – to future RSL rise along parts of this coastline and so should be considered in future RSL-projection analyses. As a final remark, the results in Chapter 2 indicate a relatively poor-quality fit of the model to the data in areas that are closer to the ancient ice margin and no single set of model parameters could adequately fit the entire dataset. Possible reasons behind the observed misfits are discussed in detail; however, a likely important source is lateral variability in Earth viscosity structure.

Motivated by the research presented in Chapter 2, I investigated the influence of lateral variability in Earth viscosity structure on GIA model output in Chapter 3. I built different realizations of 3D Earth structure based on different constraints and test the models by comparing output to RSL observations. In conventional GIA studies, the thickness of the lithosphere is set to a constant value which is constrained along with viscosity structure. In this research I applied two different models of lithosphere thickness, one of them is built and applied in GIA modelling for the first time as part of my thesis research contribution. Based on results using global seismic models, I concluded that the resolution of these models is not high enough to provide improved fits to the observations compared to those of a 1D (spherically symmetric) model. As an alternative, I explicitly incorporated 3D regional structure using two approaches: a regional seismic velocity model and constraints on the geometry of the Cascadia subduction zone so that the viscosity structure associated with slab and overlying mantle wedge could be incorporated. The influence of these higher resolution models of 3D structure is significant but less than anticipated and so the results are unable to explain the large data-model residuals identified in Chapter 2. The results in Chapter 3 provide an important first step towards producing more realistic models of the GIA process in western North America.

As described in section 1.3, models of the Cascadia subduction zone based on geodetic observations can be biased if the data are not corrected for the contaminating signals associated with other geodynamic processes, such as GIA. In the majority of previous studies, only the horizontal component of land motion has been used to constrain geodynamic models of the subduction process. In Chapter 4, I isolated the vertical land motion associated with the interseismic cycle of the Cascadia subduction zone in order to provide constraints on the key parameters in locking models of this tectonic boundary. To do this, I applied two different datasets that span different time periods, contemporary GPS observations and Holocene sea-level reconstructions. In addition, I modelled and removed the influence of recent (20th century) signals from excessive ground water depletion and melting glaciers. I then made a comparison between the isolated vertical land motion signal and output from a state-of-the-art subduction zone model to assess the ability of these data to constrain model parameters. There, I demonstrated that GPS-inferred vertical land motion rates are more effective than horizontal rates in constraining key model parameters. My estimates of vertical land motion (with associated uncertainty) can be used in future studies that aim to improve our understanding of this geodynamically complex segment of the North American coastline.

2

Glacial Isostatic Adjustment Along the Pacific Coast of Central North America

Statement of Contribution

I generated the research output presented in the following manuscript under the supervision of Dr. Milne. I also led the writing of the manuscript with several rounds of feedback from Dr. Milne as well as input from the other authors (Ryan Love and Lev Tarasov). Lev Tarasov developed the ice histories used in this research. The codes developed by Ryan Love are used to quantify the (heuristic) model uncertainty. All model results and figures included in the manuscript were created by me. Most of the interpretations of model output are my own, thus the bulk of the scientific discussion reflects my own thoughts and analysis.

Citation:

Yousefi, M., G.A. Milne, R. Love, & L. Tarasov, (2018), Glacial isostatic adjustment along the Pacific coast of central North America: Quaternary Science Reviews, v. 193, p. 288–311, 10.1016/j.quascirev.2018.06.017.

2.1 Introduction

The Pacific coast of central North America is a geodynamically complex region. It is the location of an active convergent plate boundary, known as the Cascadia subduction zone, where the Juan de Fuca, Explorer and Gorda plates subduct beneath the North America plate. Furthermore, parts of this coastline were once covered by the Cordilleran ice sheet and were proximal to the Laurentian ice sheet during the peak of the last major glaciation, resulting in a considerable isostatic response in many areas. This complexity is reflected in a variety of data types, including geodetic measurements of 3D land motion, instrumented (tide-gauge) and reconstructed observations of relative sea-level (RSL) change. Numerous studies have examined these data with the intent of better understanding the underlying processes and/or constraining models (Dragert et al., 1994; Hyndman and Wang, 1993, 1995; Smith-Konter, et al., 2014; Veit and Conrad, 2016; Wang et al., 2003; Wang, 2007). A common issue that arises is the difficulty in removing the unwanted component signals from the data under consideration.

A number of studies have modelled reconstructions of RSL change in the vicinity of the Cascadia subduction zone to assess the accuracy of glacial isostatic adjustment (GIA) models and constrain input parameters, such as mantle viscosity structure (e.g. Clague and James, 2002; Dalrymple et al., 2012; James et al., 2000; James et al., 2009b; Muhs et al., 2012; Roy and Peltier, 2015). Roy and Peltier (2015) modelled RSL values along the pacific coast of North America, from Vancouver Island to Central California, using the ICE6G_C ice model combined with three different radial viscosity models. A comparison between their models and the compiled RSL histories (Engelhart et al., 2015) indicates that the models do not adequately fit the whole dataset. The discrepancies between their model output and the data were notably largest in western Vancouver Island, the southern part of Georgia Strait, and parts of the California coast. Roy and Peltier hypothesised that the majority of these discrepancies are associated with tectonic effects, although estimates of this contribution are not discussed. The authors suggest that data-model misfits in southern Georgia Strait, which is close to the Cordilleran ice margin, are associated with errors in the ice history and/or subsidence due to sediment loading.

In northern Cascadia, GIA studies using RSL observations and lake-shoreline tilt suggest low-viscosity values for the upper mantle ranging from 5×10^{18} to 5×10^{19} Pas (James et al., 2000; James et al., 2005). Adopting these relatively low viscosity values leads to present-day crustal uplift rates of ~0.1 mm/yr in southern Vancouver Island (James et al., 2009a) and 0.25 mm/yr in the northern Strait of Georgia (James et al., 2005). James et al. (2009b) found that an asthenosphere with viscosity range of 3×10^{18} Pas (for a 140 km-thick asthenosphere) to 4×10^{19} Pas (for a 380 km-thick asthenosphere) can fit the observations reasonably well. Their predicted present-day uplift rate over Vancouver Island is ~0.4 mm/yr which is larger than that estimated in previous studies.

In southern regions, including southern Washington, Oregon and California, a persistent subsidence has occurred following ice retreat. This has been interpreted as peripheral bulge (forebulge) collapse (Muhs et al, 2012; Reeder-Meyers et al., 2015; Reynolds and Simms, 2015). Although the northern regions proximal to the ice covered areas are affected more by GIA, the departure of sea level observations from the sea-level change due to meltwater addition (often termed eustatic or ice-equivalent sea level) can be interpreted as the imprint of GIA and tectonics in this region. Muhs et al. (2012) considered coral terraces on San Nicolas Island (offshore southern California) dated to MIS5. They adopted an upper mantle viscosity of $5\text{x}10^{20}$ Pas and found that the observations were compatible with lower mantle viscosity values in the range $5\text{-}10\text{x}10^{21}$ Pas. Their results indicate a mean rate of uplift for San Nicolas Island of 0.25-0.27 mm/yr since MIS 5. Dalrymple et al. (2012) provided RSL model predictions for a few cities such as Pacific City, Waldport, Coos Bay, Eureka, and etc. based on the ICE-5G and ICE-6G models combined with the VM5a Earth model (Peltier and Drummond, 2008; Argus and Peltier, 2010; Peltier, 2010). These models generally predicted a higher rate of sea-level rise during late Holocene, resulting in the modelled curve being too deep compared to the observations.

The primary aim of this study is to constrain GIA model parameters for the Pacific coast region, extending from Vancouver Island to southern California. This work builds on those introduced above in several respects. Following Roy and Peltier (2015) we make use of the regional, quality assessed database of Engelhart et al. (2015) but extend this to include data from California (Reynolds and Simms, 2015). We explicitly consider and, where possible, correct for the influence of non-GIA processes on the RSL observations to arrive at relatively robust estimates of Earth viscosity structure. We consider a large range of Earth viscosity parameters (704 viscosity profiles) and ice histories (29 models) to sample parametric uncertainty more completely than in previous studies. In total, over 20,000 model runs were performed in carrying out the work presented below. A key contribution of this paper is the estimation of model parametric uncertainty. We provide spreadsheets of model output of present-day rates of vertical land motion and RSL change at 483 GPS stations and 56 tide gauge stations so that end users can remove the GIA signal and focus on that due to other processes such as tectonics. Finally, as indicated in past studies and confirmed here, there is strong evidence for lateral variations in Earth properties along the east Pacific coastline. All GIA studies to date (including this one), have applied a 1D (properties varying with depth only) Earth model. A second aim of this study is to provide a crude estimate of the lateral variations in Earth viscosity structure that will form the basis of a future study that explicitly considers lateral variations in Earth viscosity structure.

2.2 Methods

2.2.1 Observations

We have made use of two recently published compilations of sea-level records: one from Vancouver Island to Central California (Engelhart et al., 2015), and one from Central California to Southern California (Reynolds and Simms, 2015). The combined dataset is subdivided into 13 areas or sites (hereafter referred to as sites; Figure 2.1). Sites 1-11 comprise the data compiled by Engelhart et al. (2015) and we have adopted the same criteria used by these authors (e.g. tectonic setting, distance from former ice sheet) to partition the data into the 11 sites. Site 12, Central California coast, comprises data from both Engelhart et al. (2015) and Reynolds and Simms (2015). The most southerly site, 13, uses data from Reynolds and Simms (2015) only. The total dataset consists of 178 freshwater indicators (upper limiting), 163 marine indicators (lower limiting), and 680 sea-level index points (SLIPs) to constrain past sea-level change in our study region. The number of each of these data types per site and the spatial distribution of SLIPs are shown in Table S1 and Figure 2.1, respectively.

Based on the late-Quaternary ice coverage and tectonic setting of the study region, we divided the entire dataset into three sub-regions: northern (British Columbia and northern Washington), sites (1-7); central (southern Washington and Oregon), including sites 8, 9, and 10; and southern (California), including sites 11, 12, and 13. The northern region sites were once covered by the Cordilleran ice sheet with the southern margin extending, at most, to the area defined by site 7 (Clague and James, 2002; James et al., 2009a). The central region comprises the sites located south of the former ice sheet margin and north of the Mendocino Triple Junction. These sites have a similar tectonic regime and have experienced, in general, long-term crustal uplift due to the subduction of Juan de Fuca plate (Atwater, 1987; Burgette et al., 2009;

Kelsey et al., 1996; Merrits and Bull, 1989; Muhs et al., 1992). In the southern region, which extends from the Mendocino Triple Junction to southern California, the primary tectonic boundary is conservative with strike-slip motion across the San Andreas Fault system (Brown, 1990; Crowell, 1962; Grove et al., 2010; Simkin et al., 2006).

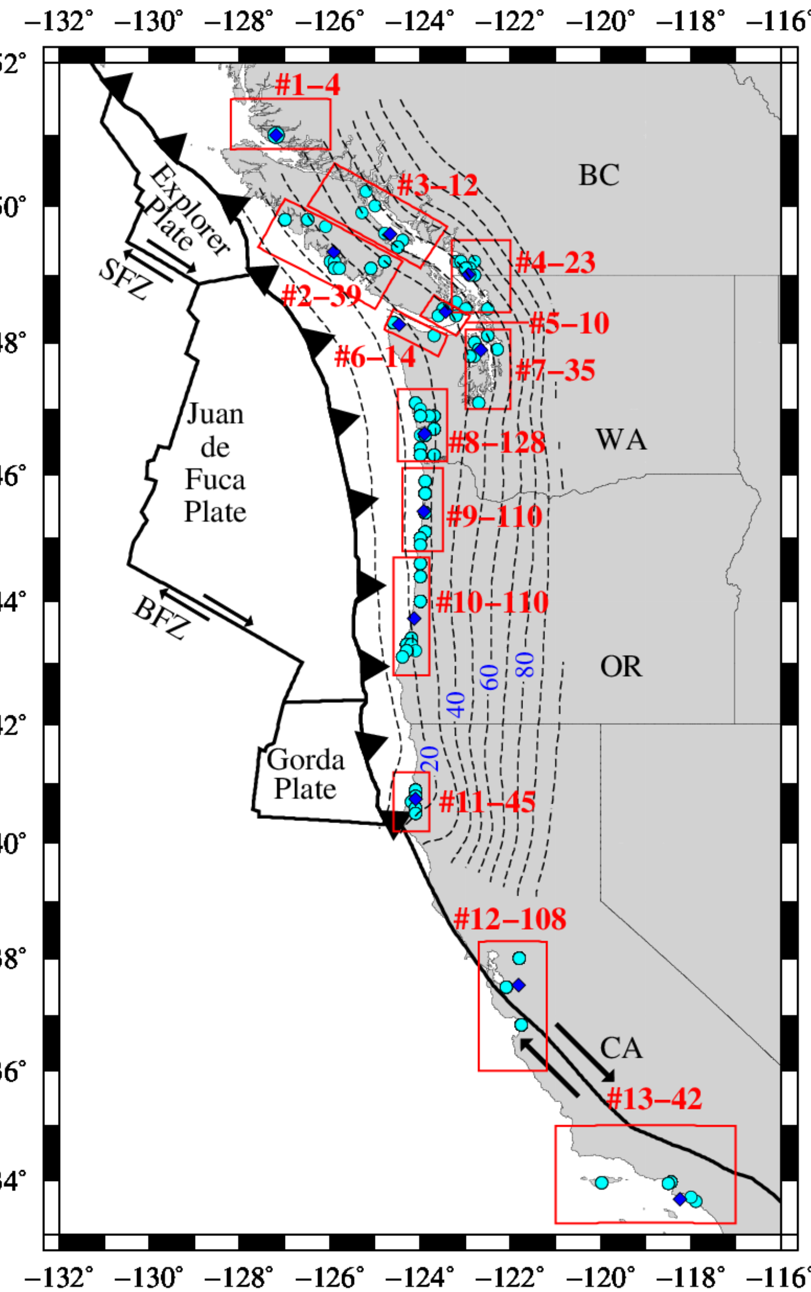

Figure 2.1. Map showing the spatial distribution of RSL data (SLIPs only) and plate boundaries.

Each of the 13 regions are indicated by a red rectangle and the number of SLIPs for each site is specified next to the site number. The locations from where SLIPs were acquired are indicated by light blue circles. The dark blue diamond in each region gives the average location of all the SLIPs for that region; this is the location at which model curves were generated for visual comparison to the observations (Figs 2.6, 2.7, 2.9, 2.11, 2.12, S1, and S4). Dashed black lines are depth contours that represent the inferred top surface of the subducted Juan de Fuca, Explorer and Gorda plates (Blair et al., 2011). Solid black lines show plate boundaries, with the triangles indicating subduction of the Juan de Fuca, Explorer and Gorda plates beneath the North American plate. SFZ and BFZ represent the Sovanco and Blanco fracture zones, respectively. US states – Washington (WA), Oregon (OR) and California (CA) – and the Canadian province British Columbia (BC) are indicated along with their geographic boundaries.

Figure 2.2 displays the sea-level data reconstructed for the 13 sites. The majority of the SLIPs in the northern region date to the pre-to-early Holocene and late Holocene. Data from the northern region record a rapid RSL fall immediately upon deglaciation of the Cordilleran ice sheet (from ~15 to ~12 ka); following this, sea levels rose gradually during early-to-mid Holocene followed by relatively stable values in the mid-to-late Holocene. At the central and southern sites, the reconstructions show RSL always below present and continuously rising during Holocene. The rate of sea level rise in the early-to-mid Holocene is higher than that in the late Holocene due, mostly, to the decrease in the rate of both meltwater input and peripheral bulge subsidence. For more discussion and details about the RSL reconstructions, please refer to Engelhart et al. (2015) and Reynolds and Simms (2015).

a)

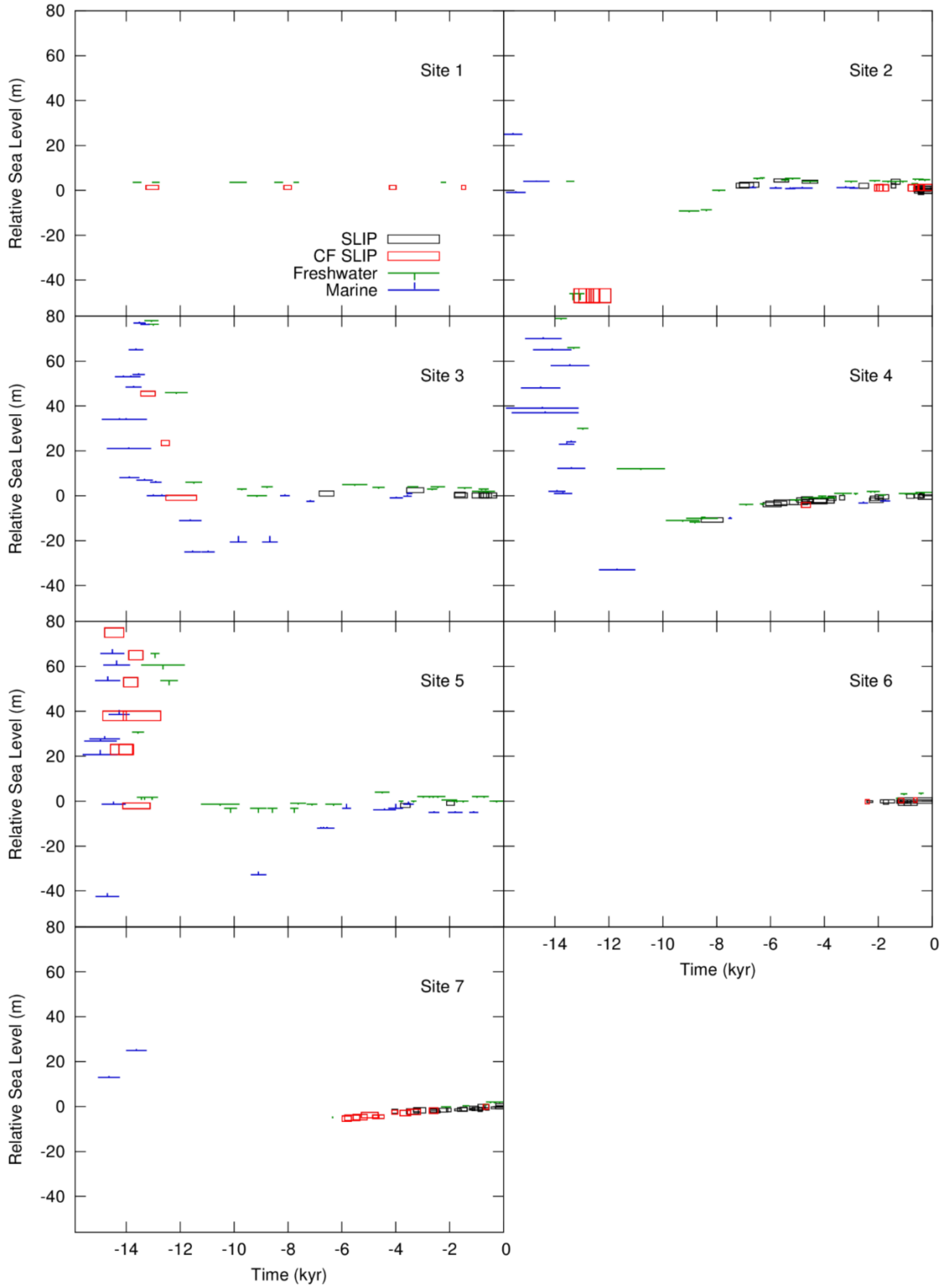

Figure 2.2. RSL reconstructions for (a) the northern region (sites 1-7) and (b) the central (sites 8-10) and southern (sites 11-13) regions. Four symbols are used to specify the type of indicator shown: SLIP, compaction free (CF) SLIP, freshwater (limiting) and marine (limiting) – see key in graphs for sites 1 and 8. The height and width of the SLIP boxes define 2σ uncertainty ranges. We note that some limiting data for sites 1, 3 and 4 lie beyond the RSL range plotted.

b)

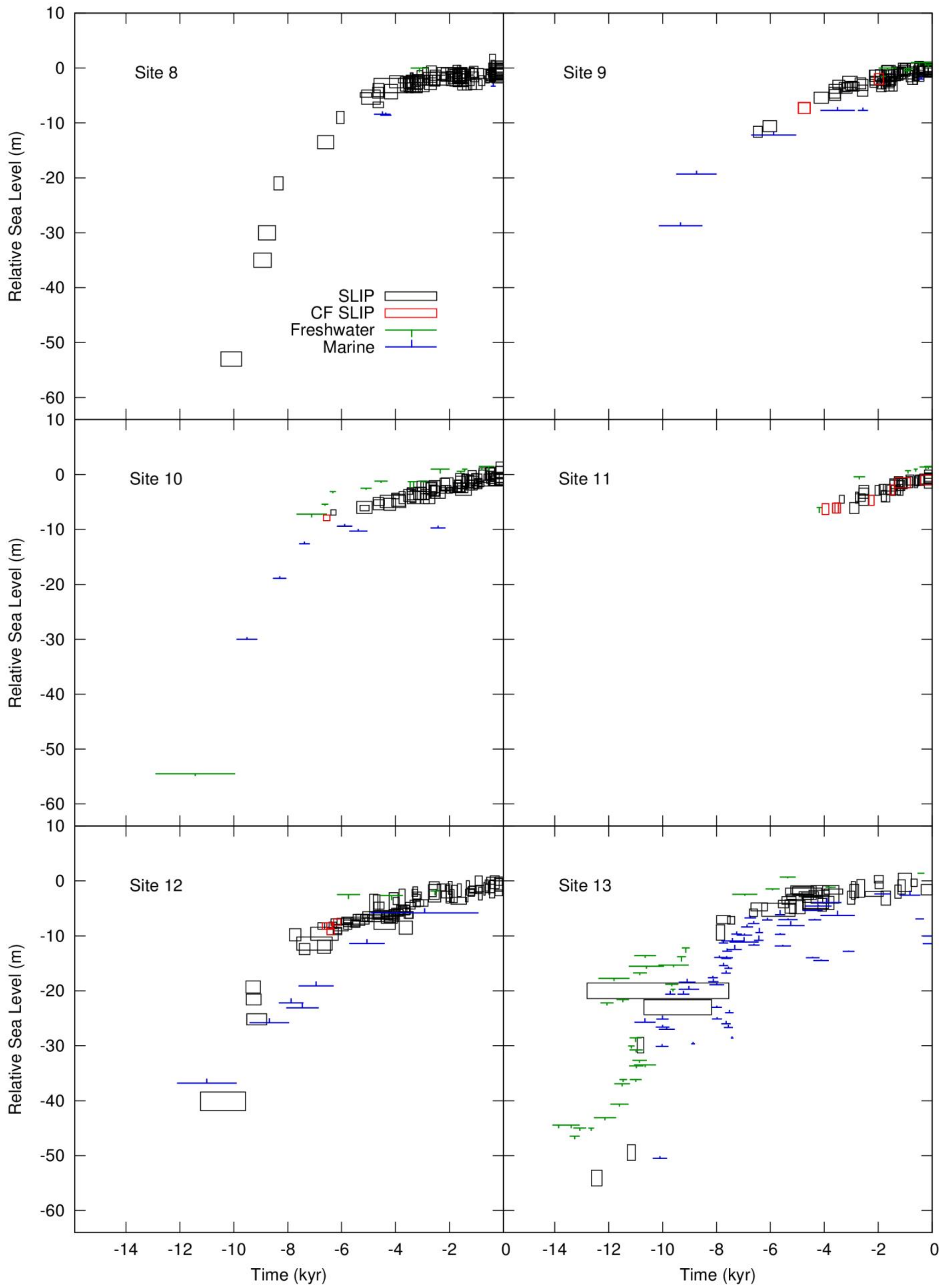

Figure 2.2. (Continued).

2.2.1.1 Isolating the GIA signal

To accurately estimate the GIA signal, the data used for determining GIA-model parameters should not be contaminated by other processes which cause RSL change, such as tectonics or sedimentary isostatic adjustment. To achieve this, either the data should be taken from a region where these processes are known to play a negligible role, or their influence can be estimated and removed from the RSL reconstructions. Compaction of sediment can also lead to erroneous results. Based on the data provided in Engelhart et al. (2015), we have identified those SLIPs that are believed to be compaction free (see Figure 2.2); however, there are only a limited number of these SLIPs and so it is not possible to robustly estimate model parameters based on these data alone.

The primary, non-GIA source of RSL in our study area is tectonic activity associated with the plate boundary that is proximal to the coastline (Figure 2.1). In order to determine the contribution of tectonics to local sea-level change, we consider results from previous studies that used the elevation of marine terraces preserved from past sea-level highstands to estimate a tectonic contribution to local RSL change (e.g., Merrits and Bull, 1989; Muhs et al., 1990, 1992). The difference between the elevation of Interglacial (MIS5a-MIS5e) marine terraces and present sea level can provide an estimate of the long-term average rate of RSL fall associated with tectonic uplift. The accuracy of this approach is limited due to a lack of knowledge on the precise height and time at which the past shoreline formed, non-tectonic contributions to the measured height difference (e.g., Creveling et al., 2015; Simms et al., 2016) and the assumption that the tectonic contribution was linear since the formation of the shoreline used to determine the tectonic signal. While we do not make any corrections to the tectonic estimates provided in past analyses, the uncertainty ranges described below are broad and so most likely accommodate the first two of these limitations. Finally, while the estimated tectonic signals are often reported as an "uplift rate"; given that they are determined from RSL indicators, it is more accurate to call them rates of RSL fall associated with tectonic uplift. This is the terminology we adopt here.

Tectonic rates of RSL fall along Washington and Oregon have been estimated in a small number of studies. For example, West and McCrumb (1988) using the Whiskey Run MIS-5a terrace proposed a range of 0.2 to 0.6 mm/yr (with an average of 0.4 mm/yr) along the northern Oregon and Washington coast. In a more recent study, Peterson and Cruikshank (2014), estimated rates of 0.1 to 0.3 mm/yr using a similar approach in the same area. The MIS-5 terraces are not well preserved along this stretch of coastline, hence the relatively broad range in estimates given. Given the difficulty in defining an accurate tectonic correction for this area, we adopted a relatively large rate of RSL fall (0.4 mm/yr) for site 9 to determine the impact this would have on our Earth viscosity parameter estimation. The impact was small, decreasing the optimum value of the upper mantle viscosity from 3×10^{21} Pas to 2×10^{21} Pas. Thus, given the large uncertainty in this value and the relatively small impact it has on our model parameter estimates, no correction was applied for site 9. Simms et al. (2016) estimated RSL rates associated with tectonic uplift along the eastern Pacific coast while explicitly considering the influence of GIA on the spatial variation in the height of marine terraces of a given age. We applied their published rates for New Port, Cape Arago, Coquille Point, and Cape Blanco to correct data from site 10 (Table 2.1).

Further south, site 11 is located just north of the Mendocino Triple Junction, where plate boundary motion changes from convergence (subducting Gorda plate) to strike-slip (San Andreas Fault System). Defining a long-term RSL rate associated with tectonic processes is difficult due to the tectonic complexity of the area. The elevation of MIS terraces suggest relatively large rates of a few mm/yr; although migration of the triple junction over the past few hundred kyr could have resulted in a significant change in this rate through time (Merritts and Bull, 1989). Using MIS-5 terraces, one arrives at a rate of ~2.4 mm/yr (Alex Simms, personal communication). However, removing this signal from the RSL data resulted in an anomalously high rate of sea level rise during late Holocene that is not compatible with those at neighboring sites (10, 12) that have relatively accurate tectonic rate estimates. For this reason, we did not apply a tectonic correction to data from site 11 but considered the influence of these data on our parameter inference and found that the results were the same whether they were included or not.

Table 2.1. Inferred rates of RSL change not associated with GIA that were applied to the RSL reconstructions before inferring GIA model parameters. The rates in the second column were assumed to be constant over the period spanned by the RSL observations. See Section 2.2.1.1 for further details.

Site	Correction to account for Non-GIA processes (mm/yr)	Reference
10	0.75 ±0.08	Simms et al. (2016) The average rate is based on marine terraces (MIS5a , MIS5c , MIS5e) at the following sites: New Port/Cape Arago/Coquille point and Cape Blanco
12	-0.2±0.1	Sacramento delta: Drexler et al. (2009) Estimated rate of RSL rise: 0.2-0.6 mm/yr
	-0.4±0.1	Southern San Francisco Bay: Atwater et al. (1977) Estimated rate of RSL rise 0.2-0.4 mm/yr
	0.33±0.02	Monterey Bay: Reynolds and Simms, (2015) Based on MIS5a Davenport terrace
13	0.18±0.04	Los Angeles Region: Reynolds and Simms (2015)
	0.65±0.06	Los Angeles Region, upside of Palos Verdes fault: Reynolds and Simms (2015)
	0.08±0.04	San Diego and Channel Islands Regions: Reynolds and Simms (2015)

Central California (site 12) hosts local faults and folds which make it difficult to determine a robust estimate of RSL change associated with vertical tectonic motion for the entire area. This area also includes river deltas which cause land subsidence due to the deposition of sediments. As a consequence of this complexity, we classified the data and the corresponding corrections into 3 locations (shown in Figure 2.3a): southern San Francisco Bay, Sacramento-San Joaquin River Delta and Monterey Bay (Elkhorn Slough, Moro Cojo Slough and Tembladero Slough). Southern San Francisco Bay has experienced subsidence between the Sangamon interglacial and Wisconsin glaciation (MIS5-MIS2; a period of ~100 kyr) (Atwater et al., 1977). Based on the elevation of Wisconsin thalweg, located at least 15 m higher than the deepest Sangamon estuarine deposits, Atwater et al. proposed a subsidence induced RSL rise of 0.2-0.4 ± 0.1 mm/yr. Neotectonic subsidence of the Sacramento delta due to motion across the Midland Fault is estimated to be 0.2-0.6 mm/yr (Weber-Band, 1998; Drexler et al., 2008). Finally, Monterey Bay is estimated to have uplifted, with a rate of RSL fall of 0.33 ± 0.02 mm/yr (Muhs et al., 2006; Reynolds and Simms, 2015). We corrected the RSL data from the Monterey Bay region using this rate but considered the full range of rates for San Francisco Bay (0.1-0.5 mm/yr) and the Sacramento delta (0.2-0.6 mm/yr). We adopted rates for the latter two areas that produced the most coherent RSL curve for site 12; specifically, RSL rates of 0.4 and 0.2 mm/yr for San Francisco Bay and Sacramento delta, respectively. As can be seen in Figure 2.3b, the data are better aligned after applying these corrections. We note that spatial variability in Holocene RSL due to GIA is small across these three locations and so cannot account for the vertical spread evident when all the SLIPs are combined on a single plot (Figure 2.3a).

a)

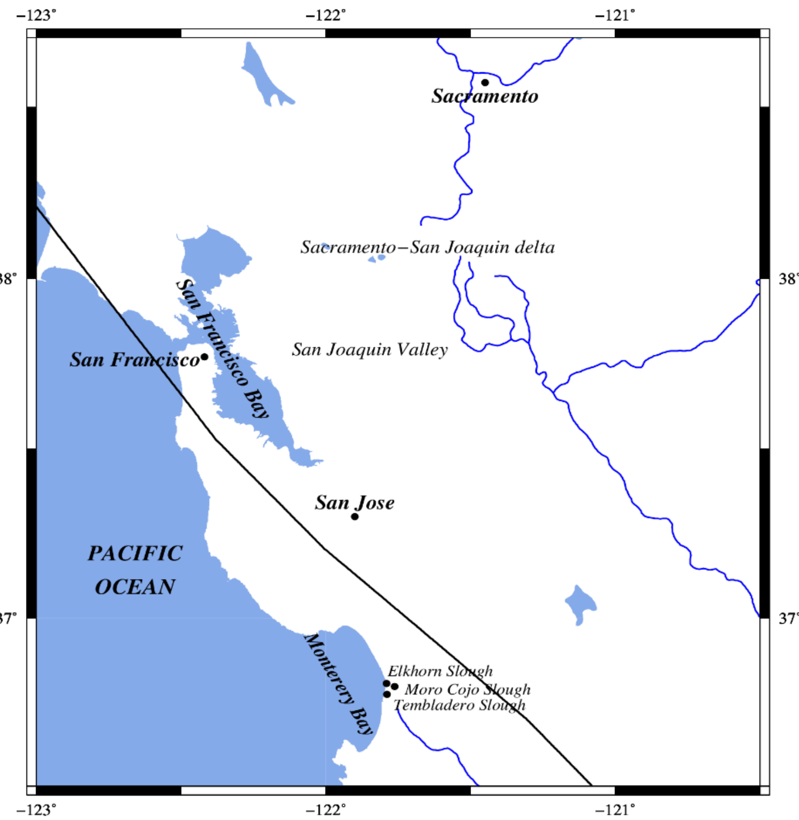

b)

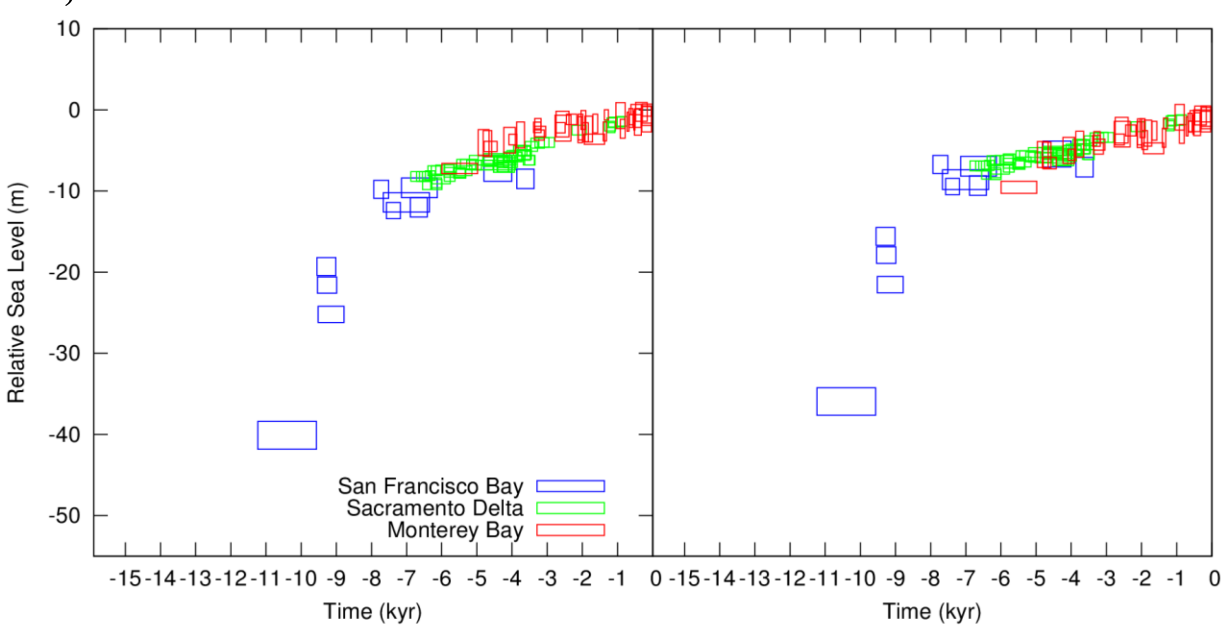

Figure 2.3. a) Map of central California showing locations mentioned in text; b) SLIPs from site 12 as published in Engelhart et al. (2015) (left) and with corrections applied for non-GIA processes (Table 2.1) (right). The height and width of the SLIP boxes define 2σ uncertainty ranges.

For southern California, site 13, we applied the tectonic corrections provided in Reynolds and Simms (2015); i.e., 0.18 mm/yr RSL fall for the Los Angeles area, 0.65 mm/yr RSL fall for the up-thrown side of the Palos Verdes fault in the Los Angeles region, and 0.08 mm/yr RSL fall for the San Diego and Channel Islands areas.

A summary of the applied tectonic corrections for sites 10, 12 and 13 is provided in Table 2.1. We note that the uncertainties in these corrections were added in quadrature to the uncertainties in the SLIPs.

In contrast to the central and southern regions, no tectonic corrections are available for the northern region as glaciation has eroded evidence of past RSL highstands. Therefore, an alternative approach must be applied to attempt to isolate the GIA signal in order to constrain GIA model parameters. Given that this region was once covered by the Cordilleran ice sheet, the rapid rebound subsequent to ice retreat, indicated by RSL fall at sites 2-5, is the dominant signal that can be uniquely associated with GIA. Therefore, the optimisation of model parameters was done using only the RSL fall component of the observations from sites 2-5 (see Section 2.3.1.1 for details and further discussion).

2.2.2 GIA model

Our GIA model calculates the response of a Maxwell (viscoelastic) spherically symmetric Earth to a specified loading history that includes ice and ocean components. We define the density and elastic structure of our model Earth using a global seismic model (Dziewonski and Anderson, 1981) and depth discretization that varies from 1 km in the crust to 30 km at the base of the mantle. The viscous structure is more crudely discretized into three shells: an outer region with variable thickness (i.e., 46, 71, 96 or 120 km) and high viscosity to represent an elastic lithosphere and two deeper regions with uniform viscosity to represent the upper and lower mantle. The upper mantle extends from just below the lithosphere to a depth of 670 km and the lower mantle extends down to the mantle-core boundary. A primary source of uncertainty in GIA model output is associated with Earth viscosity structure. In order to accommodate this source of uncertainty, we explore a large range of viscosity values (in addition to the four values for lithospheric thickness (LT) defined above). Upper mantle viscosity (UMV) spans the following 16 values: [0.005, 0.008, 0.01, 0.02, 0.03, 0.05, 0.08, 0.1, 0.2, 0.3, 0.5, 0.8, 1, 2, 3, 5] $\times 10^{21}$ Pas and lower mantle viscosity (LMV) spans the following 11 values: [1, 2, 3, 5, 8, 10, 20, 30, 50, 70, 90] $\times 10^{21}$ Pas. Note that the relatively low bound for UMV reflects results from previous studies that found the need for viscosity values as low as 3×10^{18} Pas to fit RSL observations from Vancouver Island (James et al., 2009b). In addition to the above viscosity structure, three 4-layer models are also applied to consider the influence of a possible low-viscosity asthenosphere layer, which could be associated with the mantle wedge located above subducting lithosphere (e.g., James et al., 2009b). These Earth models consist of an asthenosphere layer with viscosity of 5×10^{18} Pas and upper and lower mantle layers with viscosities of 5×10^{20} and 10^{21} Pas, respectively. Three values are assigned to the asthenosphere thickness: 103, 185 and 389 km.

The Late Pleistocene ice loading histories applied here include model reconstructions of the North American Ice Sheet Complex, including Laurentian, Cordilleran and Innuitian ice sheets, published by Tarasov et al. (2012). All of these reconstructions are based on a physics-based, glacial systems model calibrated against regional observations such as ice extent, RSL, and present-day crustal uplift rates. We use a high variance subset of 25 ice histories from this analysis. This subset of ice models was chosen to provide better fits when constrained with regional RSL data from south of Alaska and present-day uplift rates from British Columbia and Alberta. Figure 2.4 shows the average thickness of these 25 ice histories and their related standard deviation at 21 and 10 ka. At 21 ka, the modelled North American Ice Complex was at its maximum extent covering the whole of Canada and some northern parts of the United States with the thickest ice located west of Hudson Bay

(Figure 2.4a). Following 21 ka, there was no major loss of ice until ~15 ka. The majority of ice was deglaciated from western Canada by ~10 ka (Figure 2.4c); only some small areas were still covered by the remnants of Cordilleran ice sheet. Figure 2.4b indicates that the ice history is relatively well constrained in western areas compared to most other regions at 21 ka. The main areas of uncertainty at the glacial maximum are the Hudson Bay region, southeastern and northeastern Canada. At 10 ka the Hudson Bay area seems to be the least well constrained given the spatial distribution in the standard deviation of the model subset (Figure 2.4d). This is likely due to the large possible variation in ice streaming through Hudson Strait in the glaciological model. By applying this large number of regional ice models, we sample some of the parametric uncertainty associated with this model input. We note that four additional North American ice models were considered in an attempt to improve fits to RSL data in the northern region; thus, a total of twenty nine ice models were used. The regional North American ice model reconstructions were patched into the ICE-5G history (Peltier, 2004) as a background global model. The reader is referred to the original articles for further details.

The ocean load for a given Earth model and ice history was computed in a gravitationally self-consistent manner by solving the sea-level equation (Farrell and Clark, 1976). We solved the generalised form of this equation (Mitrovica and Milne, 2003; Kendall et al., 2005) to accurately account for lateral variations in shoreline position through time. The influence of Earth rotation due to GIA was also included in our calculations (Milne and Mitrovica, 1998; Mitrovica et al., 2005). Finally, spatial fields were represented using spherical harmonic functions with a truncation of degree and order 256.

a)

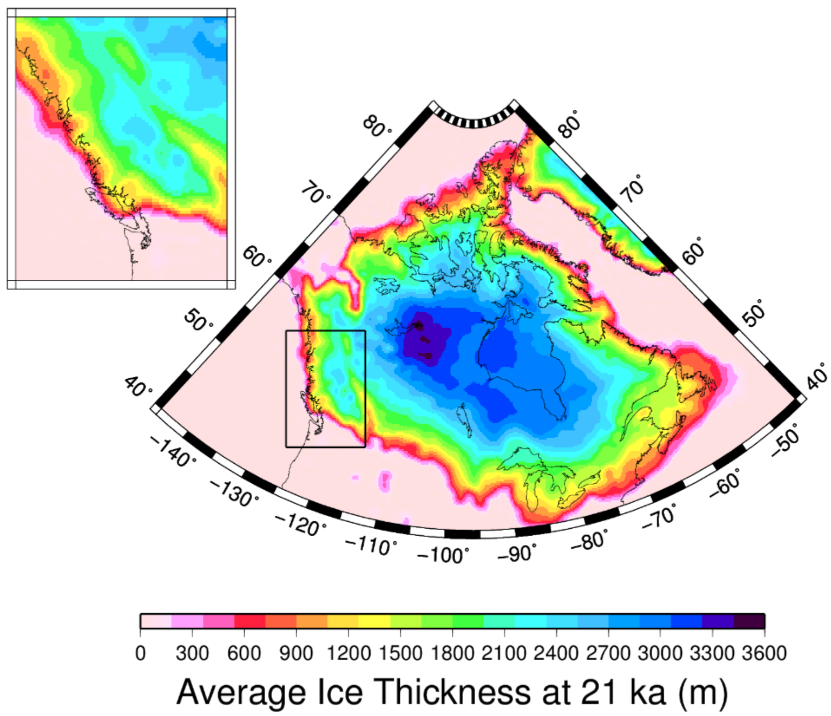

b)

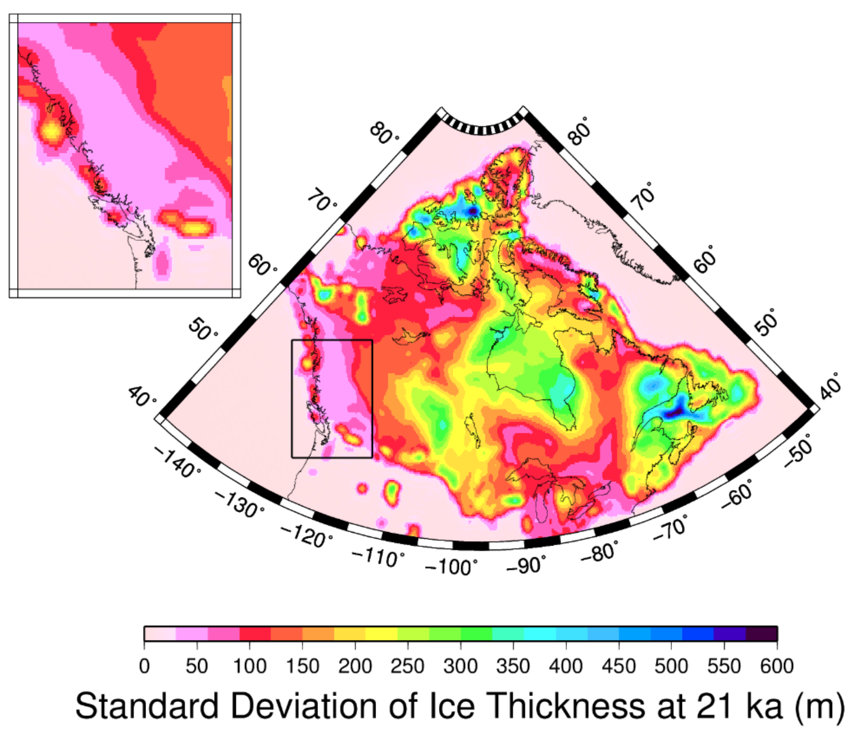

Figure 2.4. The mean (a) and standard deviation (b) of the 25 North American ice model reconstructions from Tarasov et al. (2012) adopted in this analysis for the time 21 ka.

c)

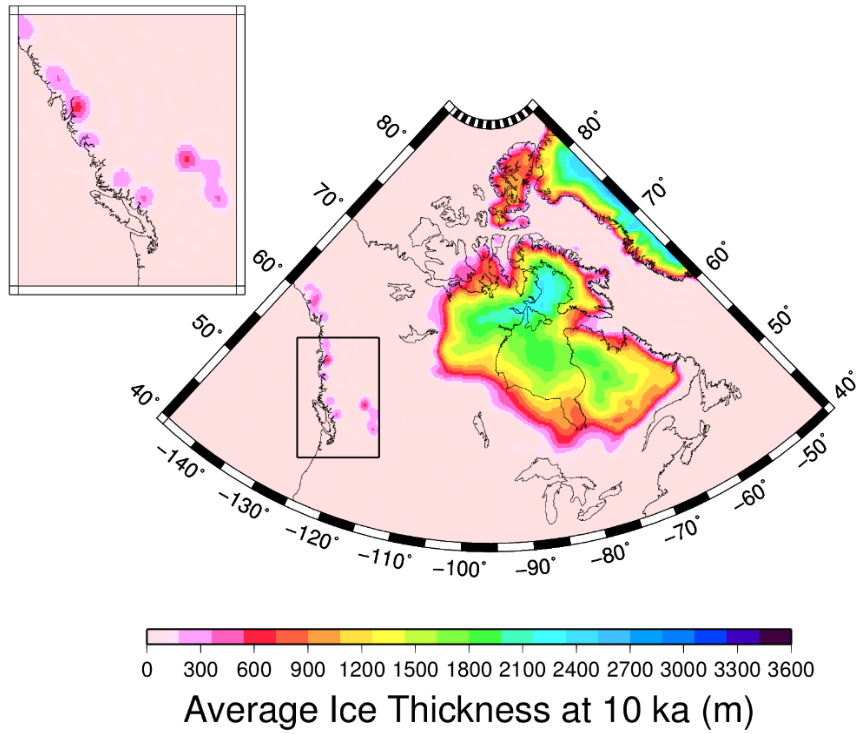

d)

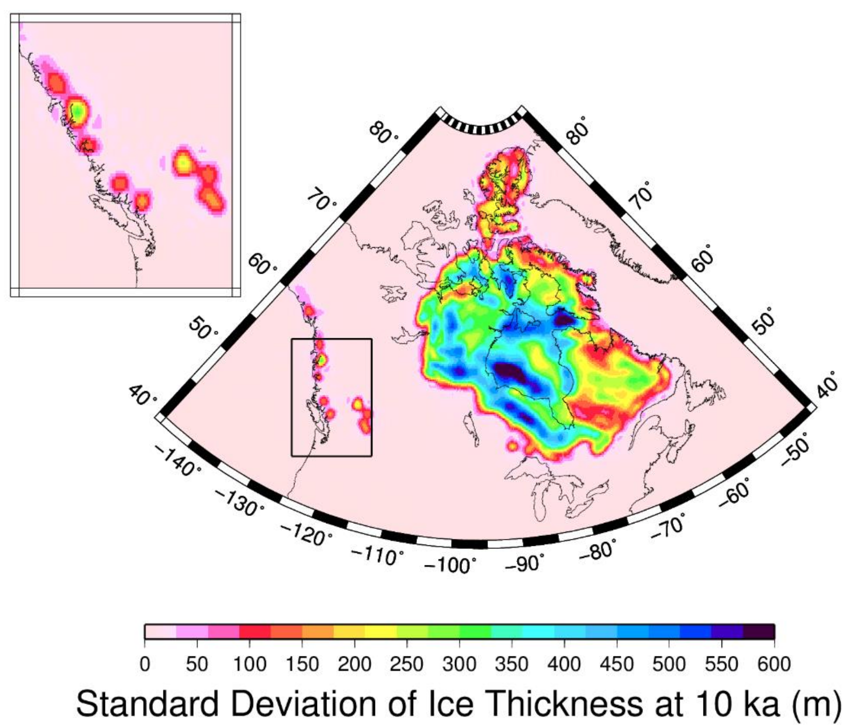

Figure 2.4. (continued). Frames (c) and (d) also show, respectively, the mean and standard deviation but for 10 ka. The left-hand map in each frame shows results for the area indicated by the black rectangle in the right-hand map and illustrates the ice coverage in the northern region.

2.2.3 Estimating model parameters

Constraining GIA model parameters and, consequently, the GIA signal was done by comparing model output to the reconstructed RSL values described above. With the exception of the northern region, limiting data were not used to infer model parameters; however, limiting data are included in figures that compare RSL data to model output and so are used to assess the overall quality of the model fits. In order to determine the best fitting 1D viscosity model, the data-model misfits are estimated for each combination of 704 Earth models and 29 ice histories (a total of 20416 model runs). To do this, the model curve is computed at each SLIP location (light blue circles in Figure 2.1) and the point on the curve with minimum distance to the SLIP is determined (i.e., the norm-2 or Euclidean distance). This procedure is repeated for all SLIPs available in the region (northern, central or southern). The chi-squared misfit of a given model parameter set is then calculated for a given region via (Mitrovica et al., 2000),

$$\delta = \frac{1}{N}\sqrt{\sum_{i=1}^{N}\left(\frac{RSL_i^{data}-RSL_i^{model}}{\Delta_{rsl,i}}\right)^2+\left(\frac{t_i^{data}-t_i^{model}}{\Delta_{t,i}}\right)^2} \tag{2.1}$$

Where, RSL_i^{data} and RSL_i^{model} are the observed and predicted RSL values for the i^{th} SLIP with 2-σ observational uncertainty of $\Delta_{rsl,i}$; t_i^{data} and t_i^{model} are the observed and predicted age values with 2-σ observational uncertainty of $\Delta_{t,i}$. N is the total number of SLIPs in the region. As noted in Section 2.2.1, uncertainty in the tectonic correction is included in the height uncertainty of the SLIPs. The best fitting 1D model for a given region is defined as that with the parameter set that minimises the δ value.

Along with isolating the optimal GIA parameter set, it is important to provide a robust estimation of the uncertainty range as a reliability criterion for the estimated model parameters. In this paper we follow Love et al. (2016) and apply a heuristic approach by considering a confidence interval of (P+(100-P)/2)% as the bounding criteria (with confidence level of P = 68.27% for a 1σ bound, etc). The procedure for determining the model bounds includes: first, for each set of model parameters we determine the percentage of SLIPs which pass above and below a given model curve. The derived percentages for each model run are then compared with the threshold value ([P+(100-P)/2]%). If the percentages of the SLIPs which lie above the model curve are greater than the assumed threshold, the model run is categorized as a lower bounding model (vice versa for the upper bounding case). Among all of these bounding model runs, the two with the minimum misfit values are then selected as the lower and upper bounding runs. In some regions, this procedure does not result in both an upper and lower bounding run and so a different approach was applied.

Again, we follow Love et al. (2016) and apply a Bayesian approach as an alternative method to determine the model uncertainty. However, given that certain requirements of this approach cannot be robustly met, this approach is not applied rigorously and is thus referred to as "nominally Bayesian." In order to determine 1σ bounds from this approach, we apply Bayes' theorem as follows:

$$P(m|d) \propto P(d|m)\, P(m) \tag{2.2}$$

Where, $P(m)$ is the prior probability, $P(d|m)$ is the likelihood function and $P(m|d)$ is the posterior probability, for model parameters m and observational data d. The likelihood function is an indicator of closeness of a given model output to the observations. Here, we consider the likelihood as an exponential function with negative δ values as its exponent (e.g. Hauser et al., 2012). The prior represents our knowledge about the model parameterization before analyzing the data. We consider a uniform prior such that the posterior estimates sum to one. Then a sub-ensemble of model parameters with the highest posteriors are chosen by adopting a 1σ threshold (0.68). The assumptions made here, such as assuming a uniform prior or considering

δ values as the log-likelihood and not taking to account the multivariate structure of the residuals, may affect the accuracy of our posterior estimates (Love et al., 2016).

The non-uniform distribution of RSL data in both space and time can bias the obtained results (Briggs and Tarasov, 2013) when the multivariate residual structure is ignored. To test whether this is the case here, we reduce the effect of data clustering by applying a spatio-temporal weighting method. This weighting method involves scaling both the observed elevations and time uncertainties so that the clustered data would be less weighted for the misfit calculations. We first applied spatial weighting by considering data from each site in a region as one group. We scaled the elevation uncertainties by the square root of the number of SLIPs at each site divided by the square root of the total number of data in that region (north, central or south). Then a temporal partitioning was applied by considering 5 time intervals: from present to 2 ka, 2 ka to 4 ka, 4 ka to 6 ka, 6 ka to 8 ka and older than 8 ka. For each site, the observations which lie within each time interval are identified and the weighting scale for age uncertainties was computed as the square root of the number of SLIPs in each time bin divided by the square root of total number of regional data. After scaling the uncertainties, the misfit between observations and the model predicted values were calculated via eq. (2.1) using the scaled uncertainties. The δ results were normalised to facilitate the comparison of weighted and non-weighted values.

2.3 Results and Discussion

2.3.1 Estimating Model Parameters

2.3.1.1 Northern region

As discussed at the end of Section 2.2.1.1, no estimates of the tectonic signal are available for the northern region and so to minimise any potential bias due to a tectonic overprint on the RSL curves, we focus on the large and rapid RSL fall associated with major ice retreat from the region. Not all sites record this fall and so the optimisation of model parameters is based only on RSL records from sites 2 (Western Vancouver Island), 3 (Northwestern Georgia Strait), 4 (Southeastern Georgia Strait) and 5 (Victoria region) which cover the time window of rapid RSL fall (from ~15 to ~12 ka). To focus on the RSL fall portion of the observations, we chose the youngest SLIP during the RSL fall time window at each site to define a reference time and height such that the model curve is vertically shifted to pass through this reference datum. In doing this, the influence of any tectonic activity occurring after the reference time will be removed and the calculated model misfits will be dependent only on the large RSL fall associated, primarily, with regional deglaciation. The model-data misfits were calculated using the same misfit criterion as before but using the chosen reference SLIP rather than present-day RSL (i.e. 0 m). Since there are relatively few SLIPs in the RSL fall time window (total of 16), we also used limiting data where available (46 marine and 19 terrestrial data). However, given that the limiting data only provide a one-sided bound on RSL, it was not possible to accurately determine the norm-2 distance (see Section 2.2.3). Therefore, we applied a simplified misfit criterion that considers only the height of the limiting data:

$$\delta = \frac{1}{N}\sqrt{\sum_{i=1}^{N}\left(\frac{RSL_i^{data} - RSL_i^{model}}{\Delta_{rsl,i}}\right)^2} \tag{2.3}$$

The misfit value is set to one if the model curve passes above/below a lower/upper limiting data point; otherwise, the value is computed using equation 2.3. The δ values are plotted in Figure 2.5.

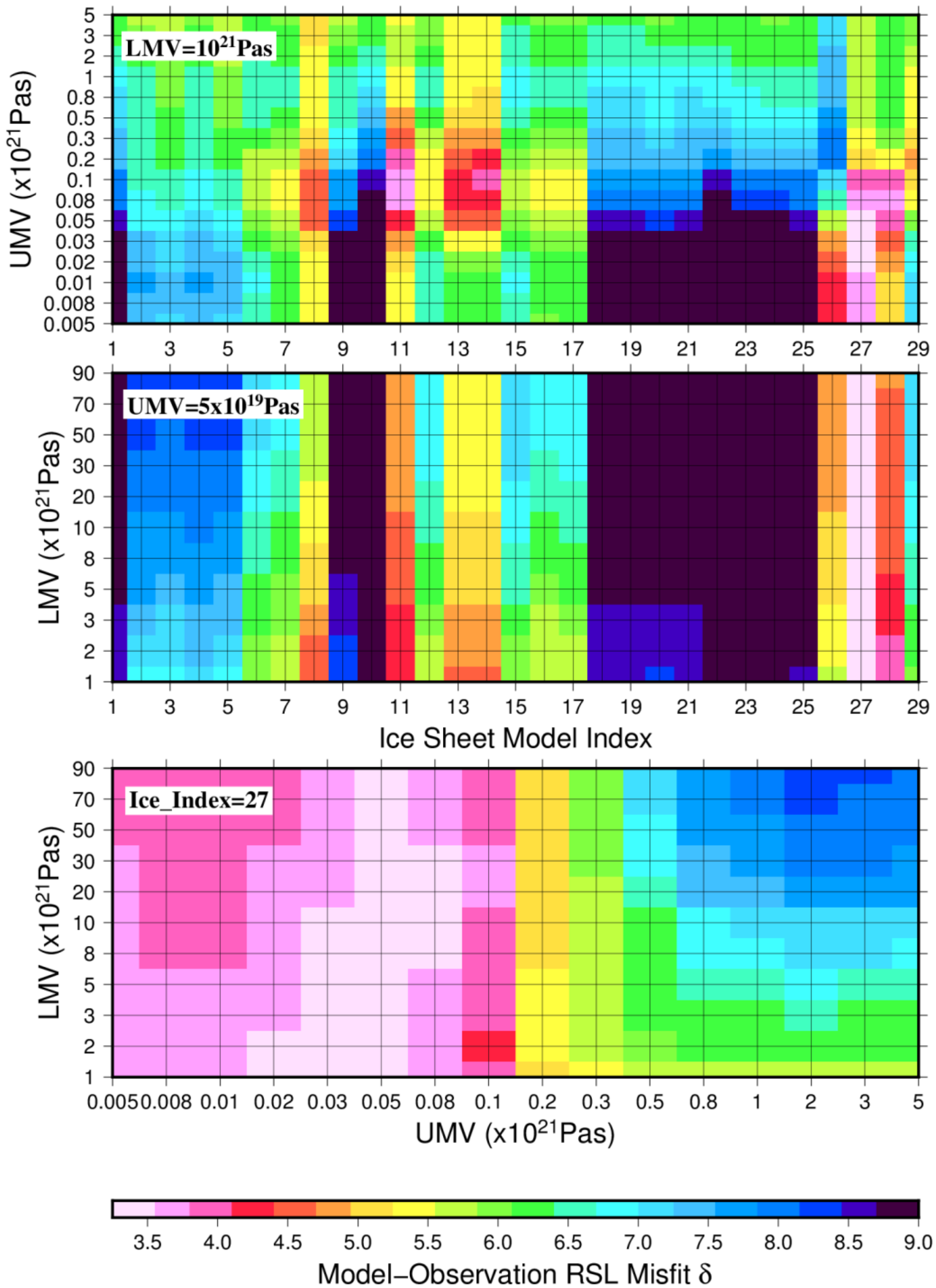

Figure 2.5. Data-model misfit values for the northern region. The upper panel displays the misfit values when the LMV is constant (10^{21} Pas) and δ is only a function of UMV and ice model. The middle panel shows δ as a function of LMV and ice model with the UMV fixed at 5×10^{19} Pas. The lower panel shows the δ values in terms of varying LMV and UMV for the case of ice model 6885R (index number 27). In all 3 plots, the lithosphere thickness is constant and has a value of 46 km. The misfit values for this data set are higher than those for the central and southern regions due, in part, to the inclusion of limiting data in the calculation.

Being so close to the ice margin, the data-model misfits for this region are extremely sensitive to the deglaciation history. All of the original 25 ice models were unable to match well the timing of RSL fall. Those that deglaciated relatively late produced the lowest misfit values (e.g. index numbers 8, 13, 14, 16, 17) and so we generated 4 additional models to explore the impact of this aspect of the model on the δ values. Two of these models (index numbers 28 and 29), were generated by changing the local climate forcing (e.g., amplifying the local precipitation and extra cooling during the last glacial maximum) for one of the original models (9927; index number 22) that produced the best fits to the observations from the whole North America in the study of Tarasov et al. (2012). The other two models (index numbers 26 and 27), were produced by delaying the deglaciation chronology of a model which provided the best fit to the observations from the northern region (6885; index number 11), by 1000 and 500 years, respectively. Specifically, a period of no change in ice extent was imposed between 17-16 ka or 17-16.5 ka. As evident from Figure 2.5, the model with deglaciation delayed by 500 years (index number 27) provides the best fit to the observations. The need to create these additional four ice models reflects the fact that our original 25-model subset is relatively small compared to that required to more effectively span the range of plausible deglaciation scenarios (see Tarasov et al. (2012) for a discussion of this point).

The bottom panel in Figure 2.5 indicates that for a given ice model there is a preference for very low viscosity values in the upper mantle but no clear preference for a specific LMV value. This was the case for the majority of ice models used and is a consequence of the deformation being focused in the upper mantle due to the large contrast in the UMV versus LMV values. The minimum data-model misfits were obtained with: LT = 46 km, UMV = 5×10^{19} Pas, LMV = 10^{21} Pas and ice model 6885R (index number 27). Our inference of UMV is in agreement with the range inferred in previous studies (5×10^{18} - 5×10^{19} Pas; James et al., 2000, Clague and James, 2002, James et al., 2009b).

The optimum model curve is plotted in Figure 2.6 along with the data in the RSL fall time window for sites 2, 3, 4 and 5. The model curve is shifted vertically such that it passes through the reference SLIP (i.e. the youngest in the RSL fall time window), except for site 4 where no SLIPs fall within this window and so the data point at ~8 ka was used. Inspection of Figure 2.6 indicates that the optimised parameter set can simulate reasonably well the reconstructed RSL records. However, even by choosing a very low viscosity for the upper mantle, it is difficult to capture all the SLIP data from the Victoria region (site 5) which date back to 14-15 ka.

Model RSL curves for the entire data time window based on the above optimal parameters are shown in Figure 2.7. The model captures the majority of the data (SLIP and limiting) at sites 4, 5 & 6. However, we note that the parameters tuned to match the large RSL fall do not provide good quality fits at most sites. There are a number of possible reasons to explain the relatively poor fits in this region. The existence of a significant tectonic overprint is one possible explanation. Since there are no direct observational constraints on this signal (see Section 2.2.1), we estimated it by considering data-model residuals. However, the results (not shown) did not indicate the existence of a coherent secular uplift signal at all sites, suggesting model inaccuracy as a more likely explanation. One possible limitation in this regard is the relatively low spatial resolution of the ice model (1 degree longitude by 0.5 degrees latitude, or about 55 km) which would not capture well the short wavelength and high variability climate and ice dynamic processes characteristic of regions with dramatic topography. As for the Earth model, the assumption of a linear Maxwell rheology could be a significant source of error. Departures from this simple model could be related to, for example, power-law deformation (e.g. Wu, 1995; James et al., 2009b), such that the high stresses during initial deglaciation would lead to relatively low effective viscosities during this time period with an increase to higher values as stresses relax; also, one cannot rule out a possible contribution from GIA-induced faulting (Steffen et al., 2014; Wu and Hasegawa, 1996) during the early deglaciation period at some locations. Ultimately, by focusing on the observed RSL fall to obtain the greatest (GIA) signal to noise ratio, one limitation is that the amplitude and rate of the signal make the assumption of a linear Maxwell rheology more tenuous.

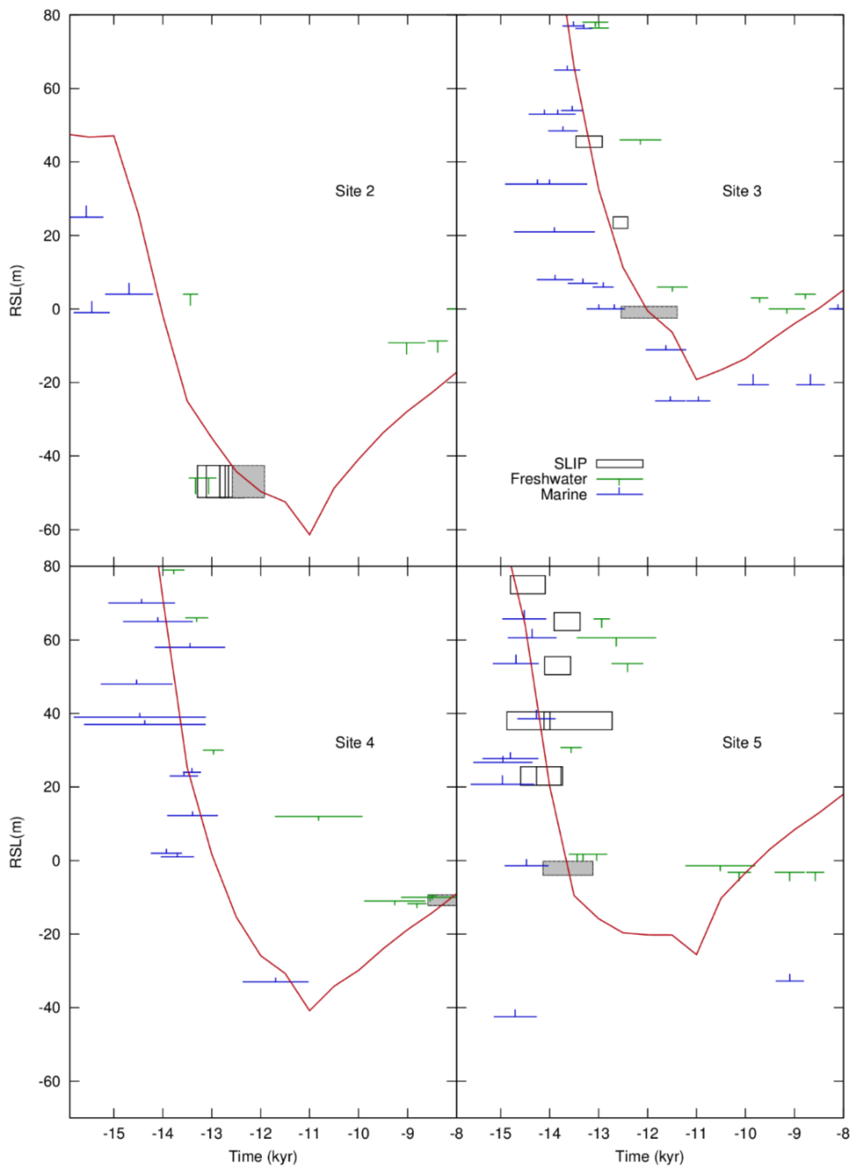

Figure 2.6. Data-model comparison for sites 2, 3, 4 and 5 in the northern region when using the youngest SLIP that fell within the RSL fall time window (~15-12 ka) as the reference height (except for site 4, where the SLIP dated to ~8 ka was used). All reference SLIPs are shaded grey.

The optimal curve (red) is plotted based on the following model parameters: UMV of 5×10^{19} Pas, LMV of 10^{21} Pas and ice model number 6885R (index number 27). The lithosphere thickness is set to 46 km. The meaning of each data symbol is indicated in the frame for site 3. The height and width of the SLIP boxes define 2σ uncertainty ranges.

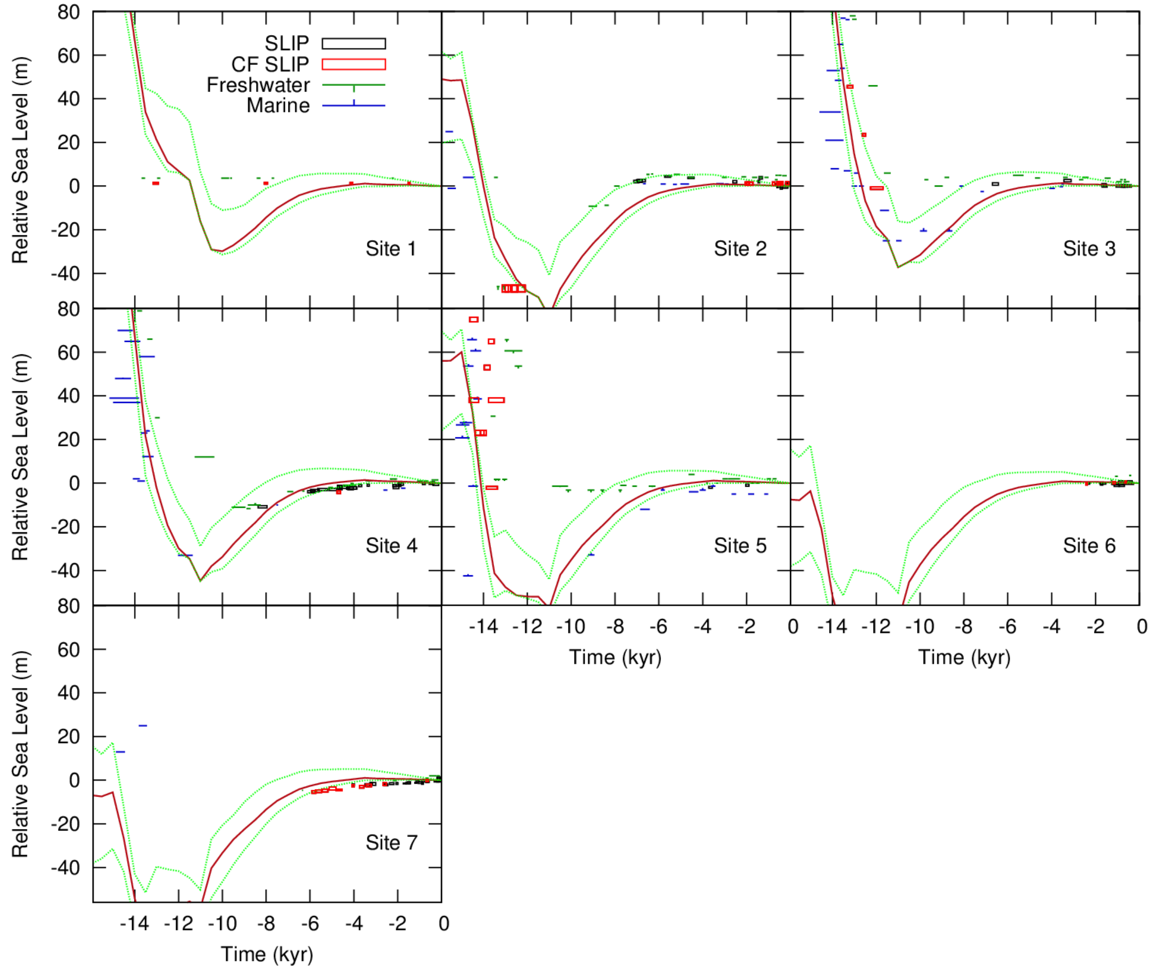

Figure 2.7. Data-model comparison for the northern region. The optimal curve shown is the same as that in Figure 6. Model uncertainty (1σ) calculated using the nominally Bayesian approach is indicated by the green-dotted lines. To be consistent with the indicated model uncertainty, the SLIP boxes were drawn to represent 1σ uncertainty in height and age. The meaning of each data symbol is indicated in the key for site 1.

Another possibility relates to our adopted depth parameterisation of (sub-lithosphere) viscosity structure: two layers might not be sufficient to capture the sensitivity of the RSL observations to the actual variation of this parameter. For example, if a low viscosity region were to exist, it would likely be quite limited in depth extent as this is more compatible with it being associated with the sub-oceanic asthenosphere and/or a continental mantle wedge above the subduction zone (James et al., 2009b). In either of these cases, the flow within this layer will be more horizontal and channel like. We explored this possibility by considering a layer of low-viscosity asthenosphere with a background mantle defined by UMV = 5×10^{20} Pas and LMV = 10^{21} Pas. The corresponding results are shown in Figure S1 for 3 different thicknesses of asthenosphere: 103, 192 and 394 km along with the optimum model curve derived from the RSL fall window. The model with the thickest asthenosphere layer do produce a slightly better fit to younger data for some sites: southeast of Strait of Georgia (site 4), southern Vancouver Island (site 5), northern Washington coast (site 6), and Puget Sound (site 7). However, there is no clear preference over the optimum model curve as it deviates from data at other sites, especially younger data from western Vancouver Island (site 2) and northwest of the Strait of Georgia (site 3). Although based on small set of model runs, these results suggest that a 1D representation of shallow viscosity structure cannot capture well the observed spatial and temporal variability of RSL evolution in the northern region.

We applied the heuristic method described in Section 2.2.2 to quantify the uncertainty bounds of the GIA model for the northern region. Since no upper bound could be distinguished using uncertainties in model input parameters, we also applied the nominally Bayesian method described in Section 2.2.2 to estimate the uncertainty ranges. The obtained uncertainty bounds using this method are shown by the green-dotted lines in Figure 2.7.

To conclude this section, we determined model parameters using all the SLIPs in the northern region. This was done to provide a comparison to the results obtained when considering the period of RSL fall only and to examine a potential bias introduced by ignoring possible tectonic overprints. The results are presented in

Figures S2 (unweighted) and S3 (weighted). The optimized model parameters for the unweighted dataset are the same as those estimated using the RSL-fall time window. When data weighting is applied, the preferred UMV reduces by an order of magnitude from 5×10^{19} to Pas to 5×10^{18} Pas. In this case, the optimized model parameters for LT, LMV and ice history are: 46 km, 10^{21} Pas, and 9927K (index number 28). Thus, when we apply the more accurate (weighted) approach, the inferred optimal parameters differ from those based on the RSL fall immediately after local deglaciation. One possible interpretation of this difference is that it reflects the influence of tectonics on the RSL curve. Specifically, tectonic uplift would shift the heights of the older SLIPs (to higher values) due to a steady uplift (RSL fall) since Late glacial times. (Note that, by focusing on the RSL fall only (i.e. referencing the SLIPs to a time at the end of RSL fall interval), the influence of such an overprint would be considerably reduced). Fitting this enhanced RSL fall for a given load history would require a larger uplift in a given time, hence the need for lower viscosity in the upper mantle. Although the change to the optimal model parameters, particularly UMV, is substantial, the impact on the form of the misfit function is not large (compare Figs 2.5 & S3; note that the markedly different absolute values of the misfit function in these figures is a consequence of using limiting data when calculating misfits using the RSL fall approach).

The optimal model curve derived from applying the weighting approach is plotted in Figure S4. The optimized model curve in this case shows a similar pattern to the model curve derived from considering the RSL fall time window only (Figure 2.7). There are differences, however, particularly between the late glacial and the mid-Holocene when the parameters tuned to fit the observed RSL-fall produce a curve that is significantly lower than that based on the entire weighted data set. There are also differences in the timing of RSL fall, reflecting differences between the two ice models preferred in each case.

The results obtained for this region (Figures 2.7, S4) suggest that no single 1D model can fit the whole dataset, with discrepancies likely arising from a number of model limitations, including tectonic effects of the Cascadia Subduction Zone, lateral variation in viscosity structure, or other unmodelled processes as outlined above.

2.3.1.2 Central region

Using the total number of 348 SLIPs for sites 8-10, the preferred model parameters determined using the spatio-temporal weighting approach are: LT = 71 km, UMV = 2×10^{20} Pas, LMV = 10^{22} Pas and ice model 9858. The sensitivity of the misfit function (δ) to different model parameters is shown in Figure 2.8; specifically, δ values are plotted in terms of two pairs of model parameters while the others are constant.

The results show that, for the ranges in input parameters explored, the δ values show the least sensitivity to changes in the chosen ice history and the greatest sensitivity to changes in UMV. Regardless of the adopted ice model, the observations prefer an UMV of 2×10^{20} Pas and a LMV in the range $5\text{-}30\times10^{21}$ Pas. Using the optimal ice model (9858; index number 15), the optimal LMV was determined to be 10^{22} Pas. The influence of data weighting is relatively minor, as evident when comparing Figure 2.8 to Figure S5 which shows equivalent results when no weighting was applied. In this case, the optimal parameters were determined to be: LT = 96 km, UMV = 2×10^{20} Pas, LMV = 8×10^{21} Pas and ice model 9858. Comparison between different LT and LMV values reflects the relatively low sensitivity of δ to changes in these model parameters. Although the changes in some parameters seem significant, the predicted RSL curves for each parameter set are very similar (Figure 2.9), indicating that the results obtained in the non-weighted case are not significantly biased. The results in Figure 2.9 also demonstrate that the optimum model curve provides a good fit to the majority of the data. The older SLIPs at site 8 are driving the preference for relatively low viscosities in the upper mantle as the SLIPs from sites 9 & 10 prefer higher values.

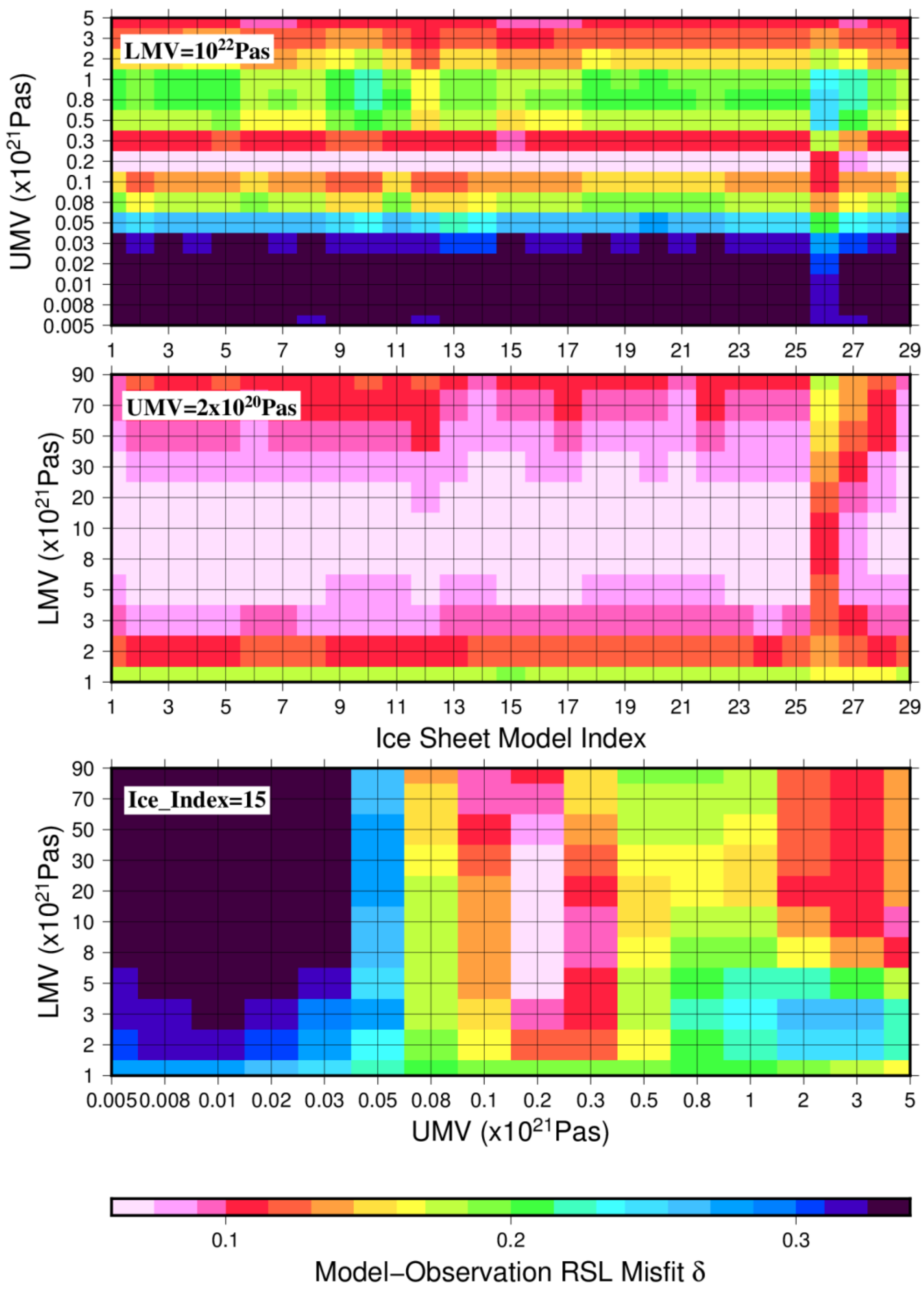

Figure 2.8. Data-model misfit values for the central region when applying the data weighting approach. The upper panel displays the misfit values when the LMV is constant (10^{22} Pas) and δ is only a function of UMV and ice model. The middle panel shows δ as a function of LMV and ice model with the UMV fixed at 2×10^{20} Pas. The lower panel shows the δ values in terms of varying LMV and UMV for the case of ice model 9858 (index number 15). In all 3 plots, the lithosphere thickness is constant and has a value of 71 km.

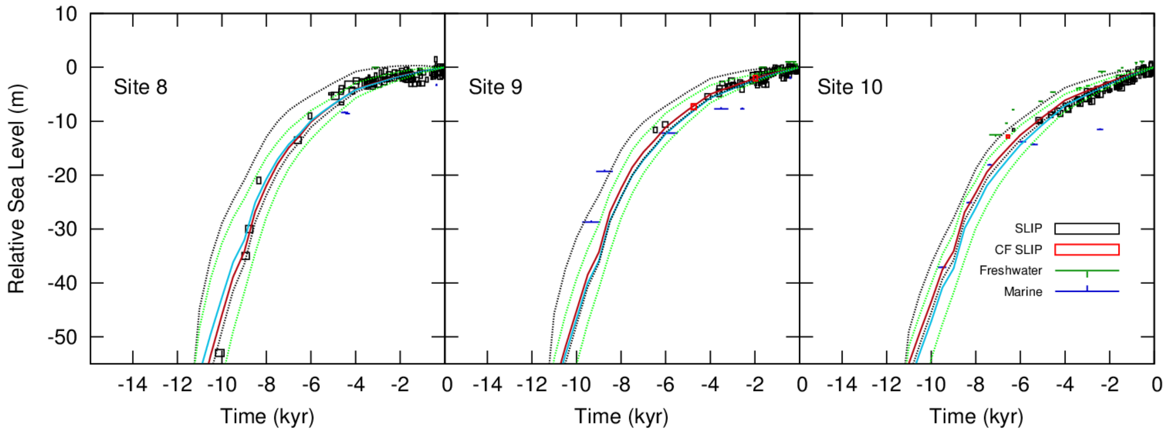

Figure 2.9. Data-model comparison for sites located in the central region. Optimal model curves are shown by the red (data-weighting included) and green lines. Bounding models (1σ) are indicated by the black-dotted lines. Model uncertainty (1σ) calculated using the nominal Bayesian approach is indicated by the green-dotted lines. To be consistent with the indicated model uncertainty, the SLIP boxes were drawn to represent 1σ uncertainty in height and age. The meaning of each data symbol is indicated in the key (site 10 frame).

It is evident from Figure 2.9 that the optimal model curves are not compatible with some of the older marine limiting data at sites 9 & 10, indicating that the model is not able to capture the spatial gradient in the observations. It is important to recall that the limiting data were not used in estimating the optimal model parameters. This data-model discrepancy can be explained in different ways. Tectonic corrections were not applied to data from sites 8 and 9 in the results shown in Figure 2.9 given the large uncertainty in these corrections and the relatively minor impact it had on the parameter estimation results (see Section 2.2.1). However, plausible spatial variations in the tectonic contribution could explain this discrepancy. A correction for possible uplift would shift the sea level data to lower values and so, if this is the primary contributor to the difference, our results suggest that a greater tectonic correction should be applied for northern Oregon (site 9) compared to southern Washington (site 8).

There are other possible explanations of the noted discrepancy. One is lateral variation in rheology causing a decrease in UMV going from northern Oregon to southern Washington. For example, P-wave velocity anomalies averaged over the 100-400 km depth range, which indicate faster anomalies beneath northern Oregon (Eakin et al., 2010). Assuming that seismic velocity anomalies are mainly attributed to variations in temperature, this is consistent with higher UMV underneath northern Oregon. Compaction of the sediments from which the SLIPs were reconstructed at site 8 is another possibility. This area hosts three major Bays: Grays Harbor, Willapa Bay and Columbia River estuary which have accommodated deposition of sediments during the Holocene. The majority of the data during early Holocene are peat samples from Grays Harbor. Since all of these index points were reconstructed from intercalated sediments and derived from boreholes at depths of ~30 m or more, there is a good likelihood of compaction due to the overburden pressure of the above sediments. Although the influence of compaction on inferences of past sea-level changes can be quantified (e.g., Horton and Shennan, 2009), applying this procedure to remove compaction from the reconstructed SLIPs is beyond the scope of our study.

The 1σ model uncertainty ranges are estimated from the procedures explained in Section 2.2.2 and are shown in Figure 2.9. When using all data in the heuristic approach, only an upper bounding (1σ) model could be distinguished. A lower bounding model could be determined using the compaction-free SLIPs; though we note there are only 3 from this region (2 at site 9 and 1 at site 10), which will impact the accuracy of this bound.

2.3.1.3 Southern region

Data-model misfits were computed for the 195 SLIPs from this region (Figure 2.10). The optimum model parameters in this case are: LT = 71 km, UMV = 5×10^{20} Pas, LMV = 2×10^{22} Pas and ice model 5962. As above, we computed δ values with and without data weighting (Figure S6 shows results without) and in each case the optimal parameters are identical. As can be seen from the top and middle panels in

Figure 2.10, the misfit values are insensitive to the chosen ice model. This is to be expected as the data sites become further from the region of past ice loading. Also, there is a consistent preference for an UMV of 5×10^{20} Pas and LMV values in the range $2\text{-}3\times10^{22}$ Pas for different sets of model parameters. The UMV is consistent with a previous study by Muhs et al. (2012) and lies in the high-end of their proposed range ($2\text{-}5\times10^{20}$ Pas). Furthermore, our preferred LMV is higher than their proposed range ($5\text{-}10\times10^{21}$ Pas). Considering lower LMV values results in a model curve which passes below the SLIPs in the 4-8 ka time window.

The best fitting model and the curves representing model uncertainty are plotted along with the RSL data in Figure 2.11. As for the central region, no lower bounding model parameter set that satisfied the conditions defined in Section 2.2.3 could be found when considering all SLIPs. Therefore, the lower (heuristic) uncertainty bound is derived from compaction-free SLIPs only (a total of 21). The model provides a high-quality fit to the data (both SLIPs and limiting data), except for the oldest two SLIPs at site 13. There is a very sharp rise in sea level between 11.5 and 11 ka associated with a contribution to meltwater pulse 1B (sourced from Antarctica in the ICE-5G model). The older SLIPs at site 13 would be better fit by scaling up this contribution by ~30%. We explored the effect of ignoring the tectonic signal on our model parameter inferences and found that the results are biased toward a thicker lithosphere (120 km) when no tectonic correction was applied.

Our results suggest a preference for a higher upper mantle viscosity for the southern region compared to the central region. The tectonic regime of each region is different due to the transition from subduction to lateral slip at the Mendocino Triple Junction. Seismic studies and shear wave splitting analyses indicate a significant change of the mean fast direction above and below the Mendocino Triple junction (Eakin et al., 2010). Moreover, tomography studies using P and S wave velocities reveal a low-velocity anomaly in southern Oregon at 200-300 km that reduces in amplitude south of the triple junction (Xue and Allen, 2010). Assuming that temperature is a primary control on the velocity anomalies, this is compatible with the difference between our estimates of UMV in the two regions.

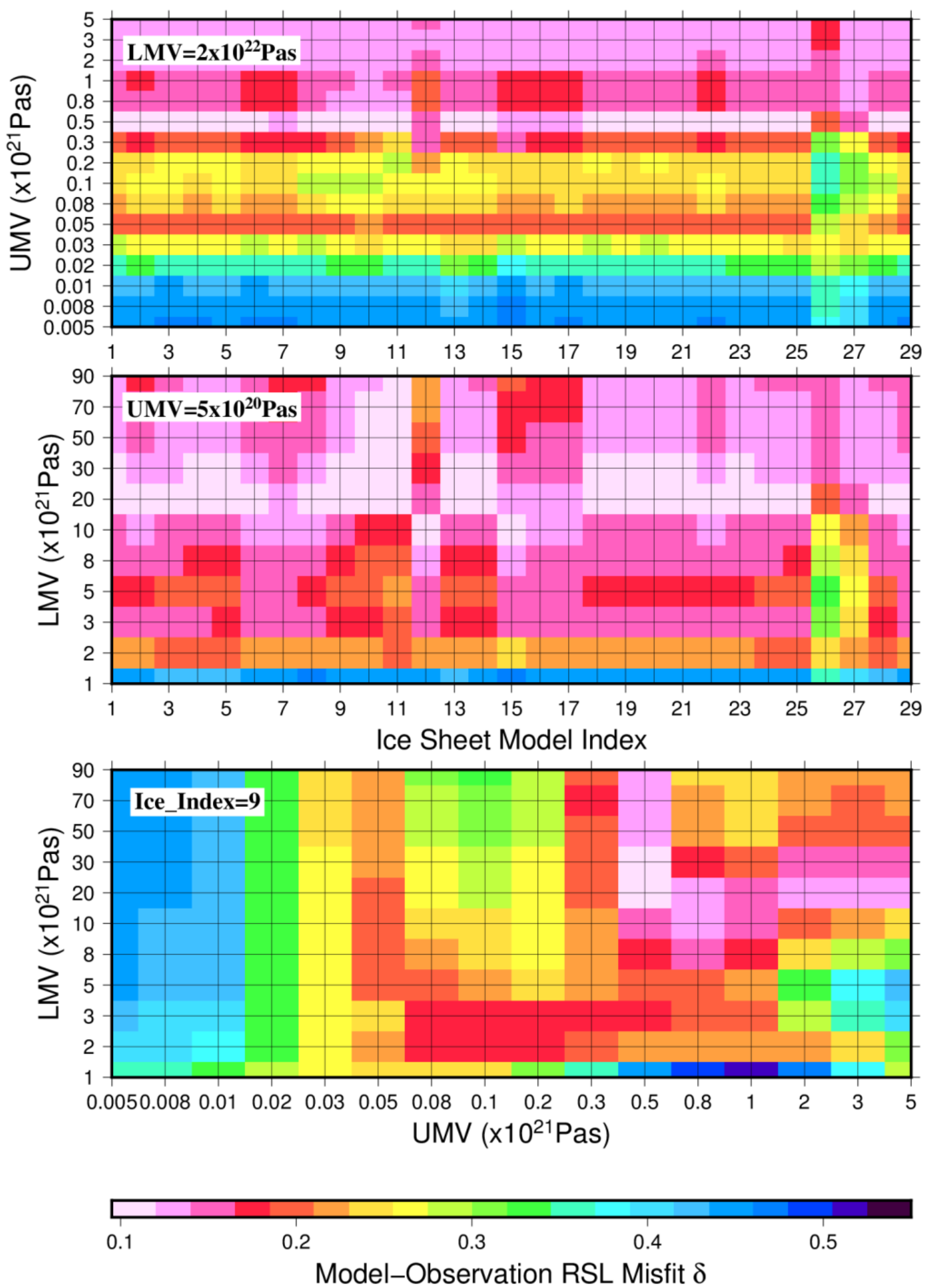

Figure 2.10. Data-model misfit values for the southern region, when applying the data weighting approach. The upper panel displays the misfit values when the LMV is constant (2×10^{22} Pas) and δ is

only a function of UMV and ice model. The middle panel shows δ as a function of LMV and ice model with the UMV fixed at 5×10^{20} Pas. The lower panel shows the δ values in terms of varying LMV and UMV for the case of ice model 5962 (index number 9). In all 3 plots, the lithosphere thickness is constant and has a value of 71 km.

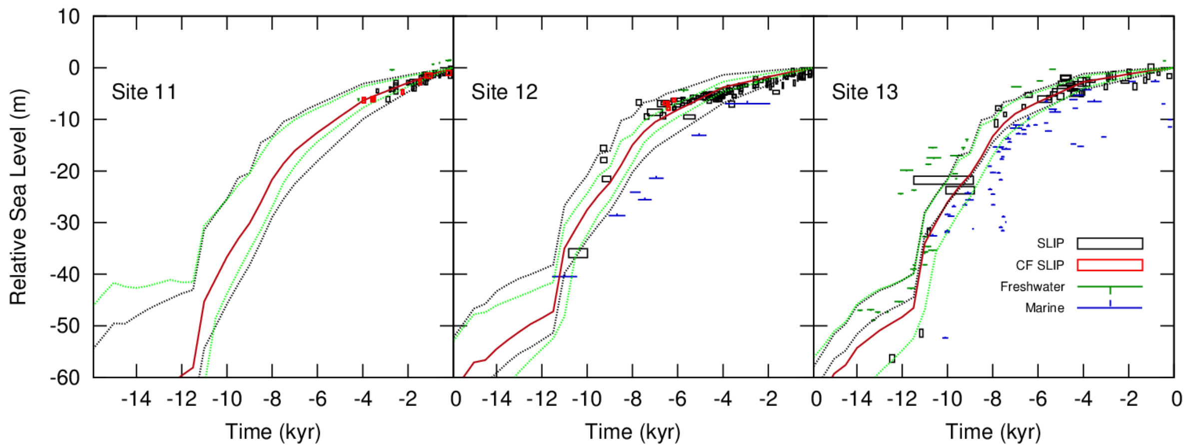

Figure 2.11. Data-model comparison for sites located in the southern region. Bounding models (1σ) are indicated by the black-dotted lines. Model uncertainty (1σ) calculated using the nominal Bayesian approach is indicated by the green-dotted lines. To be consistent with the indicated model uncertainty, the SLIP boxes were drawn to represent 1σ uncertainty in height and age. The meaning of the different data symbols are indicated in the key (site 13 frame).

2.3.1.4 Comparison of results for the three regions

A summary of the optimal and bounding model parameters for each region is presented in Table 2.2. The results indicate substantial spatial variability in the inferred viscosity structure, with very low UMV in the northern region (5×10^{19} Pas) compared to higher values in the central (2×10^{20} Pas) and southern (5×10^{20} Pas) regions. Similarly, the proposed LMV for the northern region is lower (10^{21} Pas) in comparison with the central (10^{22} Pas) and southern (2×10^{22} Pas) regions. We note that the RSL observations from northern sites will have a different depth sensitivity to Earth viscosity structure compared to data at sites in central and southern regions. Specifically, we would expect the northern data to have greater sensitivity to local and shallower structure compared to central and southern sites due to the latter being located on the peripheral bulge. The inferred viscosities are likely to be influenced by the tectonic regime, i.e., the location of the sites relative to the subducting Juan de Fuca, Explorer and Gorda slabs for northern and central regions and the transition from subduction to lateral slip for the southern region.

Table 2.2. Optimal and bounding model parameters for northern, central and southern regions. See Section 2.2.4 for a description of the criteria used to infer these parameter sets.

Region	Model Type	Ice Model	Lithosphere Thickness (Km)	Upper Mantle Viscosity ($\times 10^{21}$ Pas)	Lower Mantle Viscosity ($\times 10^{21}$ Pas)
Northern	Optimal	6885R (#27)	46	0.05	1
Central	Optimal	9858 (#15)	71	0.2	10
	Upper bound	9858 (#15)	71	0.08	70
	Lower bound	9960 (#24)	71	0.2	20
Southern	Optimal	5962 (#9)	71	0.5	20
	Upper bound	9858 (# 15)	120	1	20
	Lower bound	9894 (#20)	120	0.3	90

In order to emphasise the necessity for spatial clustering of the data into sub-regions, we determined the optimum model parameters for the entire dataset: LT = 46 km, UMV = 8×10^{19} Pas, LMV = 3×10^{21} Pas and ice model 6885 (index number 11). Model RSL curves in this case are plotted in Figure 2.12 along with the optimum model curves for each region (Table 2.2). The models tuned to each region (red line) provide a better fit to the observations at most sites with the exception of sites 4, 6 & 7 where the fits are similar between the two model parameter sets. These results indicate that the spatial variability in the GIA response as recorded in RSL changes cannot be captured well by a single model parameter set, reflecting the contribution of lateral viscosity structure to this response.

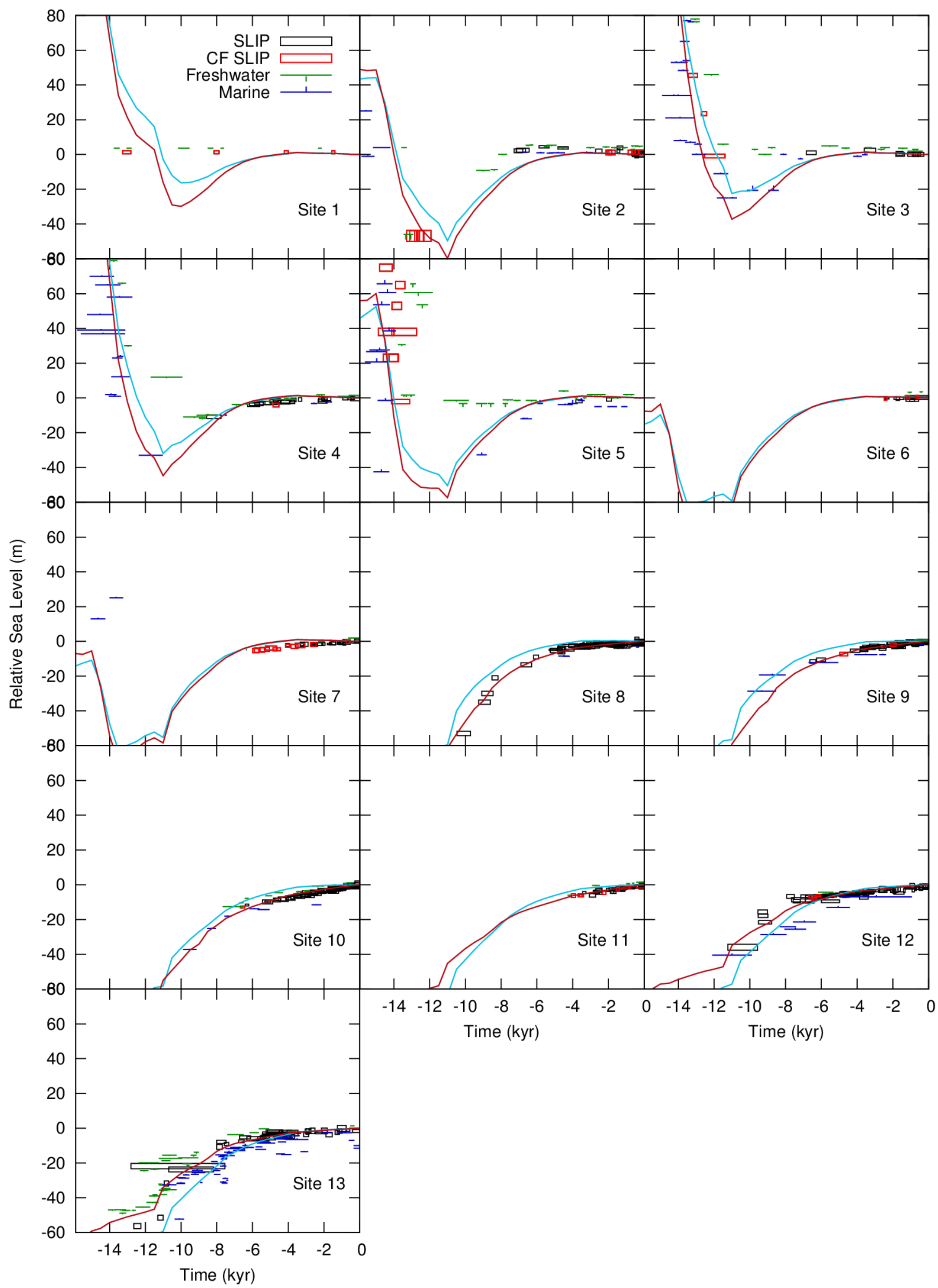

Figure 2.12. Data-model comparison for the entire weighted dataset. The RSL curve plotted in red is the optimal curve for parameters tuned to each sub-region (Table 2.2). The blue line indicates the

model curve tuned to the entire dataset with the following parameters: UMV of 8×10^{19} Pas, LMV of 3×10^{21} Pas and ice model number 6885 (index number 11). The lithosphere thickness is set to 46 km. Observational uncertainty is indicated at the 2σ level.

2.3.2 Present-day vertical motion

In this section we use our estimates of model parameters for each region to calculate the GIA contribution to present-day vertical land motion and compare this to the total signal observed using GPS monitoring, which includes the influence of other processes such as tectonics. Modelled and observed rates for each sub-region are given in Figure 2.13. Model uncertainty ranges (1σ) for predicted vertical motion rates are plotted in Figure S7. As can be seen in Figure 2.13, GIA contributes a long-wavelength signal that is mainly uplift in the northern region and subsidence in the central and southern regions. We note that the reference frame implicit in our modelled uplift rates (centre of mass that includes deformation of the solid Earth as well as mass re-distribution in the ice and ocean loads) is different to that used to determine the rates via GPS (Blewitt, 2003). However, this issue likely produces data-model uplift rate differences that are relatively uniform across our study region with an amplitude well below the mm/yr level (Argus, 2012).

In the northern region, our optimal model results indicate that all of Vancouver Island is experiencing uplift with rates less than 1 mm/yr and decreasing towards the northeast. A center of subsidence (less than 1 mm/yr) is located just above the northeastern part of Vancouver Island which is thought to be dominated by changes in glacier mass loss in areas peripheral to this region Southern and eastern parts of Vancouver Island and other locations, including Puget Sound and the Olympic Peninsula, experience GIA uplift rates of 0.5-1 mm/yr. Our modelled rates for the northern Strait of Georgia and Vancouver Island are compatible with those in James et al. (2005, 2009b), although we note that model uncertainty is estimated to be large (several mm/yr; Figure S7).

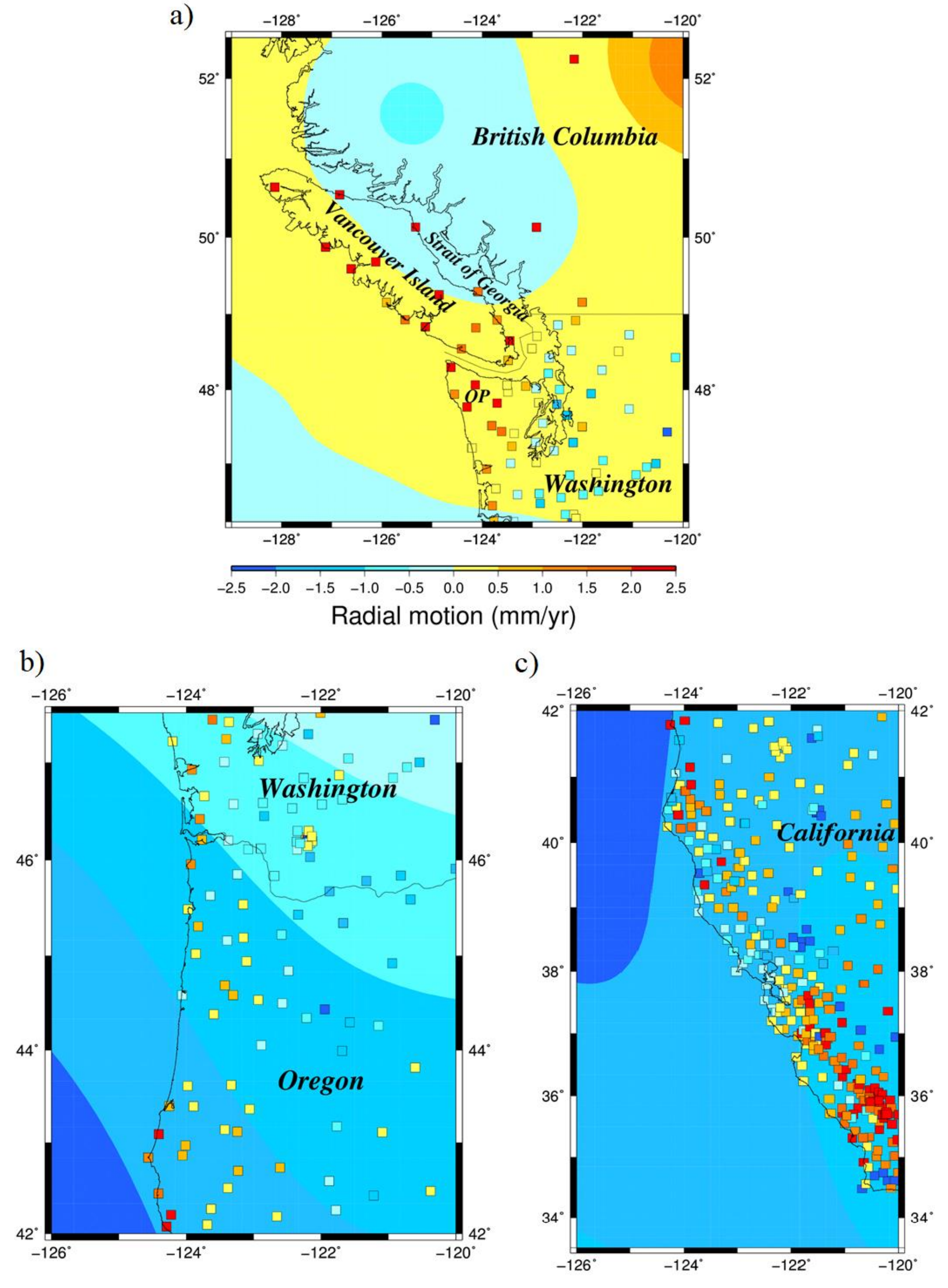

Figure 2.13. Modelled present-day vertical land motion in (a) northern, (b) central, and (c) southern regions. Results are based on the optimal model parameters for each region (Table 2.2). Coloured squares indicate the locations of the GPS sites and the observed rates of vertical motion. OP represents the Olympic Peninsula.

In the central and southern regions, our model results indicate that GIA produces widespread subsidence reaching ~2 mm/yr in southern Oregon and northern California. It is evident from Figure 2.13 that the vertical velocities obtained via GPS (483 stations, velocities are provided in IGS08 reference frame by UNAVCO for Plate Boundary Observatory (PBO), ftp://data-out.unavco.org/pub/products/velocity/) show greater spatial variability than the GIA model output. This is not surprising given the importance of tectonic and other processes along this coast that exhibit shorter spatial wavelengths.

The residuals between observed and modelled (GIA) uplift rates (i.e. GPS rates minus model rates) are shown in Figure S8. These residuals reveal more clearly the contribution of tectonic processes to vertical land motion. For example, there is a change in the orientation of the subducted slab in the vicinity of Juan de Fuca Strait (see Figure 2.1). Various subduction zone models suggest that this landward tilt of the forearc region may produce uplift rates of 1-4 mm/yr as a result of interseismic strain accumulation along the plate interface (Hyndman and Wang, 1995; Mazzotti et al., 2007 and 2008; Wang et al., 2003). This signal is more clearly seen when GIA rates are removed, with the area to the northwest of the Strait (including Vancouver Island and the Olympic Peninsula) uplifting and the area to the southeast (northern, central and eastern parts of Washington State) subsiding.

A similar pattern is evident for the central region, where the sites that are located close to the coast experience tectonic-induced uplift and the inland sites experience subsidence or lower rates of uplift compared to coastal sites. The amplitude and sign of the GIA signal (order 1 mm/yr) is significant in that when removed, the GPS rates give greater rates of uplift along the coast and these rates have been used to infer the extent of the plate locking. While most of these studies applied a GIA correction (Burgette et al., 2009; Wang et al., 2003), only a single model estimate was used which may not accurately represent the actual signal (Mazzotti et al., 2008). As indicated in

Figure S7, there is considerable uncertainty in the GIA signal which should be considered in future analyses of plate locking.

For the southern region, the general pattern of residuals is a rising coast with the highest rates in northern and southern California. However, there are some localities, such as the San Joaquin Valley and the Sacramento delta, where there is localized and rapid subsidence due to excessive ground water pumping and the resulting compaction of sediments. This complex spatial variability can be recognized throughout the southern region, where local processes such as ground water changes and sediment compaction contribute significantly to the observed vertical motion.

2.3.3 Sea-level projections

Similar to the previous section, we use our estimates of model parameters for each region to calculate the GIA contribution to recent past and future sea-level variations at 56 tide-gauge stations (Supplementary Material). Rates of sea-level change for the 21st century (i.e., modelled RSL at 2100 CE minus that at 2000 CE) and the corresponding net contribution to RSL change at 9 major cities along the west coast are presented in Table 2.3. The GIA-related RSL rates vary significantly, from a value of -0.22 mm/yr (Seattle) to 1.52 mm/yr (Crescent City); when considering parametric uncertainty (1σ), this range increases to -1.35 mm/yr (Victoria) to 2.00 mm/yr (Crescent City). These rates are used to determine the contribution of GIA to RSL at these 9 cities (Table 2.3, column 3) during the 21st century which can be compared to the change estimated in the recent assessment report of the IPCC (Church et al., 2013) that includes the effect of ocean steric and dynamic changes, future melting of land ice and GIA. We note that, at some locations, our estimates of the GIA contribution differ considerably to those used in Church et al. (2013) (see Table S2).

Table 2.3. Rates and values of RSL changes for the 21st century for 9 major cities along the west coast of North America. The second column represents the GIA contribution to the rate of RSL with the corresponding uncertainty range (1σ) estimated from nominal Bayesian approach. The third column indicates the contribution of GIA to the projected RSL for 2081-2100 CE relative to 1986-2005 CE with the corresponding estimated uncertainty range (1σ). The fourth column represents the projected RSL changes for 2081-2100 CE relative to 1986-2005 CE for the Representative Concentration Pathway 4.5 and several different processes (see text for details; Church et al., 2013). The fifth column is the estimated background non-climatic rate of sea-level changes derived from tide-gauge data (from Sweet et al. (2017)). The sixth column is the residual between the background RSL rate and the GIA-induced RSL rate (i.e., 'Background' minus 'GIA').

Location	GIA RSL rate (mm/yr)	GIA RSL for 2081-2100 CE (cm)	Total RSL projection for 2081-2100 CE (cm)	Background rate (mm/yr)	Residual rate (mm/yr)
Vancouver	-0.09 [-1.32 0.10]	-0.85 [-12.54 0.95]	28.95	-1.37 [-1.50 -1.24]	-1.28 [-1.6 0.08]
Victoria	-0.19 [-1.35 -0.01]	-1.8 [-12.82 -0.09]	28.00	-1.21 [-1.34 -1.08]	-1.02 [-1.33 0.27]
Seattle	-0.22 [-1.33 -0.06]	-2.09 [-12.63 -0.57]	27.72	0.21 [0.09 0.33]	0.43 [0.15 1.66]
Astoria	0.78 [0.26 1.04]	7.41 [-2.47 9.88]	42.23	-2.15 [-2.28 -2.02]	-2.93 [-3.32 -2.28]
Charleston	1.34 [0.84 1.71]	12.73 [7.98 16.24]	49.92	-1.11 [-1.35 -0.87]	-2.45 [-3.06 -1.71]
Crescent City	1.52 [0.88 2.00]	14.44 [8.36 19]	52.62	-2.67 [-2.81 -2.53]	-4.19 [-4.81 -3.41]
San Francisco	1.05 [0.69 1.25]	9.97 [6.55 11.87]	45.61	-0.07 [-0.16 0.02]	-1.12 [-1.41 -0.67]
Los Angeles	0.65 [0.42 0.87]	6.17 [3.99 8.26]	36.17	-1 [-1.13 -0.87]	-1.65 [-2.0 -1.29]
San Diego	0.60 [0.34 0.84]	5.7 [3.23 7.98]	40.11	0.22 [0.09 0.35]	-0.38 [-0.75 0.01]

Figure 2.14 illustrates the contribution of GIA (estimated here) to future RSL changes, along with that of due to other contributing processes, including ocean steric and dynamic changes, melting of glaciers and ice sheets, and ground water extraction (Church et al., 2013). The values presented here are based on a median scenario of increasing anthropogenic climate forcing (Representative Concentration Pathway (RCP) 4.5). As can be seen in Figure 2.14, ocean steric and dynamic changes

are the dominant cause of future sea-level change in this region (more than 60% of the total RSL variations for northern sites and more than 40% for the other locations). The contribution of GIA is relatively small in the northern region (Vancouver, Victoria and Seattle), while, in the central and southern regions, it is more important, with contributions exceeding 10 cm at some sites by 2100 CE. The contribution of the GIA signal to future RSL rise for central and southern sites ranges from 6 cm to 15 cm; specifically, 10 cm (22% of the total signal) in San Francisco, 13 cm (26%) in Charleston and 15 cm (28%) in Crescent City. The amplitudes of these GIA contributions are similar to those found in a recent study that considered the Atlantic coast of North America (Love et al., 2016), with, for example, 12 cm in Washington and New York and 18 cm in Halifax (giving a GIA contribution ranging from 25-33% of the projected value that includes the processes discussed above).

We also include in Table 2.3 (5th column), estimates of the contribution of secular processes (e.g. GIA, tectonics, sediment compaction, ground water loading) to past RSL change as measured by tide gauges (Sweet et al., 2017). These non-climatic background RSL rates were estimated using a spatio-temporal statistical model tuned to the tide gauge data (Sweet at al., 2017). By subtracting our estimated GIA rates from these non-climatic background rates (Table 2.3, 6th column), we can examine the residual which should reflect the contributions from other processes (tectonics, etc). The residuals are all negative (falling RSL contribution), with maximum rate of 4.19 mm/yr at Crescent city in central Oregon, with the exception of Seattle which shows a modest RSL rise signal. This pattern of RSL fall (or land uplift) is broadly compatible with that of Cascadia subduction zone models which predict RSL fall along the west coast and RSL rise for Puget Sound in the amplitude range 1-4 mm/yr (Mazzotti et al., 2008; Wang et al., 2003). The fall in RSL at 3 southern cities below the triple junction (San Francisco, Los Angeles and San Diego), is consistent with the RSL fingerprint associated with ground water depletion (Veit and Conrad, 2016) and the interseismic tectonic deformation of the San Andereas Fault system (Smith-Konter et al., 2014). However, we note that the amplitude of the residuals at these 3 locations (Table 2.3, 6th column), is larger than that estimated in the cited studies.

a)

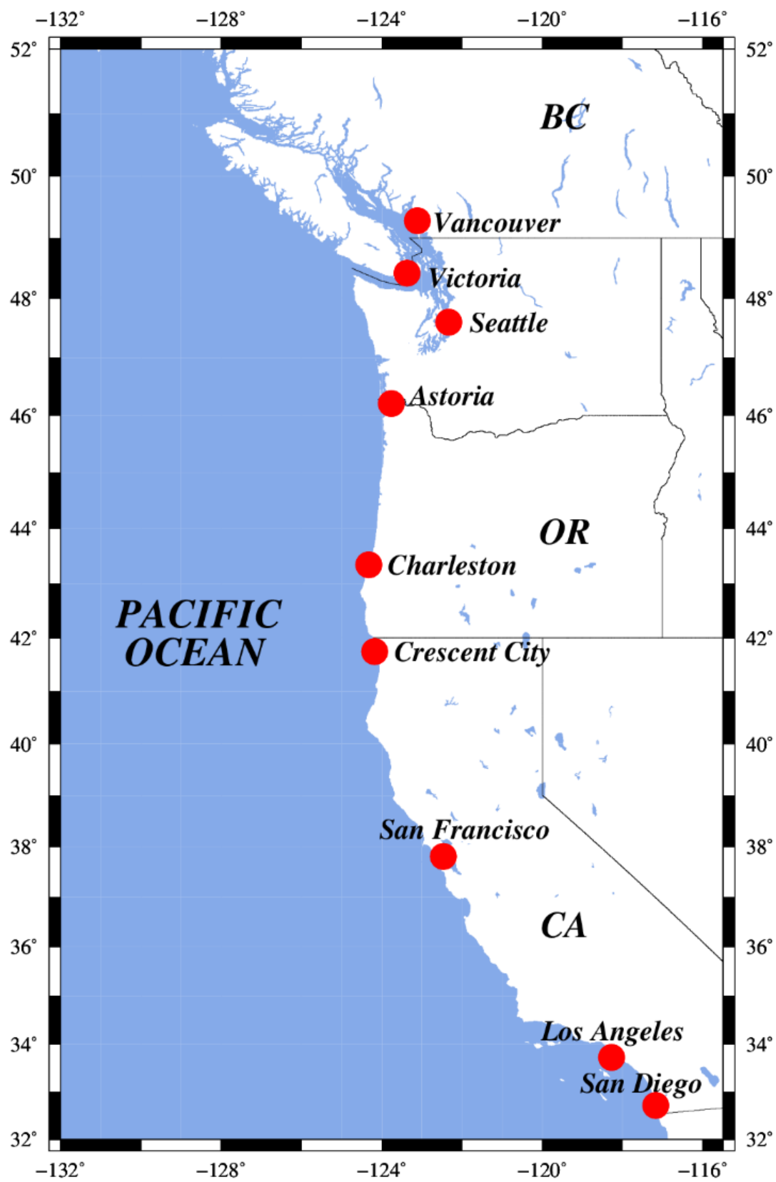

Figure 2.14. a) Map showing the locations of the cities mentioned in Tables 2.3, S2 and Figure 2.14(b)

b)

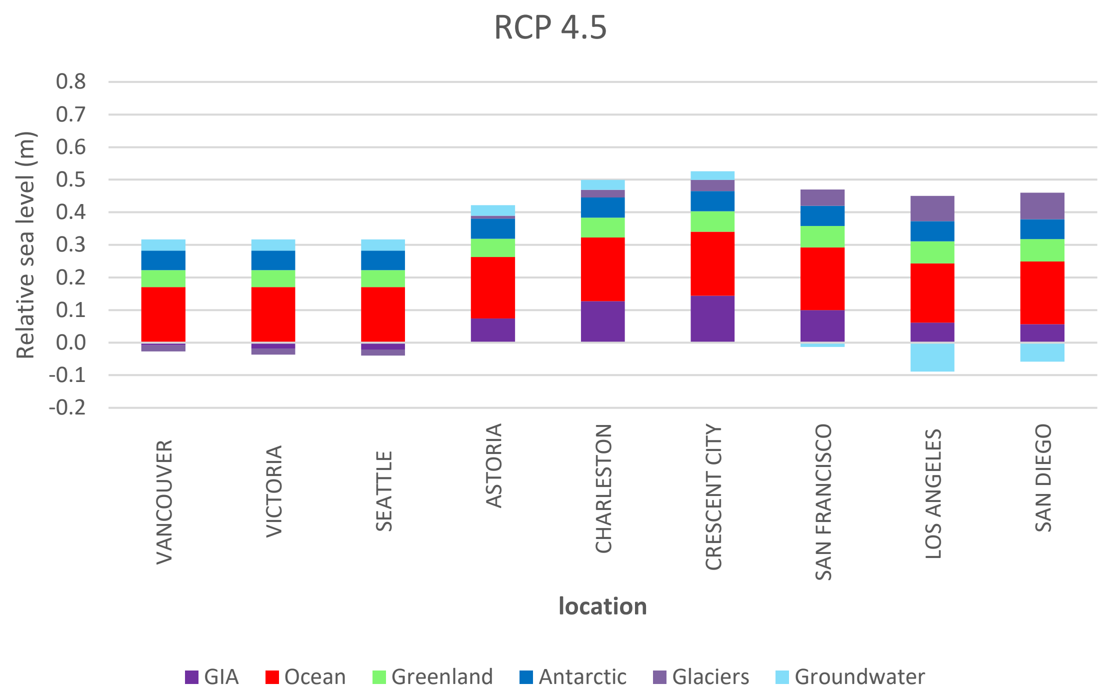

Figure 2.14. (continued). b) RSL projections for 2081-2100 relative to 1986-2005 for the Representative Concentration Pathway scenario 4.5. Other than GIA, the values are from the IPCC AR5 (Church et al., 2013).

2.4 Conclusions

In this study we infer the GIA signal and its uncertainty along the central Pacific coast of North America using 680 sea-level index points and over 20,000 model runs sampling >700 (1D) Earth viscosity models and 29 ice models. Due to the large spatial extent and different tectonic settings of the study area, we divided it into three sub-regions (northern, central and southern) for which model parameters were inferred separately. Also, given that this region is tectonically active, the influence of this process (as well as sediment isostatic adjustment) was accounted for, where possible, by removing it from the data using published estimates. In locations where the tectonic influence was not known or poorly quantified, we estimated model parameters with and without specific subsets of RSL data to check that our parameter inferences were not significantly biased by including data with a potentially large tectonic overprint.

For the northern region, which was once glaciated, the RSL data indicate a high sensitivity to the input ice history. These data, which record a rapid fall in RSL, suggest that ice models generated from a glacial systems model (Tarasov et al., 2012) retreat around 500 years too early from this region. These RSL data also prefer a low upper mantle viscosity (5×10^{19} Pas), a lower mantle viscosity of 10^{21} Pas and lithosphere thickness of 46 km. The preference for a low viscosity upper mantle is consistent with findings from previous GIA modelling studies from this region (e.g. James et al., 2009b). We were unable to determine a single set of model parameters that could produce satisfactory fits to both the older (> 8 ka) and younger RSL data; particularly for southeastern Georgia Strait (site 4) and Puget Sound (site 7). Considering the presence of a low-viscosity asthenosphere layer of different thicknesses did not resolve this problem. This likely reflects either the influence of long-term tectonic effects and/or limitations of our model, particularly the Earth component (e.g. not accounting for transient or nonlinear deformation and the neglect of lateral variability).

In the central region, including Washington and Oregon States, the reconstructed sea-level rise is monotonic over the period spanned by the observations, reflecting the influence of peripheral bulge subsidence. Compared to the northern region, the model results are much less sensitive to the chosen ice history and prefer higher mantle viscosity values (2×10^{20} Pas and 10^{22} Pas, respectively). While good quality fits were obtained to the SLIPs in this region, we note that the optimal model curve is incompatible with some limiting data suggesting that the older SLIPs from southern Washington (site 8) are influenced by sediment compaction.

In the southern region, which covers California State, RSL reconstructions indicate a similar RSL signal to that for the central region, indicating that the influence of the peripheral bulge extends to this area. The results indicate that the data prefer a moderately higher upper mantle viscosity (5×10^{20} Pas) compared to the central region, which may arise from the different tectonic regime of this region (strike-slip versus convergent for the central and northern regions). The significant variability in our viscosity inferences between the three regions indicates the importance of applying Earth models that can explicitly accommodate lateral viscosity structure.

Using our parameter estimates, we compute present-day, GIA-induced vertical land motion at 483 GPS stations and sea-level change at 56 tide-gauge stations (see Supplementary Material) for use by end-user communities seeking to interpret the geodetic observations in terms of other processes. Our results show that contemporary rates of vertical land motion and RSL change reach amplitudes of a few mm/yr with uncertainties that are of order 1 mm/yr in many areas. Therefore, accurate interpretation of these data for a non-GIA signal requires that the latter be removed in many locations. Furthermore, our results indicate that GIA will be a significant contributor to RSL changes this century, reaching values well in excess of 10 cm at a number of locations.

Acknowledgements

We thank Volker Klemann and two anonymous reviewers for providing constructive reviews of our original manuscript. We also thank Alex Simms, Laura Reynolds and Simon Engelhart for providing information on the RSL data and tectonic corrections used in this study. Funding support was provided by the Natural Sciences and Engineering Research Council, the Canada Research Chairs Program, and the University of Ottawa. We acknowledge the Integrated Climate Data Center (ICDC, icdc.cen.uni-hamburg.de) University of Hamburg, Hamburg, Germany for providing regional sea level data from IPCC AR5 distributed in netCDF format. This paper is a contribution to the PAGES and INQUA supported PALSEA2 working group.

References

Argus, D.F. (2012), Uncertainty in the velocity between the mass center and surface of Earth, J. Geophys. Res. Solid Earth, 117, doi:10.1029/2012JB009196.

Argus, D.F., Peltier W.R. (2010), Constraining models of postglacial rebound using space geodesy: A detailed assessment of model ICE-5G (VM2) and its relatives, Geophysical Journal International, 181, 697-723.

Atwater, B.F., Hedel C.W., Helley E.J., (1977), Late Quaternary Depositional History, Holocene Sea-level Changes, and Vertical Crust Movement, Southern San Francisco Bay, California. US Geological Survey Professional Paper 1014, Washington, DC.

Atwater, B.F., (1987), Evidence for great Holocene earthquakes along the outer coast of Washington State, Science, 236 (4804), 942-944, doi: 10 .1126 /science .236.4804 .942.

Austermann, J., Mitrovica J. X., Latychev C., Milne G.A. (2013), Barbados based estimate of ice volume at Last Glacial Maximum effected by subducted plate, Nat. Geosci., 6, 553–557, doi: 10.1038/ngeo1859.

Blewitt, G. (2003), Self-consistency in reference frames, geocenter definition, and surface loading of the solid Earth, J. Geophys. Res. Solid Earth, 108 (B2).

Brown Jr., R.D. (1990), Quaternary deformation, In: Wallace, R.E. (Ed.), The San Andreas Fault System, California, U.S. Geological Survey Professional Paper, 1515 (Chapter 4), 82-113.

Burgette, R.J., Weldon, R.J., Schmidt, D.A., 2009. Interseismic uplift rates for western Oregon and along-strike variation in locking on the Cascadia subduction zone, J. Geophys. Res. Solid Earth, 114 (B1), 1978-2012, doi: 10.1029/2008JB005679.

Church, J. A., P. Clark, A. Cazenave, J. Gregory, S. Jevrejeva, A. Levermann, M. Merrifield, G. Milne, R.S.Nerem, P. Nunn, A. Payne, W. Pfeffer, D. Stammer, and A. Unnikrishnan (2013), Sea level change, in Climate Change 2013: The Physical Science Basis, edited by T. F. Stocker, D. Qin, G.-K. Plattner, M. Tignor, S. Allen, J. Boschung, A. Nauels, Y. Xia, V. Bex, and P. Midgley, Cambridge University Press, Cambridge, UK and New York, NY. USA.

Clague, J.J., James T.S. (2002), History and isostatic effects of the last ice sheet in southern British Columbia, Quat. Sci. Rev., 21, 71 – 87, doi: 10.1016/S0277-3791(01)00070-1.

Crowell, J.C. (1962), Displacement along the San Andreas Fault, California, New York, Geological Society of America, 61 p.

Dalrymple, R.A., Breaker L.C., Brooks B.A., Cayan D.R., Griggs G.B., Han W., Horton B.P., Hulbe C.L., McWilliams J.C., Mote P.W., Pfeffer T., Reed D.J., Shum C.K. (2012), Sea-level Rise for the Coasts of California, Oregon, and Washington: Past, Present, and Future. The National Academies Press, Washington, doi: 10.17226/13389 .

Dragert, H., Hyndman R.D., Rogers G.C., Wang K. (1994), Current deformation and the width of the seismogenic zone of the northern Cascadia subduction thrust. Journal of Geophysical Research, 99, 654-668, doi: 10.1029/93JB02516.

Drexler J.Z., de Fontaine C.S., Brown T.A. (2009), Peat accretion histories during the past 6,000 years in marshes of the Sacramento-San Joaquin Delta of California, USA. Estuaries and Coasts, 32, 871–892, doi: 10.1007/s12237-009-9202-8.

Dziewonski, A., Anderson D. (1981), Preliminary reference earth model, Physics of the Earth and Planetary Interiors, 25, 297-356.

Engelhart, S.E., Vacchi M., Horton B.P., Nelson A.R., and Kopp R.E. (2015), A sea-level database for the Pacific coast of central North America, Quat. Sci. Rev., 113 (0), 78–92, doi: 10.1016/j.quascirev.2014.12.001.

Farrell, W.E., Clark J.A., (1976), On postglacial sea level, Geophys. J. R. astr. Soc., 46, 647–667, doi: 10.1111/j.1365-246X.1976.tb01252.x.

Grove, K., Sklar L.S., Scherer R., Lee G., Davis J. (2010), Accelerating and spatially-varying crustal uplift and its geomorphic expression, San Andreas fault zone north of San Francisco, California, Tectonophysics, 495, 256–268, doi: 10.1016/j.tecto.2010.09.034.

Hauser, T., Keats A., Tarasov L. (2012), Artificial neural network assisted Bayesian calibration of climate models, Climate Dynamics, 39(1), 137–154, doi: 10.1007/s00382-011-1168-0.

Hyndman, R.D., Wang K. (1993), Thermal constraints on the zone of major thrust earthquake failure: the Cascadia subduction zone, Journal of Geophysical Research, 98, 2039-2060.

Hyndman, R.D., Wang K., (1995), The rupture zone of Cascadia great earthquakes from current deformation and the thermal regime, Journal of Geophysical Research, 100, 22133-22154.

James, T. S., Clague J.J., Wang K., Hutchinson I. (2000), Postglacial rebound at the northern Cascadia subduction zone, Quat. Sci. Rev., 19, 1527–1541, doi: 10.1016/S0277-3791(00)00076-7.

James, T.S., Hutchinson I., Barrie J.V., Conway K.W., Mathews D. (2005), Relative sea-level change in the northern Strait of Georgia, British Columbia. Geogr. Phys. Quat., 59, 113-127, doi: 10.7202/014750ar.

James, T.S., Gowan E.J., Hutchinson I., Clague J.J., Barrie J.V., Conway K.W. (2009a), Sea-level change and paleogeographic reconstructions, southern Vancouver Island, British Columbia, Canada. Quat. Sci. Rev., 28, 1200-1216, doi: 10.1016/j.quascirev.2008.12.022.

James, T.S., Gowan E.J., Wada I., Wang K. (2009b), Viscosity of the asthenosphere from glacial isostatic adjustment and subduction dynamics at the northern Cascadia subduction zone, British Columbia, Canada. J. Geophys. Res., 114, doi: 10.1029/2008JB006077.

Karato, S. (2008), Deformation of Earth Materials: An Introduction to the Rheology of Solid Earth, Cambridge: Cambridge University Press, doi: 10.1017/CBO9780511804892.

Kelsey, H.M., Ticknor R.L., Bockheim J.G., Mitchell C.E. (1996), Quaternary upper plate deformation in coastal Oregon: Geological Society of America Bulletin, 108, 843–860, doi: 10.1130/0016-7606(1996)108<0843:QUPDIC>2.3.CO;2.

Kendall, R., Mitrovica J., Milne G.A. (2005), On post-glacial sea level - ii. Numerical formulation and comparative results on spherically symmetric models, Geophysical Journal International, 161 (3), 679-706.

Latychev, K., Mitrovica J., Tromp J., Tamisiea M., Komatitsch D., Christara C. (2005), Glacial isostatic adjustment on 3D earth models: a finite-volume formulation, Geophys. J. Int., 161(2), 421–444, doi:10.1111/j.1365-246X.2005.02536.x.

Love, R., Milne G.A., Tarasov L., Engelhart S., Hijma M., Latychev K., Horton B.P., Törnqvist T. (2016), Projections of sea level change along the east and Gulf coasts of North America. Earth's Future, doi: 10.1002/2016EF000363.

Mazzotti, S., Lambert A., Courtier N., Nykolaishen L., Dragert H. (2007), Crustal uplift and sea level rise in northern Cascadia from GPS, absolute gravity, and tide gauge data, Geophys. Res. Lett., 34, L15306, doi: 10.1029/2007GL030283.

Mazzotti, S., Jones C., Thomson R. E. (2008), Relative and absolute sea-level rise in western Canada and northwestern U.S. from a combined tide gauge-GPS analysis, J. Geophys. Res., 113, C11019, doi: 10.1029/2008JC004835.

Merritts, D., Bull W.B. (1989), Interpreting Quaternary uplift rates at the Mendocino triple junction, northern California, from uplifted marine terraces, Geology, 17, 1020–1024, doi: 10.1130/0091-7613(1989)017<1020: IQURAT>2.3.CO;2.

Milne, G.A., Mitrovica J.X., (1998), Postglacial sea-level change on a rotating Earth, Geophysical Journal International, 133, 1–19, doi: 10.1046/j.1365-246X.1998.1331455.x.

Mitrovica, J.X., Forte A.M., Simons M. (2000), A reappraisal of postglacial decay times from Richmond Gulf and James Bay, Canada, Geophysical Journal International, 142(3), 783–800, doi: 10.1046/j.1365-246x.2000.00199.x.

Mitrovica, J.X., Milne G.A. (2003), On post-glacial sea level: I. general theory, Geophysical Journal International, 154, 253-267.

Mitrovica, J.X., Wahr J., Matsuyama I., Paulson A. (2005), The rotational stability of an ice-age earth, Geophys. J. Int., 161(2), 491–506, doi: 10.1111/j.1365-246X.2005.02609.x.

Muhs, D.R., Kelsey H.M., Miller G.H., Kennedy G.L., Whelan J.F., and McInelly G.W. (1990), Age estimates and uplift rates for late Pleistocene marine terraces: Southern Oregon portion of the Cascadia forearc, Journal of Geophysical Research, 95, 6685–6698, doi: 10.1029/JB095iB05p06685.

Muhs, D.R., Rockwell T.K., Kennedy G.L. (1992), Late Quaternary uplift rates of marine terraces on the Pacific coast of North America, southern Oregon to Baja

California Sur, Quaternary International, 15-16, 121–133, doi: 10.1016/1040-6182(92)90041-Y.

Muhs, D.R., Simmons, K.R., Schumann, R.R., Groves, L.T., Mitrovica, J.X., Laurel, D. (2012), Sea-level history during the Last Interglacial complex on San Nicolas Island, California: implications for glacial isostatic adjustment processes, paleozoogeography and tectonics. Quat. Sci. Rev., 37, 1-25, doi: 10.1016/j.quascirev.2012.01.010.

Peltier, W., (2004), Global glacial isostasy and the surface of the ice-age Earth: The ICE-5G (VM2) model and GRACE, Annual Review of Earth and Planetary Sciences, 32, 111-149.

Peltier, W.R. (2010), Closing the budget of global sea level rise: The GRACE correction for GIA over the oceans, in Workshop Report of the Intergovernmental Panel on Climate Change Workshop on Sea Level Rise and Ice Sheet Instabilities, T.F. Stocker, D. Qin, G.-K. Plattner, M. Tignor, S. Allen, and P.M. Midgley, eds., University of Bern, IPCC Working Group Technical Support Unit, Bern, Switzerland, 157-159.

Peltier, W.R., Drummond R. (2008), Rheological stratification of the lithosphere: A direct inference based upon the geodetically observed pattern of the glacial isostatic adjustment of the North American continent, Geophysical Research Letters, 35, L16314, doi:10.1029/2008GL034586.

Peterson, C.D., Cruikshank K.M. (2014), Quaternary Tectonic Deformation, Holocene Paleoseismicity, and Modern Strain in the Unusually–Wide Coupled Zone of the Central Cascadia Margin, Washington and Oregon, USA, and British Columbia, Canada, doi: 10.5539/jgg.v6n3p1.

Reynolds, L.C., Simms A.R. (2015), Late Quaternary relative sea level in Southern California and Monterey Bay, Quaternary Science Reviews, 126, 57–66, doi:10.1016/j.quascirev.2015.08.003.

Roy, K., Peltier W. (2015), Glacial isostatic adjustment, relative sea level history and mantle viscosity: reconciling relative sea level model predictions for the U.S. east coast with geological constraints, Geophys. J. Int., 201(2), 1156–1181, doi:10.1093/gji/ggv066.

Simkin, T., Tilling R.I., Vogt P.R., Kirby S.H., Kimberly P., Stewart D.B. (2006), This dynamic planet; World map of volcanoes, earthquakes, impact craters, and plate tectonics, U.S. Geological Survey Geologic Investigations Series Map I-2800 scale 1:30,000,000.

Simms, A.R., Rouby H., Lambeck K. (2016), Marine terraces and rates of vertical tectonic motion: the importance of glacio-isostatic adjustment along the Pacific coast of central North America, Geological Society of America Bulletin, 128, 81–93, doi: 10.1130/B31299.1.

Smith-Konter, B.R., Thornton G.M., Sandwell D.T. (2014), Vertical crustal displacement due to interseismic deformation along the San Andreas Fault: Constraints from tide gauges, Geophys. Res. Lett., 41, 3793–3801, doi: 10.1002/2014GL060091.

Steffen, R., Wu P., Steffen H., Eaton D.W. (2014), On the implementation of faults in finite-element glacial isostatic adjustment models, Computers & Geosciences, 62, 150-159, doi: 10.1016/j.cageo.2013.06.012.

Sweet, W.V., Kopp R.E., Weaver C.P., Obeysekera J., Horton R.M., Thieler E.R., Zervas C. (2017), Global and Regional Sea Level Rise Scenarios for the United States. NOAA Technical Report NOS CO-OPS 083. NOAA/NOS Center for Operational Oceanographic Products and Services.

Tarasov, L., Dyke A. S., Neal R. M., Peltier W. R. (2012), A data calibrated distribution of deglacial chronologies for the North American ice complex from glaciological modeling, Earth Planet. Sci. Lett., 315–316, 30–40.

Veit, E., Conrad C.P. (2016), The impact of groundwater depletion on spatial variations in sea level change during the past century. Geophys. Res. Lett., 43, 3351–3359, doi: 10.1002/2016GL068118.

Wang, K., Wells R., Mazzotti S., Hyndman, R.D., Sagiya T. (2003), A revised dislocation model of interseismic deformation of the Cascadia subduction zone, J. Geophys. Res., 108(B1), 2026, doi: 10.1029/2001JB001227.

Wang, K. (2007), Elastic and viscoelastic models of crustal deformation in subduction earthquake cycles, in The Seismogenic Zone of Subduction Thrust Faults, edited by T. H. Dixon and J. C. Moore, 540– 575, Columbia Univ. Press, New York.

Weber-Band, J. (1998), Neotectonics of the Sacramento-San Joaquin Delta area, east central Coast Ranges, California, Ph.D. thesis, University of California, Berkeley, California, USA.

West, D.O., McCrumb D.R. (1988), Coastline uplift in Oregon and Washington and the nature of Cascadia subduction-zone tectonics, Geology, 16, 169–172.

Wu, P. (1995), Can observations of postglacial rebound tell whether the rheology of the mantle is linear or nonlinear?, Geophys.Res.Lett., 22, 1645-1648.

Wu, P., Hasegawa H.S. (1996), Induced stresses and fault potential in Eastern Canada due to a disc load: a preliminary analysis, Geophysical Journal International, 125, 415-430, doi: 10.1111/j.1365-246X.1996.tb00008.x.

Supplementary Figures and Tables of Chapter 2

Contents of this section

Tables S1 to S2 and Figures S1 to S10. This supplemental section contains additional figures to complement discussion and figures presented in the main text. All of the figures below are referred to in the main text. See captions for further details.

Additional Supplementary Material (Model output at GPS station locations and tide gauge sites) can be found online at:

https://doi.org/10.1016/j.quascirev.2018.06.017.

Table S1. Number of limiting data and sea-level index points (SLIPs) data for each of the 13 sites indicated on Figure 1.

Site #	Terrestrial data	Marine data	SLIPs	Total number of data
1	10	3	4	17
2	21	9	39	69
3	21	30	12	63
4	25	17	23	65
5	28	22	10	60
6	3	0	14	17
7	7	2	35	44
8	1	3	128	132
9	7	6	110	123
10	14	6	110	130
11	6	0	45	51
12	3	7	108	118
13	32	58	42	132

Table S2. The contribution of GIA to the projected RSL for 9 major cities along the west coast of North America for the period of 2081-2100 CE relative to 1986-2005 CE. The RSL values and the corresponding uncertainty range (1σ) derived from our study are presented in the second column. The third column shows the results from the IPCC report, AR5 (Church et al., 2013).

Location	Projected RSL – Our Study (cm)	Projected RSL – AR5 (cm)
Vancouver	-0.85 [-12.54 0.95]	-9.78 [-11.18 -8.37]
Victoria	-1.8 [-12.82 -0.09]	-2.32 [-9.67 5.02]
Seattle	-2.09 [-12.63 -0.57]	2.02 [-6.93 10.97]
Astoria	7.41 [-2.47 9.88]	7.11 [-0.84 15.06]
Charleston	12.73 [7.98 16.24]	8.07 [2.25 13.90]
Crescent City	14.44 [8.36 19]	6.29 [-3.41 16.00]
San Francisco	9.97 [6.55 11.87]	5.50 [-4.11 15.10]
Los Angeles	6.17 [3.99 8.26]	5.41 [-2.72 13.55]
San Diego	5.7 [3.23 7.98]	5.50 [-2.09 13.10]

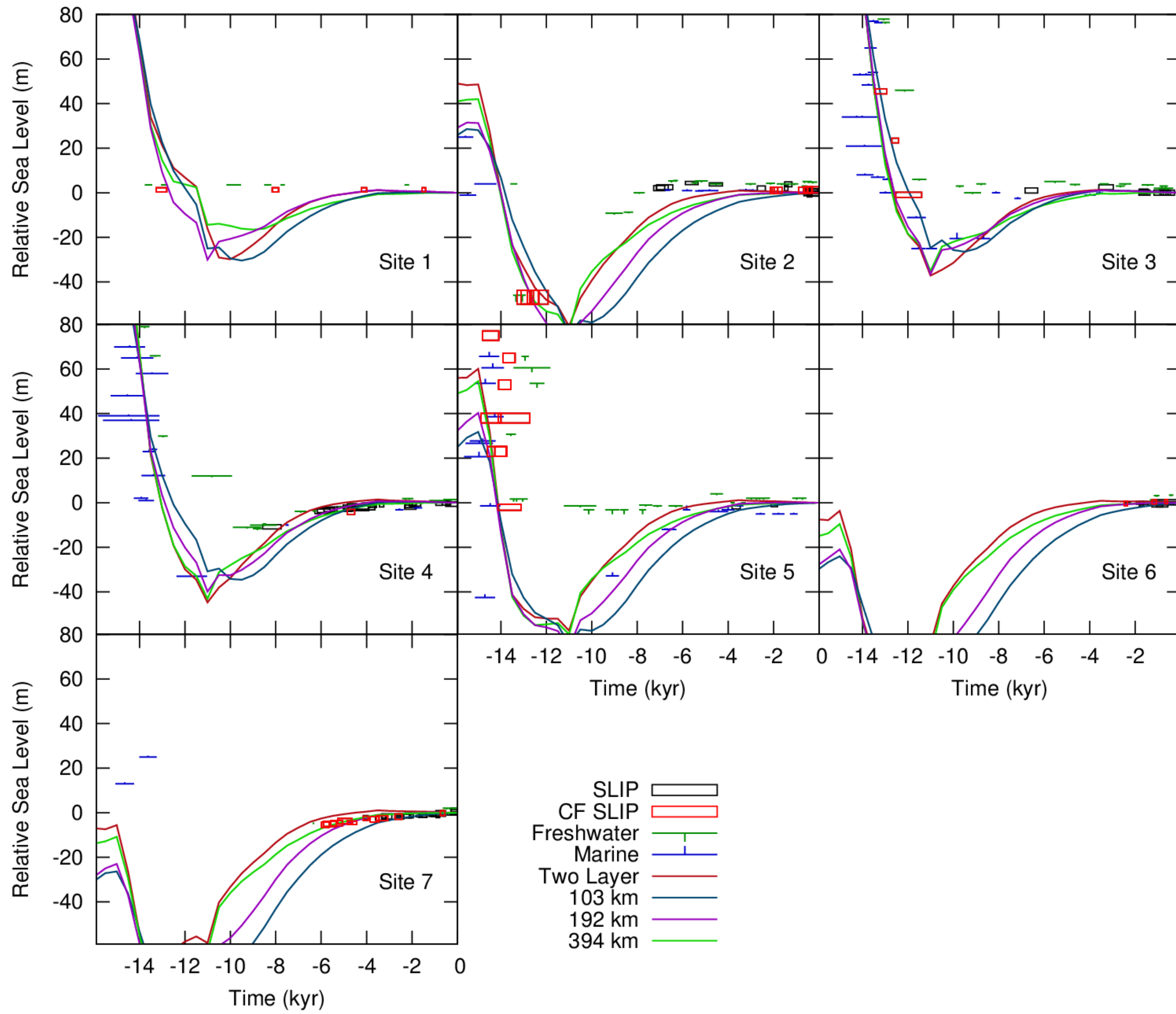

Figure S1. Data-model comparison for the northern region. The results are shown for 4 model curves: 3 models consider the inclusion of an asthenosphere layer with viscosity of 5×10^{19} Pas and thickness of 103, 192 and 394 km (see key on bottom right of figure). The asthenosphere layer was included in a model with an UMV of 5×10^{20} Pas and LMV of 10^{21} Pas. The red curve shows the two-layer optimal model curve with the following parameters: UMV of 5×10^{19} Pas, LMV of 10^{21} Pas and ice model number 6885R (index number 27). The lithosphere thickness is set to 46 km. Observational uncertainty is indicated at the 2σ level.

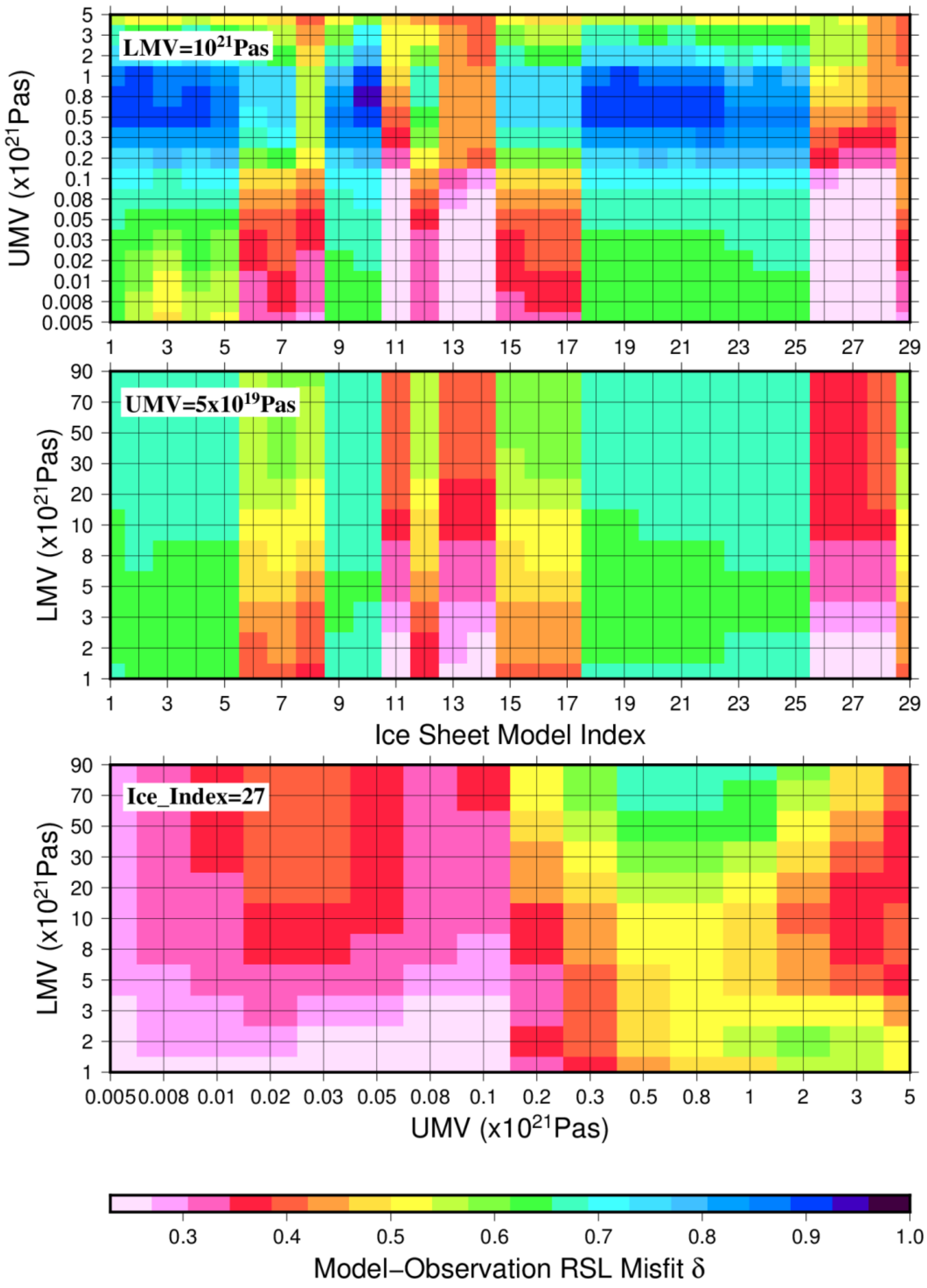

Figure S2. Data-model misfit values for the whole northern dataset (sites 1-7) without applying any data weighting. The upper panel displays the misfit values when the LMV is constant (10^{21} Pas) and δ is only a function of UMV and ice model. The middle panel shows δ as a function of LMV and ice model with the UMV fixed at 5×10^{19} Pas. The lower panel shows the δ values in terms of varying LMV and UMV for the case of ice model 6885 (index number 11). In all 3 plots, the lithosphere thickness is constant and has a value of 71 km.

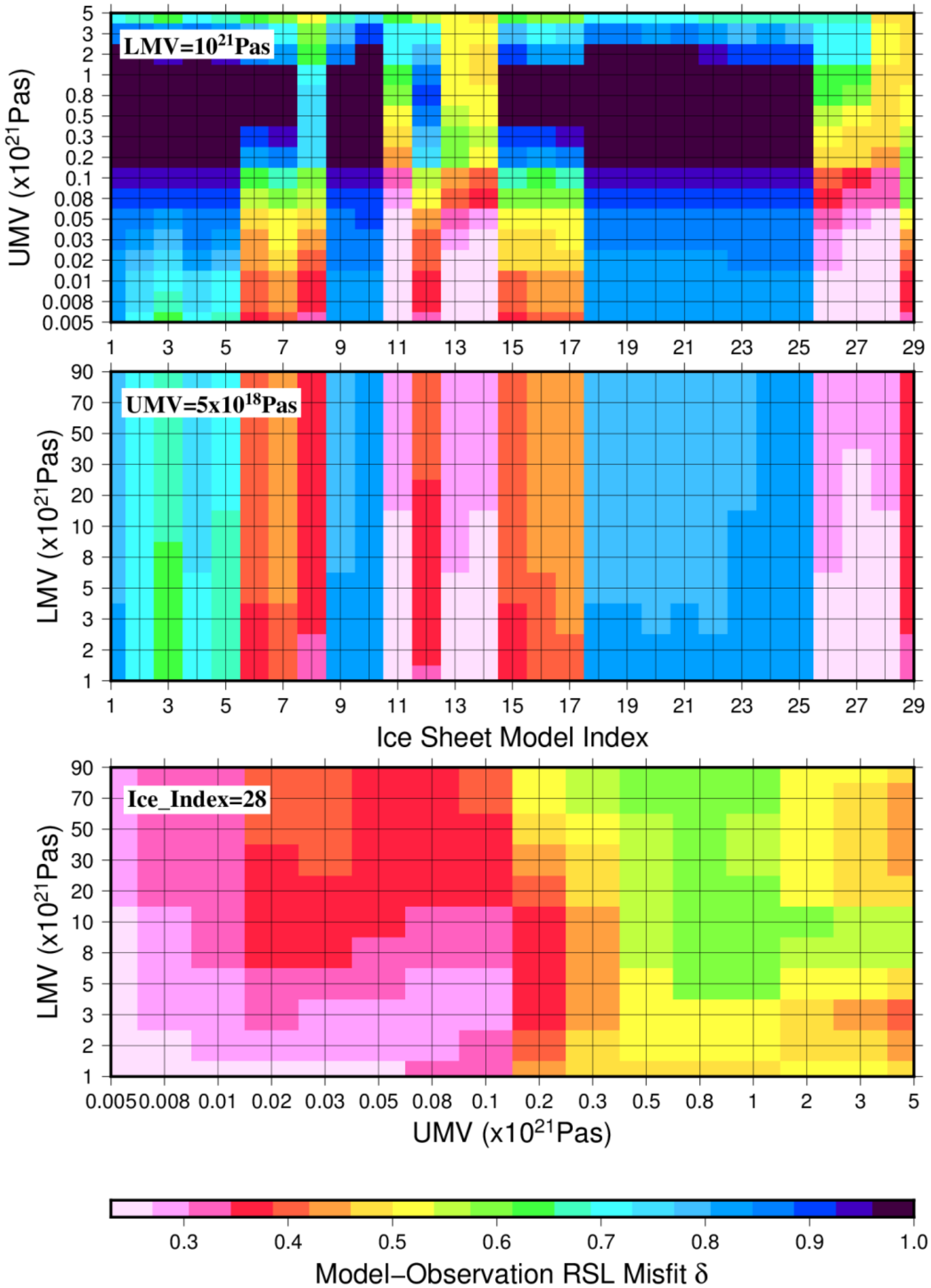

Figure S3. Data-model misfit values for the whole northern dataset (sites 1-7) when applying the data weighting approach. The upper panel displays the misfit values when the LMV is constant (10^{21} Pas) and δ is only a function of UMV and ice model. The middle panel shows δ as a function of LMV and ice model with the UMV fixed at 5×10^{18} Pas. The lower panel shows the δ values in terms of varying LMV and UMV for the case of ice model 9927K (index number 28). In all 3 plots, the lithosphere thickness is constant and has a value of 46 km.

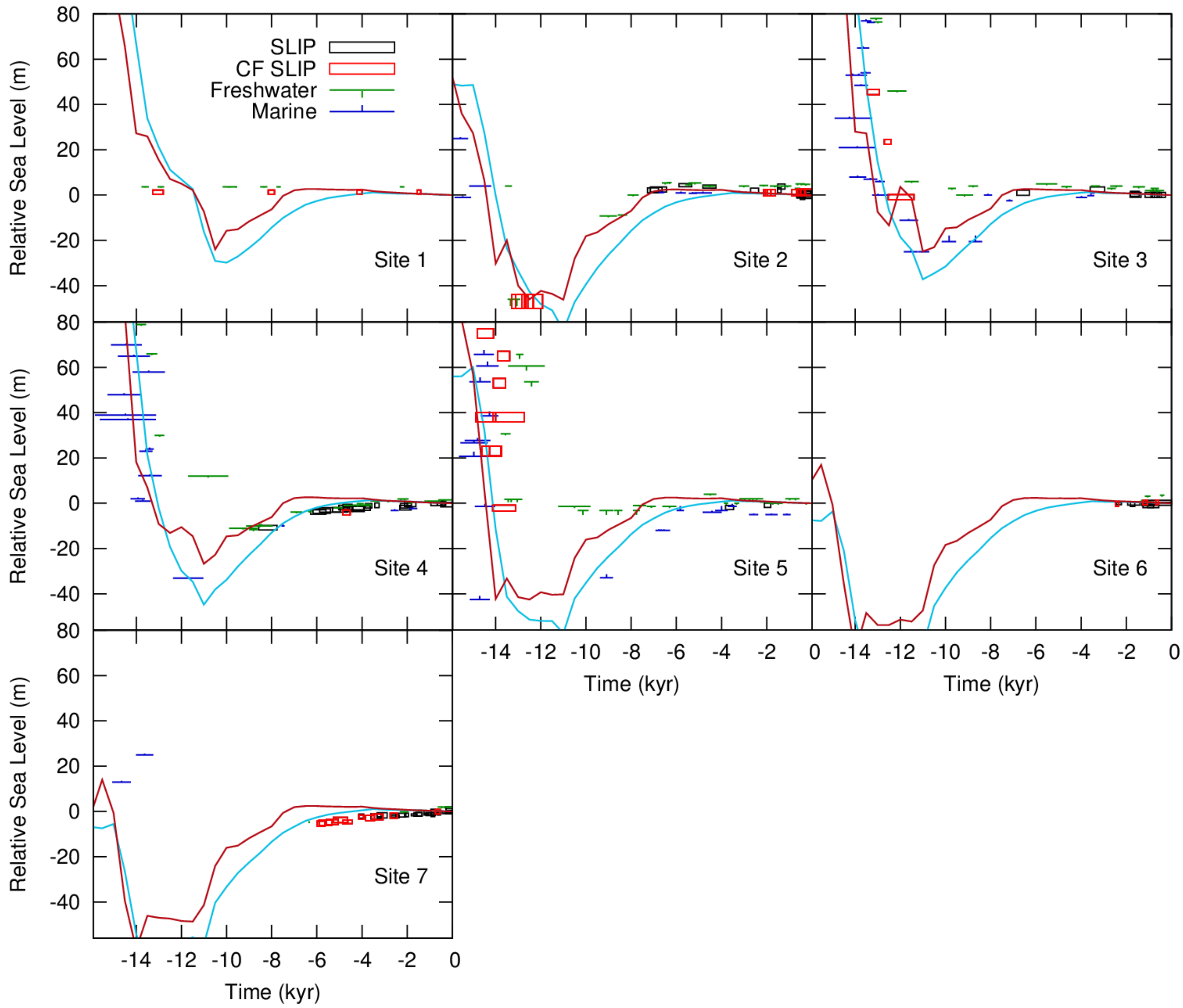

Figure S4. Data-model comparison for the northern region when using the whole northern weighted dataset. The optimal curve in this case is plotted in red and adopts the following parameters: UMV of 5×10^{18} Pas, LMV of 10^{21} Pas and ice model number 9927K (index number 28). The lithosphere thickness is set to 46 km. The model curve obtained by considering data that capture the late-glacial RSL fall window is plotted in light blue. Observational uncertainty is indicated at the 2σ level.

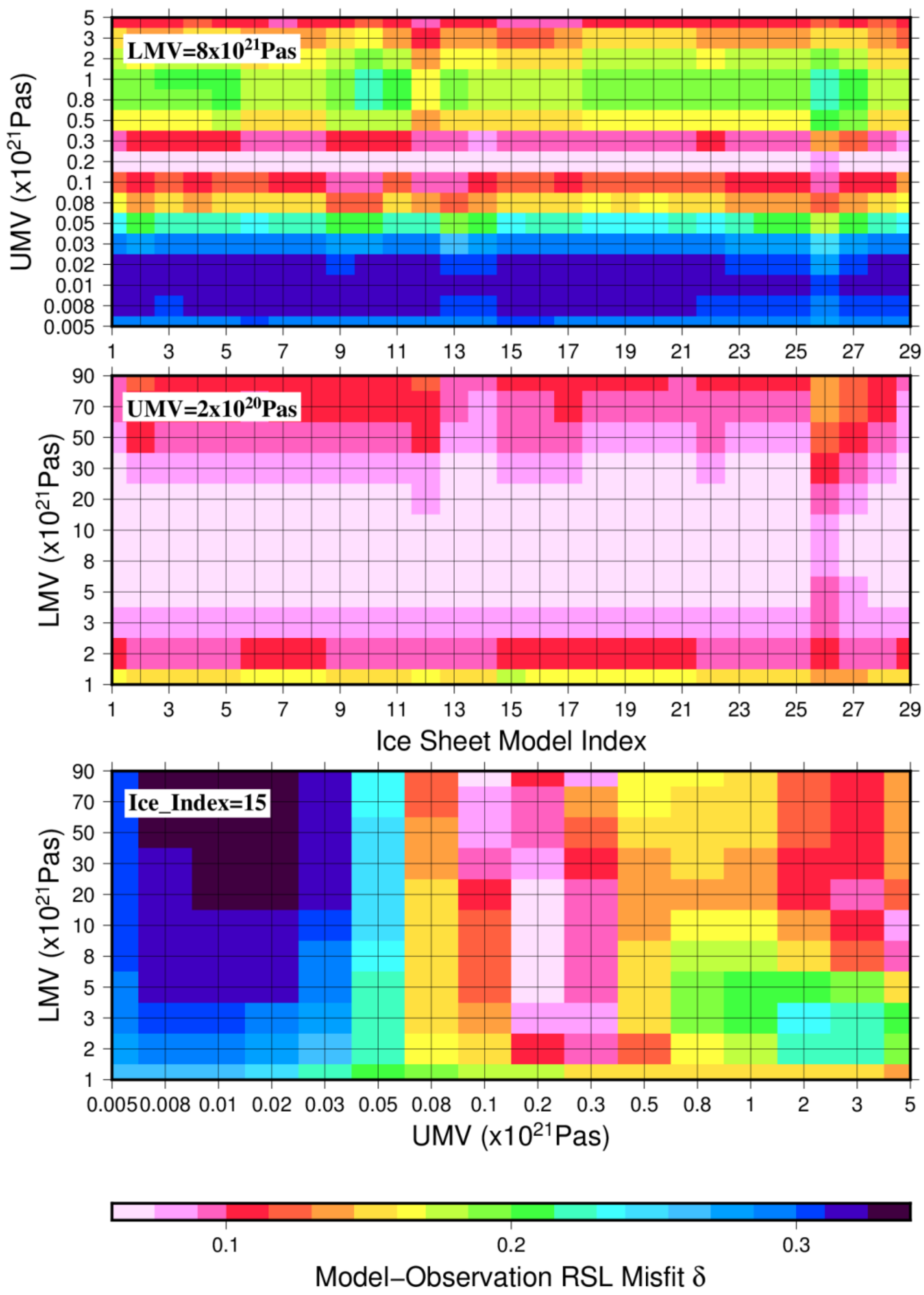

Figure S5. Data-model misfit values for the central region without applying any data weighting. The upper panel displays the misfit values when the LMV is constant (8×10^{21} Pas) and δ is only a function of UMV and ice model. The middle panel shows δ as a function of LMV and ice model with the UMV fixed at 2×10^{20} Pas. The lower panel shows the δ values in terms of varying LMV and UMV for the case of ice model 9858 (index number 15). In all 3 plots, the lithosphere thickness is constant and has a value of 96 km.

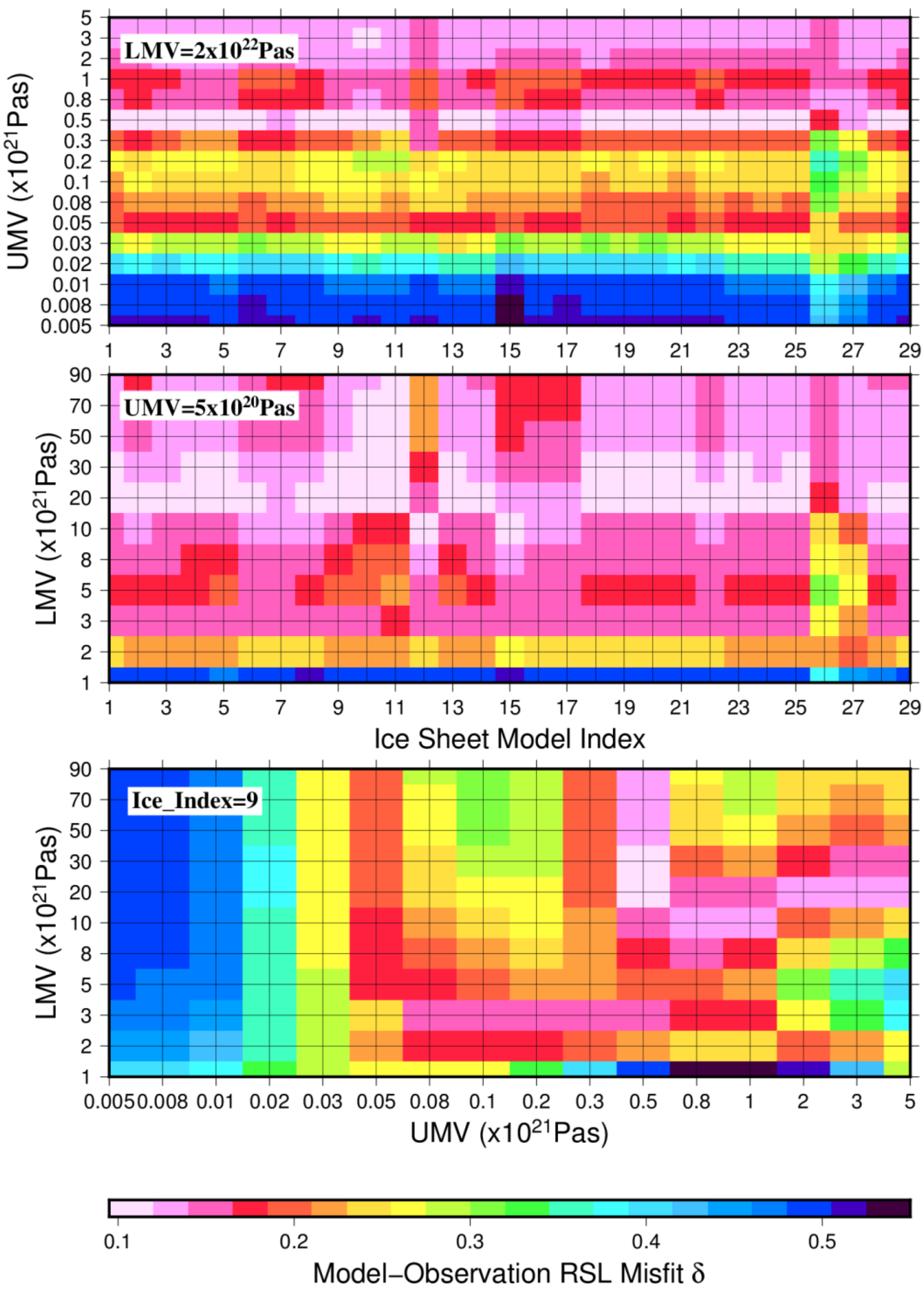

Figure S6. Data-model misfit values for the southern region without applying any data weighting. The upper panel displays the misfit values when the LMV is constant (2×10^{22} Pas) and δ is only a function of UMV and ice model. The middle panel shows δ as a function of LMV and ice model with the UMV fixed at 5×10^{20} Pas. The lower panel shows the δ values in terms of varying LMV and UMV for the case of ice model 5962 (index number 9). In all 3 plots, the lithosphere thickness is constant and has a value of 71 km.

a)

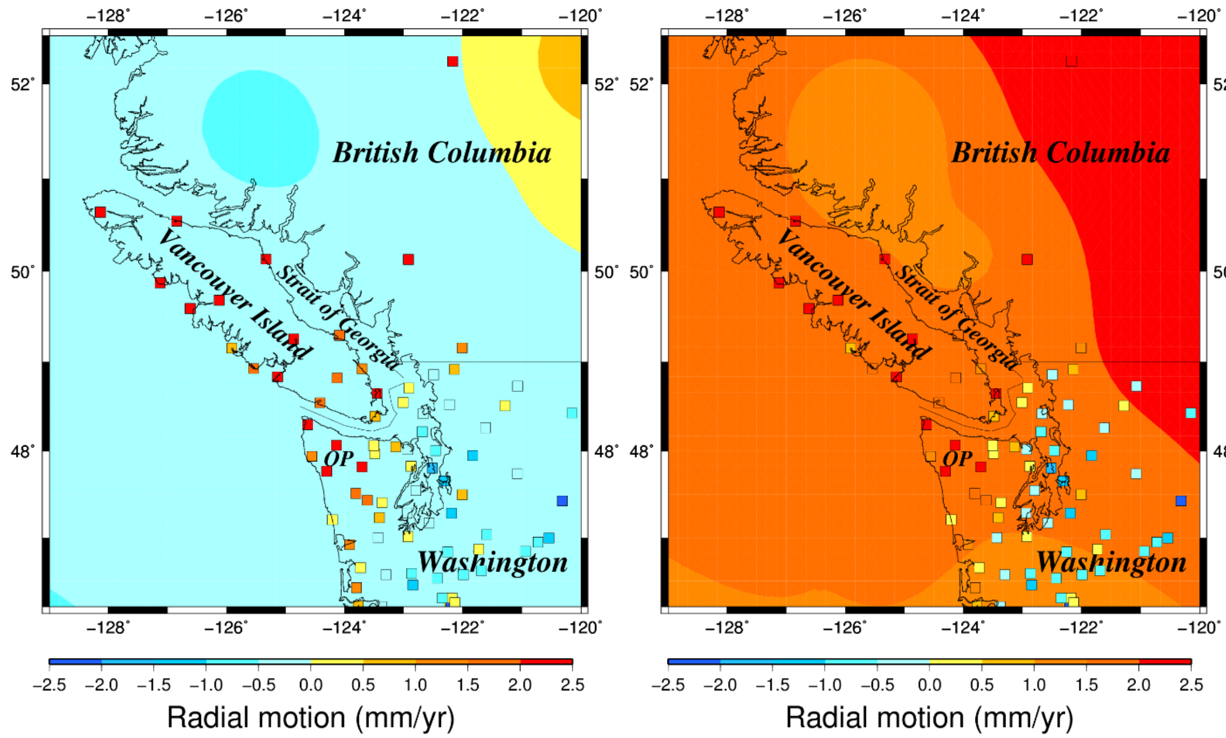
British Columbia
Vancouver Island
Strait of Georgia
OP
Washington
Radial motion (mm/yr)
British Columbia
Vancouver Island
Strait of Georgia
OP
Washington
Radial motion (mm/yr)

b)

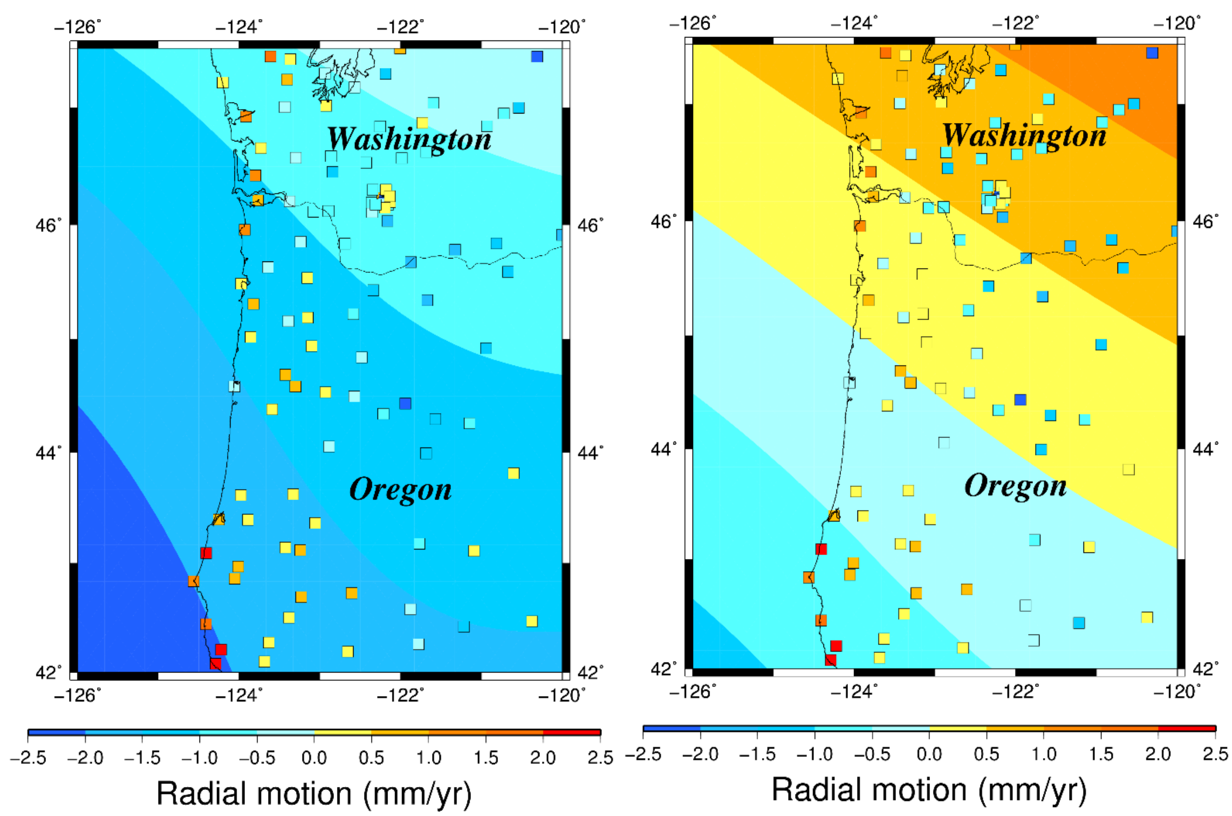
Washington
Oregon
Radial motion (mm/yr)
Washington
Oregon
Radial motion (mm/yr)

c)

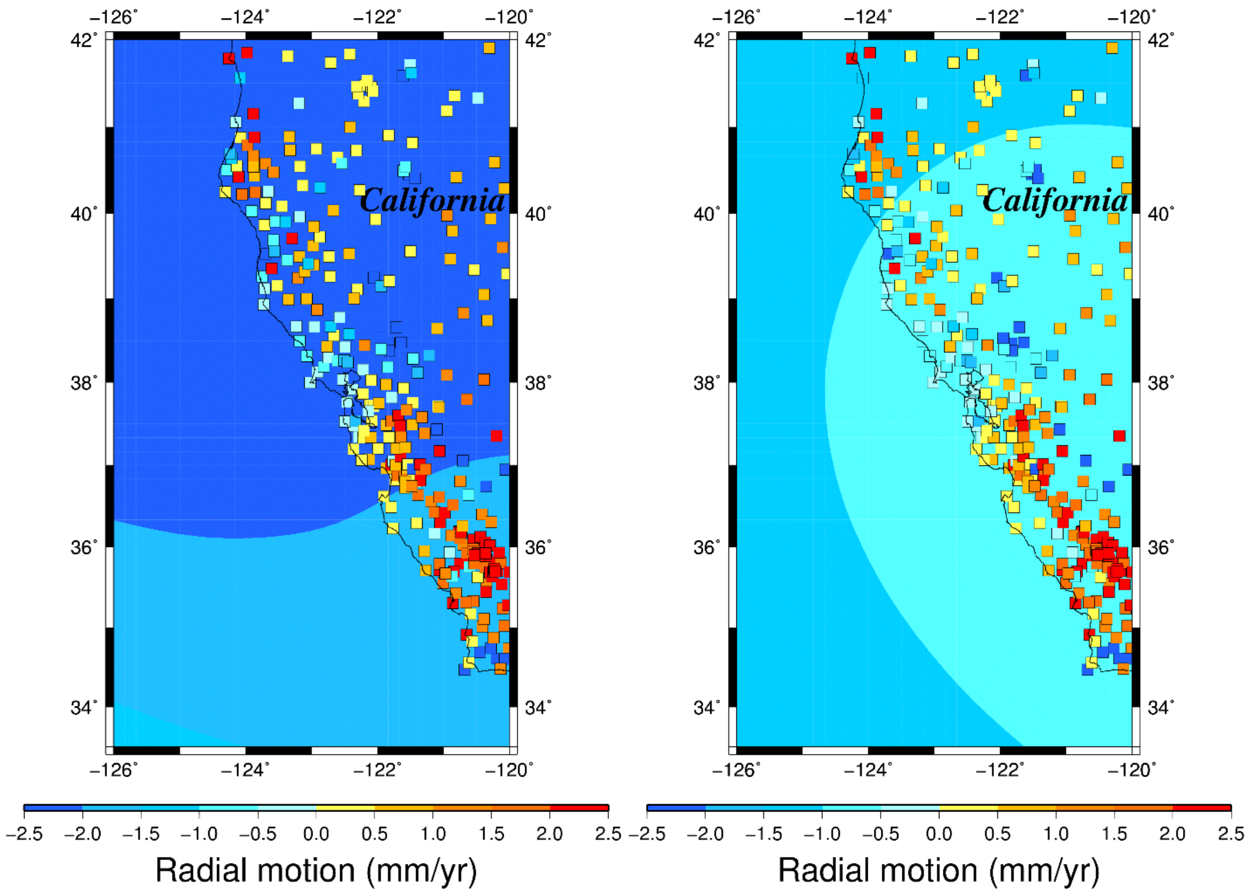

Figure S7. Lower and upper bound rates (left and right frames, respectively) for present-day vertical land motion in (a) northern, (b) central, and (c) southern regions. Coloured squares indicate the locations of the GPS sites and the observed rates of vertical motion. The bounds for central and southern regions were determined using the heuristic approach; those for the northern region were determined using the nominal Bayesian approach. OP represents the Olympic Peninsula.

a)

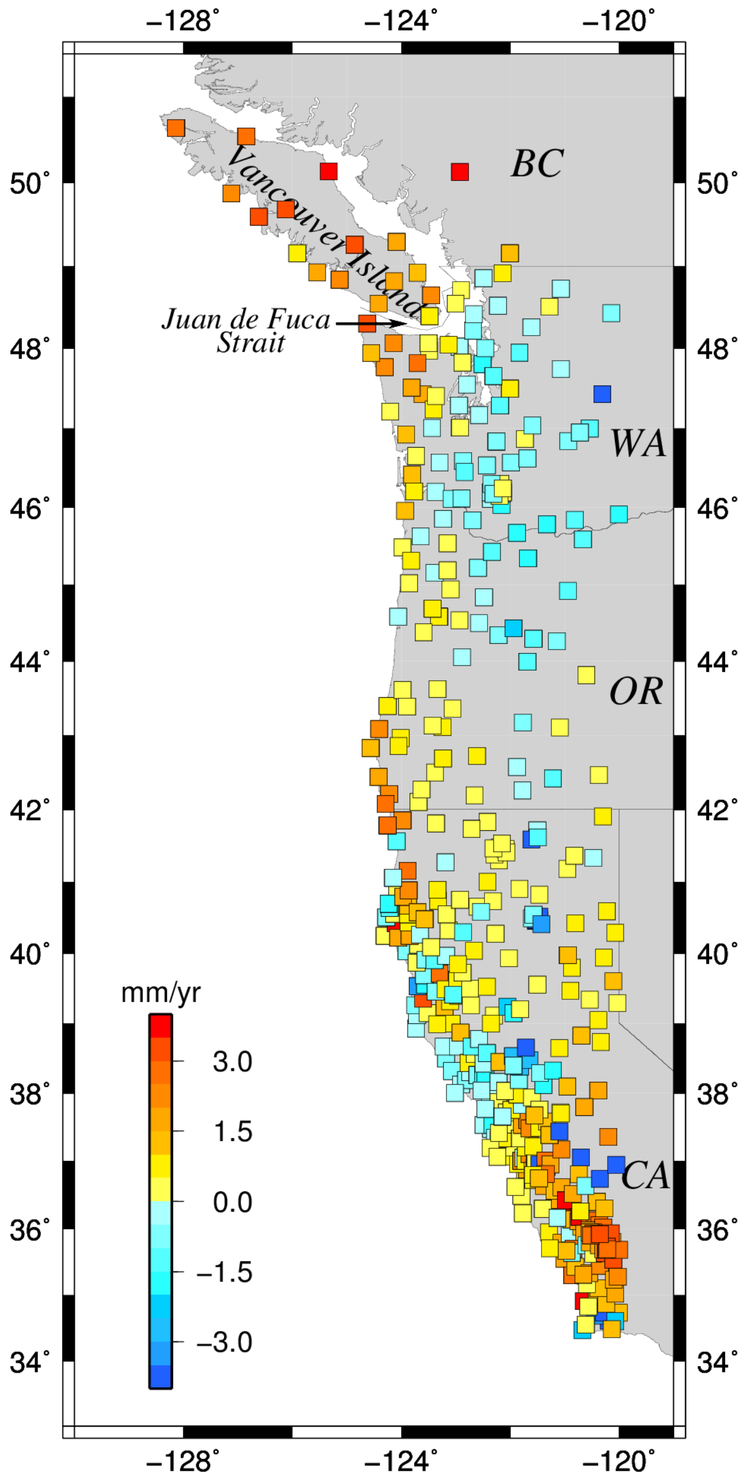

−128˚
−124˚
−120˚
50˚
48˚
46˚
44˚
42˚
40˚
38˚
36˚
34˚
BC
Vancouver Island
Juan de Fuca
Strait
WA
OR
CA
mm/yr
3.0
1.5
0.0
−1.5
−3.0

b)

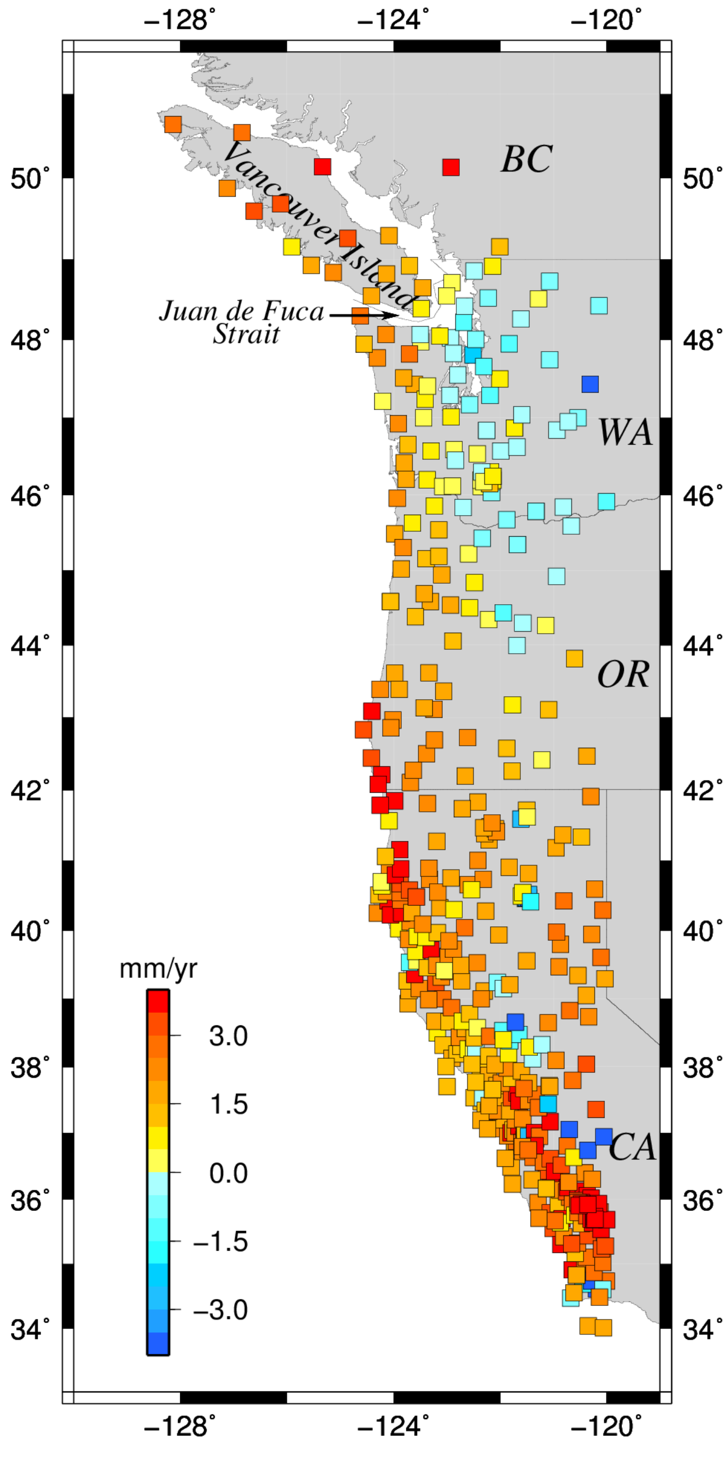

Figure S8. a) Map of observed GPS vertical motion rates; b) The residual (observed minus modelled) uplift rates at each GPS station location. US states – Washington (WA), Oregon (OR) and California (CA) – and the Canadian province of British Columbia (BC) are indicated along with their geographic boundaries. Model output is based on the optimal parameter set for each of the three regions (Table 2.2).

3

Glacial Isostatic Adjustment of the Pacific Coast of North America: The Influence of Lateral Earth Structure

Statement of Contribution

The research presented in the following manuscript is written by me under the supervision of Dr. Milne. I led the writing of the manuscript with several rounds of feedback from Dr. Milne as well as input from Konstantin Latychev. Konstantin Latychev provided us with his developed 3D GIA code. I generated all model results and all figures included in the manuscript. Most of the interpretations of model output are my own, thus the bulk of the scientific discussion reflects my own thoughts and analysis.

3.1 Introduction

The isostatic response of the Earth to the most recent global-scale deglaciation (approximately 21,000 to 7,000 yr before present) dominates secular changes in land height, the gravity field and relative sea level (RSL) in formerly glaciated regions and adjacent areas (Clark et al., 1978; Lambeck et al., 1998; Mitrovica and Peltier, 1989). The Pacific coast of North America was proximal to the Laurentian ice sheet and partially covered by the Cordilleran ice sheet during the last glacial period and thus is significantly influenced by this process, commonly termed glacial isostatic adjustment (GIA). The effect of GIA is reflected in various data types, including paleo reconstructions of RSL change (e.g. Engelhart et al., 2015) and measurements of land motion determined via the Global Positioning System (GPS; e.g. Montillet et al., 2018). Numerous studies have applied RSL reconstructions to constrain two primary components of GIA models in this region: solid Earth viscosity structure and the regional ice loading history (Clague and James, 2002; James et al 2000, 2005, 2009a,b; Muhs et al., 2012; Roy and Peltier, 2015; Yousefi et al, 2018). All of these studies are based on the conventional spherically-symmetric Earth models which consider only a radially variable viscosity structure.

Due to the proximity of this coastline to an active plate boundary, that includes the Cascadia Subduction zone, the observations mentioned above are also affected by the associated tectonic activity. A major component of this signal is a result of the convergence and subduction of the remnants of the ancient Farallon oceanic plate,that is Juan de Fuca, Gorda and Explorer plates, beneath the North American plate (Severinghaus & Atwater, 1990). In order to use RSL and land motion observations to constrain GIA model parameters, it is first necessary to estimate and remove the contribution from tectonic processes.

In a comprehensive 1D GIA study for the west coast of North America, Yousefi et al. (2018) constrained GIA model parameters using a regional RSL dataset with geographic extent from northern Vancouver Island to southern California. They adopted a broad range of model parameters, comprised of 704 Earth viscosity models and 29 different ice history models to constrain these primary GIA model parameters. One aspect that was addressed in their study is the effect of tectonic activity on local RSL change in this area and its potential impact of the GIA parameter inferences. Their results suggest significant spatial variability in mantle viscosity with a preference of lower values in the northern sector and increasing values towards the south. They also showed that no single 1D model can fit the entire dataset, emphasising the potential importance of lateral structure to accurately model the GIA response.

There has been increasing interest in applying 3D Earth models that can accommodate lateral viscosity structure when modelling the GIA response at regional scales (e.g., Austermann et al., 2013; Kuchar et al., 2019; Li et al., 2018; Milne et al., 2018; Paulson et al., 2007; Van der Wal et al., 2013 & 2015; Wu and Van der Wal, 2003). A common approach taken in most of these studies is the use of seismic velocity models to infer the lateral mantle viscosity variations. Clark et al. (2019) presented 3D GIA modelling results for central Cascadia, from northern Washington to central Oregon. In particular, they considered the sensitivity of Holocene RSL predictions to a scaling factor used in the conversion of seismic velocity anomalies, from the global S40RTS model (Ritsema et al. 2011), to viscosity anomalies. Their results suggest a low-viscosity asthenosphere (~8×10^{19} Pas) and higher viscosity values at mid-upper mantle depths (slightly higher than 10^{21} Pas). Their results also highlight the significant impact of lateral viscosity variations on predicted Holocene RSL change in central Cascadia.

In this study, we expand and complement the results of Clark et al. (2019) by considering a larger study area that extends north to northern Vancouver Island and south to southern California. As noted in Yousefi et al. (2018), the RSL data from southern British Columbia represent the greatest challenge for model fitting due to the highly non-monotonic changes that are typical of sites close to the ice margin. Uncertainty and error in the ice loading history are important aspects to consider at these sites as well as the influence of lateral Earth structure. A second aspect of our study that also extends the work of Clark et al. (2019) is that we consider four seismic models in estimating the lateral viscosity structure of the region as well as two global models of lithosphere thickness. Thus, we can assess if the RSL data indicate a preference for a particular seismic model.

We also consider two different approaches to define higher resolution lateral structure in the region given the relatively low resolution of the (global) seismic models. As the first approach, we use a state-of-the-art regional shear-wave seismic velocity model (Hawley and Allen, 2019) and integrate it with two of the global seismic models. Alternatively, we use information on the extent of the Cascadia slab (Blair et al., 2011) to define a high-viscosity slab beneath the North American plate and a low-viscosity region between the subducting slab and the overlying continental lithosphere, the so-called "mantle wedge." The Cascadia forearc mantle wedge is stagnant and heavily serpentinized owing to the fluids produced from the shallow dehydration of the young and warm slab (Brocher at al., 2003; Wada et al., 2008). The relatively small scale of the subducting slab and mantle wedge are not captured in the global seismic models. We evaluate the accuracy of these different 3-D viscosity models by comparing output to observations of RSL change.

3.2 Methods

3.2.1 The RSL Observations

We use two published compilations of sea-level datasets along the Pacific coast of North America to evaluate the accuracy of the models developed in this study: one from Vancouver Island to Central California (Engelhart et al., 2015), and one from Central California to Southern California (Reynolds & Simms, 2015). The specific distribution of sites was chosen based on various criteria such as tectonic setting and distance from former ice sheet (Engelhart et al., 2015; Yousefi et al., 2018). Each site comprises a relative sea-level dataset including both sea-level index points (SLIPs) and limiting data (freshwater and marine indicators) as illustrated in the original publications that the data are extracted from (Engelhart et al., 2015; Reynolds and Simms, 2016). We note that only the location of index points and the corresponding average of these are plotted in Figure 3.1 and we use a version of the data that are corrected for the effect of tectonics (Yousefi et al., 2018, see their section 2.1.1 for more details).

3.2.2 The Model

We apply a forward modelling approach using a numerical finite-volume method for computing the response of a self-gravitating, Maxwell (viscoelastic) Earth to a specified surface loading history (Latychev et al., 2005). The model solves the underlying equations (e.g. Wu and Peltier, 1982) to compute solid Earth deformation on a spherical tetrahedral grid and output surface observables such as vertical displacement, changes in gravity and relative sea-level change. The global tetrahedral grid is a multi-layered spherical structure with triangulated spherical surfaces at user defined depths. Each tetrahedron has four vertices, known as grid nodes. A number of physical properties, including density, elastic Lamé parameters, and viscosity are allocated to each of the computational grid nodes. Lateral resolution of the grid is ~12-15 km at the top surface and decreases with depth, with an average spacing of ~60 km at the Core-Mantleboundary. Similarly, the radial resolution of the grid is greatest near the surface (~12 km) and decreases towards the Core-Mantle boundary (~50 km).

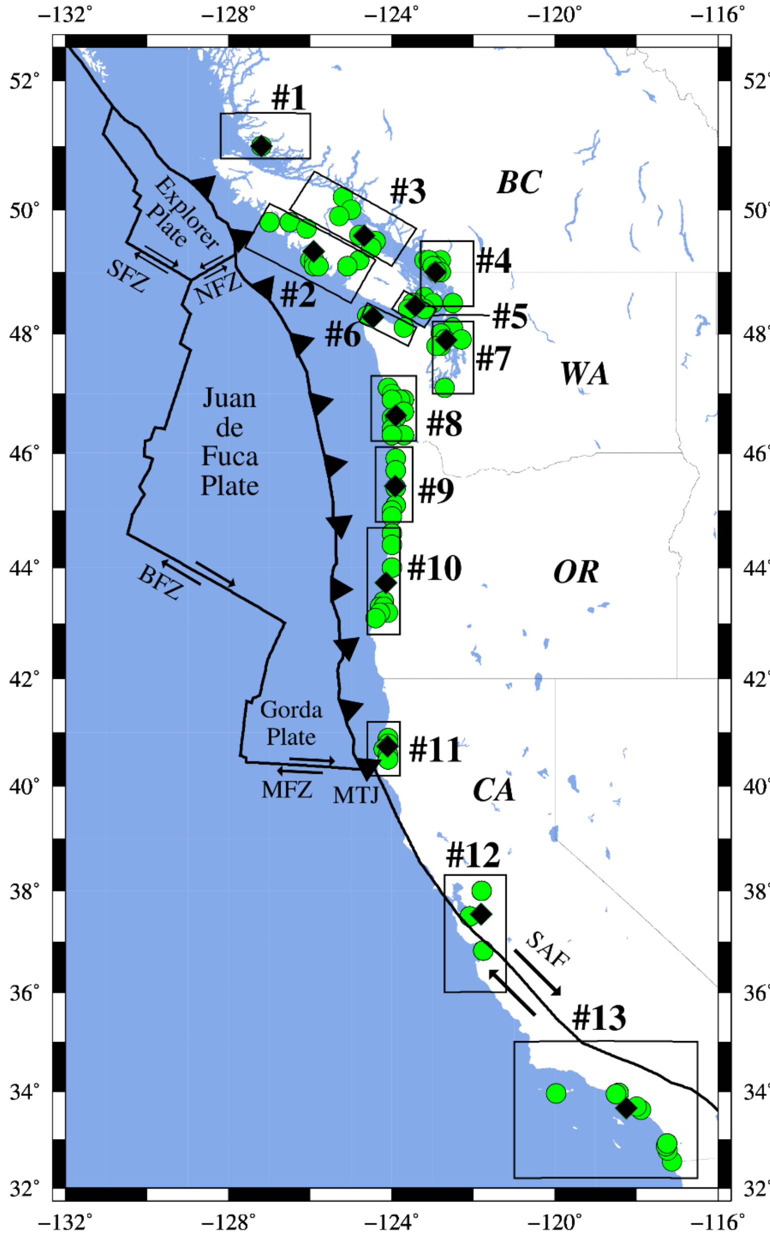

Figure 3.1. Map showing the spatial distribution of RSL data. The black lines show plate boundaries, with the triangles indicating subduction of the Juan de Fuca, Explorer and Gorda plates beneath the North American plate. The black rectangles correspond to each of the 13 regions considered. The locations from where RSL data were acquired are indicated by green circles. The black diamonds in each region gives the average location of the RSL data for that region. MTJ represents the Mendocino Triple Junction; SFZ, BFZ, MFZ, and NFZ represent the Sovanco, Blanco and Mendocino fracture zones, and Nootka fault zone, respectively; SAF is the abbreviation for the San Andreas Fault. US states – Washington (WA), Oregon (OR) and California (CA) – and the Canadian province British Columbia (BC) are indicated along with their geographic boundaries (grey lines).

The sea-level calculator solves the generalised sea-level equation (Mitrovica and Milne, 2003; Kendall et al., 2005) and so accounts for the evolution of coastlines. The influence of Earth rotation on GIA observables is also built into the software (Milne and Mitrovica, 1998; Mitrovica et al., 2005). Solving the sea-level equation requires two key model inputs: an ice loading history and a viscoelastic model of the Earth. The ice loading component is a spatio-temporal model of thickness and extent of the Late Pleistocene ice sheets. The ice loading model is established by projecting the ice thickness values on the surface nodal grid points of the global tetrahedral grid. We use a specific model "6885" selected from a large set of reconstructions of the North American Ice Sheet Complex (Tarasov et al., 2012) which is embedded in a background global model of ice evolution (ICE5G; Peltier, 2004). The North American ice sheet reconstructions were simulated using a glacial systems model which includes a variety of physical processes related to ice sheet evolution in response to a defined climate forcing. Model output was calibrated against various types of regional observations such as RSL, ice extent, paleo-lake levels, and present-day crustal uplift rates. See Tarasov et al. (2012) for more detail on the glacial systems model and calibration procedure. We chose the 6885 ice model following the work of Yousefi et al. (2018) who showed that this particular ice loading history provides the best fit to the regional RSL data.

The 3D viscoelastic Earth models that we develop and apply here consist of a high viscosity lithosphere (to simulate an elastic medium on GIA timescale) with laterally variable thickness. We define the lateral variations in lithosphere thickness using two global models that are based on different approaches and observations as detailed in section 3.2.2.1. We scaled the lithosphere thickness to a pre-defined value to enable comparison to output from 1D models. In this study, this scaling results in a global average thickness of 46 km to be consistent with the optimal value inferred in the analysis of Yousefi et al. (2018). It is also compatible with the mean value inferred in a global analysis of RSL observations (Lambeck et al., 2014).

The lateral viscosity structure of the mantle is superimposed on a 1D reference viscosity profile, which we describe below. In this study, three different approaches are used to define departures from our 1D reference model: two give global estimates of 3D viscosity structure with one of these models including a higher resolution regional model beneath our study region and one includes lateral structure in our study region only (sections 3.2.2.2 and 3.2.2.3). The density and elastic structure of the Earth model are defined only in 1D (with depth) and are given by the seismic model PREM (Dziewonski & Anderson, 1981).

The viscous structure of the reference 1D model is the same as the one outlined in Yousefi at al. (2018) and is characterized by uniform viscosity within the upper mantle (below the lithosphere down to 670 km depth) and the lower mantle (from 670 km depth to the Core-Mantle boundary). Yousefi et al. (2018) divided their entire study area into 3 sub-regions: northern, from northern Vancouver Island to northern Washington; central, from southern Washington to southern Oregon; and southern, from northern California to southern California. Table S1 represents a summary of the optimal model parameters that were inferred using RSL data from each sub-region, as well as those inferred from the entire dataset. For this analysis, we use the optimal 1D profile associated with the central region: (upper mantle viscosity (UMV) = 2×10^{20} Pas, lower mantle viscosity (LMV) = 10^{22} Pas) as it is centrally located in our study region and is broadly consistent with a global analysis of RSL observations (Lambeck et al., 2014).

3.2.2.1 Lithosphere thickness models

We apply two global models of lateral variations in lithosphere (elastic) thickness: a model presented by Zhong et al. (2003) which is a modified version of an earlier model (Watts, 2001), hereafter referred to as the WA model; a model that we have constructed based on the global model of Audet and Bürgmann (2011) which will be referred to as the AB model in the following. The continental lithosphere thickness in the WA model is estimated using a forward modelling technique based on the results of flexural loading studies. For oceanic regions, the elastic thickness depends on the thermal structure of the oceanic lithosphere (mainly controlled by its age) and is defined as the depth to the 750°C isotherm (Zhong et al., 2003).

The AB model is a compilation of four components: a global model of oceanic lithospheric thickness, a global model of elastic thickness in continental areas (Audet and Bürgmann, 2011) and two regional estimates of lithospheric thickness beneath Greenland (Steffen et al., 2018) and Antarctica (Chen et al., 2017). Over oceanic areas, we follow the formulations presented in Caldwell and Turcotte (1979) and assume that thermal structure and thickness of lithosphere are functions of square root of the ocean-floor age. We apply a global seafloor age dataset that is based on marine magnetic anomaly isochrones (Müller et al., 2008) and define the base of the oceanic lithosphere to correspond to the depth of the 700°C isotherm. The continental lithosphere elastic thickness in the AB model was estimated using an inverse modelling approach by computing the spectral coherence between topography and gravity anomalies and comparing it to model predictions (Audet and Bürgmann, 2011). The model of Audet and Bürgmann (2011) covers all major continents except for Greenland and Antarctica. For this reason, we integrated it with the regional models that use a similar inverse modelling technique to infer the elastic thickness beneath Greenland (Steffen et al., 2018) and Antarctica (Chen et al., 2017). Figure 3.2 shows the lateral variations in lithospheric thickness in both global and regional scales which illustrates that there is generally good agreement between the two models. However, there are some differences, with the AB model showing markedly lower values in most regions except for Africa, North America, and northwestern Eurasia. At the regional scale, the WA model represents much greater thickness values for the oceanic lithosphere which can be attributed to the higher isotherm considered for constraining the base of the oceanic lithosphere by Zhong et al., (2003). The discrepancy observed between the two models can be primarily explained by the different methodologies applied and the improved datasets used in the more recent analyses. However, as mentioned in the previous section, the two models are scaled to give a user defined (e.g., 46 km in this study) global mean.

a)

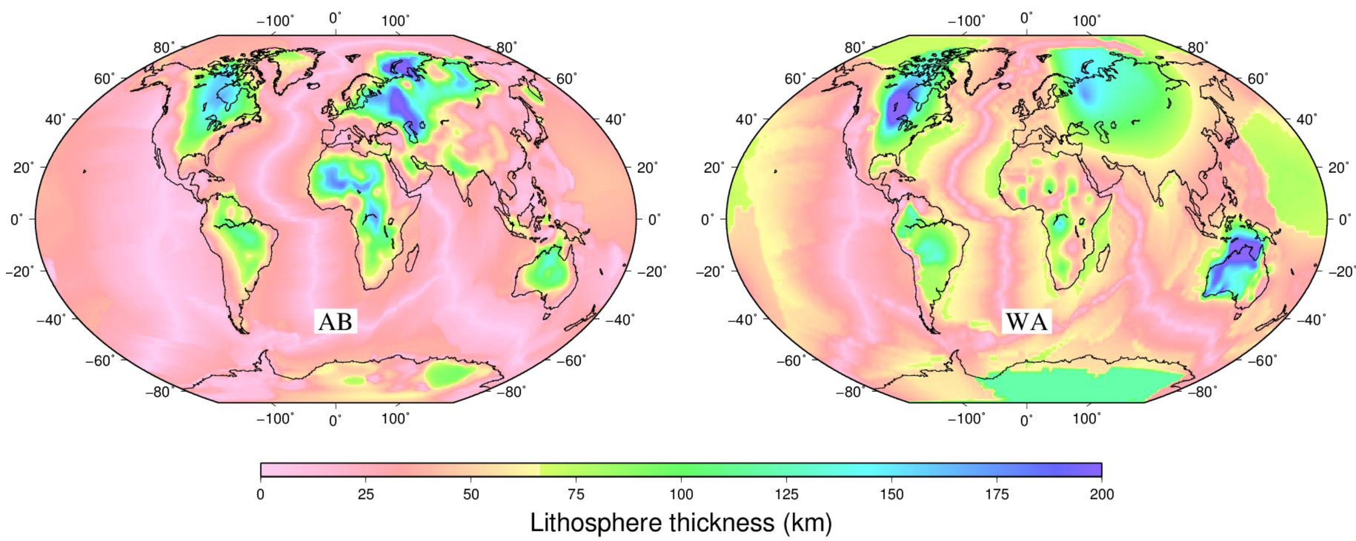

Figure 3.2. (a) Global and (b) regional Lateral variations in elastic thickness of the lithosphere based on the global continental model of Audet and Bürgmann (2011), referred to as the AB model (left) and that presented by Zhong et al. (2003) referred to as the WA model (right). See text for further information.

b)

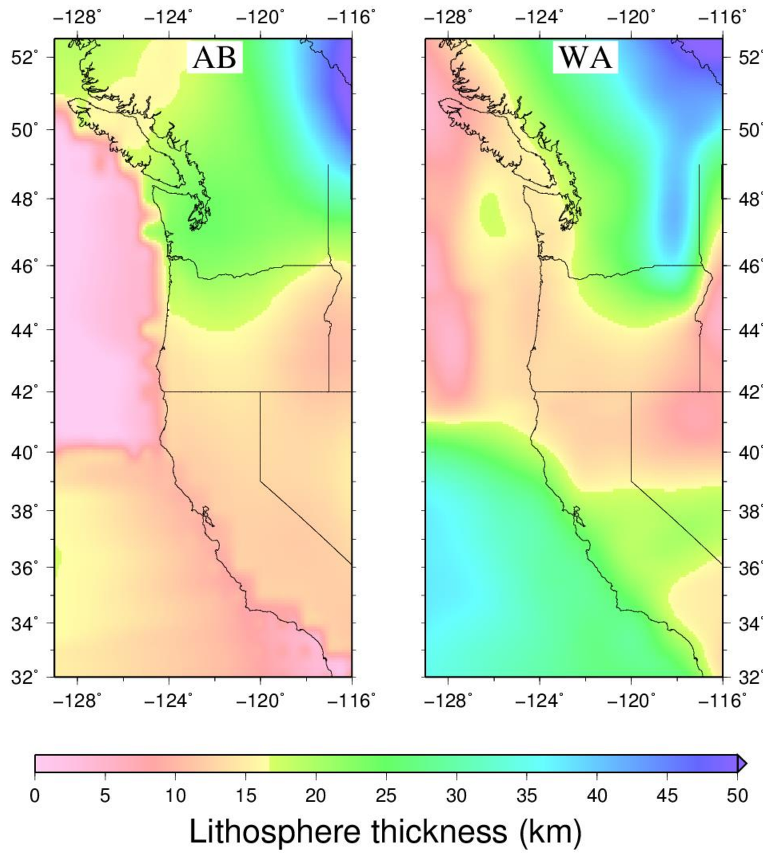

Figure 3.2. Continued.

3.2.2.2 Global Viscosity Structure

We apply four different global seismic tomography models to estimate lateral viscosity variations: S40RTS (Ritsema et al. 2011), Savani (Auer et al., 2014), SEMUCB-WM1 (French & Romanowicz, 2014), and SL2013 (Schaeffer & Lebedev, 2013). Each of these models provides variations (relative to a global mean reference model) in shear wave velocity throughout the whole mantle, except for SL2013 which does not extend below 1000 km depth. The variations in seismic wave velocities can be attributed to the variations in thermal and/or compositional structure. Assuming that the temperature is the only driving factor, we follow Latychev et al. (2005) to determine the mantle viscosity structure using the following set of equations (3.1 to 3.3):

$$\delta\ln\rho(r,\theta,\varphi) = \frac{\partial \ln \rho}{\partial \ln v_s}(r)\, \delta \ln v_s(r,\theta,\varphi) \tag{3.1}$$

$$\delta T(r,\theta,\varphi) = -\frac{1}{\alpha(r)}\, \delta\ln\rho(r,\theta,\varphi) \tag{3.2}$$

$$\eta(r,\theta,\varphi) = \eta_0(r)\, e^{-\epsilon\, \delta T(r,\theta,\varphi)} \tag{3.3}$$

Where, r, θ and φ are the radius, colatitude and east longitude, respectively. The term $\delta \ln v_s(r,\theta,\varphi)$ represents seismic shear wave velocity perturbations and $\frac{\partial \ln \rho}{\partial \ln v_s}(r)$ is a depth-dependant logarithmic scaling factor used to convert the velocity variations to density variations ($\delta\ln\rho$) (eqn 3.1). We adopt the radial profile of Forte and Woodward (1997) for the velocity-to-density scaling coefficient with an estimated range of ~0.1-0.35. The variations in temperature (δT) are then calculated by scaling the density field using the radially variable coefficient of thermal expansion, $\alpha(r)$ (eqn 3.2). The depth-dependant thermal expansion coefficient that we use here is based on the high-temperature, high-pressure laboratory experiments of Chopelas and Boehler, 1992. Finally, the 3D viscosity structure (η) is estimated using an exponential function of the scaled temperature anomalies (eqn 3.3). The scaling factor (ϵ) appearing in the exponent of eqn 3.3, determines the degree of dependence of the viscosity structure on temperature. We set this parameter to $0.04°\mathrm{C}^{-1}$, which results in the viscosity anomaly pattern illustrated in Figure 3.3.

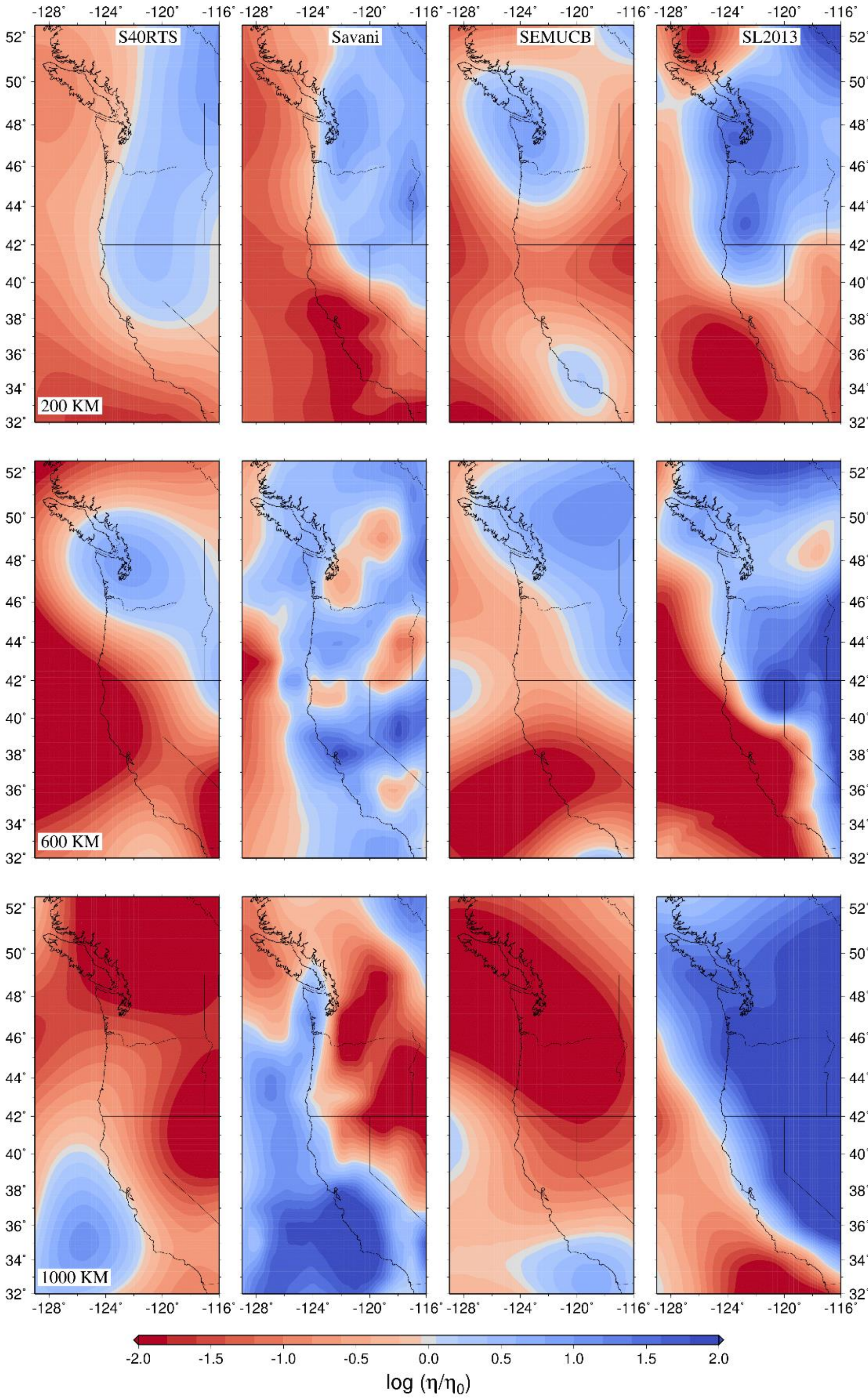

Figure 3.3. Lateral viscosity variations at depths of 200 km (top row), 600 km (middle row), and 1000 km (bottom row), associated with four global seismic models (from left column to the right): S40RTS,

Savani, SEMUCB-WM1, and SL2013. Note that these variations are relative to a chosen 1-D (radial) viscosity model (η_0(r)).

Figure 3.3 shows the viscosity variations with respect to our reference viscosity profile defined above ($\eta_0(r)$, 2×10^{20} Pas for the upper mantle, and 10^{22} Pas for the lower mantle) associated with each seismic model at three different depths: 200, 600, and 1000 km. For each model, there is considerable spatial variability in the inferred viscosity variations, with the results in Figure 3.3 suggesting smaller departures from the reference model in the shallow compared to deep mantle. The positive and negative anomaly values mainly reflect the long-wavelength heterogeneity of sub-lithospheric mantle features. For example, the relatively smooth gradient in the upper mantle viscosity, which suggests lower viscosity beneath the western side, potentially arises from a hotter and shallower asthenosphere in comparison to the colder and more stable eastern section. The global velocity models generally lack sufficient resolution to image the shorter wavelength heterogeneity thought to exist in this region. Nevertheless, the higher viscosity anomalies evident in Figure 3.3 can be attributed to the subducting Juan de Fuca-Gorda slab (200 km depth) and remnant fragments from the Farallon slab (600 km depth) (e.g., Obrebski et al., 2011; Xue and Allen, 2010). Furthermore, the localized high viscosity anomaly associated with the SEMUCB model in southern California at 200 km depth might be due to the presence of lithospheric material at the base of the asthenosphere resulting from the post-Laramide detachment of the lithospheric root (Zandt *et al.* 2004). We note that each of the seismic models use different datasets and modelling approaches which cause the differences evident in the inferred viscosity variations (Figure 3.3). For further details about the data and methodology applied for producing each seismic model, please refer to the original publications cited above.

3.2.2.3 Regional Viscosity Structure

Given the relatively low resolution of the global seismic models introduced above, we used two alternative approaches to assign regional 3D viscosity structure that resolve shorter-scale viscosity variations. For the first approach, we use the regional shear-wave seismic velocity model of Hawley and Allen (2019) and insert it into two of the global seismic models, i.e., S40RTS and SEMUCB-WM1. The lateral resolution of the regional seismic model is 0.25 degrees (~27 km) and covers the entire area enclosed within (31°N, 131°W) and (51°N, 101°W). This regional S-wave velocity model has a uniform radial resolution of 25 km from the Earth surface which extends to 1000 km depth. The conversion from seismic velocity anomaly to viscosity variations for the patched models is done with the same procedure using the same conversion factors as detailed in section 2.2.2. The lateral viscosity variability of the two models generated by insertion of the regional model into the S40RTS and SEMUCB global models are shown in Figures 3.4 and S2, respectively. Both of these composite models have a similar viscosity perturbation pattern but with some differences in amplitude which arise from the integration process that normalizes the regional average to match the global average and also the interpolation procedure that ensures a smooth transition in viscosity where the two models are joined.

From Figure 3.4 it is evident that the regional model better resolves shorter-scale features that are not captured by the global models. An example of such a feature is the subducting slab causing the positive anomaly values as indicated in Figure 3.4a which is also observed in a vertical cross section of the viscosity model at 47°N (Figure 3.4b). Another feature is a relatively strong negative anomaly representing a buoyant low-viscosity layer beneath the downgoing slab which is mapped as a north-south red layer along the western side of the slab in Figure 3.4. Although the integrated model reveals some of the shorter wavelength viscosity perturbations associated with the subduction-system, the amplitudes of the anomalies are considerably smaller than those expected in such a system (see following paragraphs). For example, the subducting slab is characterized by positive anomaly values that are only two orders of magnitude greater than the background viscosity of the upper mantle. As a second approach to build the regional 3D viscosity structure, we explicitly consider the slab geometry and possible existence of a low viscosity mantle wedge above the slab. Specifically, we incorporate a high-viscosity (10^{26} Pas) slab, a low-viscosity (10^{18} Pas) mantle wedge and a plate boundary interface between the oceanic and the continental plates with a moderate viscosity of $\sim 2 \times 10^{20}$ Pas (Figure 3.5).

a)

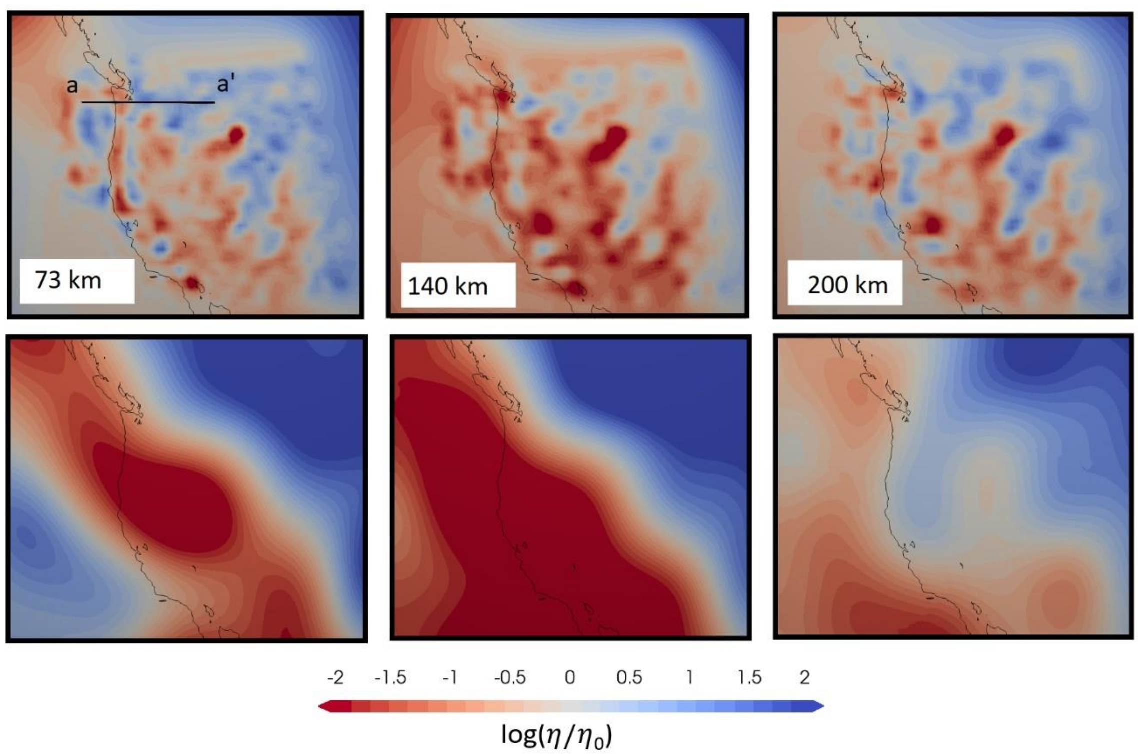

Figure 3.4. (a) Lateral viscosity anomalies at depths of 73 km, 140 km, and 200 km associated with (top row) the regional model patched with the global S40RTS model, (bottom row) the global S40RTS model. (b) A vertical cross section of the viscosity structure along the surface profile a-a' at 47°N shown in (a). The inverse black triangle marks the approximate location of the trench.

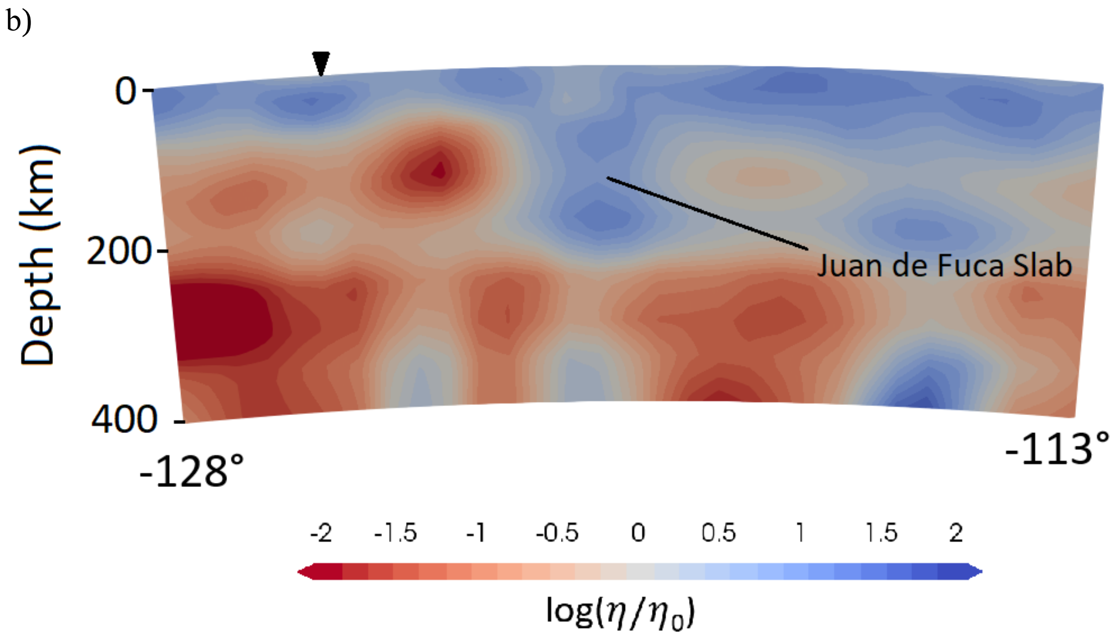

Figure 3.4. Continued.

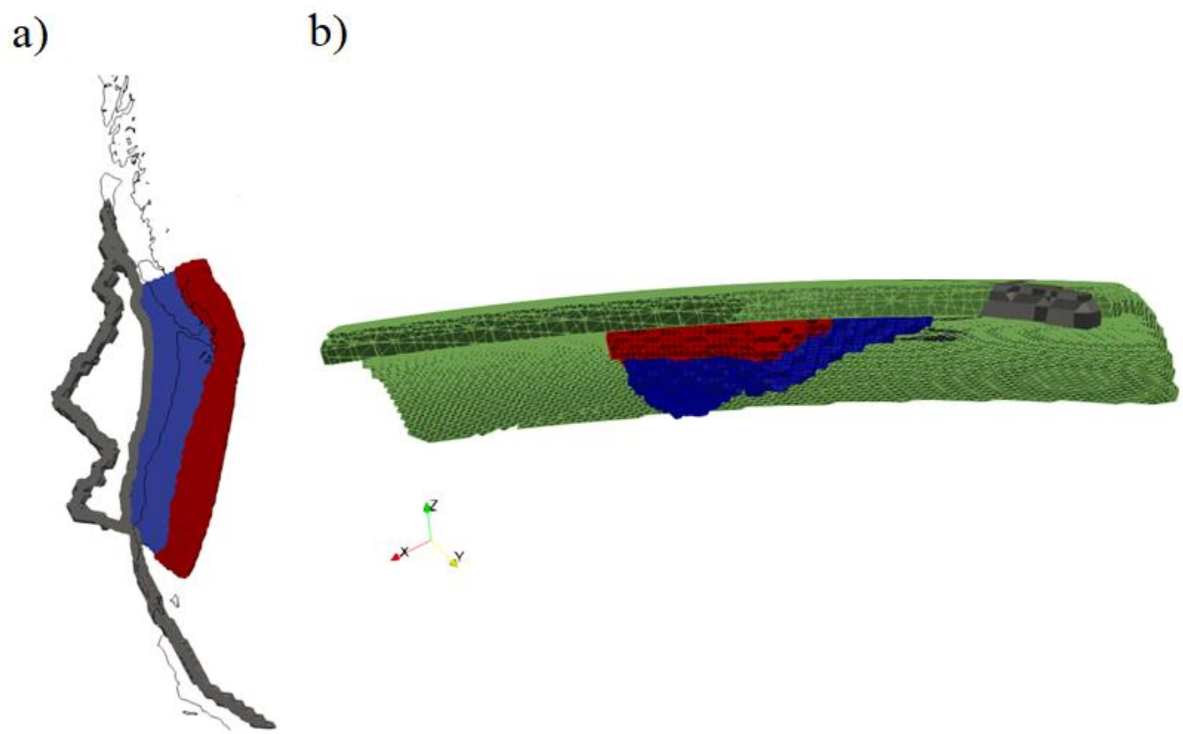

Figure 3.5. (a) Modelled regional structure of the Cascadia subduction zone in plan view: the subducting slab is shown in blue, the low-viscosity mantle wedge zone in red and the plate boundary in dark grey. (b) Alternative view of the structure shown in (a) looking south and including the objects presented in (a) as well as the lithosphere (green) which has a constant thickness of ~46 km in this particular case.

There are various factors that control the rheology of this regional structure, including temperature, water content, and composition. Observations of surface heat flow indicate no evidence of heat flow within the forearc mantle wedge and suggest that this part of the mantle is stagnant and cold (Currie et al., 2004; Wada et al., 2008). However, the influx of water-rich fluids from the subducting oceanic plate into the overlying mantle wedge generates hydrous minerals, in particular serpentine, that could reduce the viscosity of the wedge corner (Hyndman and Peacock, 2003). Although there is no direct evidence for the existence of low viscosity material within the mantle wedge, geodetic and geological constraints such as crustal strain rates and RSL observations suggest a viscosity value in range of 10^{18}-10^{19} Pas (Clark et al., 2019; James et al., 2000; Wang et al., 1994, Yousefi et al., 2018). Our considered value for the mantle wedge viscosity (10^{18} Pas) is in agreement with these previous studies. James et al. (2009) suggest that for a 10-40 km thick mantle wedge, effective viscosities in the range of 10^{15}-10^{17} Pas would be required to effectively contribute to the observed sea-level response. Therefore, we also examine the influence of a mantle wedge region with of 10^{15} Pas.

Although we adopt a constant value of 10^{26} Pas for the slab viscosity, in reality, this value is not constant with variations in the range of 10^{3}-10^{6} Pas (Billen, 2008). For this reason, we also perform an additional sensitivity analysis by reducing the slab viscosity to 10^{23} Pas. The slab geometry is generated based on a gridded slab surface dataset (Blair et al., 2011). This reconstruction of the slab surface was primarily determined using three types of the data: regional earthquake hypocenter profiles, teleseismic travel-time data, and seismic reflection and refraction transects. We define the base of the slab by assuming that it is characterised by a uniform thickness of ~55 km. The low-viscosity zone mantle wedge is then added as an elongated 3D triangular volume between the down-going oceanic slab and the overlying continental lithosphere (Figure 3.5).

3.3 Results and Discussion

3.3.1 3D Global Earth Models

Figure 3.6 shows the contribution of GIA as well as the associated loading components (i.e., the ice and ocean loads) to the spatial variation in RSL at 10 ka computed using the reference 1D model. The ice loading dominates the GIA signal causing a net RSL rise in parts of southern British Columbia and net RSL fall in the rest of the study area since 10 ka. The ocean loading component (right-panel in Figure 3.6), produces a tilting pattern with a net RSL rise offshore and RSL fall at onshore locations which reflects the effect of continental levering (Clark et al., 1978; Mitrovica et al., 2001). In order to examine the influence of lateral viscosity structure on the predicted RSL change, we calculate the spatial and temporal variations in RSL for the above-described realizations of lateral viscosity structure. The results in Figure 3.6(a) represent a useful reference that the 3D results are compared to in the following.

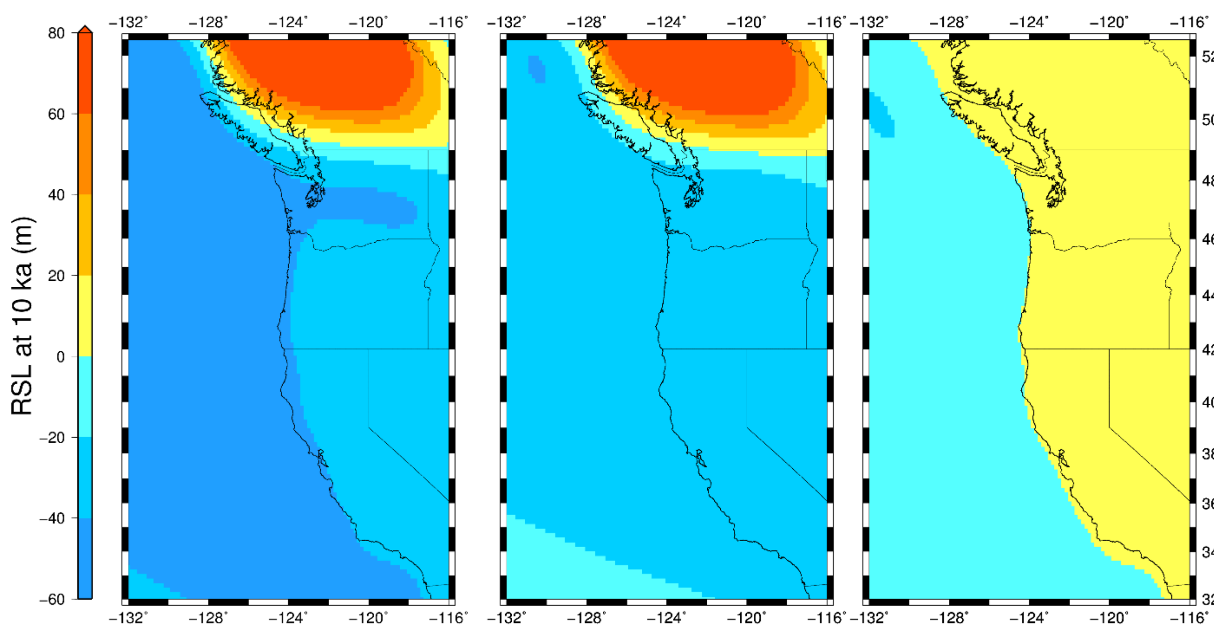

Figure 3.6. Modelled RSL for the 1D reference model (UMV=2×10^{20} Pas, LMV=10^{22} Pas, and lithosphere thickness= 46 km) at 10 ka (left plot). The contribution to this signal from ice and ocean

loads are plotted in the middle and right plots, respectively. The results in the left-hand plot are not simply the sum of those in the other two plots due to the contributions from Earth rotation, meltwater addition (barystatic sea-level change) and syphoning which are included in (a).

Figure 3.7 shows the effect of sub-lithosphere mantle viscosity structure on modelled RSL at 10 ka associated with four different global seismic models as well as the influence of variations in lithosphere thickness. The effect of sub-lithosphere variability in mantle viscosity results in a long wavelength pattern of RSL change that generally lies within ±10 m relative of the 1D model results along the coastline. Although there are some similarities between the contribution from each global viscosity model, such as the positive RSL departure from the 1D reference model in northern California and southern Oregon, there are also differences in terms of both sign and magnitude. For example, the Savani model results in negative RSL anomalies along the coasts of British Columbia, Washington, and northern Oregon, whereas the other models generally produce positive values in these areas. Another example is the negative RSL values in central and southern California associated with SL2013 model, while the other models give a positive departure from the 1D model output. In comparison to the effect of the sub-lithosphere mantle structure, adding laterally variable lithosphere thickness causes shorter-scale RSL spatial anomalies with greater amplitude (lower-panel plots in Figure 3.7). The high positive RSL values relative to the 1D model exceeding 30 m in north-central Vancouver Island (northern Salish Sea) is one good example of this shorter wavelength but higher amplitude change. The RSL signals associated with the two different lithosphere models generally follow similar patterns with some noticeable amplitude differences, especially in the Vancouver Island area. This discrepancy reflects the effect of the thicker/thinner lithosphere in damping/amplifying the Earth response to the applied ice loading.

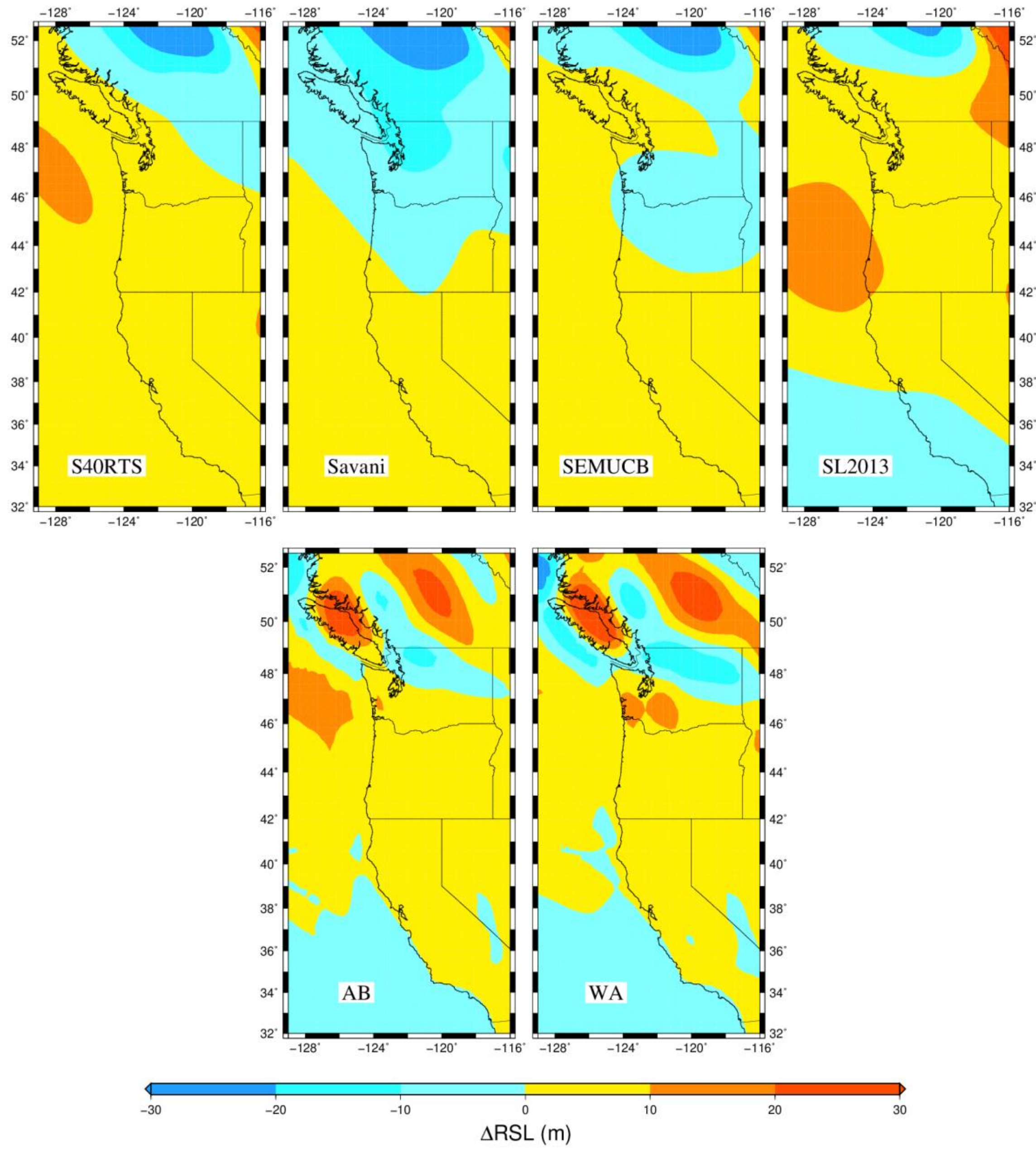

Figure 3.7. Modelled RSL changes compared to results for the reference 1D viscosity model at 10 ka (Figure 3.6a) when adding (top) lateral sub-lithosphere viscosity structure and (bottom) lateral variability in lithosphere thickness. All plots show 3D model results minus those for the reference 1D viscosity model.

The combined influence of lateral mantle viscosity variations and laterally variable lithosphere structure associated with the AB model on RSL relative to the 1D case is plotted in Figure 3.8. Figure S1 shows the same results as Figure 3.8 but for the WA lithosphere model. Building on our discussion of the results in Figure 3.7, comparable interpretations apply to Figures 3.8 and S1: the longer-wavelength variations can be attributed to the sub-lithosphere viscosity structure and the smaller-scale, often higher-amplitude RSL signals, particularly around Vancouver Island, originate from lateral variations in lithosphere thickness. The influence of lateral structure is less than 10 m along the coast from southern Washington to southern California for all models except for S40RTS model which results in slightly higher RSL values (10-20 m) in Washington and Oregon states. In the northern region, however, greater localized departures (> 20 m) from the 1D model are evident for all considered seismic models in northern Salish Sea.

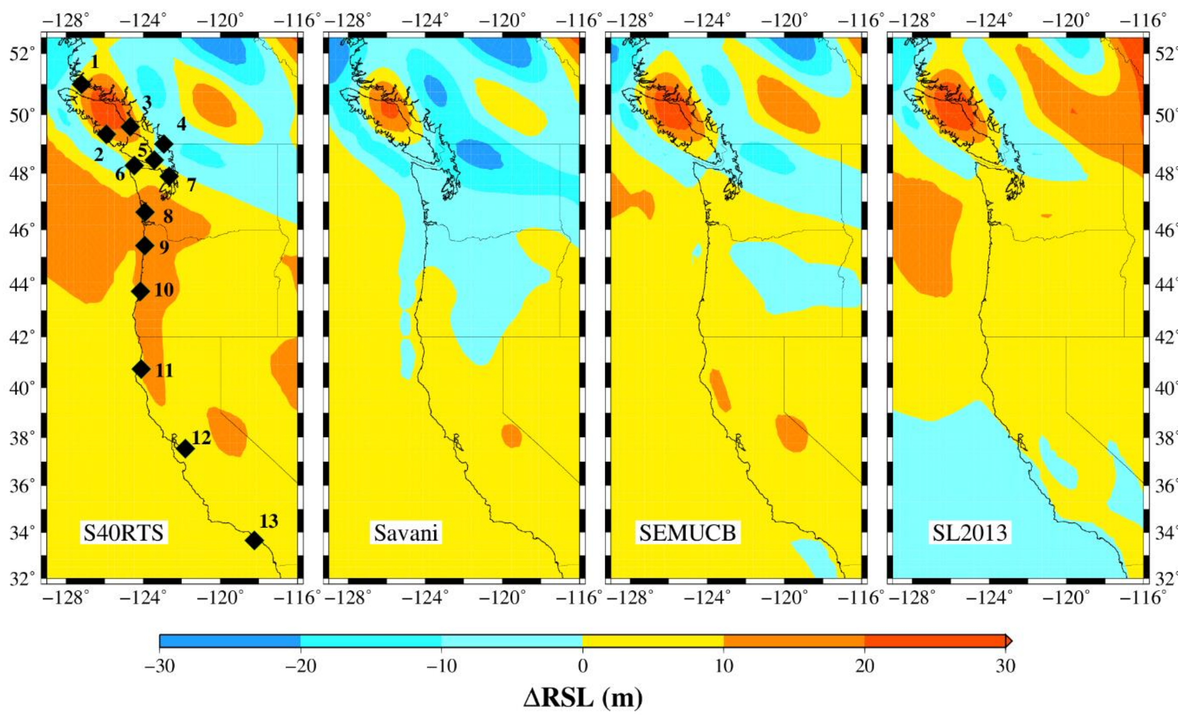

Figure 3.8. Modelled RSL changes compared to results for the reference 1D viscosity model at 10 ka (Figure 3.6a) when considering the combined effect of the lateral sub-lithosphere structure and elastic lithosphere thickness from the AB model. All plots show 3D model results minus those for the reference 1D viscosity model. The black diamonds indicate the average locations of the RSL data for each specific region where RSL curves shown in Figure 3.9 are computed.

Figure 3.9 shows modelled RSL curves for the 1D model case (UMV=2×10^{20} Pas, LMV=10^{22} Pas, and a constant lithosphere thickness of 46 km) along with results for the eight different realizations of lateral viscosity structure as illustrated in Figures 3.8 and S1. We compute the modelled RSL curves at the average locations within each of the 13 sites as shown in Figure 3.1 (black diamonds). The modelled RSL curves for sites in the northern region (sites 1-7) suggest a rapid RSL fall upon deglaciation followed by a gradual RSL rise during the early-to-mid Holocene and then relatively stable values towards the present time. In central and southern regions, sites 8-13, results demonstrate persistent sea-level rise throughout the Holocene reflecting the influence of peripheral bulge collapse as well as the addition of the meltwater to the oceans. As shown in Figure 3.9 and described by Yousefi et al. (2018), the RSL curves based on an optimal 1D viscosity model do not capture well the observed variability in RSL data across the study region and only provide relatively good fits at a subset of sites (6, 7, 8, and 11). However, the SLIPs from sites 6 and 11 are younger than ~4ka and so a broader range of 1D viscosity models can adequately fit the data from these sites (Yousefi et al., 2018).

Adding lateral variations in viscosity structure results in a spread of the modelled curves (Figure 3.9) that generally diminishes with distance from the northern region that was once ice covered. Prior to ~10 ka, RSL curves in the northern Salish Sea (site 3) show the greatest spread (more than 40 m) which reflects the results presented in Figures 3.7 and S1. On the other hand, sites in the southern region (11-13) show the least spread (around 10 m or so). Over the mid-late Holocene, model curves for the central region (sites 8-10) demonstrate a relatively large range in RSL that is similar to that at northern sites (~10 - 15 m). This is due to the S40RTS seismic model which produces notably higher RSL values in southern Washington and northern Oregon. One potential reason for these anomalously high RSL values is the existence of lower viscosity values in the mantle for this model compared to the three others considered.

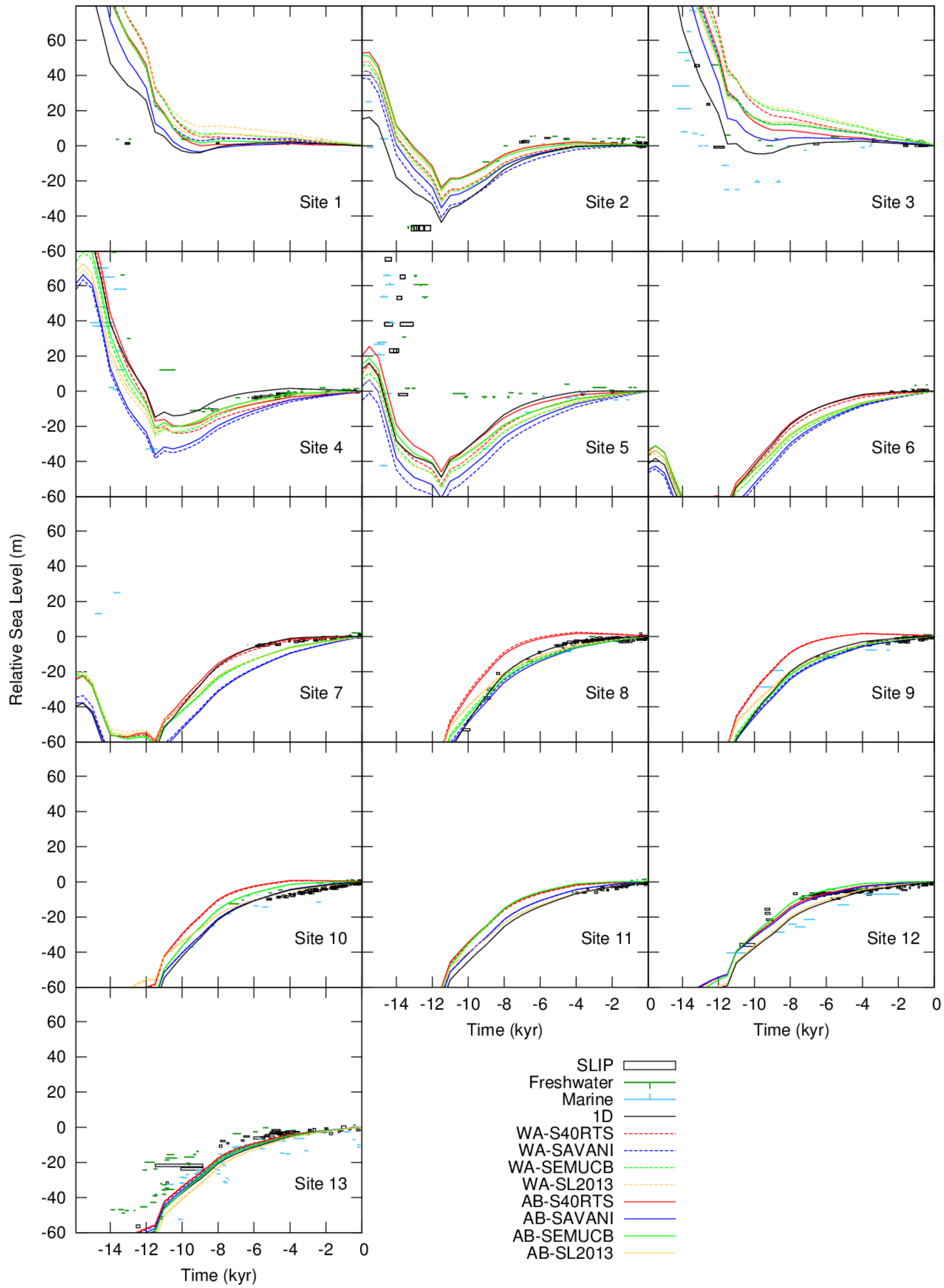

Figure 3.9. RSL data-model comparison for the combined effect of the sub-lithosphere viscosity structure and laterally varying lithosphere thickness at the 13 sites shown in Figure 3.8 (dark-black diamonds). RSL for the 1D reference viscosity model is shown by the black line. The SLIP boxes

represent 1σ uncertainty in height and age. The meaning of each data symbol and the 3D viscosity model represented by each curve is indicated in the key.

A comparison between the regional sub-lithosphere viscosity structure between all four seismic models (Figure S3) indicates significant variability among different models which makes the interpretations of the RSL differences non trivial. However, most areas in the upper mantle associated with the S40RTS model appear to have lower viscosity values than the other models.

A visual assessment on the model-data misfits (Figure 3.9) reveals that the addition of the lateral structure can improve the fit to the RSL observations at a small number of sites, e.g., see the SMUCB model curve in northern Oregon (site 9) and central California (site 12). However, results at the majority of sites seem to be relatively similar to that of the 1D case, or, in some locations such as sites 3 and 8, the 1D model provides a better fit to the data. All of the models struggle to capture the rapid RSL fall immediately after deglaciation, especially at sites 2, 3 and 5. One part explanation for this is the presence of higher viscosity values beneath this area (Fig S3) which is, in general, at least one order of magnitude greater than the proposed range in previous studies, i.e., UMV: 5×10^{18}- 5×10^{19} Pas, LMV: 1-3×10^{21} Pas (James et al., 2000, 2009; Yousefi et al., 2018). The other potential reason for this observed discrepancy is inaccuracy in the adopted ice model, which is be discussed in section 3.3.3.

In order to examine whether there is a statistical preference between the eight different 3D viscosity models considered, we calculate the data-model misfits using the following misfit criteria (Mitrovica et al., 2000):

$$\delta = \frac{1}{N}\sqrt{\sum_{i=1}^{N}\left(\frac{RSL_i^{obs}-RSL_i^{model}}{\sigma_{rsl,i}}\right)^2 + \left(\frac{t_i^{obs}-t_i^{model}}{\sigma_{t,i}}\right)^2} \quad (3.4)$$

Where, RSL_i^{obs} and RSL_i^{model} are the observed and predicted RSL values for the i^{th} SLIP with observational uncertainty of $\sigma_{rsl,i}$; t_i^{obs} and t_i^{model} are the observed and predicted age values with observational uncertainty of $\sigma_{t,i}$; and N is the total number of SLIPs. Note that the model values ($t_i^{model}, RSL_i^{model}$) are chosen such that the distance from the model curve to a given observation point is minimised (Mitrovica et al., 2000; Yousefi et al., 2018). Since data from the northern region are more challenging to fit, we also provide the misfit value when considering only the northern sites. A comparison between the misfit values suggest a small preference for the AB lithosphere model over the WA model (Figure 3.10a). This preference is more distinguishable when comparing values obtained for northern data only (Figure 3.10b), which is also evident from the model curves shown in Figure 3.9 (solid lines versus dashed lines). The calculated misfits based on the entire dataset do not reveal any clear preference of the seismic models. However, they suggest that the WA-S40RTS model results in slightly larger values than the other models which likely reflects the results for this model being outliers for central sites (8-10, Figure 3.9). On the other hand, misfit values calculated using the observations for the northern region indicate that the AB-S40RTS model provides the best fit to the data. Overall, these results indicate that adding the eight realisations of lateral structure described above does not significantly improve the model fits relative to a 1D model optimised to fit data from the central sub-region.

a)

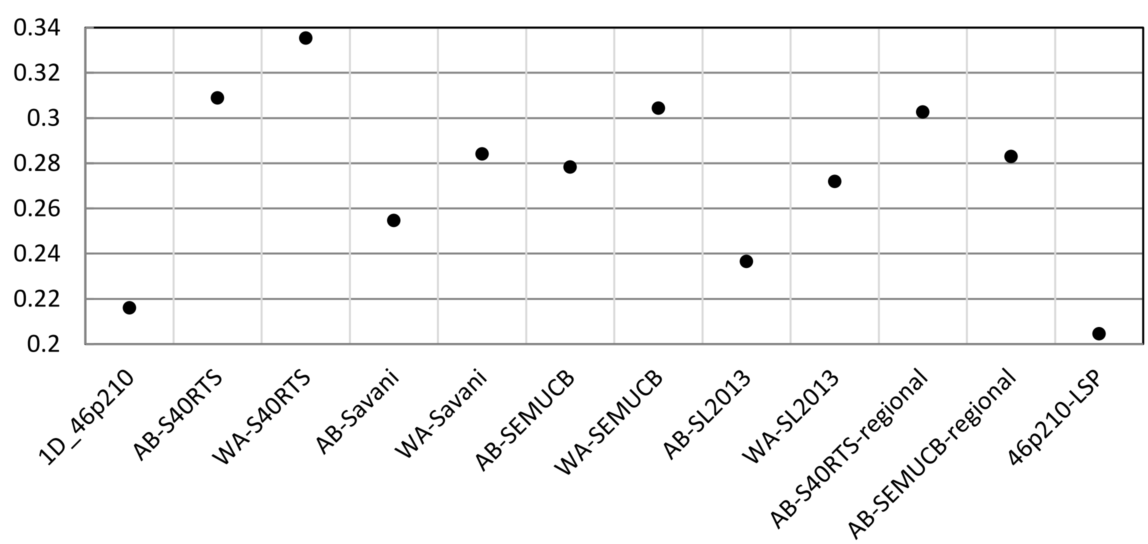

b)

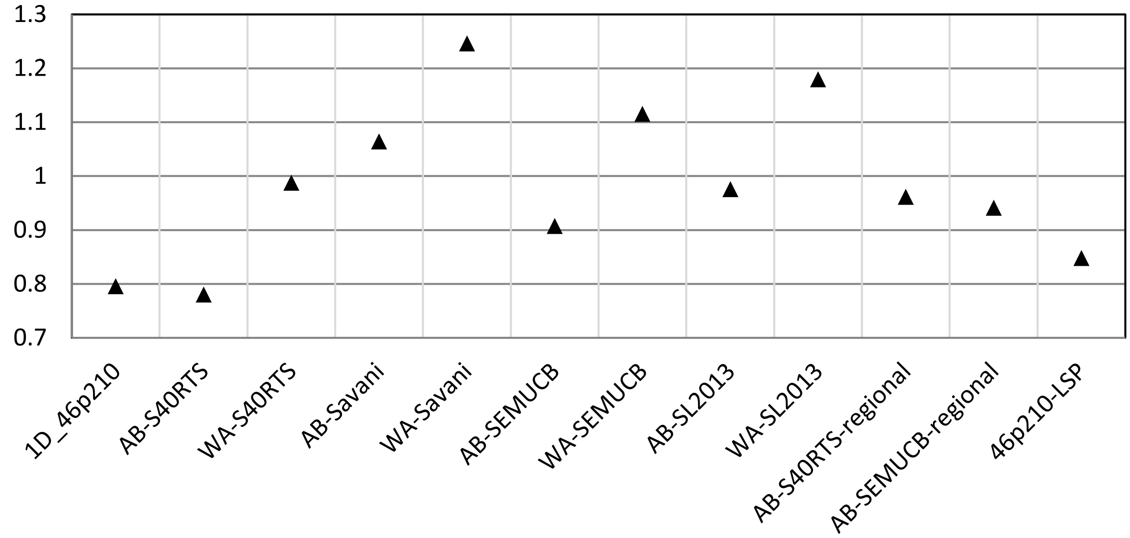

Figure 3.10. Data-model misfit values calculated based on: (a) the entire dataset (circles); and (b) data from northern region only (triangles).

3.3.2 The Influence of Regional Structure

In this section we consider the results from two different approaches, as described in section 3.2.2.3, that capture the regional viscosity structure more accurately than the global seismic models. We first present the results inferred from patching a regional seismic tomography model within two of the global models. Then we investigate the sensitivity of the model outputs to the Earth model that consider subduction zone geometry and plate boundary locations.

3.3.2.1 Seismic Inference

Figure 3.11 represents the spatial variation in RSL at 10 ka relative to the 1D reference model associated with the two models generated by insertion of the regional seismic model into the global S40RTS and SEMUCB seismic models. The lateral variability in lithosphere thickness is adopted from the AB model for both integrated models. The results suggest that the RSL anomalies have a similar order of amplitude to those obtained from the global models (compare with Figure 3.8) with maximum RSL differences compared to the 1D reference model of ~30 m in north-central Vancouver Island which is mainly governed by lateral variations in lithosphere structure. The longer wavelength signals of the regional model also follow a relatively similar pattern to those of the corresponding (background) global models with positive RSL departures along most parts of the coast south of Puget Sound. In order to highlight the influence of the higher-resolution viscosity structure from the regional seismic model, the difference between the RSL model outputs from the patched models and the global models (Figure 3.8) is plotted in Figure 3.11 (right-panel plots). These differences for regional model embedded within the S40RTS model are generally small and in the range of ±2 m along the majority of the coastline but with larger deviations in Puget Sound. The negative RSL anomalies in Puget Sound area and northern California are likely due to the higher-viscosity structure of the subducting slab. The positive RSL departures that appear between ~42°N and ~45°N, and more apparent in the SEMUCB case, might reflect the combined effect of the slab hole and the reduced viscosities of the mantle wedge (Figures 3.4 and S2). Results for the SEMUCB model produce larger deviations (± 4-10 m) in the northern and central region, particularly in southeastern Georgia Strait in the Salish Sea (site 4) and Oregon State (sites 8-10) which is likely the result of the normalization process described in section 3.2.2.3.

Figure 3.12 illustrates the model RSL curves for the seismically inferred regional structure embedded within the two global models at the average locations of our 13 sites. The RSL curves associated with the S40RTS and SEMUCB seismic models are also shown in the same plot. The departure of the regional RSL curves from the 1D model follow closely the corresponding global model curves with some notable differences in northern and central sites. The central sites are particularly affected by the model with SEMUCB as background due to the amplified influence of the slab hole and relatively lower viscosities in the mantle wedge as stated above. The calculated data-model misfit values (Figure 3.10) do not indicate preference of the 3D regional models over the 1D case or the global models. The inclusion of the high-resolution regional structure produces larger misfits than the background global models when considering the data from the northern region which is consistent with the increased misfit observed for sites 4, 5, and 7 in Figure 3.12.

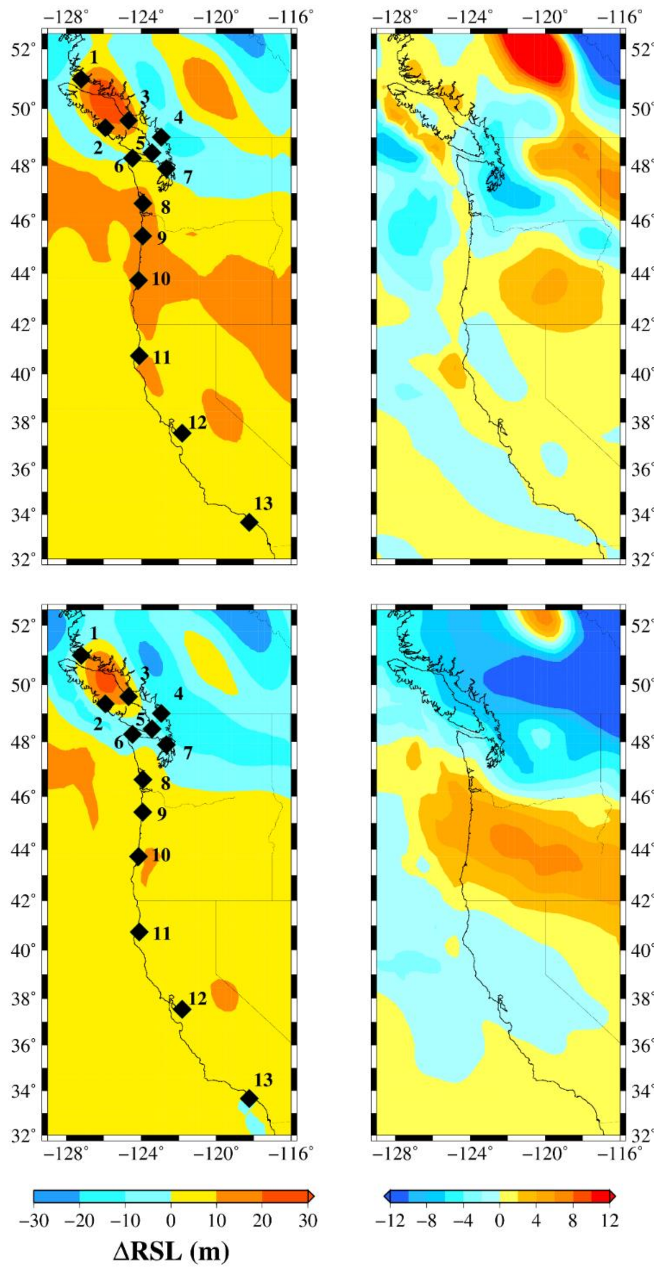

Figure 3.11. (Left) Modelled RSL changes relative to the reference 1D viscosity model at 10 ka for the integrated high-resolution regional model into (top) S40RTS, and (bottom) SEMUCB global models. (Right) The difference between these integrated models with the results inferred from the associated global models as shown in Figure 3.8. The elastic lithosphere thickness considered in all models is

adopted from the AB model. The black diamonds indicate the average locations of the RSL data for each specific region where RSL curves shown in Figure 12 are computed.

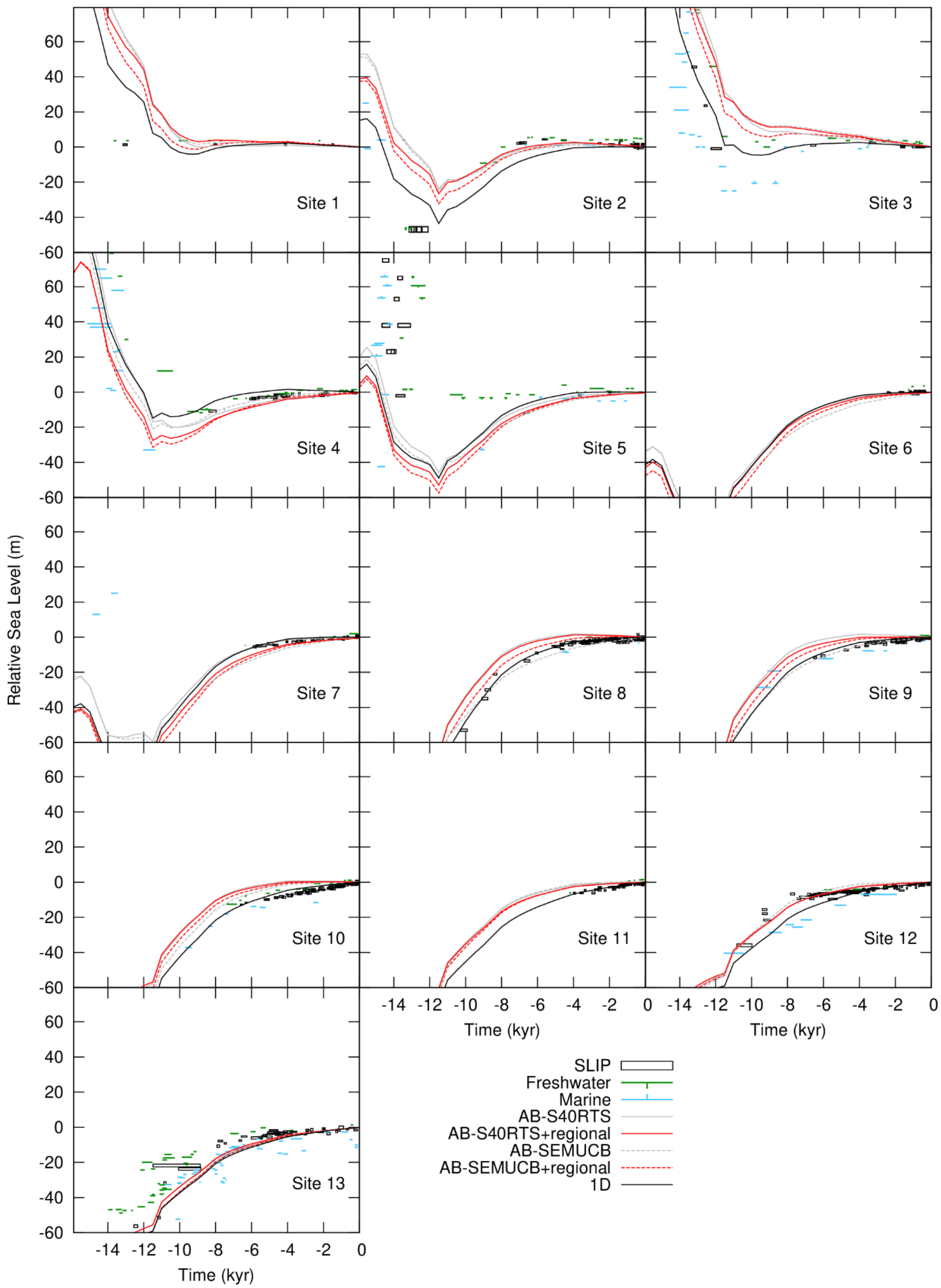

Figure 3.12. RSL data-model comparison for the high-resolution regional model embedded within the S40RTS model (solid red line) and the SEMUCB model (dashed red line). The RSL models

corresponding to the S40RTS and SEMUCB global models are shown in the grey solid and dashed lines, respectively. RSL for the 1D reference viscosity is shown by the black line. The AB lithosphere thickness model was used for all results plotted in this figure.

3.3.2.2 Slab and Mantle Wedge Model

Figure 3.13 shows modelled RSL at 10 ka relative to the 1D reference model for four different 3D cases that consider: (1) the mantle wedge low-viscosity zone (LVZ); (2) slab; (3) LVZ and slab; (4) LVZ, slab and plate boundary. These results show that our estimates of this regional structure cause smaller RSL variations, with a peak of ~15 m, in comparison to the 3D structure inferred from global and regional seismic models. According to Figure 3.13a, the low-viscosity layer has a small effect of less than ±1 m that could be due to its position relative to the ice loading. This low sensitivity to the LVZ is quite surprising, since a numerical experiment of the glacial isostatic response in southern Chile subduction zone suggested that the presence of a low-viscosity wedge enhances the modelled displacement field over a region that extends beyond that immediately above the LVZ (Klemann et al., 2007). The authors attribute this wide-ranging effect of the LVZ to the loading induced flux of the wedge material which is dependnt on the slab length and geometry. However, they also indicate that the influence of the LVZ in amplifying the deformation field depends strongly on the location of the wedge which, in their case, is located directly beneath the loading (Klemann et al., 2007). The slab structure has a greater impact on the RSL variations (Figure 3.13b) reaching a maximum (~15 m) in the northern tip of Vancouver Island and Puget Sound; the latter being located just off the northern edge of the slab. The influence of the slab structure on RSL can be explained by the damping effect of the higher viscosity slab on both the isostatic rebound and the peripheral bulge collapse which cause positive and negative RSL signals, respectively, with respect to the reference model (Figure 3.5a). The combined effect of the LVZ and the slab (Figure 3.13c) is dominated by the slab structure so that the influence the LVZ is not visually distinguishable from the case of including the slab only. Similarly, addition of a moderate-viscosity plate boundary results in small negative perturbations over this area thus amplifying the effect of the slab structure (Figure 3.13d). We performed an additional simulation by decreasing the slab viscosity by three orders of magnitude (10^{23} Pas). The resulting perturbations on RSL predictions at 10 ka is less than ±1 m (Figure S5). We also performed a sensitivity analysis to assess the effect of reducing the mantle wedge viscosity from 10^{18} Pas to 10^{15} Pas and no significant difference was observed.

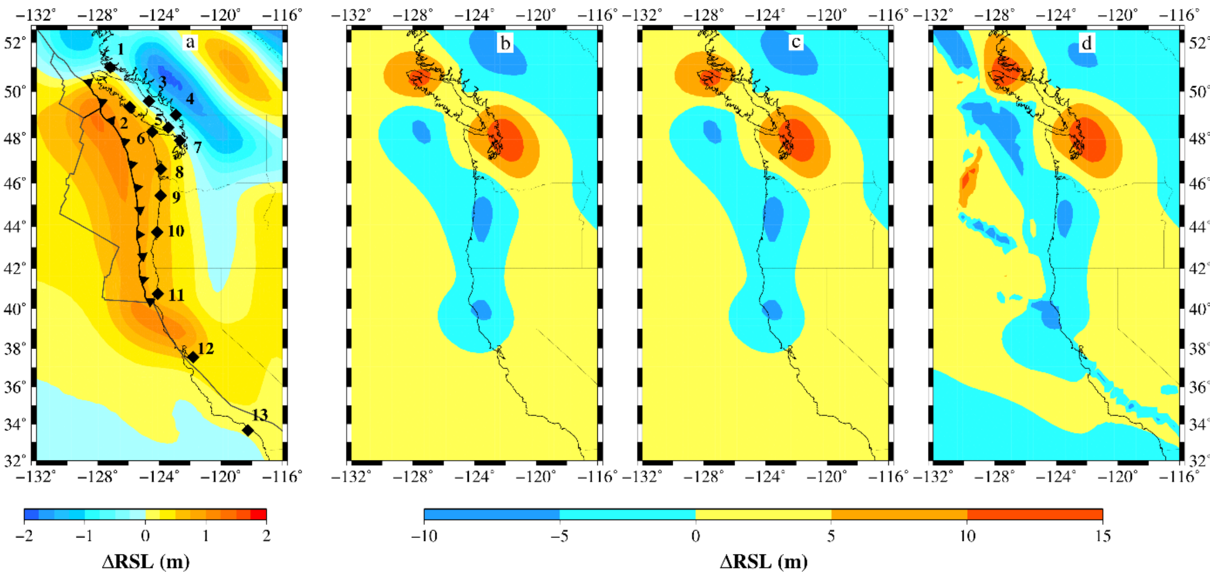

Figure 3.13. Modelled RSL changes relative to the 1D reference model at 10 ka when considering regional tectonic structure of the Cascadia subduction zone and immediate vicinity: (a) LVZ; (b) subducting slab; (c) LVZ plus slab; and (d) LVZ plus slab and plate boundary. The black diamonds indicate the average locations of the RSL data for each specific region where RSL curves shown in Figure 3.14 are computed.

In Figure 3.14 we evaluate the effect of the 3D structure shown in Figure 3.4 on the temporal variation of RSL at our 13 sites. The results show that RSL sensitivity to the regional structure varies from site to site. The largest model spread occurs prior to 10 ka and (mostly) in the northern region, particularly in Queen Charlotte strait and Puget Sound (sites 1 and 7). On the other hand, southern Washington (site 8), central and southern California (sites 12 and 13) indicate low sensitivity to this realisation of lateral viscosity structure.

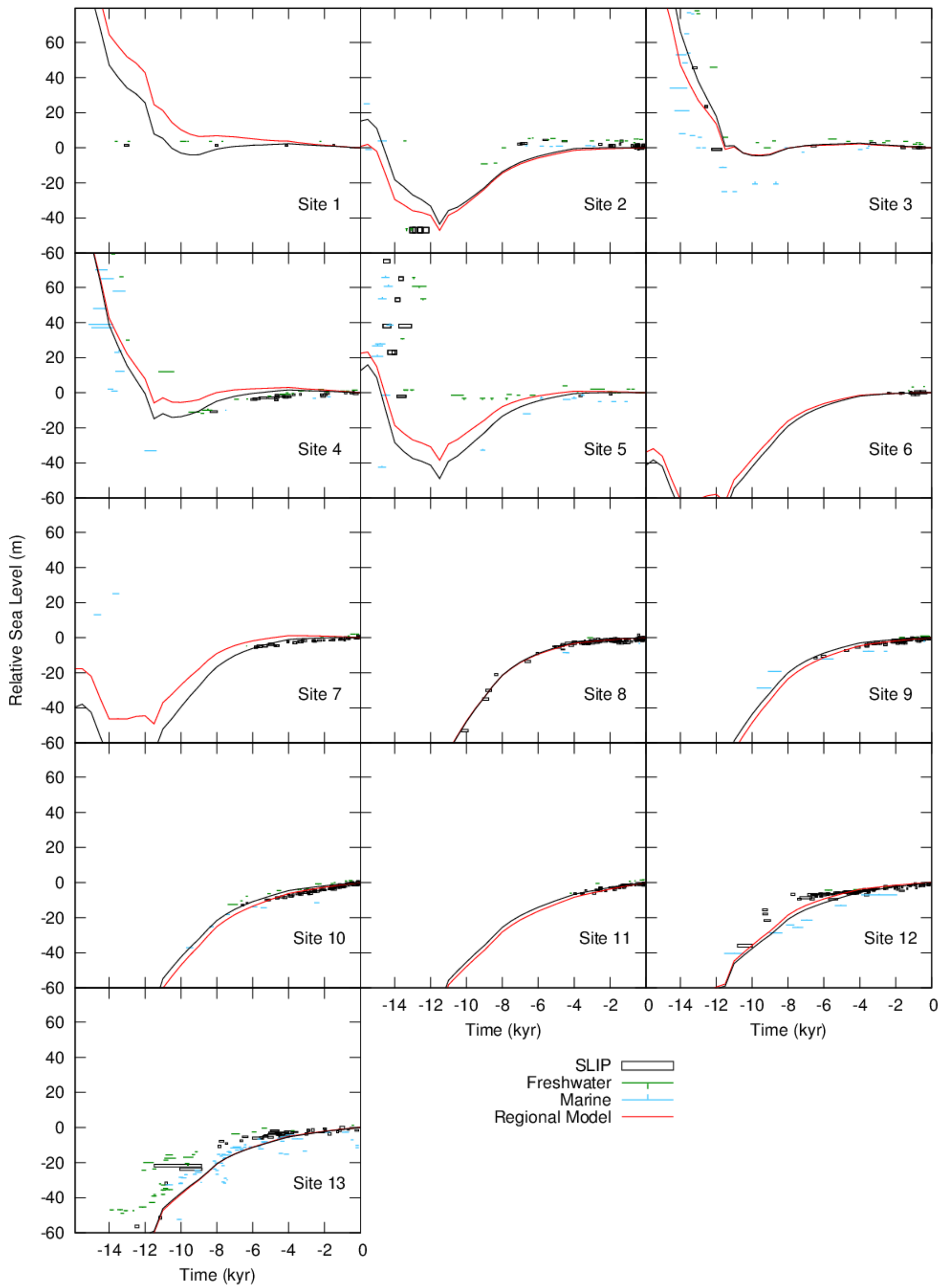

Figure 3.14. RSL data-model comparison for a 3D viscosity model (red line) based on the

regional tectonic structure of the Cascadia subduction zone and immediate vicinity, i.e., LVZ plus the subducting slab and the plate boundary. RSL for the 1D reference viscosity is shown as a solid black line.

A comparison between the 1D model case with the 3Dcase reveals that there is no clear improvement in data-model misfits, other than in central Oregon (site 10). However, the misfit value calculated based on the entire dataset (Figure 3.10a) is slightly less than those associated with the 1D reference model and the regional and global seismic models.

3.3.3 General Discussion

In this section we try to address some of the possible reasons behind the data-model mismatch which can motivate future work.

The uncertainty in the model results reflects our incomplete knowledge of both the applied Earth model and ice loading history. Although there is insufficient data to completely resolve this ambiguity and ensure a unique GIA solution, there are some approaches that can reduce sensitivity to one of these two model inputs so that the other can be more robustly determined. These methods are restricted to the application of RSL observations in either near-field regions, close to the center of the ice mass (Mitrovica and Peltier 1993), or far-field regions, distant from major glaciation centres (Nakada and Lambeck 1989), and thus neither can be applied here. However, performing a sensitivity analysis by exploring a large parameter space enables us to assess the relative importance of each component. In the 1D GIA study of Yousefi et al. (2018), more than 20000 model runs were performed to find an optimal set of parameters that best fits the regional RSL data set. Their results indicate that the contribution from the ice model becomes particularly important for those sites located in northern Cascadia, as they show high sensitivity to differences in the applied ice model (see their Figure 5). One example of this sensitivity is the rapid fall of RSL from the high-stand elevation of >70m around 14 ka recorded at southern Vancouver Island (site 5), which cannot be reproduced with the model curves shown in Figure 3.9.

Yousefi et al. (2018) applied different ice models with deglaciation delayed by 500 and 1000 years and showed that a model with a 500 year delay (red curve in Figure S6) best fits the observations from northern sites. However, the only model that can capture the oldest high-stand sea level at site 5 is that produced by delaying the deglaciation chronology by 1000 years combined with an upper mantle viscosity that is two orders of magnitude lower than our reference model (blue curve in Figure S6). In order to emphasize the importance of an accurate ice loading history, a model curve is also plotted based on this lower viscosity Earth model and a 500 year delay in deglaciation (green curve in Figure S6). A comparison between these model results indicates that delaying the deglaciation by ~1000 years is necessary to reproduce the rapid RSL fall at site 5 with an amplitude that matches the observations.

The ice model that is used in this study (#6885) is selected from a larger ensemble of reconstructed deglacial histories of North American ice complex (Tarasov et al., 2012).which have been calibrated with the radiocarbon dataset of Dyke et al. (2003) and Dyke (2004). The ice margin extent of our model shows good agreement with these observational constraints which suggest the full retreat of ice sheet from the southeastern tip of Vancouver Island occurred after 15 ka (Figure S7, see also Gowan, 2007). However, given that there is limited dating control on the ice margin chronology during the initial stages of deglaciation, the isochrons have relatively large temporal uncertainty (~±1000 years) (Dalton et al., 2020), and so one cannot rule out the possibility of delaying the retreat of our ice model from the Victoria region by 500-1000 years. The source of this uncertainty in defining the ice chronology can be attributed to: the limited available radiocarbon ages (Dalton et al., 2020), uncertainties associated with radiocarbon dating and calibration (Törnqvist et al., 2015), and relating these calibrated dates to the actual pattern of ice retreat

(Tarasov et al., 2012). This uncertainty and the importance of the ice history in computing RSL curves in southern British Columbia emphasizes the need for improved chronological constraints on the early deglacial history in this region. This can be partly fulfilled with acquisition and incorporation of additional radiocarbon data as well as the application of alternative dating methods such as ^{10}Be (Ullman et al., 2016; Darvill et al., 2018).

A previous GIA study in northern Cascadia by James et al. (2009) showed that including a low-viscosity asthenosphere layer can replicate the rapid RSL fall in the Victoria region. Based on the results in this study and those of Yousefi et al. (2018), we conclude that the ability of the GIA model in James et al. (2009) to fit the observations is mainly the result of their applied ice sheet reconstruction rather than the applied Earth model. Our conclusion is based on the fact that James et al. (2009) modified both the size of the ice load and the timing of deglaciation to fit the rapid sea level fall in Victoria region. As a result of this modification, their ice model features ~2150 m of ice in the southeastern tip of Vancouver Island with ice reaching its maximum extent at 15.4 ka. Our ice model, in contrast, reaches a maximum thickness of ~1000 m at ~16-17 ka which had reduced to ~500 m by 15.4 ka.

Even considering possible limitations of our ice model, the inability of the 3D model results to generate a large-amplitude RSL fall as observed in the Victoria region suggests that the mantle viscosity inferred using the global and regional seismic models is not low enough in this region (Figures S3 & S4). A key source of uncertainty in estimating lateral viscosity structure is related to the scaling between seismic velocity and viscosity (e.g., Forte and Mitrovica, 2001; Wu et al., 2013). As an example, Clark et al. (2019) performed a sensitivity analysis that focused on this scaling by exploring ϵ values (see eqn 3.3 in section 3.2.2.2) in the range 0.005 to 0.04 which can cause perturbation of up to ~3.5 orders of magnitude to the viscosity field. Although they applied only one global seismic model (S40RTS), their results indicate significant influence of uncertainty associated with this parameter on the predicted RSL curves. Better quantifying model uncertainty and considering additional data sets and methods to reduce it, is an important target for future work. A recent study by Li et al. (2020) aimed to quantify the Earth-model-related uncertainty in GIA model results by applying different realizations of 3D viscosity structure. We note that our results show greater sensitivity to different realisations of lateral structure, particularly within the lithosphere (e.g., compare our Figure S8 with Fig. S12a in Li et al., 2020). This is likely related to the spatial resolution of the GIA models used and the different size of study regions. However, this indicates that a spatial resolution of ~10 km (as opposed to ~50 km in the Li et al. model) is required to accurately simulate the influence of lateral structure in our study region.

In our analysis, we assume that the seismic velocity anomalies and the viscosity variations are driven by temperature only. Several studies indicate that there can be significant contributions from heterogeneity in chemical composition, water content, and partial melting (Li et al., 2018; Wang et al., 2008; Wu et al., 2013). Separating the effect of each individual factor is not straightforward and requires complementary constraints such as seismic wave attenuation, electrical conductivity, heat flow, and density (Karato, 2008; Dalton et al., 2009) and/or applying a joint inversion of seismic and other geodynamic observables (Afonso et al., 2016 & 2019). In this regard, interpretation of the seismic velocity and attenuation models together may help to better explain the role of each contributor to the variations of seismic velocity and subduction zone structure. For instance, a slower seismic velocity joint with high attenuation can be attributed to elevated temperatures and the presence of melt or increased water content (Dalton et al., 2009). The estimated S-wave attenuation in coastal areas of western North America suggest that there are considerable variations in seismic attenuation along the coastline indicating higher values in southern Oregon and north-northwestern Washington (e.g., Eilon and Abers, 2017). Along with these high attenuation values, several tomographic studies feature low seismic velocity anomalies beneath these areas (Hawley et al., 2016; Bodmer et al., 2018; Hawley and Allen, 2019). Bodmer et al. (2018) argue that the dominant controlling mechanism of the sub-slab mantle structure in northern Cascadia is the nearby oceanic hot spot, however, the observed low velocity in this region cannot be entirely due to temperature variations. They propose that decompression melting is also at play in this region and, more importantly, in southern Cascadia as a result of rapid motion of the Pacific plate relative to the Gorda deformation zone which promotes mantle upwelling. These results provide an explanation as to why our estimates for viscosity in this region appear to be biased high.

A part of the uncertainty in developing the lateral viscosity structure is associated with the applied seismic velocity model. Although the regional tomographic model used here is generally compatible with the other models, there are some inconsistencies. One example is the margin-wide, sub-slab low velocity zone featured in our seismic model; there is a debate that this low velocity anomaly is not continuous and is localized to northern (>46°N) and southern (<43°N) Cascadia (Bodmer et al., 2018). A similar along-strike heterogeneity has been proposed for the shallower (<80 km) structure of the forearc mantle (Delph et al., 2018). Regarding the relatively low variability in the age of the subducting plates (~ 4-9 Myr), it is still an open discussion as to whether the apparent trench-parallel variations in seismic velocity originates from thermal structure and the subsequent changes in slab hydration state or variations in the permeability of the down-going slab (Delph et al., 2018).

Regarding the rheology of our applied Earth model, another limitation is that brittle failure is not simulated. Studies have shown that faults can be reactivated during periods of rapid ice thinning resulting in large surface displacements (e.g. Arvidsson, 1996; Steffen et al., 2020). The Victoria region is located in vicinity of the

Leech River-Devil's mountain fault system that appears to have ruptured during Holocene (the last ~9000 years) (Morell et al., 2017 & 2018; Barrie and Greene, 2018). Although there is still no geomorphological evidence of fault displacement after deglaciation, we suggest that the data obtained from this region should be further investigated for the potential offset introduced from fault rupture during Holocene as well as Late Glacial periods.

In simulating Earth deformation, we consider a Maxwell steady-state rheology where the relation between stress and strain rate is linear. There is the possibility that the behaviour of the mantle follows a power-law deformation where lower effective viscosity values are induced by the high stress levels upon the onset of the deglaciation and the viscosity increases with stress reduction (e.g., Wu and Wang, 2008; James et al, 2009). Another possible departure from a Maxwell rheology is the existence of a transient response as evident in the more general Burgers rheology, where the apparent viscosity is less than that of the steady state deformation during periods of rapid changes in driving stress (Ranalli, 1998). The more rapid deformational response that is characteristic of these more complex models might be necessary to accurately capture the large and rapid signal evidence in the northern RSL observations.

3.4 Conclusions

In In this study we examined the influence of the lateral Earth structure on GIA model results along the west coast of North America. We first developed eight different realizations of laterally variable viscoelastic Earth models based on four global seismic velocity models and two global lithosphere thickness models. The results from the 3D models are compared to the results derived from a reference 1D model with UMV= 2×10^{20} Pas, LMV= 10^{22} Pas, and a lithosphere thickness of 46 km.

The effect of sub-lithosphere mantle viscosity on RSL output varies from one seismic model to the other but generally lies within ±10 m relative to the 1D background model results. The variability in lithosphere structure causes localized higher amplitude changes with a more or less similar pattern for two lithosphere models. The combined effect of the sub-lithosphere viscosity variations and laterally variable lithosphere structure cause less than ±20 m RSL change along the coastline from northern Washington coast to southern California. The departure from 1D model is maximum in northern region, particularly in northern Salish Sea, where the RSL variations exceed 20 m. RSL data-model comparison do not reveal any clear preference of any particular seismic model or significant improvement in model misfits. However, the results suggest a small preference for one of the lithosphere models (the AB model).

Given the lack of spatial resolution in the global seismic models, we also considered two different approaches to incorporate the regional lateral structure associated with Cascadia subduction zone: one based on a regional seismic model and the other using constraints on slab geometry. Regardless of the approach taken, the results indicate that the influence of the regional structure is dominated by the slab structure with a peak amplitude of ~15 m in the northern tip of Vancouver Island and Puget Sound. The RSL model outputs show minimal sensitivity toa postulated low-viscosity mantle wedge, less than a tenth of meter, which is likely due to its relative position with respect to the ice loading.

The different approaches considered in this study to add the lateral variations in viscosity structure do not significantly improve the data-model misfits, particularly in sites located in northern Cascadia, where all of the models struggle to capture the rapid RSL fall immediately upon deglaciation. However, different realizations of the 3D Earth structure applied in this study gives insight into the spread of modelled RSL values and is a necessary step towards estimating model uncertainty due to lateral variability in Earth viscosity structure. Overall, our results indicate that a more precise and accurate ice chronology in addition to improvements in defining 3D Earth structure and modeling the rheological response in this complicated region are required to better reproduce the rapid RSL fall at northern sites.

References

Afonso J.C., Rawlinson N., Yang Y., Schutt D.L., Jones A.G., Fullea J., & Griffin W.L. (2016), 3-D multiobservable probabilistic inversion for the compositional and thermal structure of the lithosphere and upper mantle: III. Thermochemical tomography in the Western-Central US, J. geophys. Res., 121(10), 7337–7370, doi: 10.1002/2016JB013049.

Afonso, J.C., Salajegheh, F., Szwillus, W., Ebbing, J. & Gaina, C. (2019), A global reference model of the lithosphere and upper mantle from joint inversion and analysis of multiple data sets. Geophys. J. Int. 217, 1602–1628.

Arvidsson, R. (1996), Fennoscandian earthquakes: Whole crustal rupturing related to postglacial rebound, Science, 274, 744-746.

Audet, P., and Burgmann, R. (2011), Dominant role of tectonic inheritance in supercontinent cycles, Nat. Geosci., 4, 184–187.

Auer, L., Boschi, L., Becker, T.W., Nissen-Meyer, T. & Giardini, D. (2014), Savani: A variable resolution whole-mantle model of anisotropic shear velocity variations based on multiple data sets, J. Geophys. Res. Solid Earth, 119, 3006–3034.

Austermann, J., Mitrovica, J.X., Latychev, C., Milne, G.A. (2013), Barbados based estimate of ice volume at Last Glacial Maximum effected by subducted plate, Nat. Geosci., 6, 553–557, doi: 10.1038/ngeo1859.

Barrie, V., & Greene, H. G. (2018), An active Cascadia upper plate zone of deformation, Pacific Northwest of North America. Sedimentary Geology, 364, 228–241. https://doi.org/10.1016/j.sedgeo.2017.12.018.

Billen MI. (2008), Modeling the dynamics of subducting slabs, Annu. Rev. Earth Planet. Sci. 36:325–56.

Blair, J.L., McCrory, P.A., Oppenheimer, D.H., & Waldhauser, F., (2011), revised (2013), A Geo-referenced 3D model of the Juan de Fuca Slab and associated seismicity: U.S. Geological Survey Data Series 633, v.1.2, https://pubs.usgs.gov/ds/633/.

Bodmer, M., Toomey, D.R., Hooft, E.E.E., & Schmandt, B. (2018), Buoyant asthenosphere beneath Cascadia influences megathrust segmentation, Geophys. Res. Lett., 45, 6954-6962. https://doi.org/10.1029/2018GL078700.

Brocher, T.M., Parsons T., Tréhu A.M., Crosson, R.S., Snelson C.M., Fisher M.A. (2003), Seismic evidence for widespread serpentinized forearc upper mantle along the Cascadia Margin Geology, 31, pp. 267-270.

Caldwell, J.G., and Turcotte, D.L. (1979), Dependence of the thickness of the elastic lithosphere on age, J. Geophys. Res., 84, 7572-7576.

Chen, B., Haeger, C., Kaban, M. K., & Petrunin, A. G. (2017). Variations of the effective elastic thickness reveal tectonic fragmentation of the Antarctic lithosphere. Tectonophysics, 746, 412–424. https://doi.org/10.1016/j.tecto.2017.06.012.

Chopelas, A. & Boehler, R., (1992), Thermal expansivity in the lower mantle, Geophys. Res. Lett, 19, 1983–1986.

Clark, J.A., Ferrel, W.E., & Peltier, W.R. (1978), Global changes in postglacial sea level: a numerical calculation. Quat. Res. 9, 265–287.

Clark, J., Mitrovica, J. X., & Latychev, K. (2019), Glacial isostatic adjustment in Central Cascadia: Insights from three-dimensional Earth modeling. Geology, 47(4), 295–298.

Clague, J.J., James, T.S. (2002), History and isostatic effects of the last ice sheet in southern British Columbia, Quat. Sci. Rev., 21, 71 – 87, doi: 10.1016/S0277-3791(01)00070-1.

Currie, C.A., Wang, K., Hyndman, R.D., & He J. (2004), The thermal effects of steady-state slab-driven mantle flow above a subducting plate: The Cascadia subduction zone and backarc, Earth Planet. Sci. Lett., 223, 35 – 48.

Dalton, C.A., Ekström, G., & Dziewonski A.M. (2009), Global seismological shear velocity and attenuation: A comparison with experimental observations, Earth Planet. Sci. Lett., 284, 65–75, doi:10.1016/j.epsl. 2009.04.009.

Darvill, C.M., Menounos, B., Goehring, B.M., Lian, O.B., & Caffee, M.W. (2018), Retreat of the western Cordilleran Ice Sheet margin during the last deglaciation. Geophysical Research Letters 45, 9710–9720, doi: 10.1029/2018GL079419.

Delph, J.R., Levander, A., & Niu, F. (2018), Fluid controls on the heterogeneous seismic characteristics of the Cascadia margin. Geophys. Res. Lett.45 (20), 11,021–11,029, https://doi .org /10 .1029 /2018GL079518.

Dyke, A.S., Moore, A., & Robertson, L. (2003), Deglaciation of North America. Tech. Rep. Open File 1574, Geological Survey of Canada, Thirty-Two Maps at 1:7000000 Scale with Accompanying Digital Chronological Database and One Poster (in Two Sheets) with Full Map Series.

Dyke, A.S. (2004), An outline of North American deglaciation with emphasis on central and northern Canada. In: Ehlers, J., Gibbard, P.L. (Eds.), Quaternary Glaciations-Extent and Chronology, Part II, Vol. 2b. Elsevier, pp. 373–424.

Dziewonski, A., & Anderson, D. (1981), Preliminary reference earth model, Physics of the Earth and Planetary Interiors, 25, 297-356.

Eilon, Z.C., & Abers, G.A. (2017), High seismic attenuation at a mid-ocean ridge reveals the distribution of deep melt. Science Advances, 3(May), e1602829. https://doi.org/10.1126/sciadv.1602829.

Engelhart, S.E., Vacchi, M., Horton, B.P., Nelson, A.R., & Kopp, R.E. (2015), A sea-level database for the Pacific coast of central North America, Quat. Sci. Rev., 113 (0), 78–92, doi: 10.1016/j.quascirev.2014.12.001.

Forte, A.M. & Woodward, R.L. (1997), Seismic-geodynamic constraints on three-dimensonal structure, vertical flow, and heat transfer in the mantle, J. geophys. Res., 102, 17 981–17 994.

French, S. & Romanowicz, B. (2014), Whole-mantle radially anisotropic shear-velocity structure from spectral-element waveform tomography, Geophys. J. Int., 199, 1303-1327.

Gowan, E.J., (2007), Glacio-isostatic adjustment modelling of improved relative sea-level observations in southwestern British Columbia, Canada, MSc. thesis, 148 pp., Univ. of Victoria, Victoria, B. C., Canada.

Hawley, W. B., Allen, R. M., & Richards, M.A. (2016), Tomography reveals buoyant asthenosphere accumulating beneath the Juan de Fuca plate, Science, 353(6306), 1406-1408, doi: 10.1126/science.aad8104.

Hawley, W. B., & Allen, R.M. (2019), The fragmented death of the Farallon Plate. Geophys. Res. Lett., 2019GL083437, doi: 10.1029/2019GL083437.

James, T. S., Clague, J.J., Wang, K., Hutchinson, I. (2000), Postglacial rebound at the northern Cascadia subduction zone, Quat. Sci. Rev., 19, 1527–1541, doi: 10.1016/S0277-3791(00)00076-7.

James, T.S., Hutchinson, I., Barrie, J.V., Conway, K.W., & Mathews, D. (2005), Relative sea-level change in the northern Strait of Georgia, British Columbia. Geogr. Phys. Quat., 59, 113-127, doi: 10.7202/014750ar.

James, T.S., Gowan, E.J., Hutchinson, I., Clague, J.J., Barrie, J.V., Conway, K.W. (2009a), Sea-level change and paleogeographic reconstructions, southern Vancouver Island, British Columbia, Canada. Quat. Sci. Rev., 28, 1200-1216, doi: 10.1016/j.quascirev.2008.12.022.

James, T.S., Gowan, E.J., Wada, I., Wang, K. (2009b), Viscosity of the asthenosphere from glacial isostatic adjustment and subduction dynamics at the northern Cascadia subduction zone, British Columbia, Canada. J. Geophys. Res., 114, doi: 10.1029/2008JB006077.

Karato, S. (2008), Deformation of Earth Materials: An Introduction to the Rheology of the Solid Earth, pp. 463, Cambridge Univ. Press.

Kendall, R., Mitrovica, J.X., & Milne, G.A. (2005), On post-glacial sea level - ii. Numerical formulation and comparative results on spherically symmetric models, Geophysical Journal International, 161 (3), 679-706.

Klemann, V., Ivins E.R., Martinec Z., & Wolf D. (2007), Models of active glacial isostasy roofing warm subduction: Case of the South Patagonian Ice Field, J. Geophys. Res., 112, B09405, doi:10.1029/2006JB004818.

Kuchar J., Milne, G.A., Latychev, K. (2019), The importance of lateral Earth structure for North American glacial isostatic adjustment, Earth planet. Sci. Lett., 512, 236–245. 10.1016/j.epsl.2019.01.046.

Lambeck, K., Smither, C., Johnston, P. (1998), Sea-level change, glacial rebound and mantle viscosity for northern Europe. Geophys. J. Int. 134, 102–144.

Lambeck, K., Rouby, H., Purcell, A., Sun, Y., & Sambridge, M. (2014), Sea level and global ice volumes from the Last Glacial Maximum to the Holocene, Proceedings of the National Academy of Sciences, 111.43, pp. 15296–15303, doi: 10.1073/pnas.1411762111.

Latychev, K., Mitrovica, J.X., Tromp, J., Tamisiea, M., Komatitsch, D., & Christara C. (2005), Glacial isostatic adjustment on 3D earth models: a finite-volume formulation, Geophys. J. Int., 161(2), 421–444, doi:10.1111/j.1365-246X.2005.02536.x.

Li, T., Wu, P., Steffen, H., Wang, H.S. (2018), In search of laterally heterogeneous viscosity models of Glacial Isostatic Adjustment with the ICE-6G_C global ice history model, Geophys. J. Int., 214, 1191-1205 doi: 10.1093/gji/ggy181.

Li, Tanghua, Wu, P., Wang, H., Steffen, H., Khan, N. S., Engelhart, S.E., Vacchi, M., Shaw, T. A., Peltier, W. R., Horton, B.P. (2020), Uncertainties of Glacial Isostatic Adjustment Model Predictions in North America Associated With 3D Structure, Geophys. Res. Let., 47, 10, https://doi.org/10.1029/2020GL087944.

Milne, G.A., & Mitrovica, J.X. (1998), Postglacial sea-level change on a rotating Earth, Geophysical Journal International, 133, 1–19, doi: 10.1046/j.1365-246X.1998.1331455.x.

Milne, G.A., Latychev, K., Schaeffer, A., Crowley, J.W., Lecavalier, B.S., & Audette, A. (2018), The influence of lateral Earth structure on glacial isostatic adjustment in Greenland, Geophys. J. Int., 214, 1252-1266.

Mitrovica, J. X., & Peltier, W.R. (1989), Pleistocene deglaciation and the global gravity field, J. Geophys. Res., 94, 13,65143,671.

Mitrovica, J.X., & Peltier, W.R. (1993), A new formalism for inferring mantle viscosity based on estimates of post glacial decay times: Application to RSL variations in N.E. Hudson Bay, Geophys. Res. Lett., 20, 2153-2186.

Mitrovica, J.X., Forte, A.M. & Simons, M. (2000), A reappraisal of postglacial decay times from Richmond Gulf and James Bay, Canada, Geophysical Journal International, 142(3), 783–800, doi: 10.1046/j.1365-246x.2000.00199.x.

Mitrovica, J.X., Milne G.A., & Davis, J.L. (2001), Glacial isostatic adjustment on a rotating Earth, Geophys. J. Int., 147, 562– 579.

Mitrovica, J.X., & Milne, G.A. (2003), On post-glacial sea level: I. general theory, Geophysical Journal International, 154, 253-267.

Mitrovica, J.X., Wahr, J., Matsuyama, I., & Paulson, A. (2005), The rotational stability of an ice-age earth, Geophys. J. Int., 161(2), 491–506, doi: 10.1111/j.1365-246X.2005.02609.x.

Montillet J.P., Melbourne, T.I., & Szeliga, W.M. (2018), GPS vertical land motion corrections to sea-level rise estimates in the Pacific Northwest, J Geophys Res 123(2):1196–1212, doi: 10.1002/2017JC013257.

Morell, K.D., Regalla, C., Leonard, L.J., Amos, C., & Levson, V. (2017), Quaternary rupture of a crustal fault beneath Victoria, British Columbia, Canada. GSA Today, 27(3), 4–10.

Morell, K. D., Regalla, C., Amos, C., Bennett, S., Leonard, L., Graham, A., et al. (2018). Holocene surface rupture history of an active forearc fault redefines seismic hazard in southwestern British Columbia, Canada. Geophysical Research Letters, 45, 11,605–611,611. https://doi. org/10.1029/2018GL078711.

Muhs, D.R., Simmons, K.R., Schumann, R.R., Groves, L.T., Mitrovica, J.X., & Laurel, D. (2012), Sea-level history during the Last Interglacial complex on San Nicolas Island, California: implications for glacial isostatic adjustment processes, paleozoogeography and tectonics. Quat. Sci. Rev., 37, 1-25, doi: 10.1016/j.quascirev.2012.01.010.

Müller, R.D., Sdrolias, M., Gaina, C. & Roest, W.R. (2008), Age spreading rates and spreading asymmetry of the world's ocean crust, Geochemistry, Geophysics, Geosystems, 9, Q04006, doi:10.1029/2007GC001743.

Nakada, M., & Lambeck, K. (1989), Late Pleistocene and Holocene sea-level change in the Australian region and made rheology, Geophys. J. Int., 96, 497-517.

Obrebski, M., Allen, R.M., Pollitz, F. & Hung, S.H. (2011), Lithosphere-asthenosphere interaction beneath the Western United States from the joint inversion of body-wave traveltimes and surface-wave phase velocities, Geophys. J. Int., 185, 1003–1021.

Paulson, A., Zhong, S. & Wahr, J. (2007), Inference of mantle viscosity from GRACE and relative sea level data, Geophys. J. Int., 171, 497–508.

Peltier, W.R. (2004), Global glacial isostasy and the surface of the ice-age Earth: The ICE-5G (VM2) model and GRACE, Annual Review of Earth and Planetary Sciences, 32, 111-149.

Reynolds, L.C., & A.R. Simms, (2015), Late Quaternary relative sea level in Southern California and Monterey Bay, Quaternary Science Reviews, 126, 57–66, doi:10.1016/j.quascirev.2015.08.003.

Ritsema J., Deuss, A., van Heijst, H.J., & Woodhouse, J.H. (2011), S40RTS: a degree-40 shear-velocity model for the mantle from new Rayleigh wave dispersion, teleseismic traveltime and normal-mode splitting function measurements, Geophys. J. Int., 184(3), 1223–1236

Roy, K., Peltier, W.R. (2015), Glacial isostatic adjustment, relative sea level history and mantle viscosity: reconciling relative sea level model predictions for the U.S. east coast with geological constraints, Geophys. J. Int., 201(2), 1156–1181, doi:10.1093/gji/ggv066.

Severinghaus, J., & Atwater, T. (1990), Cenozoic geometry and thermalstate of the subducting slabs beneath western North America. In: Wernicke, B.P. (Ed.), Basin and Range Extensional Tectonics Nearthe Latitude of Las Vegas, Nevada. Geological Society of AmericaMemoir, vol. 176. Boulder, Colorado.

Schaeffer, A.J. & Lebedev, S. (2013), Global shear speed structure of the upper mantle and transition zone, Geophys. J. Int., 194(1), 417–449.

Steffen, R., Audet, P., & Lund, B. (2018), Weakened lithosphere beneath Greenland inferred from effective elastic thickness: A hot spot effect? Geophys. Res. Lett., 45, pp. 4733-4742, 10.1029/2017GL076885.

Steffen, R., Steffen, H., Weiss, R., Lecavalier, B.S., Milne, G.A., Woodroffe, S.A., & Bennike, O. (2020), Early Holocene Greenland-ice mass loss likely triggered earthquakes and tsunami, Earth and Planetary Science Letters, 546, 116443, https://doi.org/10.1016/j.epsl.2020.116443.

Tarasov, L., Dyke A.S., Neal R.M., Peltier W.R. (2012), A data calibrated distribution of deglacial chronologies for the North American ice complex from glaciological modeling, Earth Planet. Sci. Lett., 315–316, 30–40.

Ullman, D. J., Carlson, A. E., Hostetler, S. W., Clark, P. U., Cuzzone, J., Milne, G.A., Winsor, K., & Caffee, M. (2016), Final Laurentide ice-sheet deglaciation and Holocene climate-sea level change. Quaternary Science Reviews, 152, 49–59. https://doi.org/10.1016/j.quascirev.2016.09.014.

van der Wal, W., Barnhoorn, A., Stocchi, P., Gradmann, S., Wu, P., Drury, M., Vermeersen, L.L.A. (2013), Glacial isostatic adjustment model with composite 3D earth rheology for Fennoscandia. Geophys. J. Int., http://dx.doi.org/10.1093/gji/ggt099.

van der Wal, W., Whitehouse, P.L., & Schrama, E.J.O. (2015), Effect of GIA models with 3D composite mantle viscosity on GRACE mass balance estimates for Antarctica, Earth and Planetary Science Letters 414.

Wada, I., Wang, K., He, J., & Hyndman R.D. (2008), Weakening of the subduction interface and its effects on surface heat flow, slab dehydration, and mantle wedge serpentinization, J. Geophys. Res. 113, B04402, doi 10.1029/2007JB005190.

Wang, H., Wu, P., & van der Wal, W. (2008), Using postglacial sea level, crustal velocities and gravity-rate-of-change to constrain the influence of thermal effects on mantle lateral heterogeneities, J. Geodyn., 46, 104–117.

Watts, A.B. (2001), Isostasy and flexure of the lithosphere: Cambridge, Cambridge University Press, 458p.

Wu, P., & Peltier W.R. (1982) Viscous gravitational relaxation, Geophys. J. R. Astron. Soc., 70, 435-486.

Wu P., Van Der Wal, W. (2003), Postglacial sea levels on a spherical, self-gravitating viscoelastic earth: effects of lateral viscosity variations in the upper mantle on the inference of viscosity contrasts in the lower mantle, Earth planet. Sci. Lett., 211(1), 57–68.

Wu, P., & Wang H. (2008), Postglacial isostatic adjustment in a selfgravitating spherical earth with power-law rheology, J. Geodyn., 46, 118 – 130, doi:10.1016/j.jog.2008.03.008.

Wu, P., Wang, H. & Steffen, H. (2013), The role of thermal effect on mantle seismic anomalies under Laurentia and Fennoscandia from observations of Glacial Isostatic Adjustment, Geophys. J. Int., 192(1), 7–17.

Xue, M., & Allen, R.M. (2010), Mantle structure beneath the western United States and its implications for convection processes, J. Geophys. Res. 115, B07303, doi:10.1029/2008JB006079.

Yousefi, M., Milne, G.A., Love, R. & Tarasov, L. (2018), Glacial isostatic adjustment along the Pacific coast of central North America: Quaternary Science Reviews, v. 193, p. 288–311, 10.1016/j.quascirev.2018.06.017.

Zandt G., Gilbert, H., Owens, T.J., Ducea, M., Saleeby, J., & Jones, C.H. (2004), Active foundering of a continental arc root beneath the southern Sierra Nevada in California Nature, 431, pp. 41-46.

Zhong, S.J., Paulson, A. & Wahr, J. (2003), Three-dimensional finite element modelling of Earth's viscoelastic deformation: Effects of lateral variations in lithospheric thickness. Geophys. J. Int., 155, 679-695.

Supplementary Figures and Tables of Chapter 3

Contents of this section

Table S1 and Figures S1 to S6. This supplemental section contains additional figures to complement discussion and figures presented in the main text.

Table S1. Optimal model parameters for northern, central and southern regions. See Yousefi et al. (2018) for a description of the methodology used to infer these parameter sets.

Region	Ice Model	Lithosphere Thickness (Km)	Upper Mantle Viscosity ($\times10^{21}$ Pas)	Lower Mantle Viscosity ($\times10^{21}$ Pas)
Northern	6885R	46	0.05	1
Central	9858	71	0.2	10
Southern	5962	71	0.5	20

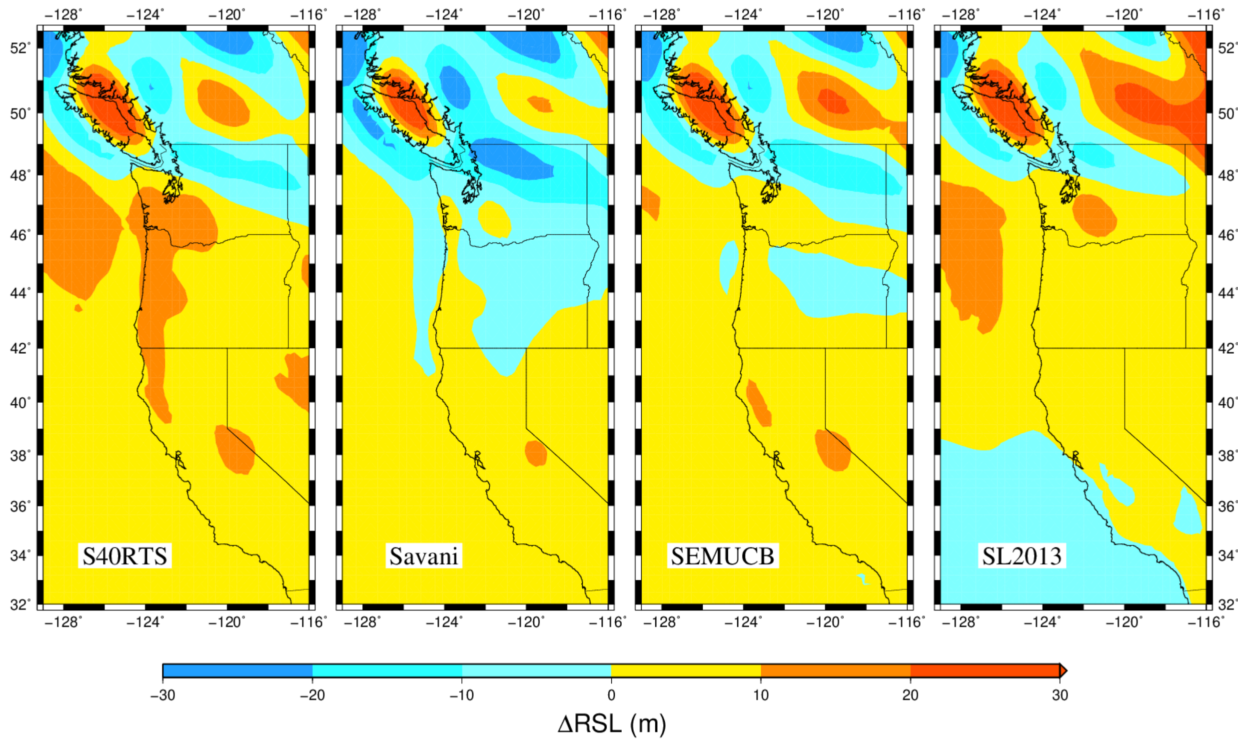

Figure S1. Modelled RSL changes compared to results for the reference 1D viscosity model at 10 ka (Figure 3.4a) when considering the combined effect of the lateral sublithosphere structure and the lithosphere structure from the WA model. All plots show 3D model results minus those for the reference 1D viscosity model.

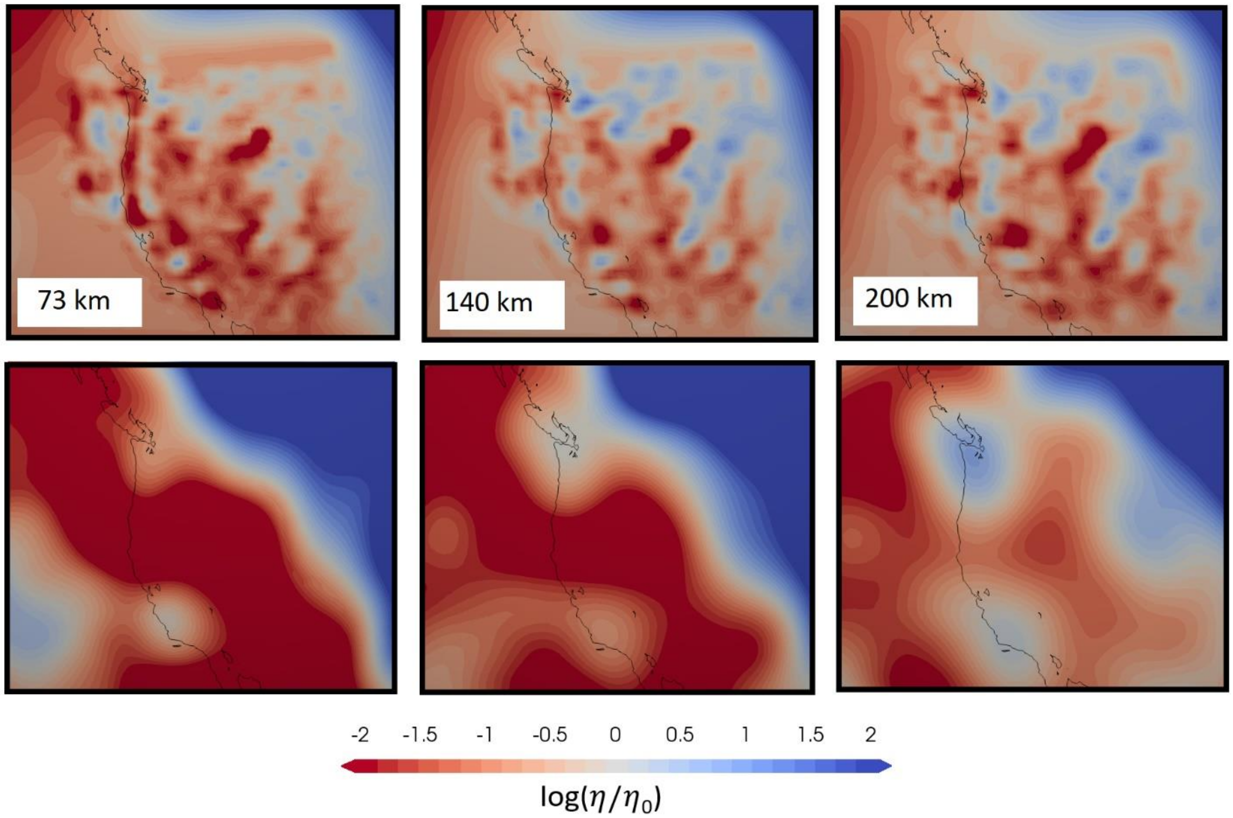

Figure S2. Lateral viscosity anomalies at depths of 73 km, 140 km, and 200 km associated with the with (top row) the regional model patched with the global SEMUCB-WM1 model, (bottom row) the global SEMUCB-WM1 model.

a)

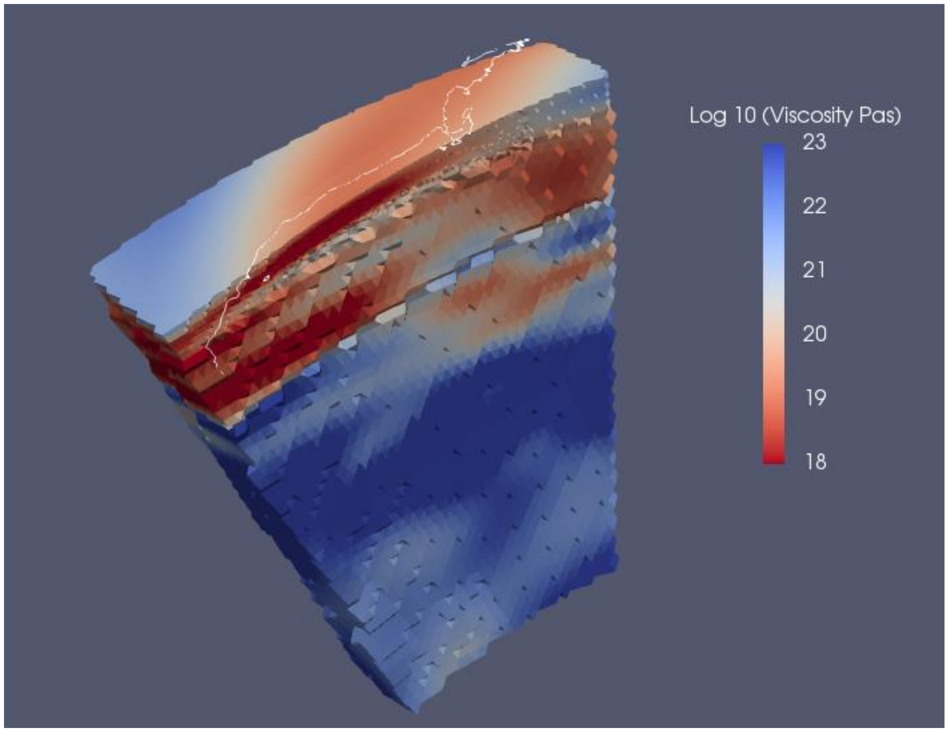
Log 10 (Viscosity Pas)
23
22
21
20
19
18

b)

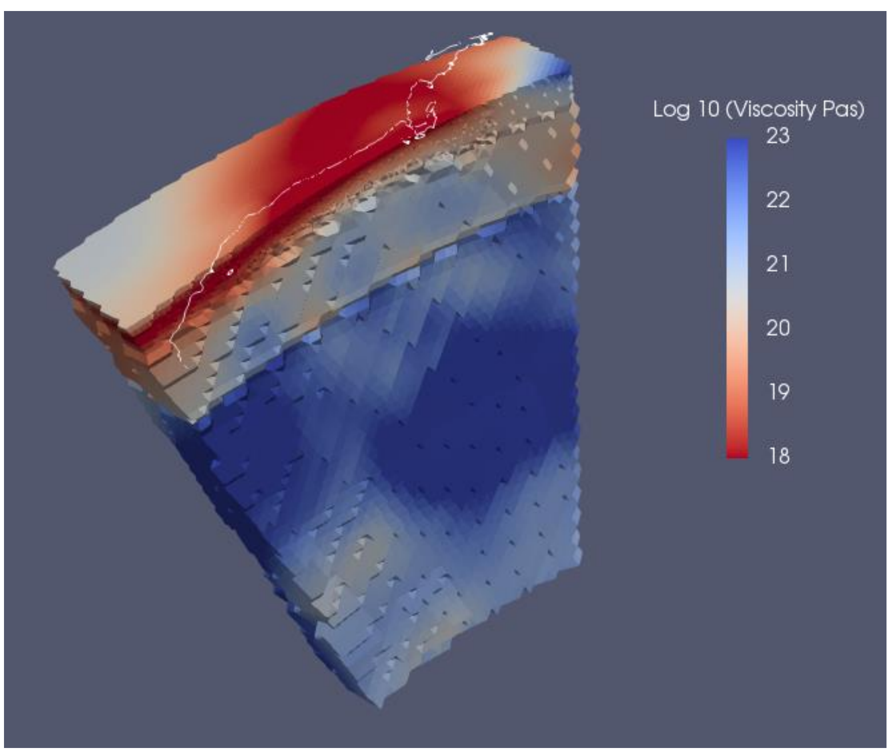
Log 10 (Viscosity Pas)
23
22
21
20
19
18

c)

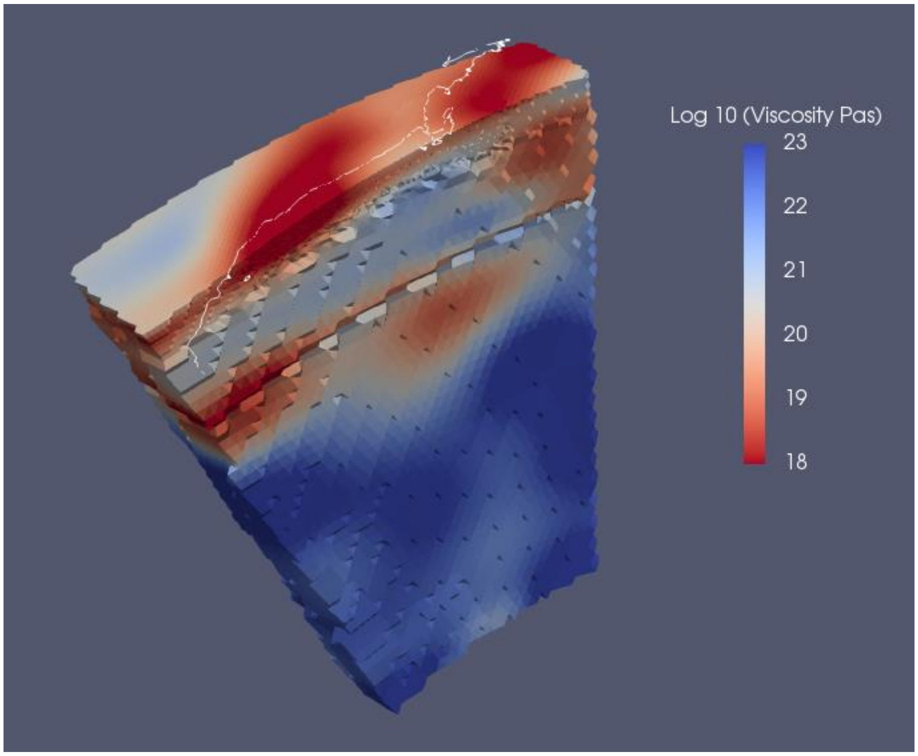

d)

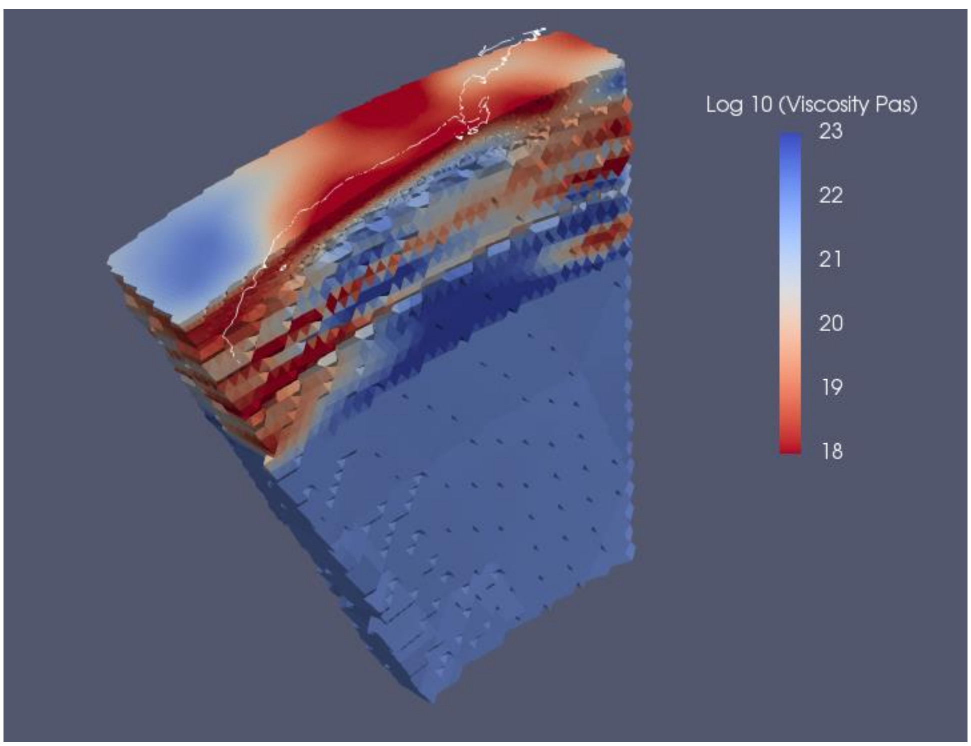

Figure S3. Sub-lithosphere mantle viscosity variations beneath our study region associated with the four considered global seismic models: (a) S40RTS, (b) Savani, (c) SEMUCB-WM1, and (d) SL2013.

a)

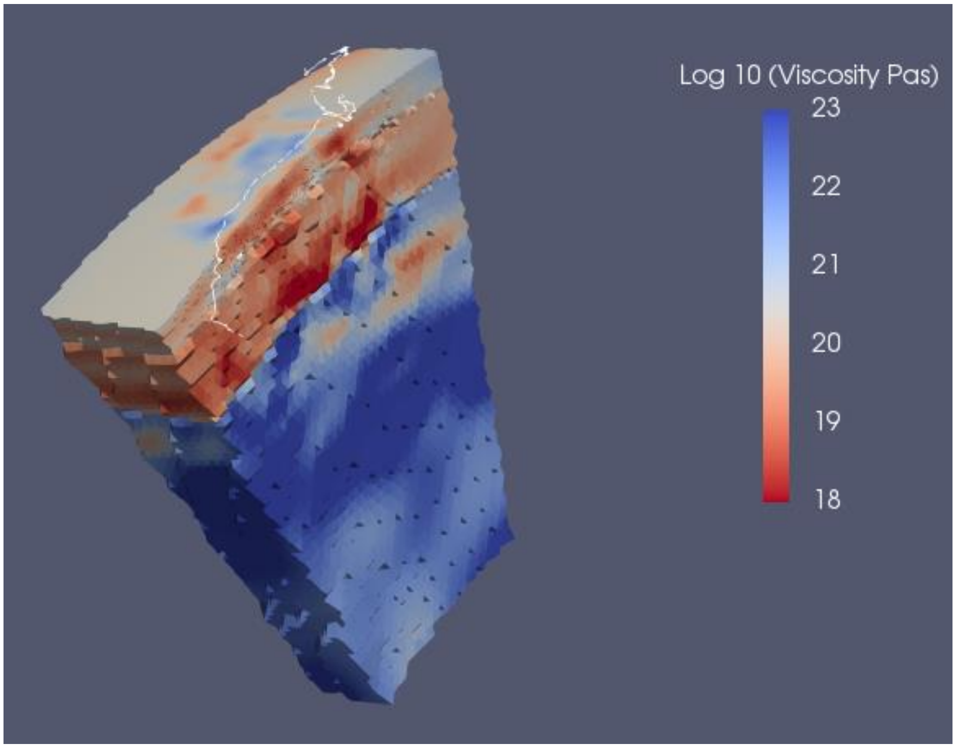

b)

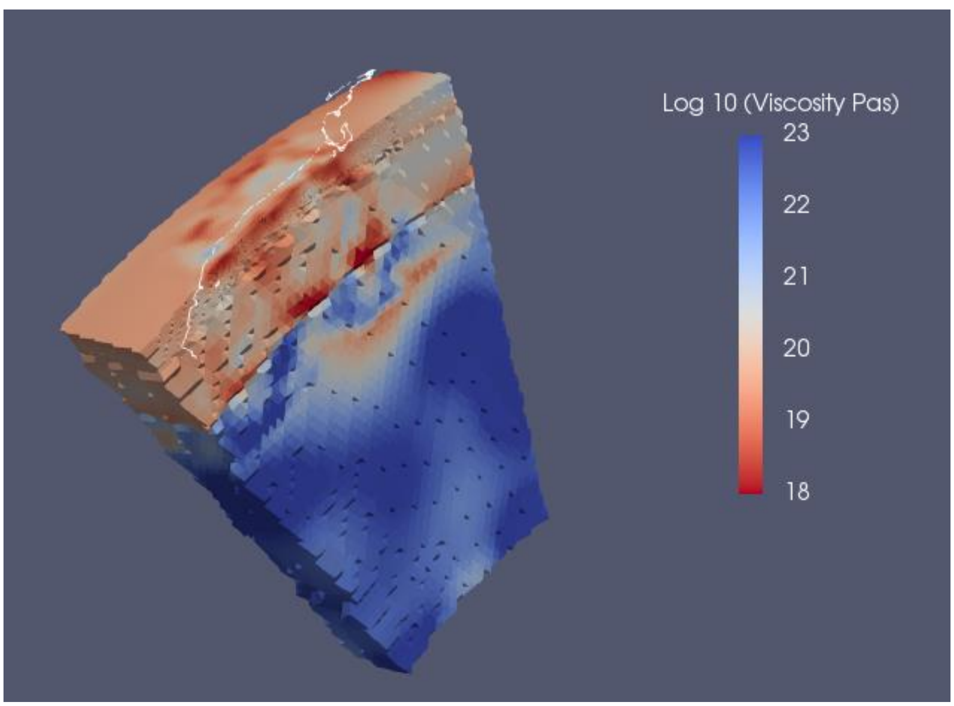

Figure S4. Sub-lithosphere mantle viscosity variations associated with the insertion of the regional model in two of the global seismic models: (a) S40RTS, and (b) SEMUCB-WM1.

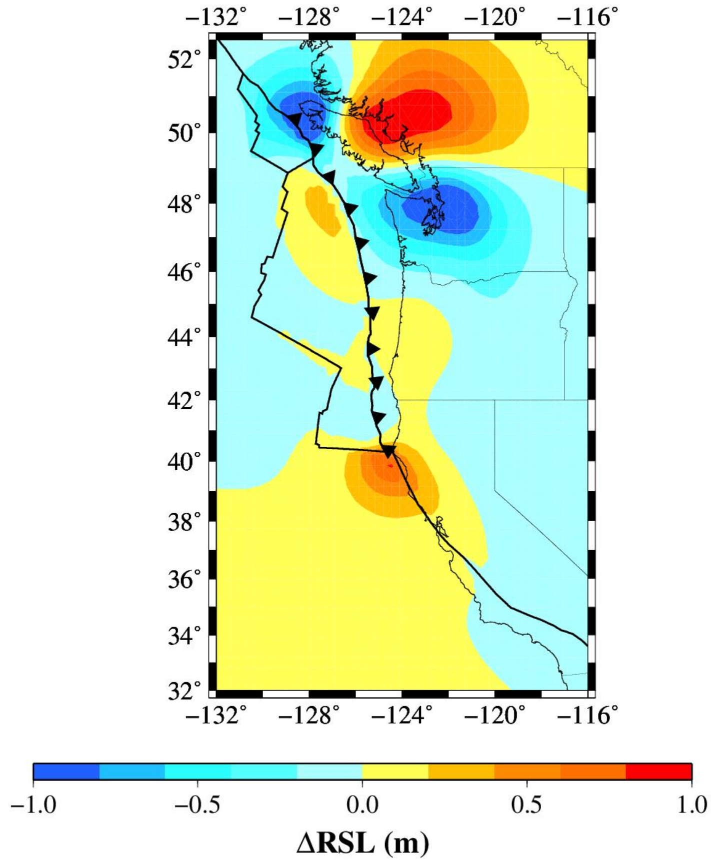

Figure S5. The perturbations to the modelled RSL changes at 10 ka when considering regional tectonic structure of the Cascadia subduction zone and immediate vicinity and the slab viscosity is decreased by three orders of magnitude.

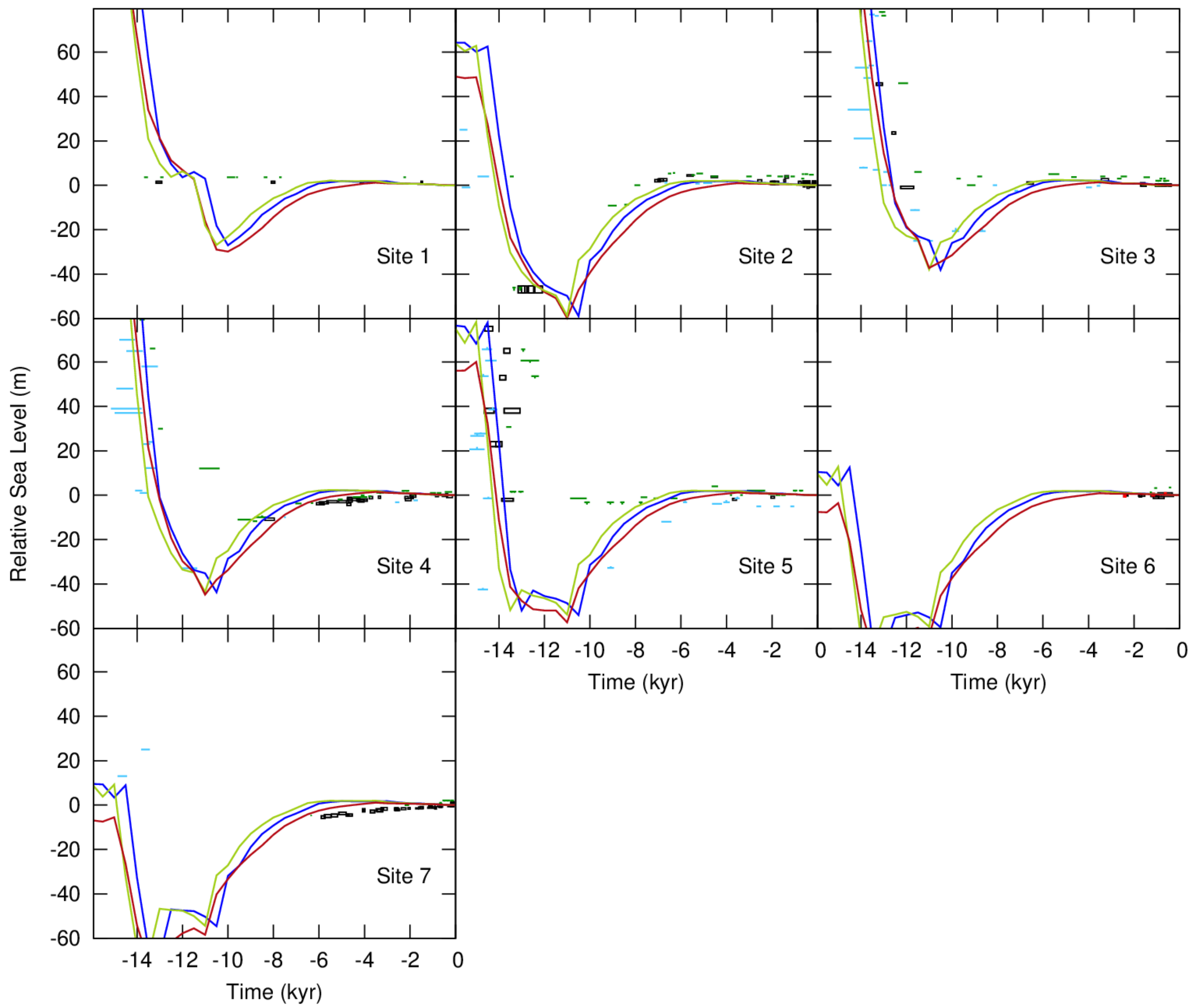

Figure S6. RSL data-model comparison for the northern region. The RSL curve plotted in red is the optimal curve for parameters tuned to northern region (Table S1: UMV of 5×10^{19} Pas, LMV of 10^{21} Pas and ice model number 6885R which is a revised version of 6885 model with 500 yr delay in deglaciation). The green line indicates a model curve with the same ice model and LMV as the red line, but an UMV of 5×10^{18} Pas. The blue line is model output with the same UMV and LMV of the green line, but with the 6885 ice model delayed in deglaciation by 1000 yr. The lithosphere thickness is set to 46 km.

a)

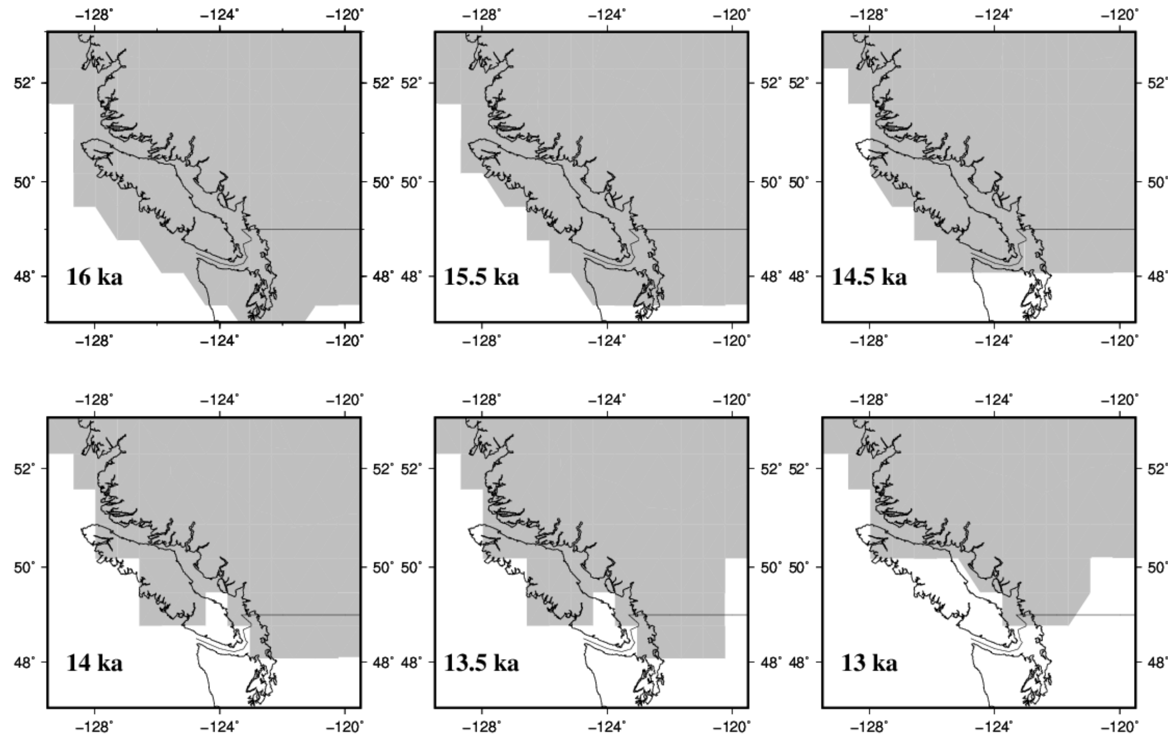

b)

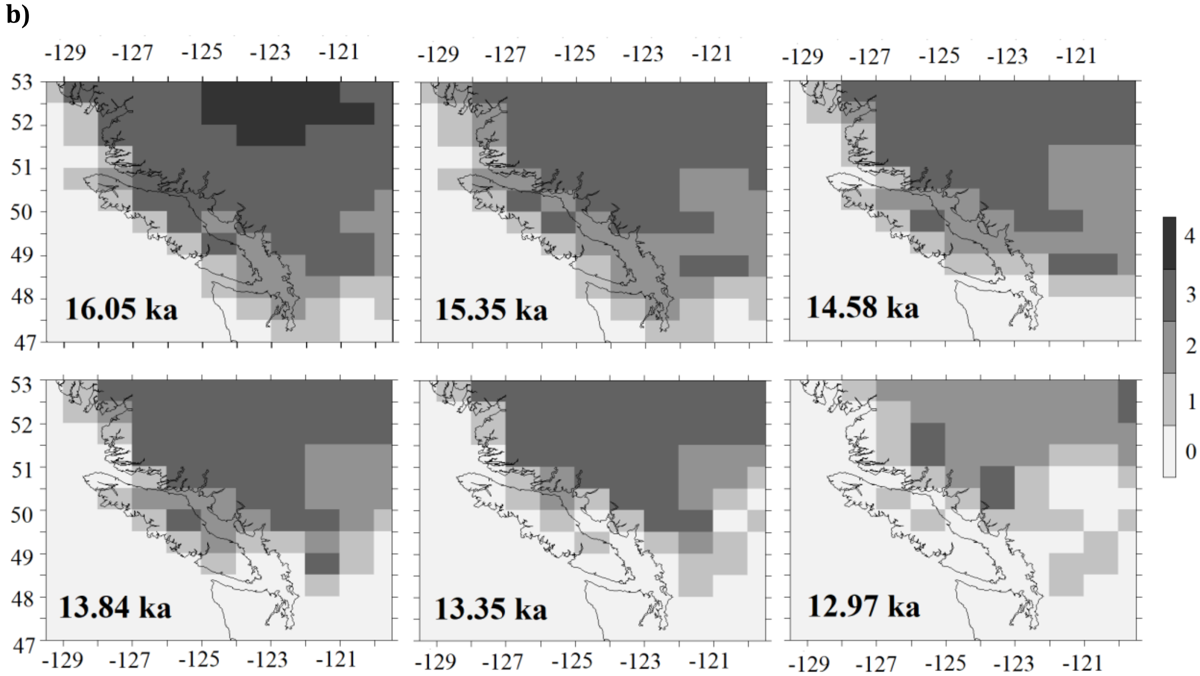

Figure S7. (a) Ice margin extent associated with ice model #6885. (b) A rasterized map of ice margin chronology applied in Tarasov et al. (2012) to calibrate the ice model shown in (a). The raster zone 0 correspond to the areas free of ice and the shaded regions (zones 1-4) represent the grid cells that have ice in the associated time slices and/or within the temporal ±1000 years

uncertainty. For more details about each raster zone, the reader is referred to the original article.

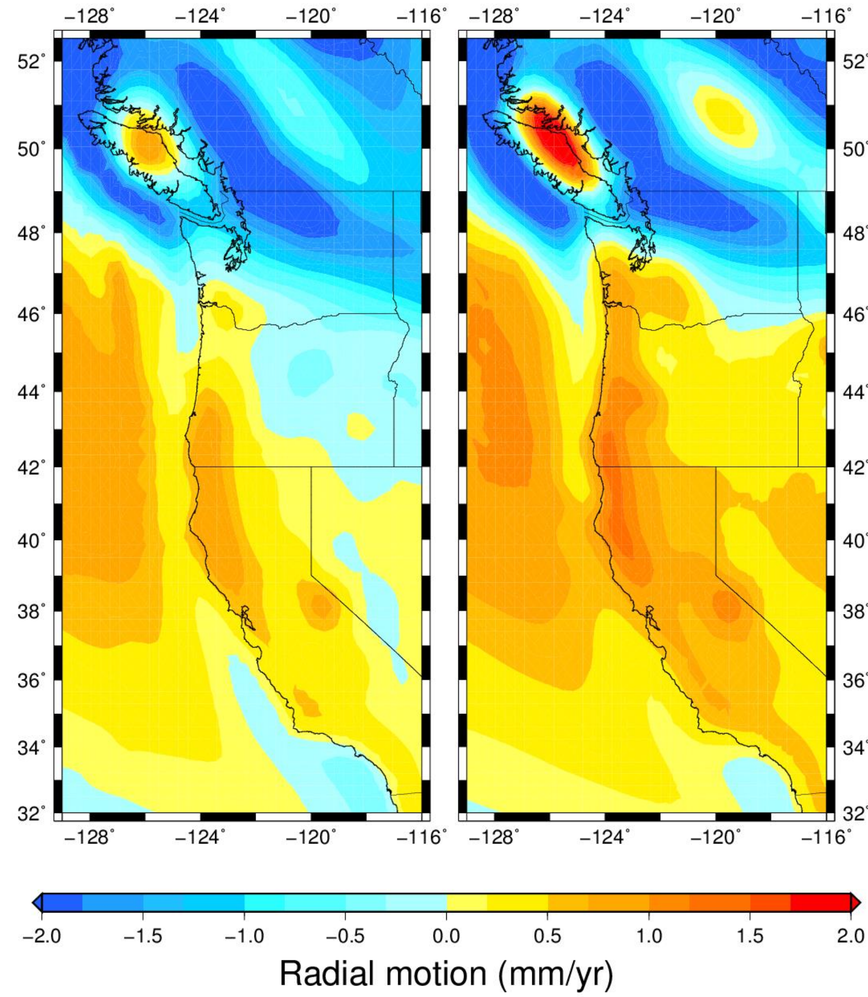

Figure S8. The sensitivity of the present-rate of crustal radial motion to the variations in lithosphere thickness inferred from the AB model (left panel) and the WA model (right panel).

4

Constraining Interseismic Deformation of the Cascadia Subduction Zone: New Insights from Estimates of Vertical Land Motion over Different Timescales

Statement of Contribution

The research presented in the following manuscript is written by me under the supervision of Dr. Milne. I led the writing of the manuscript with several rounds of feedback from Dr. Milne as well as input from the other authors (Shaoyang Li and Kelin Wang). Shaoyang Li and Kelin Wang provided us the Cascadia locking model outputs. I used the code of Alan Bartholet to estimate the glacier thickness change over different time steps. I generated all model results (except for the fault locking model) and all figures included in the manuscript. Most of the interpretations of model output are my own, thus the bulk of the scientific discussion reflects my own thoughts and analysis.

Citation:

Yousefi, M., G.A. Milne, S. Li, K. Wang, & A. Bartholet, (2020), Constraining Interseismic Deformation of the Cascadia Subduction Zone: New Insights From Estimates of Vertical Land Motion Over Different Timescales, JGR: Solid Earth, v. 125, issue 3, doi: 10.1029/2019JB018248.

4.1 Introduction

The Pacific coast of North America is a geodynamically complex region due to the relatively large number of processes that are active. Tectonic activity in this area is associated mainly with two active plate boundaries: the Cascadia subduction zone (from Vancouver Island to northern California), where the Juan de Fuca, Explorer and Gorda plates subduct beneath the North American plate (Severinghaus & Atwater,1990), and the strike-slip San Andreas Fault System, south of the Mendocino Triple Junction (Wallace, 1990). In addition to the land motion and deformation associated with tectonic activity, there is considerable glacial isostatic adjustment (GIA) in many areas because parts of this coastline were once covered by the Cordilleran ice sheet and were proximal to the Laurentian ice sheet during the peak of the last major glaciation (Peltier, 1994). In the most northerly part of this coastline (British Columbia), the relatively recent (20^{th}-century) response to mountain glaciers in the adjacent region (Schiefer et al., 2007) adds a more contemporary GIA signal. In the southern part (California), surface loading associated with groundwater removal also contributes a significant contemporary signal (Amos et al., 2014, Argus et al., 2014). This geodynamic complexity is observed in a variety of data types, including geodetic measurements of land motion and observations of relative sea-level (RSL) change obtained from tide gauges and geological reconstructions.

Numerous studies have examined geophysical and geological data with the intent of better understanding the underlying processes and/or constraining models of these processes, with the majority of studies focusing on the signal associated with tectonics (Burgette et al., 2009; Dragert et al., 1994; Hyndman & Wang, 1995; Krogstad et al., 2016; Leonard et al., 2010; Li et al., 2018; Smith-Konter, et al., 2014; Wang et al., 2003; Wang, 2007). Since the Global Navigation Satellite Systems (GNSS), in particular the U.S. Global Positioning system (GPS), became increasingly available in the late 1990's, geodetic observations of horizontal land motion have been the primary type of data used to constrain the state of megathrust locking which is an important parameter for seismic hazard estimates (e.g., Dragert & Hyndman, 1994; Li et al., 2018; McCaffrey et al., 2007; Wang et al., 2003). In the meantime, the application of vertical land motion (VLM) data for this purpose has been limited due to the lower precision of these data as well as the potentially large contamination from other processes such as those noted above (Wang & Trehu, 2016). Regardless, a handful of studies have considered observational estimates of VLM from GPS, tide gauge and leveling to constrain megathrust locking along different parts of the Cascadia coastline (Brugette et al., 2009; Krogstad et al., 2016; Schmalzle et al., 2014).

Geological reconstructions of RSL are the data set most commonly applied to constrain models of GIA (James et al., 2000; 2005; 2009; Muhs et al., 2012; Roy & Peltier, 2015; Yousefi et al., 2018). In this case, however, the influence of vertical tectonic motion can be a significant contaminating signal (Reynolds et al., 2015; Simms et al., 2016). While it is difficult to resolve this issue completely, some steps can be taken to consider and minimise the influence of tectonic signals on estimates of GIA model parameters (Yousefi et al., 2018).

In this analysis, we aim to build upon the work of Yousefi et al. (2018) to better isolate the vertical signal associated with tectonics; particularly that related to the ongoing interseismic deformation (dominated by megathrust locking of the Cascadia subduction zone) by determining rates of VLM on different time scales. Specifically, we determine the mean geologic rates of VLM over the past 4 kyr using RSL observations and incorporate the geodetic rates over decadal timescales from GPS observations. By considering the difference between these rates, we better isolate the signal associated with shorter-term processes and/or processes that have been recently activated (such as the ground water and glacier mass loss signals introduced above). The difference in geologic versus geodetic VLM rates will also reflect tectonic deformation due to interseismic locking of the Cascadia megathrust (Clague, 1997). A similar analysis was performed by Karegar et al. (2016) who compared rates from RSL and GPS observations along the US Atlantic coast to identify areas where recent anthropogenic activity has led to enhanced subsidence and therefore greater potential of nuisance flooding.

During an earthquake, many coastal areas would experience a sudden subsidence if coseismic slip is mostly offshore such as at Cascadia (Atwater, 1987; Leonard et al., 2010; Wang et al., 2013; Wang & Tréhu, 2016). Postseismic viscoelastic relaxation of the Earth occurs after the earthquake and decays through time (Wang et al., 2012). During the interseismic period, the fault is locked and strain accumulates towards the next megathrust earthquake; forearc deformation is characterised by rather stable patterns of crustal shortening and the area of coseismic subsidence will eventually experience uplift (Wang & Trehu, 2016). The earthquake-cycle deformation is accompanied with deformation due to other tectonic or non-tectonic processes as mentioned above, loosely called "non-earthquake" signals here. Contemporary VLM rates at the Cascadia forearc reflect the combined effects of both the interseismic deformation signal and the non-earthquake signals. By studying the non-earthquake deformation rates, we are able to remove them from the VLM rates and thus better isolate the interseismic signal.

The interseismic deformation originating from locking on the megathrust has been modelled in various studies (Flück et al., 1997, Wang et al., 2001, 2003, Li et al., 2018). The more recent models simulate viscoelastic deformation of the Earth and emphasize that the interseismic deformation is a time-dependant process owing to the viscoelastic relaxation of the mantle (Wang et al., 2012) and Cascadia is currently in the late stage of interseismic strain accumulation (Wang & Tréhu, 2016). A recent study by Li et al. (2018) determined the locking state of the megathrust by inverting only horizontal land motion observations using a 3D viscoelastic finite element model, but their locking model also predicted interseismic VLM rates. If we can remove the non-earthquake signals from observed VLM rates, the residual can be used to test these model-predicted interseismic rates and, in principle, further constrain the locking model parameters.

We provide estimates of millennial-scale and decadal-scale VLM rates from geologic (RSL) and geodetic (GPS) observations, respectively, at selected sites along the Pacific coastline (sections 4.2.2 and 4.2.3). The site selection procedure is described in section 4.2.4. The RSL records represent the change in the height of the ocean surface relative to the shore and hence require corrections to be converted to VLM rates. In this regard, the RSL data are corrected for the contribution from Sea Surface Height (SSH) changes (section 4.2.2). Furthermore, in order to better isolate the interseismic signal, we quantify the contribution of ground water removal and 20th-century glacier mass loss to contemporary VLM rates (sections 4.2.5.1 and 4.2.5.2, respectively). In section 4.2.1.1, we provide a description of the model that we use to estimate the Earth response to a general load applied on its surface. We also provide a brief description in section 4.2.1.2 of the Cascadia interseismic model developed by Li et al. (2018), from which output is used in section 4.3.2.1 to compare to our VLM rate differences. A general discussion of the unresolved signals and outlook for future research is included in section 4.3.2.2.

4.2 Methods

4.2.1 Models

4.2.1.1 Surface Loading Model

The formalism adopted in this study for computing the response of the Earth to a given surface load is adopted from Peltier (1974), who formulated the response of a spherically symmetric, self-gravitating, viscoelastic Earth to a general time variable surface mass load based on the Green's function approach. Green's functions represent the impulse response functions of a dynamic system, here the solid Earth, to an instantaneous point load. The ultimate response of the system is obtained by convolving the associated Green's function with a time- and space-dependant surface load. The reader is referred to Peltier (1974) and Wu & Peltier (1982) for a complete discussion of the mathematical formalism. The two conventional Green's functions that are considered in this study are associated with the radial component of deformation (GF_R, eq. 4.1) and the gravitational potential perturbation caused by the surface load (GF_Φ, eq. 4.2).

$$GF_R(\beta,t) = \frac{a}{M_E}\sum_{n=0}^{\infty}\left(h_n^V(t) + h_n^E\ \delta(t)\right) P_n(\cos\beta) \tag{4.1}$$

$$GF_\Phi(\beta,t) = \frac{ag}{M_E}\sum_{n=0}^{\infty}\left(\delta(t) + k_n^E\ \delta(t) + k_n^V(t)\right) P_n(\cos\beta) \tag{4.2}$$

Where, M_E is mass of the Earth; g is the Earth's surface gravitational acceleration; a is the model Earth's radius; $\delta(t)$ is the Dirac delta function or unit impulse function; P_n is the n^{th} Legendre polynomial; β is the angular distance between the point load and the observer. h_n and k_n are the surface load Love numbers associated with the radial deformation and the perturbation to the gravitational field, respectively. The corresponding superscripts V and E represent the contributions from viscous (time dependant) and elastic components of deformation. The Love numbers are dependent on the physical properties of the Earth, such as density and viscosity of the mantle. We computed Love numbers using the mixed collocation method (Mitrovica & Peltier, 1992).

The radial displacement (ΔR) and the perturbation to the gravitational field ($\Delta\Phi$) can now be obtained by convolving the surface mass load, $L(\theta,\lambda,t)$, with the associated Green's functions (equations 4.3 and 4.4).

$$\Delta R(\theta,\lambda,t) = \int_{t'}\int_{\lambda'}\int_{\theta'} L(\theta',\lambda',t')\, GF_R(\theta-\theta',\lambda-\lambda',t-t')\ d\theta' d\lambda' dt' \tag{4.3}$$

$$\Delta\Phi(\theta,\lambda,t) = \int_{t'}\int_{\lambda'}\int_{\theta'} L(\theta',\lambda',t')\, GF_\Phi(\theta-\theta',\lambda-\lambda',t-t')\ d\theta' d\lambda' dt' \tag{4.4}$$

Where, θ and λ are the colatitude and east longitude in a spherical coordinate system. The spatial integration of the convolution can be evaluated via a spherical harmonic expansion with a truncation degree and order 256. These equations indicate that both the applied load and the Earth model (density and rheology) structure must be accurately defined in order to determine reliable estimates of vertical land motion and gravity changes. The load models that are considered in this study are the ocean and ice loading due to the last deglaciation (section 2.2.1), the recharge and discharge of ground water reservoirs (section 2.5.1), and 20th-century glacier mass loss (section 2.5.2). In order to achieve higher resolution in spatial distribution of the glaciers, we consider a truncation degree of 512 when calculating the signal from glacier retreat.

The viscoelastic structure of the Earth model applied in this study is characterized by an elastic lithosphere as an outer shell and two deeper regions with uniform viscosity to represent the upper and lower mantle. The upper mantle extends from just below the lithosphere to a depth of 670 km and the lower mantle extends down to the mantle-core boundary. The density and elastic structures of the Earth model are defined with greater depth resolution compared to the viscosity structure depth parameterization, ranging from 3 km in the asthenosphere to 30 km in the lower mantle, using a global seismic model (Dziewonski & Anderson, 1981). The viscosity structure of the Earth is constrained by a GIA forward modelling procedure (Yousefi et al., 2018). The model of late-Pleistocene ice history is also constrained by the GIA modelling. A summary of the optimal model parameters, including the elastic thickness of the lithosphere, the upper and lower mantle viscosity and the ice history, is presented in Table S1.

4.2.1.2 Fault Locking Model

We follow the work of Li et al. (2018) who constructed a viscoelastic finite element model to invert geodetic observations of horizontal land motion to infer the current locking state of the Cascadia megathrust. After a correction for secular block motion of the upper plate, the horizontal components of the GPS data are assumed to be due only to interseismic strain accumulation. (We examine this assumption with respect to the influence of GIA in section 3.2.1.) The degree of locking is then simulated using a back-slip rate (Savage, 1983; Wang, 2007), with full locking represented by back-slipping at the subduction rate (DeMets et al., 2010) and no locking (full-rate creep) represented by zero back slip. The inversion parameters that were used in their study include limiting locking depth, boundedness of the back-slip rate, and smoothness of the back-slip distribution along the fault surface. The model parameter 'limiting locking depth' is the depth below which the megathrust is assumed to be creeping at the full subduction rate (zero back slip). Boundedness of the back-slip rate is implemented using a set of values that (1) confine the rates to be within a geologically plausible range and (2) enforce certain degree of creep at the trench, namely, no locking (zero back slip), partial locking (a prescribed maximum back-slip rate, 20 mm/yr for simplicity), and full locking (maximum back-slip rate, 40 mm/yr). The smoothness of the back-slip distribution is achieved by minimizing differences between back-slip rate vectors of neighboring fault patches. It is controlled by a smoothness factor (β), with a larger β value resulting in a smoother back-slip distribution.

4.2.2 Determining Rates of Late Holocene Relative Sea Level Change

We have made use of two published compilations of sea-level records along the Pacific coast of North America: one from Vancouver Island to Central California (Engelhart et al., 2015), and one from Central California to Southern California (Reynolds & Simms, 2015). The combined dataset is subdivided into 17 areas (hereafter referred to as sites; Figure 4.1) and comprises 674 sea-level index points. The selection of these 17 sites was not straightforward, as it depends on both the distribution of the RSL index points and the location of GPS stations. A detailed description of our site selection procedure is provided in section 2.4. Based on the late-Quaternary ice coverage and tectonic setting of the study region, we divided the entire dataset into three sub-regions: northern (British Columbia and northern Washington), sites 1-7; central (southern Washington and Oregon), sites 8-12; and southern (California), sites 13-17. We estimated an average millennial-scale constant rate of Late Holocene sea-level change (Figure S1) by considering index points dating to 4 kyr before present (BP) or younger at each site and applying the total least squares approach, accounting for the uncertainties inherent in both RSL and time. The corresponding one standard deviation (1σ) uncertainty range was estimated based on the scatter of the observations about the best fitting line. We chose 4 kyr BP as it represents a trade-off between maximising the number of available index points to improve the regression estimate and minimising the contribution to the signal from global ice melting (Shennan, 1989; Shennan & Horton, 2002): the volume of global ice melt since 4 kyr BP is estimated to be ≤1 m (Lambeck et al., 2014; Hallman et al., 2018). We note that the youngest index points date to 1818 CE, so there is no need to account for the acceleration in global mean sea level rise during the industrial era (Kopp et al., 2016) since we do not force the regression line to pass through zero at 1950 CE.

Given that the GIA response is expected to decrease through time (section 2.1.1), it is possible that a linear fit over the past 4 ka may overestimate the amplitude of the modern rates. To examine this, we used the modelled GIA induced displacement rates at each site and compared the rate for the past 100 years with the rate for the past 4 kyrs. The difference between these two rates is on order of 0.1 mm/yr at most of the sites and is less than ~0.3 mm/yr across the entire region and so we ignore this departure from linearity in the following analysis.

We note that, since the majority of RSL data are reconstructed from intercalated sediments (Engelhart et al., 2015; see their Figure 2), the calculated VLM rates might be biased low at some sites due to the influence of sediment compaction.

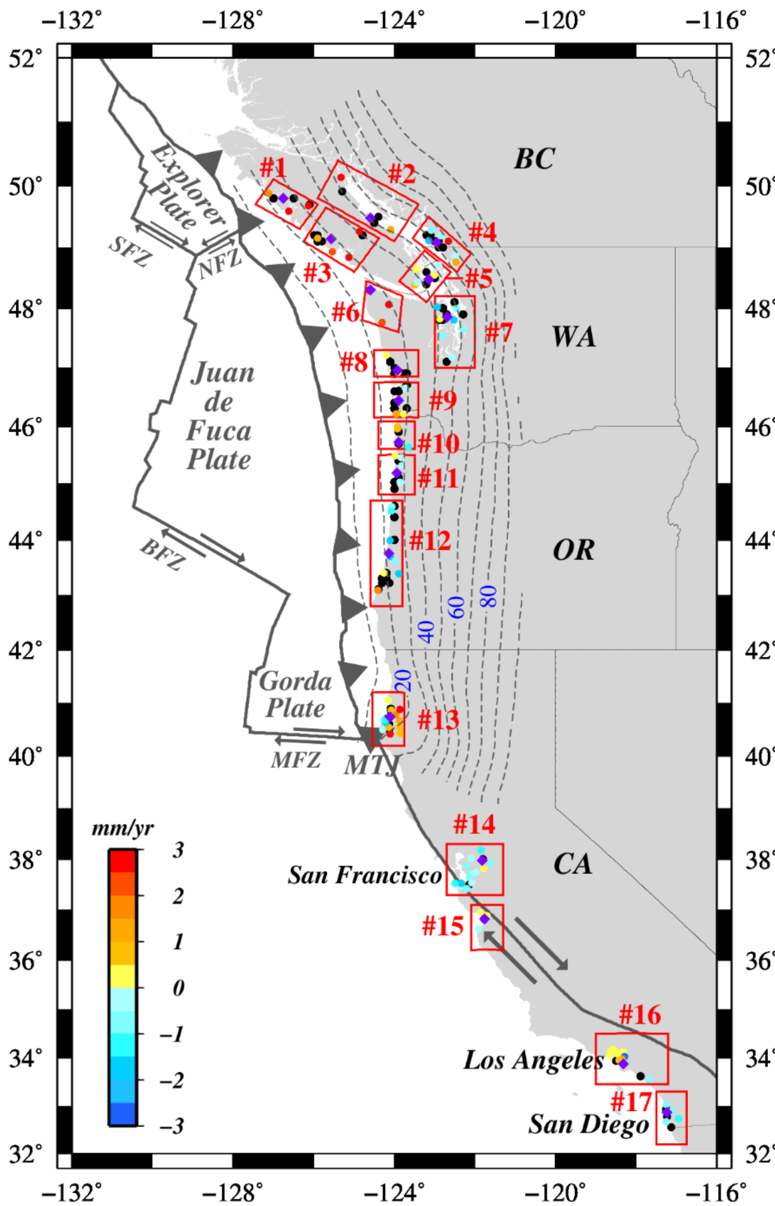

Figure 4.1. Map showing the spatial distribution of RSL data as well as GPS stations. Each of the 17 regions is indicated by a red rectangle. The locations from where RSL data were acquired are indicated by black circles. Colored circles indicate the locations of the GPS sites and the observed rates of vertical motion in NA12 reference frame. The purple diamond in each region gives the average location of the RSL data for that region. Dashed grey lines are depth contours that represent the inferred top surface of the subducted Juan de Fuca, Explorer and Gorda plates (Blair et al., 2011). Solid grey lines show

plate boundaries, with the triangles indicating subduction of the Juan de Fuca, Explorer and Gorda plates beneath the North American plate. MTJ represents Mendocino Triple Junction. SFZ, BFZ, MFZ, and NFZ represent the Sovanco, Blanco and Mendocino fracture zones, and Nootka fault zone, respectively. US states – Washington (WA), Oregon (OR) and California (CA) – and the Canadian province British Columbia (BC) are indicated along with their geographic boundaries.

4.2.2.1 Removing the Contribution from Sea Surface Height Changes

We considered two processes that could have influenced SSH changes over the late Holocene: GIA and variations in ocean temperature. The latter is known as thermosteric sea level change, which includes two contributions to SSH, a volume component due to changes in water volume and a dynamic component due to changes in ocean density structure and thus circulation. We quantified the effect of these thermosteric/dynamic changes for the late Holocene and found them to be negligible (rates of order 0.1 mm/yr; see supplementary material section S1).

The importance of GIA along the west coast of North America is due to the fact that the majority of North America was covered by ice sheets (Laurentian, Cordilleran, Innuitian) during the last glacial maximum. GIA deforms the solid Earth over a long period of time as is evident in both the late Holocene RSL data as well as contemporary GPS observations. In addition to solid Earth deformation, RSL data also include a component due to the change in gravity associated with surface ice-ocean mass transfer as well as internal deformation of the solid Earth. This gravity change influences geoid height and, therefore, sea-surface height (eq. 4.5).

$$\Delta SL(\theta,\lambda,t) = \Delta G(\theta,\lambda,t) - \Delta R(\theta,\lambda,t) + E(t) \tag{4.5}$$

Where ΔSL is the RSL change, ΔR is the vertical solid Earth motion given by eq. 4.3, and ΔG is the spatially varying geoid-height change which is determined to first order by dividing the perturbation to the gravitational potential (given by eq. 4.4) by the gravitational acceleration ($\frac{\Delta\Phi}{g}$). E is a spatially uniform height shift that ensures mass conservation within the system, i.e., the mass lost/gained by the ice sheets is gained/lost by the oceans (Farrell and Clark, 1976). This shift comprises two components: the change in ocean water mass associated with the growth/melting of the ice sheets (barystatic sea-level change) and the change in ocean basin volume associated with the spatial integration of $\Delta G - \Delta R$ over the oceans. The latter process, which is known as ocean syphoning, is driven by two processes: the collapse of glacial forebulges and the influence of ocean loading around the continents, both of which lead to an increase in ocean basin volume during the Holocene (Mitrovica & Milne, 2002).

The perturbations to the geoid (ΔG in eq. 4.5) were estimated using the model presented in section 4.2.1.1. We estimate the 1σ uncertainty range for the geoid height change by adopting the model bounds determined from the Bayesian approach described in Yousefi et al. (2018). The values and 1-sigma ranges for the rates of change of ΔG are given in Table S3.

The globally uniform change in SSH associated with the term E in eq. 4.5 was determined using the results of two global analyses: one of Peltier (2004) using the ICE-5G ice history and the related VM2 Earth model and the other using the ice and Earth model from the analysis of Lambeck et al. (2014). Using these two ice-Earth model pairs, the global mean GIA contribution (barystatic plus syphoning) was computed as the degree zero component of the solution of a generalised form of eq. 4.5 that accounts for lateral variations in shoreline position through time as well as the influence of Earth rotation due to GIA (Milne & Mitrovica, 1998; Mitrovica & Milne, 2003; Kendall et al., 2005; Mitrovica et al., 2005). The values obtained for barystatic and syphoning signals are, respectively, 0.02 and -0.3 mm/yr for the Peltier model and 0.21 and -0.39 mm/yr for the Lambeck et al. model.

The total contribution of GIA to SSH changes over the past 4 ka, including the effects of geoid-height change, ocean syphoning, and barystatic sea-level change, with the corresponding 1σ uncertainty ranges, are presented in Table S3.

4.2.3 GPS Observations

We considered various criteria to screen the appropriate GPS stations to arrive at robust estimates of VLM rates at locations where we have RSL-based estimates of this quantity. The main criteria is the proximity of the GPS sites to the location of the RSL data; we require that at least two GPS stations be present at each RSL site. Figure 4.1 shows the spatial distribution of GPS stations used in this analysis. Another criteria is the temporal coverage of the GPS time series; those with less than ~10 years of observations are excluded. Ultimately, the final selection comprises a total number of 102 GPS stations (Figure 4.1).

We used the GPS velocities and their uncertainties provided by Nevada Geodetic Laboratory (NGL), who developed and applied Median Interannual Difference Adjusted for Skewness (MIDAS) method (Blewitt et al., 2018). Velocities determined using the MIDAS robust trend estimator are resistant to step discontinuities, outliers, seasonal signals, and time-dependant noise (known as heteroscedasticity) (Blewitt et al., 2016). We used the stable North America reference frame (NA12) in determining VLM rates.

4.2.4 Site Selection

Since a key aspect of this analysis is to determine the change in VLM rates over time, it is important to minimise any signal due to spatial variability in rates resulting from the RSL and GPS observations not being co-located. Our aim is to choose an area small enough such that the signal of interest does not vary substantially (and so spatial averaging is accurate) but large enough to include sufficient RSL index points and GPS stations. A minimum number of RSL observations are required to determine a meaningful trend and several GPS stations are required to average out the influence of local or site specific processes that are not of interest (e.g. poor antenna monumentation).

We first followed the work of Yousefi et al. (2018), who used 13 sites for the entire study area based on various criteria such as tectonic setting, distance from former ice sheet, etc. Since no GPS data are available for one of the sites (Queen Charlotte Strait, site 1 in Yousefi et al., 2018), we excluded it from our analysis and thus the total number of the sites is reduced to 12 (Figure S4). The corresponding GPS and Holocene VLM rates are shown as red circles at the 1-σ confidence level in Figures S5 and S6, respectively. We subdivided sites 2, 5, 7, 8, 9, 11, and 12 to determine if there are significant gradients in either the GPS or late Holocene VLM rates within the originally defined sites selection. In addition to this, we removed two southern index points from southeastern Georgia strait (site 3 in Figure S4) and added them to southern Vancouver Island (site 4 in Figure S4). After applying these adjustments, we arrived at 19 sites (Figure S7) and the associated GPS and late Holocene VLM rates (black circles in Figures S5 and S6).

A comparison between the VLM rates derived from the two site selections illustrated in Figures S4 & S7 shows that there are considerable spatial gradients (>0.5 mm/yr) in western Vancouver Island, northern Washington coast, as well as central and southern California. This difference is largest (~1 mm/yr) in southern California (GPS data) and western Vancouver Island (late Holocene data). Therefore, subdivision of the original sites (2, 3, 11 & 12; Figure S4) is used for this analysis, giving the new sites (1, 3, 6, and 16-19, Fig S7). The reason that we excluded the eastern section of northern Washington coast (site 6, Figure S7) is the lack of sufficient RSL index points to obtain a reliable linear trend. Comparison of the VLM rates for the two site selections indicates that there is no significant spatial gradient in central Oregon (site 9, Figure S4) and thus no subdivision was applied to this site. Although the difference in VLM rates between the two site configurations is relatively small in southern Washington and northern California (< 0.3 mm/yr), there is a high gradient in the fault locking model results for these areas (see Figures 5a and 6 in section 4.3.2.1), and so the higher spatial sampling (Figure S7) was adopted. All of these considerations led to a total number of 17 sites as illustrated in Figure 4.1.

4.2.5 Removal of the Contemporary Signals

4.2.5.1 Contribution from Ground Water Changes

The substantial extraction of ground water in central and southern California (sites 14-17) is thought to contribute significantly to VLM in this region (Amos et al., 2014, Argus et al., 2014). We calculated the rates of VLM induced by this process as the response of a viscoelastic spherically symmetric Earth by applying the model outlined in section 4.2.1.1 and adopting the viscosity parameters associated with the southern region presented in Table S1. The load history is defined as a spatially variable annual groundwater distribution at 0.5° × 0.5° resolution (data from Wada et al., 2012). These data are based on a global hydrological model that calculates the difference between groundwater recharge (including natural recharge and return flow from irrigation) and human-induced groundwater extraction (Wada et al., 2012).

4.2.5.2 Contribution From Recent Glacier Mass Loss

We quantified the contribution of glacier mass change during the past century to present-day crustal motion in our study region. Using the Randolph Glacier Inventory (RGI) (RGI Consortium, 2015), it is evident that region #2 (of the 19 defined in this inventory), representing glaciers in Western Canada and US, includes some glaciers that are proximal to our northern sites (1-7).

To estimate the VLM signal associated with these region #2 glaciers, we first estimated the average thickness of the glaciers based on the areal extent of the glaciers in the RGI data base and the following scaling formulation (Huss & Farinotti, 2012):

$$\bar{h} = cS^{\gamma} \tag{4.6}$$

Where $\bar{h}$ is the mean glacier thickness, S is the glacier area, and the constants c and γ are scaling coefficients with an optimized value of 0.370 and 0.320, respectively, for Western Canada and US glaciers. In order to estimate the effect of the glacier mass loss on crustal motion, we apply the glacier mass change rate provided by Marzeion et al. (2015) from 1902 to 2013 and estimate the glacier thickness changes backward in time via a simple scaling of ice thickness in 10-year time bins. Figure S8 shows the modelled thickness and extent of the Western Canada and US glaciers before and after the estimated mass loss. Using this load history and the same viscoelastic spherically symmetric Earth as described in section 4.2.1.1, we calculated the VLM response to the glacier retreat by using the viscosity values corresponding to the northern region (Table S1).

4.3 Results and Discussion

In this section we present and compare the VLM rates inferred from the two methods outlined above, namely, direct estimates of decadal-scale geodetic rates from GPS observations and indirect estimates of millennial-scale geologic rates from RSL observations (where the SSH signal has been estimated and removed). We also make a first interpretation of the change in VLM rates (GPS minus geologic rates; section 4.3.2), which we use to constrain parameters in a model of deformation associated with interseismic megathrust locking (section 4.3.2.1).

4.3.1 Vertical Land Motion Rate Estimates

The late Holocene VLM rates (corrected for the GIA contribution to SSH change) are presented in Table S4 and plotted as black circles in Figure 4.2 along with their estimated 1σ uncertainties. The results indicate subsidence at all sites except for the northwestern Strait of Georgia (in the northern Salish Sea, site 2) and central western Vancouver Island (site 3). The estimated subsidence in the central and southern regions (sites 8-17) can be interpreted to be primarily caused by the collapse of peripheral bulge produced by the Cordilleran and Laurentide ice sheets (Long & Shennan, 1998; Engelhart et al., 2015). In the northern region, closer to the ancient ice margin, the VLM rates are indistinguishable from zero at 1-σ confidence. The rates are, in general, smaller in this region. One interpretation of this is that the system is closer to isostatic equilibrium due to the lower viscosity values of the upper mantle in this area (James et al., 2009; Yousefi et al., 2018). Our late Holocene VLM rates are generally consistent with findings of Friele & Hutchinson (1993) and Hutchinson et al. (2000) who inferred an uplift rate of ~1-1.5 mm/yr for the west coast of Vancouver Island relative to the Fraser lowland over the last several thousand years. According to Figure 4.2, this relative uplift is plausible given the data uncertainty. If robust, it could result from either long-term tectonic activity at the Cascadia margin (Hutchinson et al., 2000; Wang et al., 2003) or a GIA signal that is not captured by the current models which do not incorporate lateral heterogeneity in earth rheology.

The GPS-estimated VLM rates are presented in Table S4 and shown as magenta circles in Figure 4.2 and they are greater than the RSL-estimated rates at most locations. This dominance of higher contemporary rates reflects the underlying geodynamic processes and interpretation of this rate difference will be the focus of following sections.

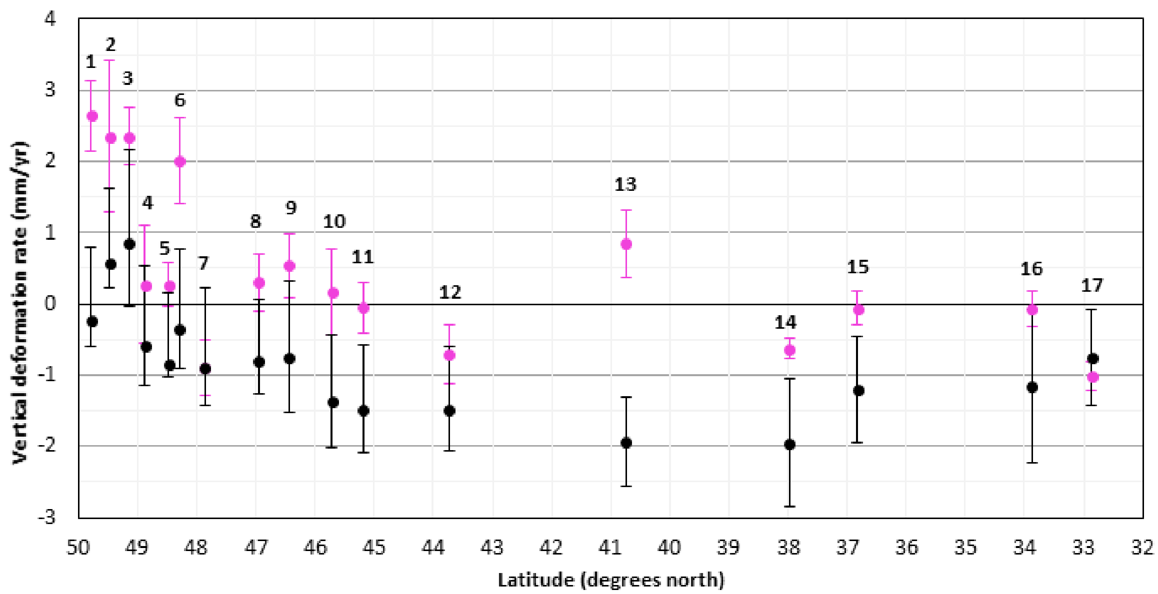

Figure 4.2. GPS VLM rates (magenta circle shows average value of all the GPS stations within each site box in Figure 1) and millennial-scale rates inferred from late Holocene RSL data (black circles), with their associated 1σ uncertainty range. The site numbers are shown above the rate estimates for each location. For clarity purpose, the average latitude of site 4 is shown by 0.2 degrees reduction of the actual latitude. This alteration is consistent for the entire figures shown throughout the manuscript as well as supplementary file.

4.3.2 Interpretation of Vertical Land Motion Rate Change

Both the geologic (RSL) and geodetic (GPS) rates are influenced by relatively slow solid-Earth processes such as GIA and millennial-scale tectonic changes. However, the GPS observations also capture processes that are more prominent on shorter timescales, or have been activated relatively recently. An example of the former is the time varying crustal deformation during the seismic cycle. Examples of the latter are ground water depletion and 20th-century glacier retreat. Therefore, the residual between GPS and geologic rates will reveal these signals more clearly. In the following, we aim to explain this residual by considering output from the geodynamic models introduced in sections 4.2.1 and 4.2.2.

The residuals between GPS and geologic VLM rates (i.e. GPS rates minus late Holocene VLM rates) are shown as grey circles in Figure 4.3. The residuals are positive and thus show uplift in all sites except for San Diego Bay in southern California (site 17). Although we note that, at several sites, the residual is indistinguishable from zero at the 1σ level.

As described in section 4.2.5.1, the VLM rates for sites 14-17 may be significantly influenced by ground water removal during the 20th century. When modelling the influence of this process (section 4.2.5.1) we find that it leads to uplift across the study region, albeit it small in most areas (≤0.1 mm/yr) except California: ~0.5 mm/yr at sites 14 and 15 and ~1 mm/yr at sites 16 and 17 (Figure 4.4). On the other hand, the VLM rates for the northern sites are most strongly influenced by 20th-century glacier mass loss (section 4.2.5.2). The contribution from this process to present-day VLM rates is in the range 0.3-1 mm/yr in the northern region and is 0.1 mm/yr or less at the other sites (Figure 4.4).

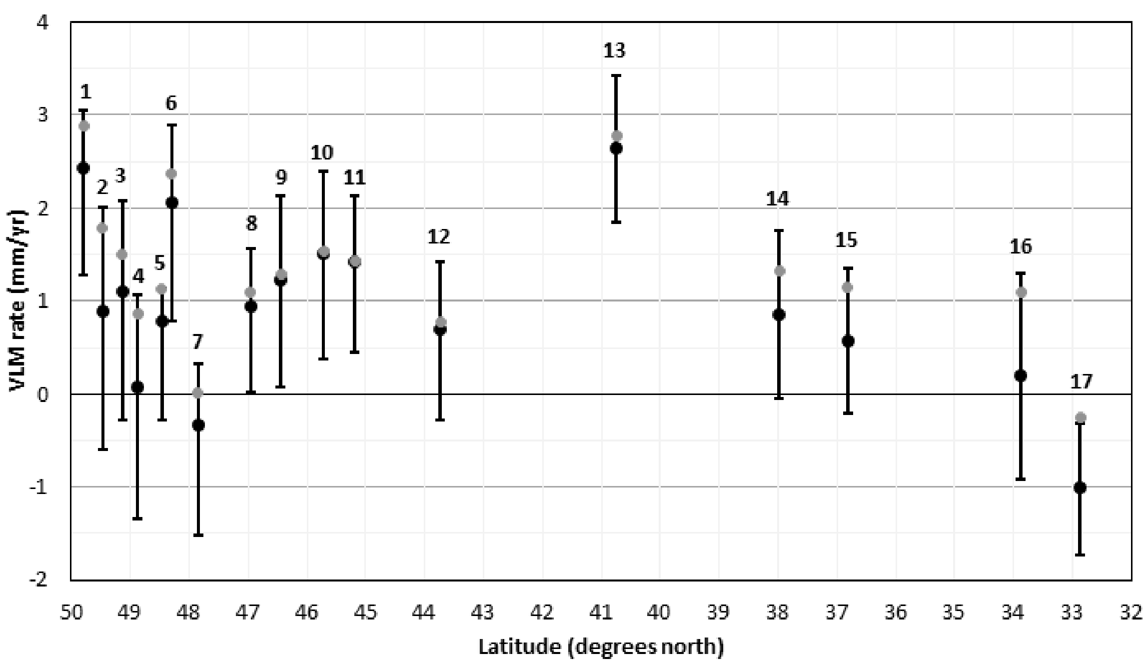

Figure 4.3. The residual between the GPS and late Holocene VLM rates (grey circles), i.e., difference between magenta and black circles in Figure 4.2. The black circles show the residual rates corrected for 20th century glacier mass loss and ground water change. The uncertainty ranges are plotted at the 1σ level for the corrected residuals. The uncertainty associated with these corrections was not estimated. For the purpose of clear illustration, the average latitude of site 4 is reduced by 0.2 degrees.

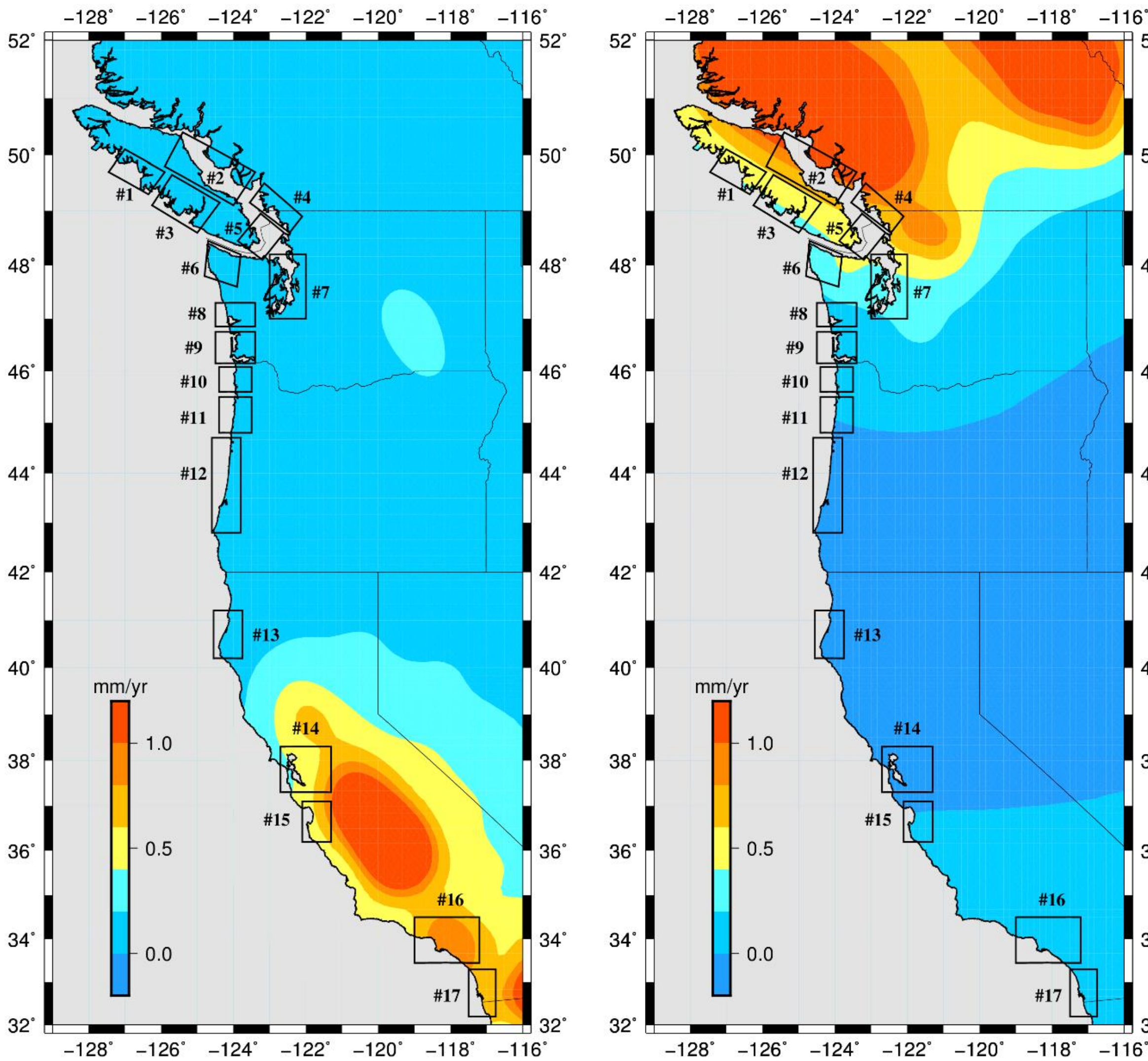

Figure 4.4. Contribution from ground water change (left panel) and glacier mass loss (right panel) to the present-day VLM rates.

Using these rate estimates to remove the ground water and glacier loading signals reduces the residuals between GPS and geologic rates at most northern and southern sites (compare grey and black circles in Figure 4.3). These 'corrected' residuals (Table S4), used for further analysis in the following section, show a similar pattern to the residual rates before applying the corrections: uplift at many of the sites. The range of the corrected residuals is ~-1 to ~2.6 mm/yr. We note that although the glacier signal is significant in most of our northern sites, it is not sufficient to explain the relatively high residuals at a small number of sites in this area. In contrast, the corrections for ground water extraction remove the residuals for sites 14-16 but result in a subsidence signal for San Diego Bay (site 17) (relative to the long-term millennial rate). As can be seen in Figure 4.3, residuals are indistinguishable from zero at the 1σ level at 9 of the 17 sites. The fact that a considerable number of residuals sit well above zero indicates that the contemporary rates are higher than those of the millennial-scale background trend even when accounting for the recent signals due to groundwater changes and glacier melting.

Central and southern California (sites 14-17) are located in the vicinity of a strike-slip plate boundary and so their contemporary VLM rates are affected by the localized crustal deformation associated with the presence of the San Andreas Fault System. Although the majority of this motion is strike slip, the interseismic loading and some minor contributions from postseismic relaxation can generate vertical deformation that can reach a few mm/yr in some localities. Smith-Konter et al. (2014) estimated the vertical deformation originating from earthquake cycle motion of the San Andreas Fault System across central and southern California by using a 3D viscoelastic earthquake cycle deformation model. Their simulated vertical velocity field suggests an uplift rate of ~0.4 mm/yr in Los Angeles and subsidence rate of ~0.2 mm/yr in San Diego. Removing these signals from our GPS-VLM estimates in these areas (sites 16 and 17) reduces the residual budget at both locations although the budget remains open at site 17, suggesting that either there is a slightly higher subsidence rate due to earthquake-cycle deformation at this site or there is an error in modelling the deformation associated with ground water extraction. As an example of the latter, we ignored the Earth's porous response to the recharge and withdrawal of groundwater which creates a VLM signal opposite in sign to the surface loading response for a given load change. However, the poroelastic effect is relevant only at GPS stations located on top of the affected aquifer (Argus et al., 2014). Although we tried to avoid using

GPS stations located within these areas, identifying which ones are affected is complex and so it is possible that some are affected by this process. In central California, the predicted vertical deformation results in uplift rates of 0.2-0.3 mm/yr in San Francisco (site 14) and ~0.4 mm/yr in Monterey (site 15), which also result in a decrease in the residual budget in these areas. Although the residual budget was already closed at sites 14-16, the signals associated with the San Andreas Fault System shift the values closer to zero giving confidence that the signal can be comfortably explained at these locations.

4.3.2.1 Cascadia earthquake deformation cycle

As mentioned earlier, non-tectonic processes are not able to explain the residual rates at sites in the central and northern regions (1-13). Accordingly, we now consider the tectonic signal associated with the Cascadia megathrust earthquake cycle, more specifically, the interseismic deformation due to megathrust locking, as a possible alternative origin of these residuals.

Figure 4.5a shows the model-predicted interseismic VLM rates using the parameter set preferred by Li et al. (2018; limiting locking depth of 80 km, smoothness factor of 400, and maximum back-slip rate of 40 mm/yr (full locking)), who inverted horizontal land motion rates using a viscoelastic finite element model. Here the large limiting locking depth (80 km) simply means that this parameter had essentially no influence on the locking distribution resolved by the inversion, which is mostly shallower than 30 km (Li et al., 2018). Due to the large uncertainties in a correction for upper-plate block rotation and a smaller number of GPS stations in northern California, the data constraints on model parameters are not very robust in this area (site 13). For other regions, a comparison between the predicted interseismic VLM rates and the residual rates (Figure 4.5b) indicates that there is good agreement at some of our sites, including central western Vancouver Island (site 3), northern Washington coast (site 6), Puget Sound (site 7), central Oregon coast (sites 11 and 12). This agreement is particularly encouraging as the locking model is based on the inversion of only horizontal rate observations. However, there are clear differences at northern sites: northwestern Vancouver Island (site 1), northwestern and southeastern Georgia Strait in northern Salish Sea (sites 2 and 4), southern Vancouver Island (site 5) as well as in southern Washington coast and northern Oregon (sites 8-10).

a)

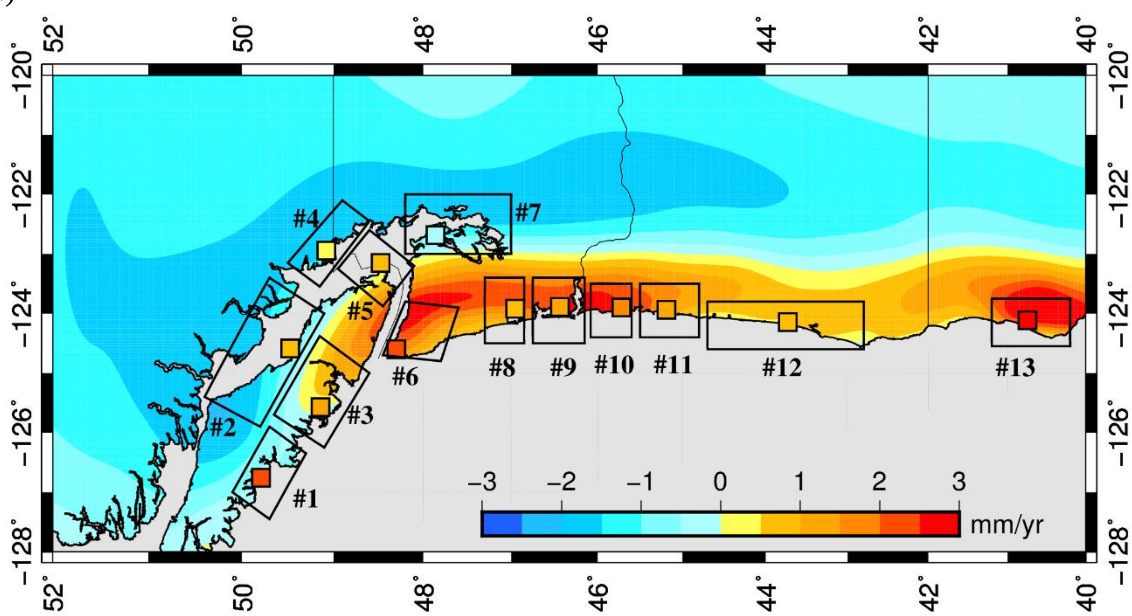

b)

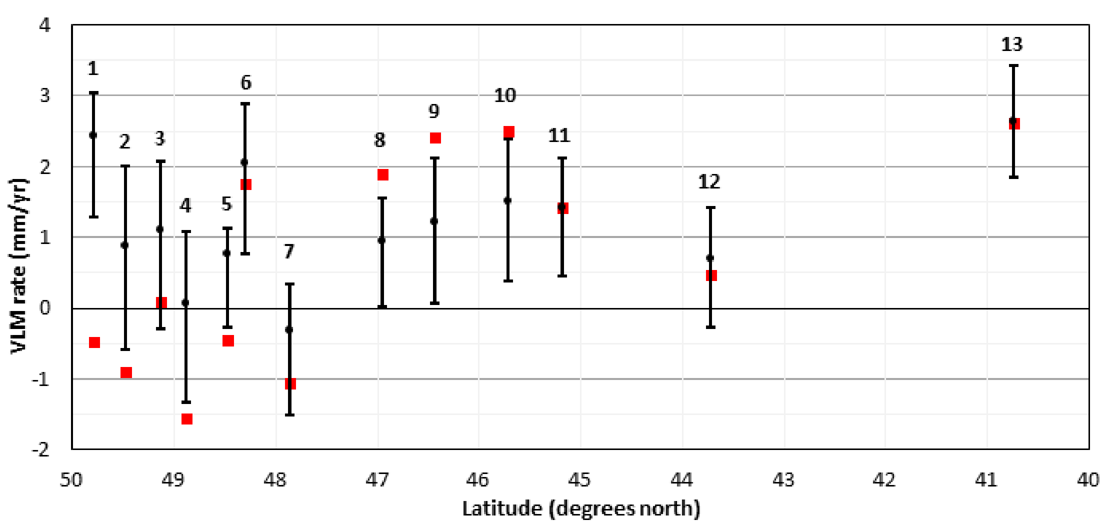

Figure 4.5. (a) Predicted VLM rates from interseismic model using the preferred viscoelastic model with limiting locking depth of 80 km, smoothness factor of 400, and maximum back-slip rate of 40

mm/yr. Colored squares indicate the residual rates (geodetic minus late Holocene rates corrected for 20th century glacier mass loss and ground water change) at sites 1-13 (Figure 4.1). (b) As in (a) but on an x-y profile; the modelled rates are shown as red squares and the corrected residual rates are shown as black circles. Error bars represent 1σ uncertainty. For clarity, the average latitude of site 4 is reduced by 0.2 degrees.

We extend our comparison by exploring six additional model results from Li et al. (2018) to consider whether the residual VLM rates can be used to discriminate between key model parameters (Figure 4.6a-c) and thus provide insight to the potential use of residual VLM rates for future model inversions. Specifically, we considered three different locking states imposed at the trench during inversion (fully locked, partially locked, and creeping; Figure 4.6a), two limiting locking depths (30 km and 80 km; Figure 4.6b), and four smoothness factors (40, 100, 400, 1600; Figure 4.6c). We also calculated the root mean square error (RMSE) for each model parameter set as a measure of misfit between predicted model results and the residual rates (Table 4.1). For the purpose of comparison, Figure S9 shows model fits to GPS estimates of horizontal land motion rates. The horizontal rates shown in this figure are spatial averages (within each site) of rates adopted from Li et al. (2018). The GPS stations considered here are not necessarily the same as those used to estimate the vertical rates. In order to be consistent with the vertical rate data, the horizontal rates were corrected for the effect of GIA signal and this correction made a significant change to the model fits (compare columns 5 & 6 in Table 4.1). GIA-induced horizontal rates were computed using the theory and procedures described in Mitrovica et al. (1994a,b; 2001). The influence of ground water loading and glacier mass changes were also computed but their effect on horizontal rates within our sites is small (<0.1 mm/yr) and so these signals were not removed from the data. The minimum misfit value between our residual rates and the model results is obtained with a limiting locking depth of 30 km, full locking and a smoothness factor of 400. Li et al. (2018) have shown that this model and their preferred model (Figure 4.5a) feature similar locking distributions and fit the horizontal GPS data equally well (Table 4.1 and Figure S9); they used the 80 km limiting locking depth for the preferred model. This relatively large limiting depth is much greater than any geologically reasonable locking depth and estimated extent of seismogenic zone of the young and warm Cascadia subduction zone, in order to emphasize the unimportance of this parameter in a viscoelastic Earth model.

a)

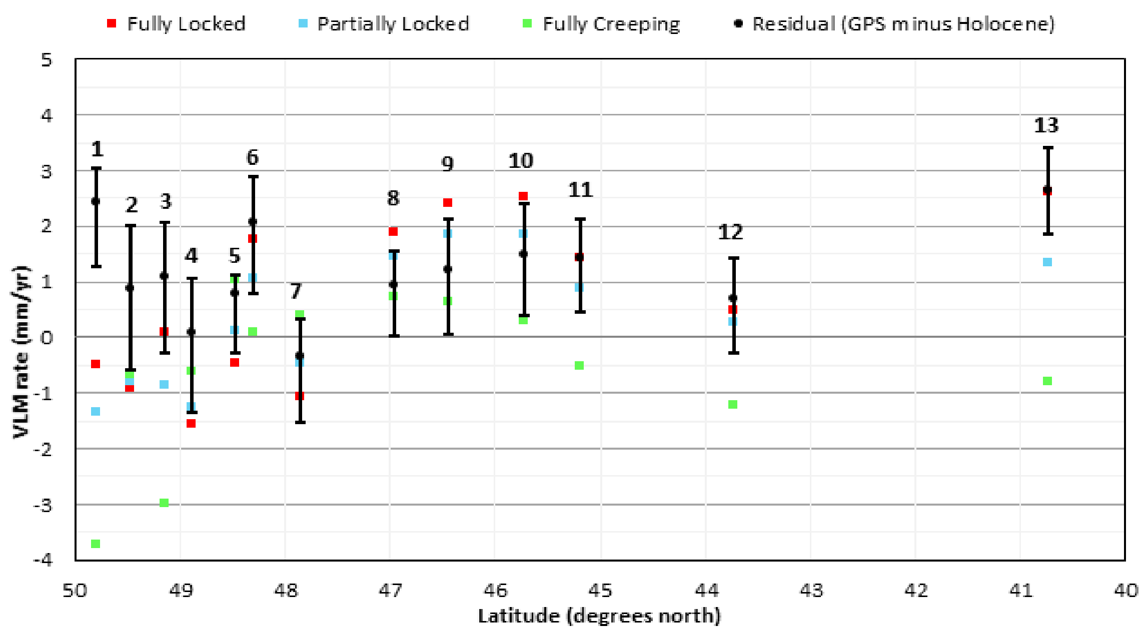

b)

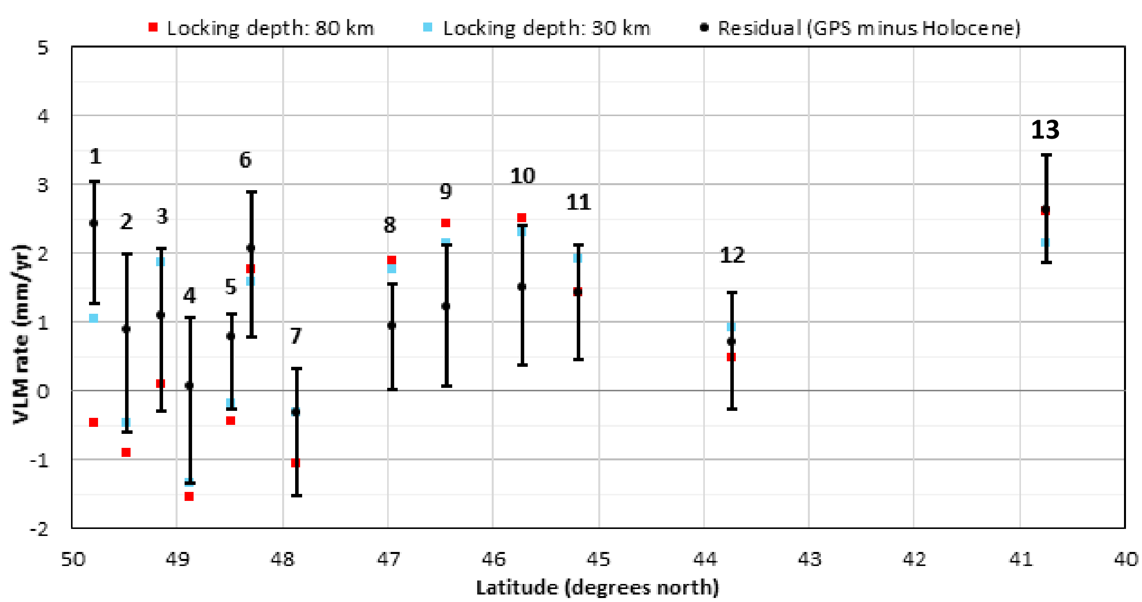

c)

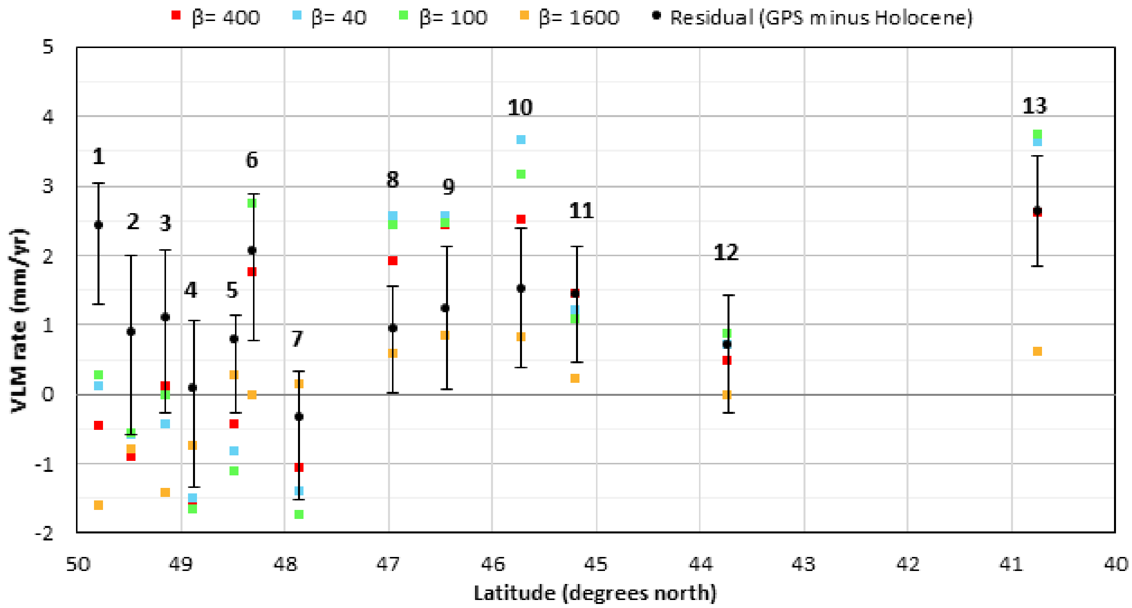

Figure 4.6. Comparison of our residual rates (black circles; as in Figure 4.3b, corrected for 20th century glacier mass loss and ground water change), to interseismic VLM rates estimated from different sets of model parameters (see main text). (a) Results for different fault locking ratios: fully locked (red), partially locked (blue), fully creeping (green); the locking depth and smoothness factor are 80 km and 400, respectively. (b) Results for different limiting locking depths: 30 (blue) and 80 km (red); smoothness factor is set to 400 and the fault is fully locked. (c) Results for different smoothing factors (β): 40 (blue), 100 (green), 400 (red), 1600 (orange); the locking depth and locking state are set to 80 km and fully locked. For clarity, the average latitude of site 4 is reduced by 0.2 degrees.

Table 4.1. Different sets of megathrust interseimic model parameters applied in this study and the corresponding root mean square error (RMSE) value derived from the comparison between model output and the vertical residual rates (4th column) and horizontal rates (5th and 6th columns). The sixth column gives RMSE values for horizontal GPS data that are corrected for the effect of GIA.

State of locking	Limiting Locking Depth (km)	Smoothness Factor	RMSE (mm/yr) Vertical Data (Residual rates)	RMSE (mm/yr) Horizontal Data	RMSE (mm/yr) Horizontal Data Corrected for GIA
Full locking	80	400	1.27	1.06	2.67
Partial Locking	80	400	1.44	1.43	2.81
Full creeping	80	400	2.52	2.04	3.22

Table 4.1. (Continued)					
Full locking	30	400	0.89	1.06	2.66
Full locking	80	40	1.43	0.66	2.53
Full locking	80	100	1.38	0.60	2.63
Full locking	80	1600	1.70	2.25	3.20

The VLM rates show relatively high sensitivity to the near-trench locking state, with differences of about 1-3.5 mm/yr at all sites except northwestern Strait of Georgia (site 2; Figure 4.6a). Li et al. (2018) imposed different locking states by prescribing variable amounts of creep at the shallowest part of the megathrust, in order to test how this boundary condition affects the inversion results. They showed that the land (horizontal) GPS data were unable to resolve near-trench locking state. For example, the full-creeping and full-locking models fitted the horizontal GPS data nearly equally well (see Figure 9 in Li et al., 2018). Their results demonstrate greater resolving power of the horizontal observations further offshore (Figure 7 in Li et al., 2018) and thus the importance of acquiring seafloor geodetic measurements. However, our VLM analysis indicates that, even in the absence of seafloor geodesy, invoking good knowledge of vertical crustal deformation can significantly improve our ability to resolve the near-trench locking state (compare Figure 4.6a to Figure S9a). Comparing the results in Table 4.1, it is evident that for a given limiting locking depth and smoothness factor, the best overall data-model fits are obtained for the fully locked model, followed by the partially locked case, with the highest RMSE values for the full creeping model. The preference for full locking is consistent with the arguments made by Wang & Trehu (2016) based on thermal and seismicity observations. Nonetheless, the difference in the RMSE between the fully and partially locked models is relatively small and so, except for a small number of sites, the data are not able to robustly distinguish between these two cases. This is reflected in

Figure 4.6a which shows that the ability of the observations to discriminate between locking states varies from site to site. The final resolution for the near-trench locking state problem awaits future seafloor geodetic measurements. VLM results for the creeping model lie outside the uncertainty range at most sites which is consistent with the relatively large RMSE values for this model.

As expected, the sensitivity of model fits to the changing limiting locking depth is relatively minor as indicated in Figure 4.6b. In general, the difference is less than 1 mm/yr except for western Vancouver Island (sites 1 and 3), where there is greater sensitivity and a clear preference for shallower fault locking. This general lack of sensitivity is compatible with the results for horizontal land motion (see Figure S9b, and Figures 4a and 5a in Li et al., 2018). We note that this parameter would be important if an elastic Earth model, deemed inappropriate for modelling earthquake-cycle deformation, is used (Li et al., 2018).

We consider the influence of the model smoothness factor only for the case of full locking and an 80 km limiting locking depth. The difference in RSME values for $\beta =$ 40, 100, 400 is small (< 0.1; Table 4.1) reflecting the relatively low sensitivity of the predicted VLM rates to the adopted degree of smoothness (Figure 4.6c). Applying a large smoothing factor of 1600 does impact the model predictions considerably at some sites but the general fit is poorer for this value with a clear jump in the RMSE value (Table 4.1). This is generally consistent with the results inferred from horizontal data that indicate a higher smoothing factor results in a smoother locking pattern but an overall poorer fit to the data and vice versa (see Figure S9c, and Figure 9 in Li et al., 2018). We note that the high β value of 1600 results in more creep at the trench; for this reason there is a good consistency between the sites that prefer high β value and those which prefer creeping or partial locking (compare results in Figure 4.6a & 6c).

4.3.2.2 General discussion and synthesis

In this section we discuss outstanding data-model misfits as well as limitations or omissions in this study that can motivate future work. The results in Figure 4.6 indicate that VLM associated with Cascadia subduction can account for the majority of the observed VLM residuals, particularly when considering plausible variations in model parameters. However, the residual VLM rate at northwestern Vancouver Island (site 1) cannot be reproduced for the parameter values explored here. This can be interpreted as being due to a variety of sources, for example: errors in our estimate of contaminating signals, bias in the observed rates, limitations in the subduction model and the relatively small parameter space considered. The signal due to 20th-century glacier mass loss might be underpredicted since we did not consider mass loss prior to this time interval. If significant mass loss occurred prior to this period, this would reduce the data-model misfit. Also, only a single viscosity model was used in computing this signal. The rapid sea-level fall observed in the northern region can be fit well for a range of asthenospheric thicknesses and low (of the order of 10^{18} or 10^{19} Pa s) viscosities (James et al., 2009), but a uniform good fit through the entire record was not found for a one-dimensional rheological profile (Yousefi et al., 2018), possibly due to: lateral Earth structure in this subduction zone, non-linear or transient rheologies, or other factors. Regarding bias in the observed rates, the linear fits for site 1 appears to be robust (Figure S1) and so this (linear) model is appropriate.

Simplifications in the model formulation of Li et al. (2018) may also be able to account for the discrepancy at site 1. For example, a homogeneous mantle wedge was assumed in the 3D viscoelastic structure and a uniform smoothing factor along the dip and strike directions of the megathrust interface were employed in the inversion scheme. A more realistic model would incorporate the dip and along-strike variations in the input model parameters. Furthermore, only a single set of mantle viscosity is assumed for the entire region (10^{19} Pas for continental mantle and 10^{20} Pas for oceanic mantle). Addressing some of these model limitations and exploring a larger parameter space are future targets for viscoelastic earthquake-cycle modelling.

The residual VLM budget also remains open at site 17. As noted above, this could be explained by a stronger subsidence signal associated with interseismic deformation along the San Andreas Fault System (Smith-Konter et al., 2014) or an error in our estimate of the groundwater extraction VLM signal which is based on a single realisation of the water loading and Earth viscosity structure. As noted above, we also ignored poroelastic deformation associated with this process which will produce a large VLM signal for GPS stations located on top of the aquifer that ground water was extracted from (Argus et al., 2014).

The processes modelled here are able to close the rate residual budget at the majority (15/17) of sites. This does not mean that unmodeled processes are unimportant. In some areas, the contribution of localized crustal faulting to VLM is likely to be important. Of particular interest in this regard are heavily faulted areas such as the Puget Georgia Basin including Puget Sound and Strait of Juan de Fuca (Barrie & Green, 2015; Hyndman et al., 2003). In some areas, volcanic activity will result in a significant time-varying VLM signal (Dzurisin et al., 2008; Houlie´ et al., 2005). None of the data we considered are proximal (order 10 km) to volcanic centres and so this process is unlikely to be a factor in our case.

A key requirement of our analysis is that the differences in the GPS- and RSL-determined rates originate from temporal changes rather than spatial variation due to the RSL and GPS data not being co-located. This issue is discussed in section 4.2.4. By revising our initial site selection, we think any spatial bias incurred due to averaging data within each site has been minimised. More sophisticated methods can be applied in computing spatial variation in the rates. A good example is the Gaussian process modelling applied by Engelhart et al. (2015) to estimate RSL rates during the late Holocene. While this method gives rates that are consistent with ours (Figure

S10), the calculated uncertainties are considerably smaller and so, if accurate, would lead to a residual VLM data set with greater ability to resolve model parameters. Another primary source of uncertainty in the late Holocene rates is the influence of GIA on SSH change (section 4.2.2.1). Better constrained GIA models for this region and more precise estimates of barystatic sea level change for the late Holocene will be beneficial in this regard.

Our results indicate the utility in comparing VLM rates over different timescales to isolate signals associated with different geodynamic processes. There is potential to extend our analysis in this regard by considering RSL changes over 100 kyr timescales and VLM rates determined over decadal timescales in the 20th century from repeated leveling. Sea level indicators dating back to the previous interglacial (~125 kyr BP) have been used to infer VLM rates on 100 kyr timescales in our study area (e.g. Muhs et al., 1990, 1992; Simms et al., 2016). While there is considerable uncertainty in estimating these longer-term rates (Creveling et al., 2015), they can be resolved and compared to those inferred on shorter timescales to provide insight on longer term tectonic processes (Kelsey et al., 1994; Okuno et al., 2014).

Coastal leveling surveys were conducted by the U.S. National Geodetic Survey (NGS) from the 1930s to the 1980s. Here, we briefly consider two datasets which were processed with the same analysis strategy: one from northern Oregon to northern California (Burgette et al., 2009) and one along the Strait of Juan de Fuca across Puget Sound (Krogstad et al., 2016). In these studies, the vertical uplift rates were estimated from differenced leveling lines that are tied to a sea level reference frame. For more details about the processing method of the leveling data please refer to Burgette et al. (2009). Figure S11 shows the rates inferred from these leveling data in comparison to site averages we inferred from RSL and GPS records. The distribution of leveling survey lines used by Burgette et al. (2009) align well with the coastline between ~42-46°N and so all the data are shown without any spatial averaging applied (small green circles). There is an apparent scatter in the leveling data that probably represents leveling routes swinging from the coast to further inland and vice versa. The longer wavelength fluctuations likely show the variability in uplift rate along this segment of the coast. The leveling surveys considered by Krogstad et al. (2016) were aligned more along an E-W orientation and so, for ease of comparison, we only show values that are spatially averaged within the areas defined by sites 6 and 7 (large green circles). The uncertainties in these rates reflect the averaging process.

The leveling data show greater VLM rates than the GPS- and RSL-based estimates. It is not clear if this difference reflects a true geophysical signal or a bias due to the different vertical referencing systems (or a combination of both). A ~1 mm/yr decrease in the leveling rates would make them consistent with the GPS rates, suggesting the difference is mainly due to height referencing. On the other hand, a decrease in uplift rate during the interseimic period is expected from modelling and repeated leveling adjacent to the Nankai subduction zone in Japan (see Figure 7 in Wang & Trehu, 2016). We note that several studies (e.g., Burgette et al., 2009, Schmalzle et al., 2014; Krogstad et al., 2016) have applied leveling data to constrain different model parameters associated with interseismic deformation of the Cascadia subduction zone but the effect of overprinting signals such as GIA was often ignored. The late Holocene VLM rates used in this study emphasizes that the effect of these processes are significant, particularly along the coast of Oregon and California (1.5 -2 mm/yr), and thus should be considered before interpreting the leveling data.

4.4 Conclusions

In this study we determined late Holocene (past 4 kyr) vertical land motion (VLM) rates using relative sea level (RSL) observations from the west coast of North America and compared these to contemporary (decadal-scale) rates inferred from GPS data. By comparing these two independent datasets that relate to different time scales we were able to improve our understanding of the underlying geodynamic processes and their effects on VLM in this region.

The late Holocene VLM rates indicate subsidence across the entire area except for northwestern Strait of Georgia and central western Vancouver Island. A landward tilt is evident in millennial-scale VLM rates of this northern region which could result from either long-term tectonic activity at the Cascadia margin or a GIA signal that is not captured by the current models. The GPS-estimated VLM rates indicate a different pattern of land motion compared to the RSL-estimated rates with uplift at many sites and higher VLM values at the majority of the 17 sites considered. We subtracted the millennial-scale VLM rates from those determined using GPS records to reveal signals that depart from the millennial-scale trend: specifically, those recently activated and short-term or transient signals originating from tectonics. The residual signal is larger than the estimated (1σ) uncertainty and indicates uplift at the majority of sites considered. Using an isostatic surface loading model, we quantified the contributions associated with ground water removal and 20th-century glacier retreat. Groundwater removal and interseismic deformation along the San Andreas Fault System can explain the residual VLM rates in central and southern California, except for San Diego Bay in southern California where a robust subsidence signal is evident. Further work is required to determine the cause of this signal which could be related to poroelastic deformation associated with groundwater extraction.

After removing modelled signals due to glacier mass loss and ground water removal, many of the residuals remain well above zero in central and some northern sites suggesting the presence of a considerable signal associated with megathrust locking along the Cascadia subduction zone. At a number of sites, the residual VLM signal compares well to the uplift rates predicted by a viscoelastic model of interseismic deformation tuned to match horizontal land motion rates (Li et al., 2018). A preliminary data-model comparison was performed to determine whether an improved fit is possible with different model parameter values and to gauge the sensitivity of the residual VLM rates to different parameters (near-trench locking state, limiting locking depth, and smoothness factor). Our results show that there is considerable sensitivity to these parameters, particularly the near-trench locking state and smoothness factor, although it is location dependent. The best-fitting set of parameter values for each site varies considerably. No set of parameter values was able to capture the residual VLM rates in northwestern Vancouver Island. Considering the data-model fit at all locations, preference was found for full locking from the trench down to a relatively shallow depth (< 30 km), although the locking state preference is not strong. This emphasizes the importance of seafloor geodetic measurements in order to better resolve the near-trench locking state. We conclude that the residual VLM data are able to provide useful model constraints and future analyses are warranted that consider both vertical and horizontal rates of land motion and a larger suite of model parameters.

Acknowledgements

We thank the reviewers, Simon Engelhart and David Schmidt, for their constructive feedback. We acknowledge Yoshi Wada for providing a global grid data of groundwater distribution. We thank Makan A. Karegar for input on some of the methods applied in this study. Funding support was provided by the Government of Ontario (via an Ontario Graduate Scholarship), the Natural Sciences and Engineering Research Council and the University of Ottawa. Model results produced in this study (present-day VLM rates due to the ground water removal and 20th-century glacier mass loss) are available through Mendeley Data, V1, doi: 10.17632/cvw8djvtgx.1. This paper is a contribution to the PALSEA working group.

References

Amos, C.B., P. Audet, W.C. Hammond R. Bürgmann, I.A. Johanson, & G. Blewitt, (2014), Uplift and seismicity driven by groundwater depletion in central California, Nature, doi:10.1038/nature13275.

Argus, D., Y. Fu, & F. Landerer, (2014), Seasonal variation in total water storage in California inferred from GPS observations of vertical land motion, Geophys. Res. Lett. 41, 1971–1980.

Atwater, B.F., (1987), Evidence for great Holocene earthquakes along the outer coast of Washington State. Science, 236(4804), 942–944, doi: 10.1126/science.236.4804.942.

Barrie, J.V., & H.G. Greene, (2015), Active faulting in the northern Juan de Fuca Strait implications for Victoria, British Columbia, Geo. Surv. Can., Current Research 2015-6, pp. 10, doi: 10.4095/296564.

Barron, J.A., L. Heusser, T. Herbert, & M. Lyle, (2003), High resolution climatic evolution of coastal Northern California during the past 16,000 years, Paleoceanography, 18, 1020, doi: 10.1029/2002PA000768.

Blewitt, G., C. Kreemer, W.C. Hammond, & J. Gazeaux, (2016), MIDAS robust trend estimator for accurate GPS station velocities without step detection, J. Geophys. Res. Solid Earth, 121, 2054–2068, doi: 10.1002/2015JB012552.

Blewitt, G., W.C. Hammond, & C. Kreemer, (2018), Harnessing the GPS data explosion for interdisciplinary science, Eos, 99, doi: 10.1029/2018EO104623.

Burgette, R.J., R.J. Weldon, & D.A. Schmidt, (2009), Interseismic uplift rates for western Oregon and along-strike variation in locking on the Cascadia subduction zone, J. Geophys. Res. Solid Earth, 114 (B1), 1978-2012, doi: 10.1029/2008JB005679.

Clague, J.J., (1997), Evidence for large earthquakes at the Cascadia subduction zone, Rev. Geophys., 35, 439–460, doi: 10.1029/97RG00222.

Creveling, J.R., J.X., Mitrovica, C.C Hay, J. Austermann, & R.E. Kopp, (2015), Revisiting tectonic corrections applied to Pleistocene sea-level highstands: Quaternary Science Reviews, v. 111, p. 72–80, doi: 10.1016/j .quascirev.2015.01.003.

Dangendorf, S., M. Marcos, G. Wöppelmann, C. P. Conrad, T. Frederikse, & R. Riva, (2017), Reassessment of 20th century global mean sea level rise, Proc. Natl. Acad. Sci. USA, 114, 5946–5951, https://doi.org/10.1073/pnas.1616007114.

DeMets, D.C., R.G. Gordon, & D.F. Argus, (2010), Geologically current plate motions, Geophys. J. Int., 181, 1–80, doi: 10.1111/j.1365-246X.2010.04491.x.

Dragert, H., R.D. Hyndman, G.C. Rogers, & K. Wang, (1994), Current deformation and the width of the seismogenic zone of the northern Cascadia subduction thrust. Journal of Geophysical Research, 99, 654-668, doi: 10.1029/93JB02516.

Dzurisin, D., M. Lisowski, M.P. Poland, D.R. Sherrod, & R.G. LaHusen, (2008). "Constraints and conundrums resulting from ground-deformation measurements made during the 2004–2005 dome-building eruption of Mount St. Helens, Washington," in A Volcano Rekindled; The Renewed Eruption of Mount St. Helens, 2004–2006, Chap. 14, eds D. R. Sherrod, W. E. Scott, and P. H. Stauffer (U.S. Geol. Survey Professional Paper 1750), 281–300.

Dziewonski, A., & D. Anderson, (1981), Preliminary reference earth model, Physics of the Earth and Planetary Interiors, 25, 297-356.

Engelhart, S.E., M. Vacchi, B.P. Horton, A.R. Nelson, & R.E. Kopp, (2015), A sea-level database for the Pacific coast of central North America, Quat. Sci. Rev., 113 (0), 78–92, doi: 10.1016/j.quascirev.2014.12.001.

Farrell, W.E., & J.A. Clark, (1976), On postglacial sea level, Geophys. J. R. astr. Soc., 46, 647–667, doi: 10.1111/j.1365-246X.1976.tb01252.x.

Flück, P., R.D. Hyndman, K. Wang, (1997), 3D dislocation model for great earthquakes of the Cascadia subduction zone. J. Geophys. Res. 102, 20539–20550, doi: 10.1029/97JB01642.

Friele, P. A., & I. Hutchinson, (1993), Holocene sea-level change on the central west coast of Vancouver Island, British Columbia, Can. J. Earth Sci., 30, 832–840.

Hallmann, N., G. Camoin, A. Eisenhauer, A. Botella, G.A. Milne, C. Vella, E. Samankassou, V. Pothin, P. Dussouillez, J. Fleury, & J. Fietzke, (2018), Ice volume and climate changes from a 6000 year sea-level record in French Polynesia. Nature Comm., 9, 285.

Houlie´, N., P. Briole, A. Nercessian, & M. Murakami, (2005), Volcanic plume above Mount St. Helens detected with GPS, Eos Trans. AGU, 86, 277 – 281.

Huss M., & D. Farinotti, (2012), Distributed ice thickness and volume of all glaciers around the globe. Journal of Geophysical Research: Earth Surface, 117(F4):n/a-n/a, 2012. ISSN 2156-2202. doi: 10.1029/2012JF002523.

Hutchinson, I., J.-P. Guilbault, J.J. Clague, & P.T. Bobrowsky, (2000), Tsunamis and tectonic deformation at the northern Cascadia margin: A 3000-year record from Deserted Lake, Vancouver Island, British Columbia, Canada, Holocene, 10, 429–439.

Hyndman, R.D., & K. Wang, (1995), The rupture zone of Cascadia great earthquakes from current deformation and the thermal regime, Journal of Geophysical Research, 100, 22133-22154.

Hyndman, R. D.,S. Mazzotti, D. Weichert, & G.C. Rogers, (2003), Frequency of large crustal earthquakes in Puget Sound – Southern Georgia Strait predicted from geodetic and geological deformation rates, J. Geophys. Res., 108(B1), 2033, doi: 10.1029/2001JB001710.

James, T. S., J.J. Clague, K. Wang, & I. Hutchinson, (2000), Postglacial rebound at the northern Cascadia subduction zone, Quat. Sci. Rev., 19, 1527–1541, doi: 10.1016/S0277-3791(00)00076-7.

James, T.S., I. Hutchinson, J.V. Barrie, K.W. Conway, & D. Mathews, (2005), Relative sea-level change in the northern Strait of Georgia, British Columbia. Geogr. Phys. Quat., 59, 113-127, doi: 10.7202/014750ar.

James, T.S., E.J. Gowan, I. Wada, & K. Wang, (2009), Viscosity of the asthenosphere from glacial isostatic adjustment and subduction dynamics at the northern Cascadia subduction zone, British Columbia, Canada. J. Geophys. Res., 114, doi: 10.1029/2008JB006077.

Katsman CA, W. Hazeleger, S.S. Drijfhout, G.J. van Oldenborgh, G. Burgers (2008), Climate scenarios of sea level rise for the northeast atlantic ocean: a study including the effects of ocean dynamics and gravity changes induced by ice melt. Clim Change 91:351–374.

Kelsey, H. M., D.C. Engebretson, C. E. Mitchell, & R. L. Ticknor, (1994), Topographic form of the Coast Ranges of the Cascadia margin in relation to coastal uplift rates and plate subduction, J. Geophys. Res., 99, 12,245-12,255.

Kendall, R., J.X. Mitrovica, & G.A. Milne, (2005), On post-glacial sea level - ii. Numerical formulation and comparative results on spherically symmetric models, Geophysical Journal International, 161 (3), 679-706.

Kienast S.S., & J.L. McKay, (2001), Sea surface temperatures in the subarctic Northeast Pacific reflect millennial-scale climate oscillations during the last 16 kyrs, Geophys. Res. Lett. 28:1563–1566.

Kopp, R. E., A.C. Kemp, K. Bitterman, B.P. Horton, J.P. Donnelly, W.R. Gehrels, C.C. Hay, J.X. Mitrovica, E.D. Morrow, & S. Rahmstorf, (2016), Temperature-driven global sea-level variability in the common era. Proceedings of the National Academy of Sciences of the United States of Amercia, 113, E1434–E1441, doi: 10.1073/pnas.1517056113.

Krogstad, R.D., D.A. Schmidt, R.J. Weldon, & R.J. Burgette, (2016), Constraints on accumulated strain near the ETS zone along Cascadia, Earth Planet. Sci. Lett., 439, 109–116, doi: 10.1016/j.epsl.2016.01.033.

Lambeck, K., H. Rouby, A. Purcell, Y. Sun, & M. Sambridge, (2014), Sea level and global ice volumes from the Last Glacial Maximum to the Holocene, Proceedings of the National Academy of Sciences, 111.43, pp. 15296–15303, doi: 10.1073/pnas.1411762111.

Leonard, L.J., C.A. Currie, S. Mazzotti, & R.D. Hyndman, (2010), Rupture area and displacement of past Cascadia great earthquakes from coastal coseismic subsidence. Geol. Soc. Am. Bull. 122 (11–12), 2079–2096, doi: 10.1130/B30108.1.

Li, S., K. Wang, Y. Wang, Y. Jiang, & S.E. Dosso, (2018), Geodetically inferred locking state of the Cascadia megathrust based on a viscoelastic Earth model. Journal of Geophysical Research: Solid Earth, 123, 8056–8072, doi: 10.1029/2018JB015620.

Long A.J. & I. Shennan, (1998), Models of rapid relative sea-level change in Washington and Oregon, USA. Holocene, 8:129–142.

Marzeion, B., P.W. Leclercq, J.G. Cogley, & A.H. Jarosch, (2015), Brief Communication: Global reconstructions of glacier mass change during the 20th century are consistent, The Cryosphere, 9(6), 2399–2404, doi:10.5194/tc-9-2399-2015.

McCaffrey, R., Qamar, A. I., King, R. W., Wells, R., Khazaradze, G., Williams, C. A., et al. (2007). Fault locking, block rotation and crustal deformation in the Pacific Northwest. Geophysical Journal International, 169(3), 1315–1340, doi: 10.1111/j.1365-246X.2007.03371.x.

Milne, G.A., & J.X. Mitrovica, (1998), Postglacial sea-level change on a rotating Earth, Geophysical Journal International, 133, 1–19, doi: 10.1046/j.1365-246X.1998.1331455.x.

Milne A.G. (2015), Sea Level, In: Coastal Environments and Global Change, pp. 28-51, doi: 10.1002/9781119117261.ch2.

Mitrovica, J.X., & W.R. Peltier, (1992), A comparison of methods for the inversion of viscoelastic relaxation spectra, Geophysical Journal International 108.

Mitrovica, J.X., J.L. Davis, & I.I. Shapiro, (1994a), A spectral formalism for computing three-dimensional deformations due to surface loads: 1. Theory, J. Geophys. Res., 99, 7057– 7073.

Mitrovica, J.X., J.L. Davis, & I.I. Shapiro, (1994b), A spectral formalism for computing three-dimensional deformations due to surface loads, 2. Present-day glacial isostatic adjustment, J. Geophys. Res., 99, 7075– 7101.

Mitrovica, J.X., A.M. Forte, & M. Simons, (2000), A reappraisal of postglacial decay times from Richmond Gulf and James Bay, Canada, Geophysical Journal International, 142(3), 783–800, doi: 10.1046/j.1365-246x.2000.00199.x.

Mitrovica, J.X., G.A. Milne, & J.L. Davis, (2001), Glacial isostatic adjustment on a rotating Earth, Geophys. J. Int., 147, 562– 579.

Mitrovica, J.X., & G.A. Milne, (2002), On the origin of late Holocene sea-level highstands within equatorial ocean basins, Quaternary Science Reviews, 21(20-22), 2179–2190, doi: 10.1016/S0277-3791(02)00080-X.

Mitrovica, J.X., & G.A. Milne, (2003), On post-glacial sea level: I. general theory, Geophysical Journal International, 154, 253-267.

Mitrovica, J.X., J. Wahr, I. Matsuyama, & A. Paulson, (2005), The rotational stability of an ice-age earth, Geophys. J. Int., 161(2), 491–506, doi: 10.1111/j.1365-246X.2005.02609.x.

Montillet J.P., T.I. Melbourne, & W.M. Szeliga, (2018), GPS vertical land motion corrections to sea-level rise estimates in the Pacific Northwest, J Geophys Res 123(2):1196–1212, doi: 10.1002/2017JC013257.

Muhs, D.R., H.M. Kelsey, G.H. Miller, G.L. Kennedy, J.F. Whelan, & G.W. McInelly, (1990), Age estimates and uplift rates for late Pleistocene marine terraces: Southern Oregon portion of the Cascadia forearc: Journal of Geophysical Research, v. 95, p. 6685–6698, doi: 10.1029/JB095iB05p06685.

Muhs, D.R., T.K., Rockwell, & G.L. Kennedy, (1992), Late Quaternary uplift rates of marine terraces on the Pacific coast of North America, southern Oregon to Baja California Sur: Quaternary International, v. 15– 16, p. 121–133, doi: 10.1016/1040-6182(92)90041-Y.

Muhs, D.R., K.R. Simmons, R.R. Schumann, L.T. Groves, J.X. Mitrovica, & D. Laurel, (2012), Sea-level history during the Last Interglacial complex on San Nicolas Island, California: implications for glacial isostatic adjustment processes, paleozoogeography and tectonics. Quat. Sci. Rev., 37, 1-25, doi: 10.1016/j.quascirev.2012.01.010.

Okuno, J., M. Nakada, M. Ishii, & H. Miura, (2014), Vertical tectonic crustal movements along the Japanese coastlines inferred from late Quaternary and recent relative sea-level changes. Quatern. Sci. Rev., 91, 42–61.

Peltier, W.R., (1974), The impulse response of a Maxwell Earth, Reviews of Geophysics 12.4, pp. 649–669.

Peltier, W.R., (1994), Ice age paleotopography, Science, 265, 195-201.

Peltier, W.R., (2004), Global glacial isostasy and the surface of the ice-age Earth: The ICE-5G (VM2) model and GRACE, Annual Review of Earth and Planetary Sciences, 32, 111-149.

Reynolds, L.C., & A.R. Simms, (2015), Late Quaternary relative sea level in Southern California and Monterey Bay, Quaternary Science Reviews, 126, 57–66, doi:10.1016/j.quascirev.2015.08.003.

RGI Consortium (2015), Randolph Glacier Inventory – A Dataset of Global Glacier Outlines: Version 5.0: Technical Report, Global Land Ice Measurements from Space, Colorado, USA. Digital Media, doi: 10.7265/N5-RGI-50.

Roy, K., & W. Peltier, (2015), Glacial isostatic adjustment, relative sea level history and mantle viscosity: reconciling relative sea level model predictions for the U.S. east coast with geological constraints, Geophys. J. Int., 201(2), 1156–1181, doi:10.1093/gji/ggv066.

Savage, J.C., (1983), A dislocation model of strain accumulation and release at a subduction zone, Journal of Geophysical Research, 88, 4984–4996, doi: 10.1029/JB088iB06p04984.

Schiefer, E., B. Menounos, & R. Wheate, (2007), Recent volume loss of British Columbian glaciers, Canada. Geophys. Res. Lett., 34 (16), L16503, doi: 10.1029/2007GL030780.

Schmalzle, G. M., R. McCaffrey, & K.C. Creager, (2014), Central Cascadia subduction zone creep. Geochemistry, Geophysics, Geosystems, 15, 1515–1532, doi: 10.1002/2013GC005172.

Schmidt, G.A., M. Kelley, L. Nazarenko, R. Ruedy, G.L. Russell, I. Aleinov, et al., (2014), Configuration and assessment of the GISS ModelE2 contributions to the CMIP5 archive. J. Adv. Model. Earth Syst., 6, no. 1, 141-184, doi: 10.1002/2013MS000265.

Severinghaus, J., & T. Atwater, (1990), Cenozoic geometry and thermalstate of the subducting slabs beneath western North America. In: Wernicke, B.P. (Ed.), Basin and Range Extensional Tectonics Nearthe Latitude of Las Vegas, Nevada. Geological Society of AmericaMemoir, vol. 176. Boulder, Colorado.

Shennan I., (1989), Holocene crustal movements and sea-level changes in Great Britain. Journal of Quaternary Science 4: 77–89.

Shennan, I., & B. Horton, (2002), Holocene land- and sea-level changes in Great Britain. Journal of Quaternary Science 17, 511–526.

Simms, A.R., H. Rouby, & K. Lambeck, (2016), Marine terraces and rates of vertical tectonic motion: the importance of glacio-isostatic adjustment along the Pacific coast of central North America, Geological Society of America Bulletin, 128, 81–93, doi: 10.1130/B31299.1.

Smith-Konter, B.R., G.M. Thornton, & D.T. Sandwell, (2014), Vertical crustal displacement due to interseismic deformation along the San Andreas Fault: Constraints from tide gauges, Geophys. Res. Lett., 41, 3793–3801, doi: 10.1002/2014GL060091.

Taylor, K.E., R.J. Stouffer, & G.A. Meehl, (2012), An Overview of CMIP5 and the experiment design, Bull. Amer. Meteor. Soc., 93, 485-498, doi: 10.1175/BAMS-D-11-00094.1.

Wada, Y., L.P.H. van Beek, F.C. Sperna Weiland, B.F. Chao, Y.-H. Wu, & M.F.P. Bierkens, (2012), Past and future contribution of global groundwater depletion to sea-level rise, Geophys. Res. Lett., 39(9), L09,402, doi:10.1029/2012GL051230.

Wallace, R. E., (1990), The San Andreas Fault System, California, U.S. Geol. Surv. Prof. Pap., 1515.

Wang, K., J. He, H. Dragert, & T. James, (2001), Three-dimensional viscoelastic interseismic deformation model for the Cascadia subduction zone, Earth, Planets and Space, 53(4), 295–306, doi: 10.1186/BF03352386.

Wang, K., Wells R., Mazzotti S., Hyndman, R.D., Sagiya T. (2003), A revised dislocation model of interseismic deformation of the Cascadia subduction zone, J. Geophys. Res., 108(B1), 2026, doi: 10.1029/2001JB001227.

Wang, K. (2007), Elastic and viscoelastic models of crustal deformation in subduction earthquake cycles, in The Seismogenic Zone of Subduction Thrust Faults, edited by T. H. Dixon and J. C. Moore, 540– 575, Columbia Univ. Press, New York.

Wang, K., Y. Hu, & J. He, (2012), Deformation cycles of subduction earthquakes in a viscoelastic Earth. Nature, 484 (7394), 327–332, doi: 10.1038/nature11032.

Wang, K., & A.M. Tréhu, (2016), Invited review paper: Some outstanding issues in the study of great megathrust earthquakes—The Cascadia example. Journal of Geodynamics, 98, 1–18, doi: 10.1016/j.jog.2016.03.010.

Wang, P.-L., S.E. Engelhart, K. Wang, A.D. Hawkes, B.P. Horton, A.R. Nelson, & R.C. Witter, (2013), Heterogeneous rupture in the great Cascadia earthquake of 1700 inferred from coastal subsidence estimates, J. Geophys. Res. 118, 1–14, doi: 10.1002/jgrb.50101.

Wu, P., & W.R. Peltier, (1982), Viscous gravitational relaxation, Geophysical Journal of the Royal Astronomical Society 70.

Yousefi, M., G.A. Milne, R. Love, & L. Tarasov, (2018), Glacial isostatic adjustment along the Pacific coast of central North America: Quaternary Science Reviews, v. 193, p. 288–311, 10.1016/j.quascirev.2018.06.017.

Yukimoto, S., Y. Adachi, M. Hosaka, T. Sakami, H. Yoshimura, M. Hirabara, et al., (2012), A new global climate model of the Meteorological Research Institute: MRI-CGCM3-model description and basic performance, J. Meteorol. Soc. Jpn., 90A, 23–64.

Supplementary Figures and Tables of Chapter 4

Contents of this section

Tables S1 to S4 and Figures S1 to S11. This supplemental section contains additional figures to complement discussion and figures presented in the main text.

This supplementary section (S1) details our estimate of the contribution of thermosteric and dynamic changes to sea surface height in our study region as well as figures and tables that complement discussion in the main text. Tables and figures follow section S1.

S1. Ocean steric/dynamic changes

In this section we aim to quantify the contribution of this steric and dynamic component to past millennial-scale SSH change by using output from atmospheric-ocean general circulation models (AOGCMs). We used model output to calculate the correlation between the variability of SSH and sea surface temperature (SST) to examine if ocean temperature variations dominate the SSH variability over the past ~1000 years. The results (below) indicate that this is the case, and so we can use paleo-climate reconstructions of SST to estimate SSH variations during the late Holocene. We have also considered the correlation between SSH and sea surface salinity, but the results are not as conclusive as those for SST, and therefore a possible halosteric signal will not be considered further.

We considered SST and SSH for the past millennia over the study region by using output from two global AOGCMs: GISS-E2-R (Schmidt et al., 2014) and MRI-CGCM3 (Yukimoto et al., 2012). Output from these models is made available through the Coupled Model Intercomparison Project Phase 5 (CMIP5, Taylor et al., 2012). Three output variables were considered from the past millennia ('past1000') experiment that covers the time span between 850 and 1850 CE in monthly resolution: SST, ZOS (represents SSH above geoid), and ZOSGA (global average SSH). SST and ZOS variables vary both spatially and temporally, while, ZOSGA is only a function of time. Since the model runs for ZOS may be affected by model drift (Katsman et al., 2008), the output of the pre-industrial control ('piControl') experiment was used to correct the ZOS variable for this effect. In addition to this, the ZOSGA variable is added to ZOS to account for the global ocean volume changes and ensure the consistency between outputs provided by different modeling groups (Dangendorf et al., 2017). Considering these two corrections, the following equation is applied to estimate the SSH change at a given location and time:

$$\delta SSH^{M}(\theta,\varphi,t) = ZOS^{M}(\theta,\varphi,t) - ZOS^{M}(\theta,\varphi,t_0) + ZOSGA^{M}(t) - ZOSGA^{M}(t_0) - \delta SSH^{M}_{drift}(\theta,\varphi,t) \quad \text{(S1)}$$

Where θ,φ are spherical coordinates, t is the time of interest and t_0 is the initial time (here January 1, 850), and the superscript M corresponds to each AOGCM model. δSSH^{M}_{drift} is the model drift and is calculated as follows:

$$\delta SSH^{M}_{drift}(\theta,\varphi,t) = (D^{picontrol,M}_{ZOS}(\theta,\varphi) + D^{picontrol,M}_{ZOSGA}) \times (t - t_0) \qquad \text{(S2)}$$

Where, $D^{picontrol,M}_{ZOS}$ and $D^{picontrol,M}_{ZOSGA}$ are the rates derived from linear regression analysis of pre-industrial control experiment outputs for each AOGCM model (M).

The SSH changes (δSSH) as well as SST changes (δSST) values with respect to the reference epoch) are then time-averaged over 100 years for each AOGCM model to remove short-term natural variability in the output. Figure S2 (a-d) shows the smoothed δSSH and δSST time series for the two GISS-E2-R and MRI-CGCM3 model runs considered for southern Washington to southern California which covers central and southern sites (8-17). The model grid point nearest to each site was used to generate the results in Figure S2.

The correlation coefficients between the SSH and SST time series for each model are calculated and shown in Table S2. The correlation coefficient values (0.69 – 0.77) for GISS-E2-R model output indicate a strong relationship between the SSH and SST, whereas those for the MRI-CGCM3 (0.39 – 0.64) indicate a weaker relationship. Using the correlation coefficients from the GISS-E2-R model, we obtain the relationship that, on average, a ~0.6 degrees reduction of SST during the past millennia results in a maximum of ~10 cm SL fall.

In order to estimate SSH variations over the past several millennia, we used the alkenone-based proxy SST record from the coast of California (Figure S3, Barron et al., 2003) which indicates an increase from ~10.8 to ~12.0°C around 3.5 ka (ignoring shorter term fluctuations), a decrease to ~11.5oC by ~2 ka and relatively stable temperatures since then (with fluctuations of amplitude ~0.1°C). Thus, assuming an extreme case, maximum rates on millennial scales are of the order 1oC, which, based on the climate model output, corresponds to a SSH change of ~17 cm, or a rate of 0.17 m/ka. Over the late Holocene (past 4 ka), the average SST (and thus SSH) rate is about one tenth of this value. These rate estimates would be lower if we adopted the SST to SSH scaling from the MRI-CGCM3 model output or using data from northeast Pacific which indicates smaller temperature changes over late Holocene as shown on Fig S3 (Kienast & McKay, 2001). We were not able to find other proxy SST records from this region and so, based on the above analysis, we conclude that the combined effect of thermosteric and dynamic processes on SSH change during the late Holocene was negligible in our study region and so is not considered further in this analysis.

Table S1. Optimal model parameters for northern, central and southern regions. See Yousefi et al. (2018) for a description of the methodology used to infer these parameter sets.

Region	Ice Model	Lithosphere Thickness (Km)	Upper Mantle Viscosity ($\times 10^{21}$ Pas)	Lower Mantle Viscosity ($\times 10^{21}$ Pas)
Northern	6885R	46	0.05	1
Central	9858	71	0.2	10
Southern	5962	71	0.5	20

Table S2. Correlation coefficients between sea-surface height variations and sea-surface temperature changes for the two models considered in this analysis.

Region	GISS-E2-R	MRI-CGCM3
Southern Washington	0.69	0.64
Northern Oregon	0.69	0.63
Central Oregon	0.71	0.58
Northern California	0.71	0.39
Central California	0.74	0.41
Southern California	0.77	0.59

Table S3. The contribution of GIA to sea-surface height change averaged over the past 4 ka. The contributions from spatially varying geoid-height change are presented in the second column with the corresponding uncertainty range (1σ). The total contribution including ocean syphoning and barystatic sea-level change are indicated in the third column with the corresponding estimated uncertainty range (1σ).

Site number	Rates of geoid-height changes (mm/yr)	SSH changes due to GIA (mm/yr)
1	-0.03 [-0.06 0.92]	-0.27 [0.15 0.97]
2	-0.02 [-0.05 0.95]	-0.26 [0.15 0.99]
3	-0.04 [-0.06 0.93]	-0.27 [0.15 0.98]
4	-0.02 [-0.05 0.98]	-0.26 [0.15 1.01]
5	-0.03 [-0.06 0.96]	-0.27 [0.15 1.01]
6	-0.04 [-0.07 0.94]	-0.28 [0.15 0.99]
7	-0.04 [-0.06 0.96]	-0.27 [0.15 1.01]
8	0.02 [-0.16 0.75]	-0.21 [0.23 0.74]
9	-0.02 [-0.18 0.70]	-0.25 [0.22 0.73]
10	-0.07 [-0.23 0.64]	-0.30 [0.22 0.72]
11	-0.10 [-0.27 0.60]	-0.34 [0.22 0.72]
12	-0.19 [-0.35 0.49]	-0.43 [0.22 0.69]
13	-0.22 [-0.37 -0.07]	-0.45 [0.21 0.21]
14	-0.28 [-0.43 -0.10]	-0.51 [0.21 0.23]
15	-0.31 [-0.47 -0.12]	-0.54 [0.21 0.24]
16	-0.35 [-0.52 -0.13]	-0.59 [0.22 0.27]
17	-0.37 [-0.54 -0.13]	-0.60 [0.22 0.28]

Table S4. Vertical land motion rate estimates: millennial-scale rates inferred from late Holocene RSL data (1st column); geodetic VLM rates inferred from GPS (2nd column); and the residual between the GPS and geologic VLM rates corrected for 20th century glacier mass loss and ground water change (3rd column). The rates are shown with their corresponding estimated uncertainty range (1σ).

Site number	**Late Holocene VLM rates (mm/yr)**	**GPS VLM Rates (mm/yr)**	**Corrected residual VLM rates (mm/yr)**
1	-0.23 [-0.61 0.80]	2.64 [2.15 3.14]	2.43 [1.28 3.05]
2	0.58 [0.23 1.62]	2.35 [1.30 3.41]	0.89 [-0.59 2.00]
3	0.85 [-0.04 2.16]	2.35 [1.95 2.75]	1.09 [-0.28 2.07]
4	-0.60 [-1.14 0.54]	0.27 [-0.56 1.11]	0.08 [-1.34 1.07]
5	-0.85 [-1.03 0.16]	0.27 [-0.03 0.58]	0.78 [-0.28 1.13]
6	-0.36 [-0.91 0.77]	2.01 [1.40 2.62]	2.06 [0.78 2.88]
7	-0.91 [-1.43 0.22]	-0.89 [-1.28 -0.50]	-0.32 [-1.52 0.33]
8	-0.79 [-1.26 0.05]	0.30 [-0.10 0.71]	0.95 [0.01 1.56]
9	-0.74 [-1.53 0.31]	0.54 [0.10 0.99]	1.22 [0.07 2.12]
10	-1.37 [-2.01 -0.42]	0.17 [-0.44 0.78]	1.50 [0.38 2.39]
11	-1.48 [-2.08 -0.58]	-0.05 [-0.40 0.31]	1.43 [0.46 2.12]
12	-1.48 [-2.08 -0.59]	-0.71 [-1.12 -0.30]	0.70 [-0.28 1.42]
13	-1.93 [-2.56 -1.31]	0.84 [0.37 1.32]	2.64 [1.85 3.42]
14	-1.96 [-2.85 -1.06]	-0.63 [-0.76 -0.49]	0.86 [-0.05 1.76]
15	-1.21 [-1.94 -0.47]	-0.06 [-0.28 0.17]	0.57 [-0.20 1.34]
16	-1.15 [-2.23 -0.07]	-0.07 [-0.32 0.18]	0.19 [-0.92 1.29]
17	-0.76 [-1.43 -0.07]	-0.07 [-0.32 0.18]	-1.01 [-1.73 -0.31]

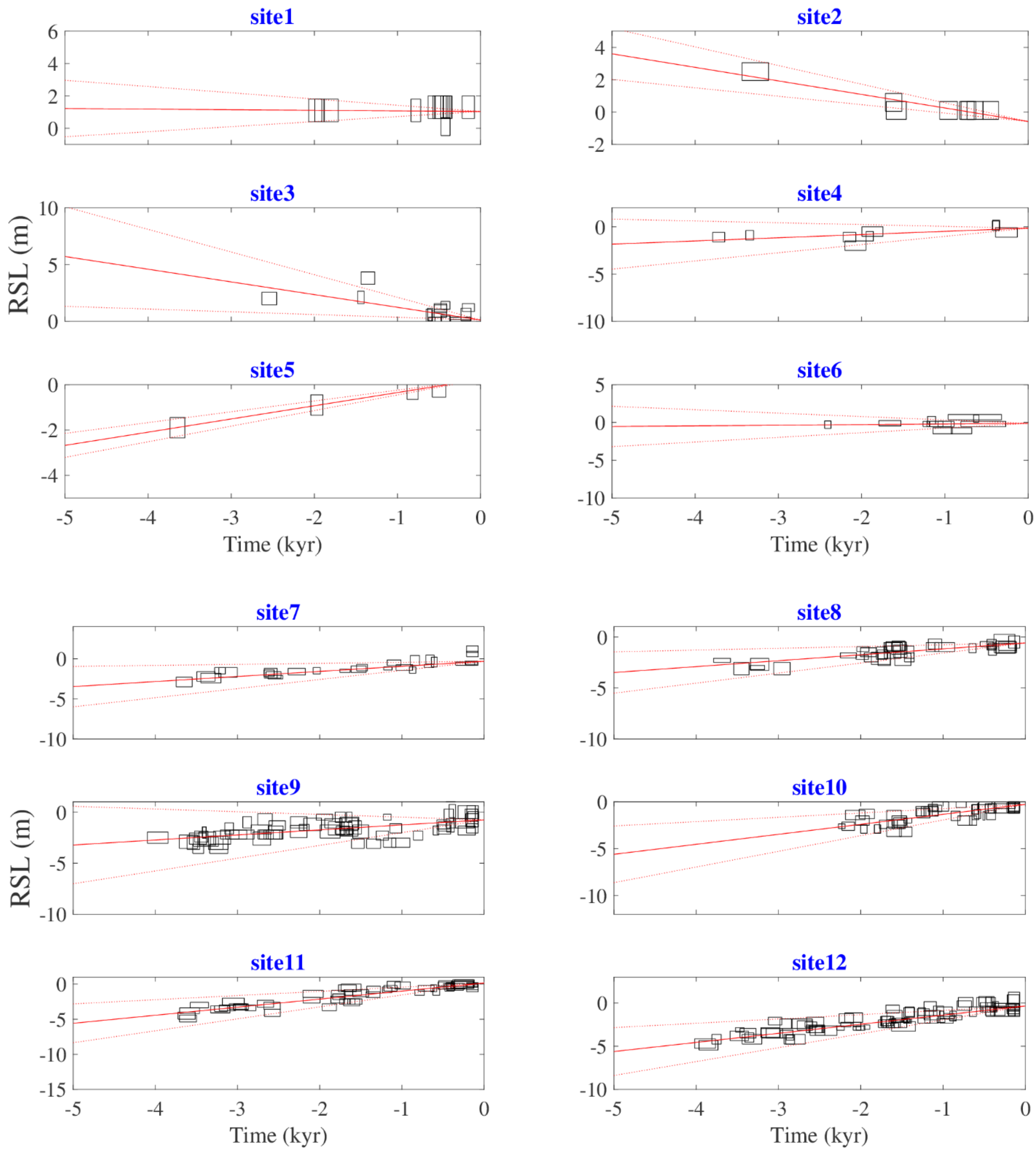

Figure S1. Linear regression was used to estimate an average millennial-scale rate of Late Holocene sea-level change at each individual site (red line). The dashed red lines indicate 1σ uncertainty bound for the estimated sea-level change rate at each site. The height and width of the index point boxes define 1σ uncertainty ranges.

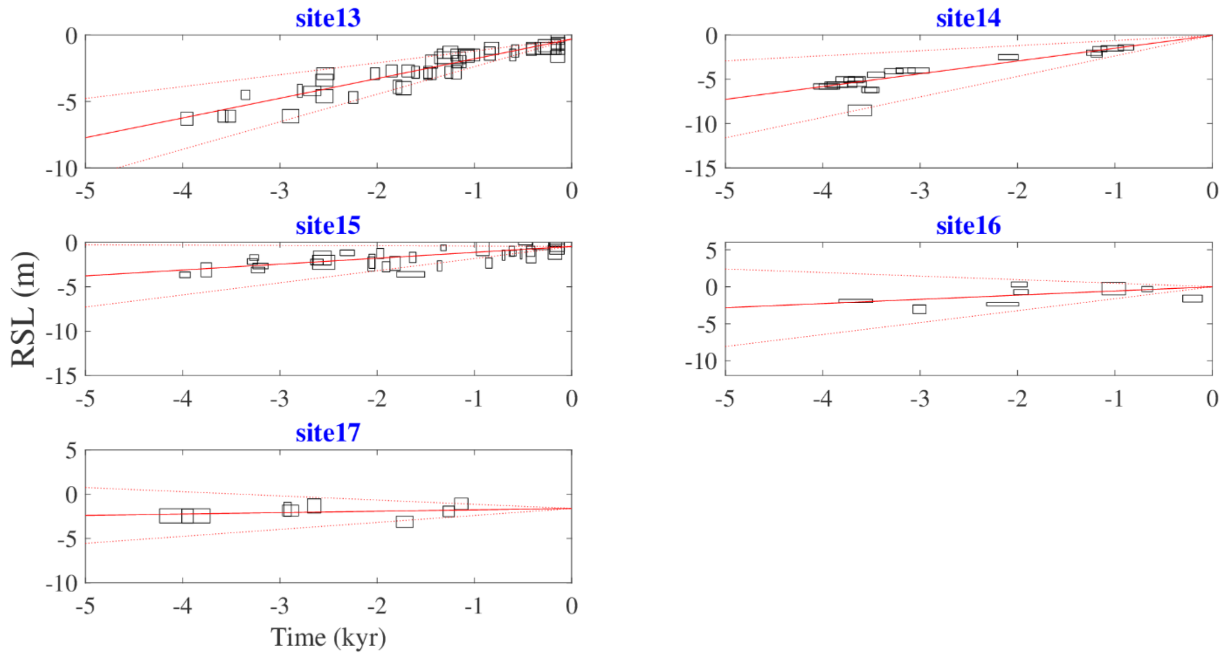

Figure S1. Continued.

a)

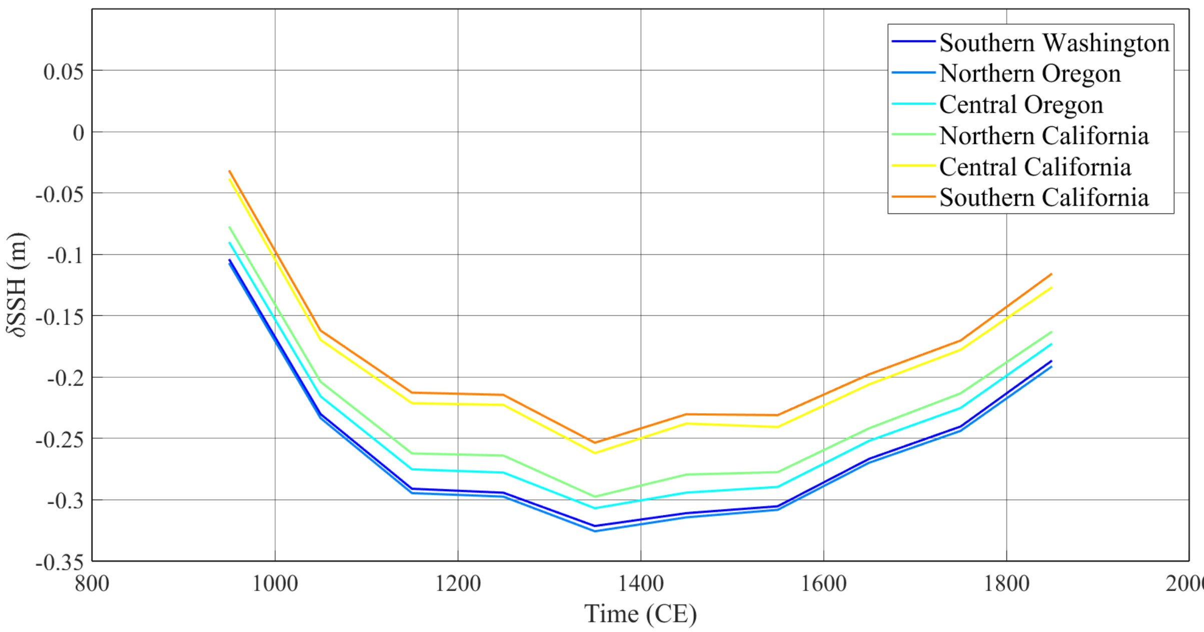
Southern Washington
Northern Oregon
Central Oregon
Northern California
Central California
Southern California
0.05
0
-0.05
-0.1
-0.15
-0.2
-0.25
-0.3
-0.35
δSSH (m)
800
1000
1200
1400
1600
1800
2000
Time (CE)

b)

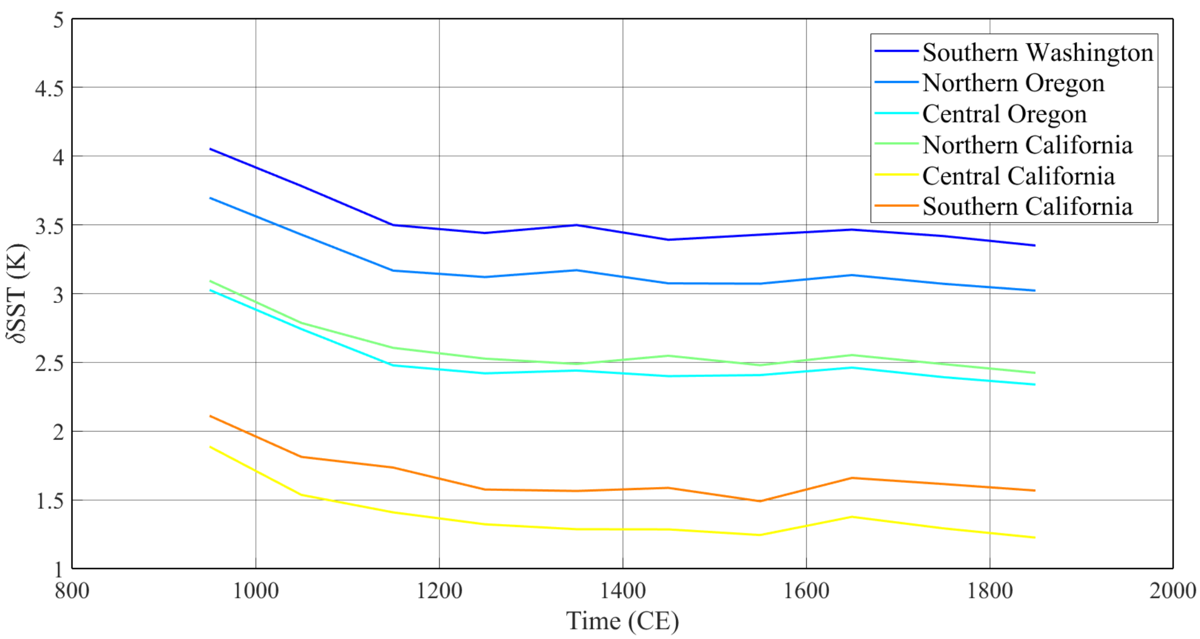
Southern Washington
Northern Oregon
Central Oregon
Northern California
Central California
Southern California
5
4.5
4
3.5
3
2.5
2
1.5
1
δSST (K)
800
1000
1200
1400
1600
1800
2000
Time (CE)

c)

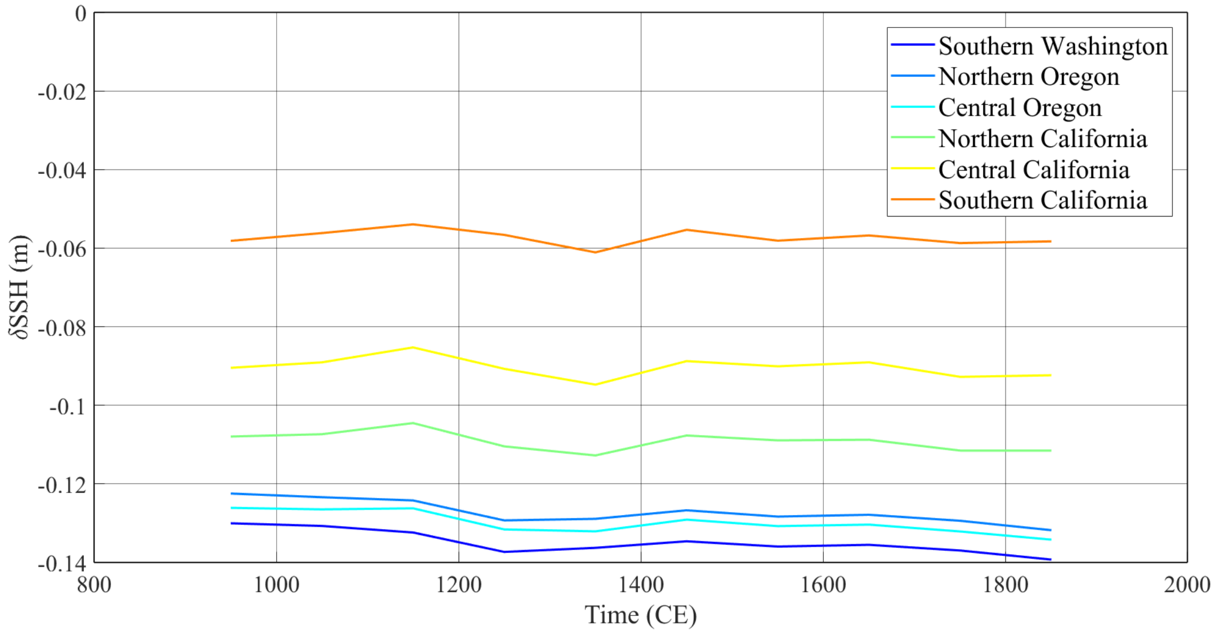

d)

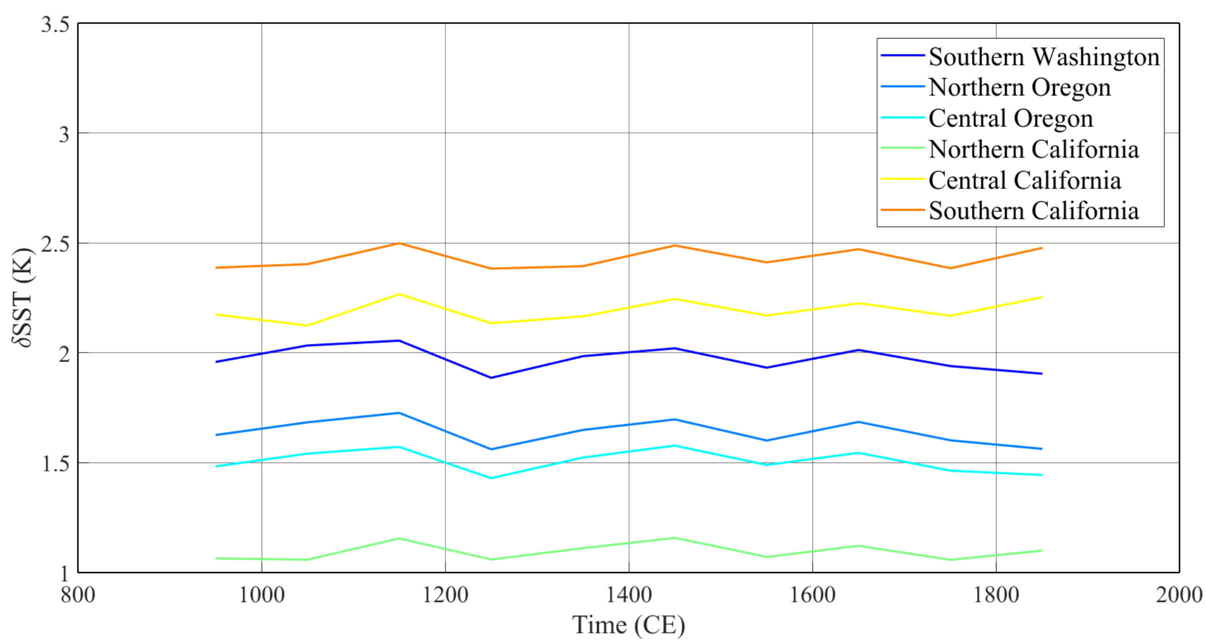

Figure S2. (a) Sea-surface height (SSH) variations derived from the GISS-E2-R model, (b) the variability of sea-surface temperature (SST) from the GISS-E2-R model, (c) and (d) are the same as (a) and (b) but for the MRI-CGCM3 model.

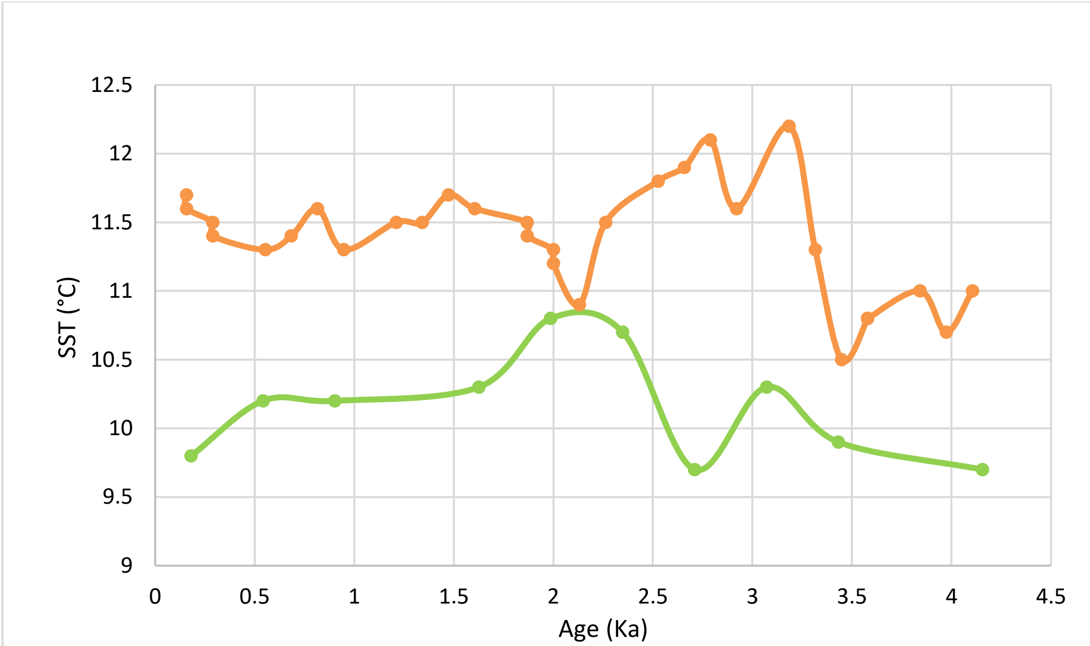

Figure S3. An alkenone-based sea surface temperature reconstruction for the past 5 thousand years. Data from northeast Pacific is shown as green line (Kienast & McKay, 2001) and data from northern California is shown as orange line (Barron et al., 2003).

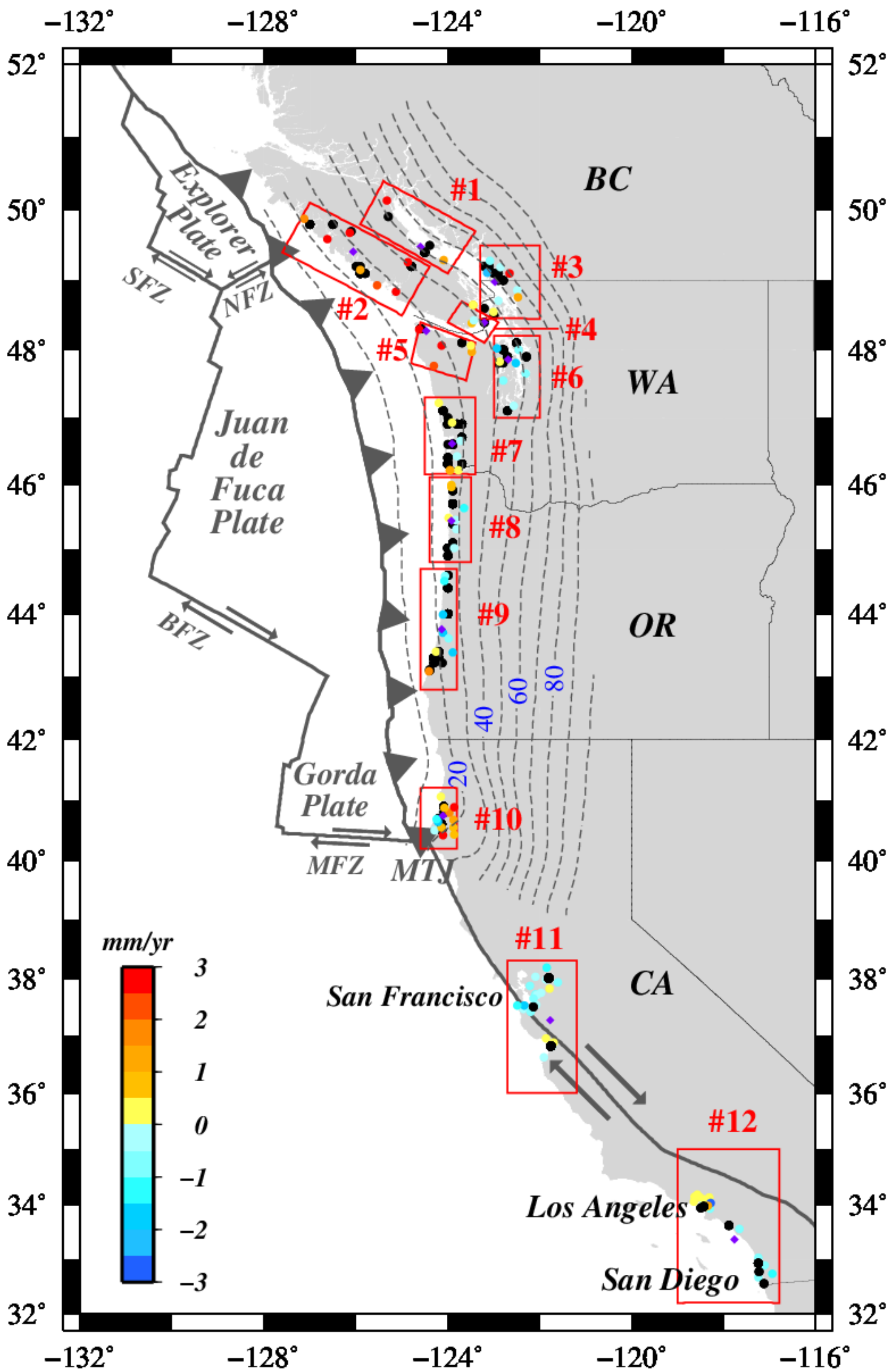

Figure S4. Map showing the spatial distribution of RSL data as well as GPS stations corresponding to the first categorizing of the dataset. All symbols are the same as Figure 4.1.

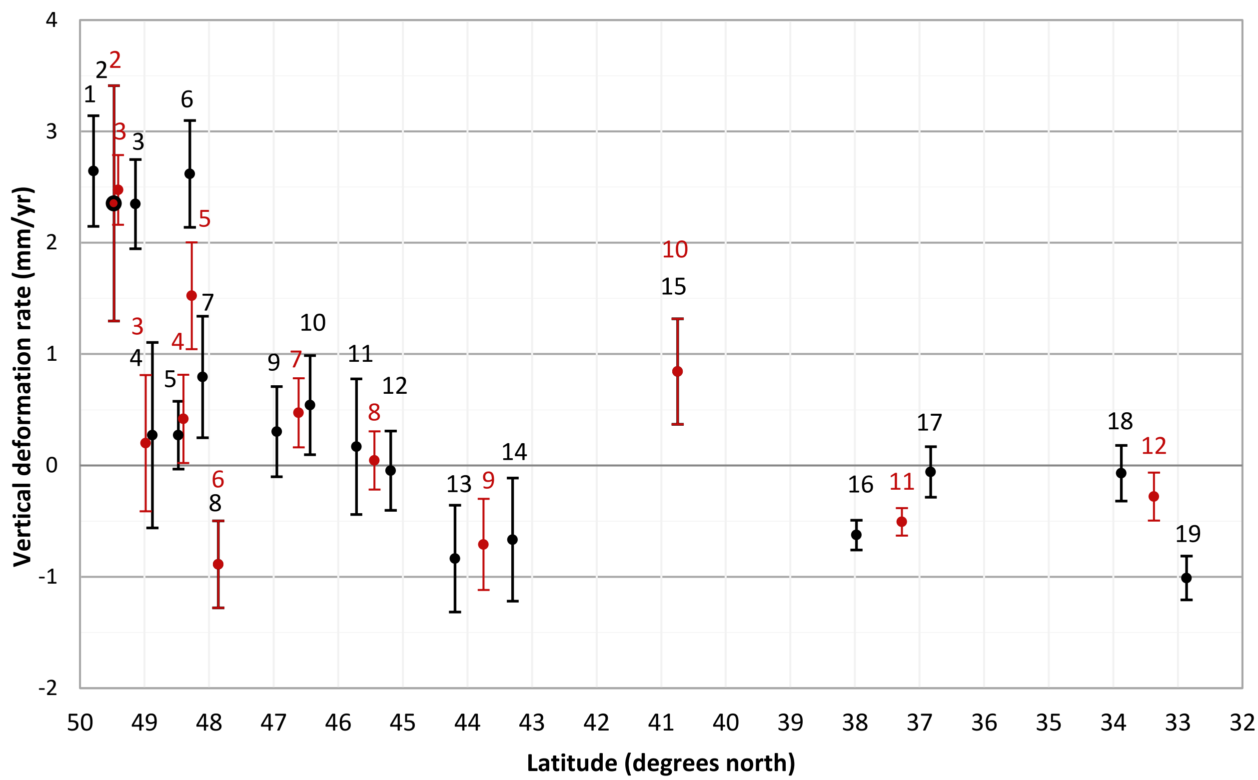

Figure S5. GPS VLM rates associated with two different site selections: 12 sites (red symbols) and 19 sites (black symbols) as shown on Figures S4 and S7, respectively. The uncertainty ranges are plotted at the 1-σ level.

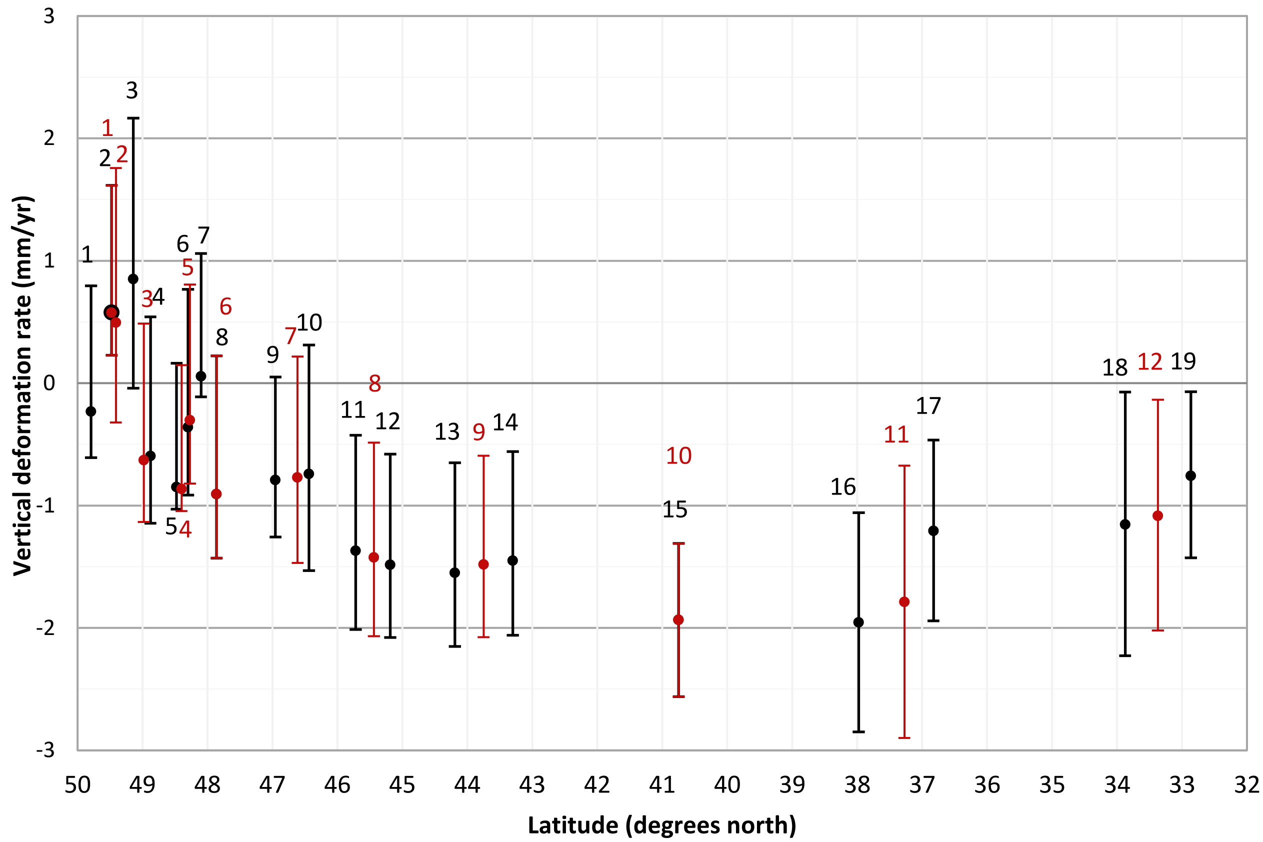

Figure S6. Late Holocene VLM rates associated with two different site selections: 12 sites (red symbols) and 19 sites (black symbols) as shown on Figures S4 and S7, respectively. The uncertainty ranges are plotted at the 1-σ level.

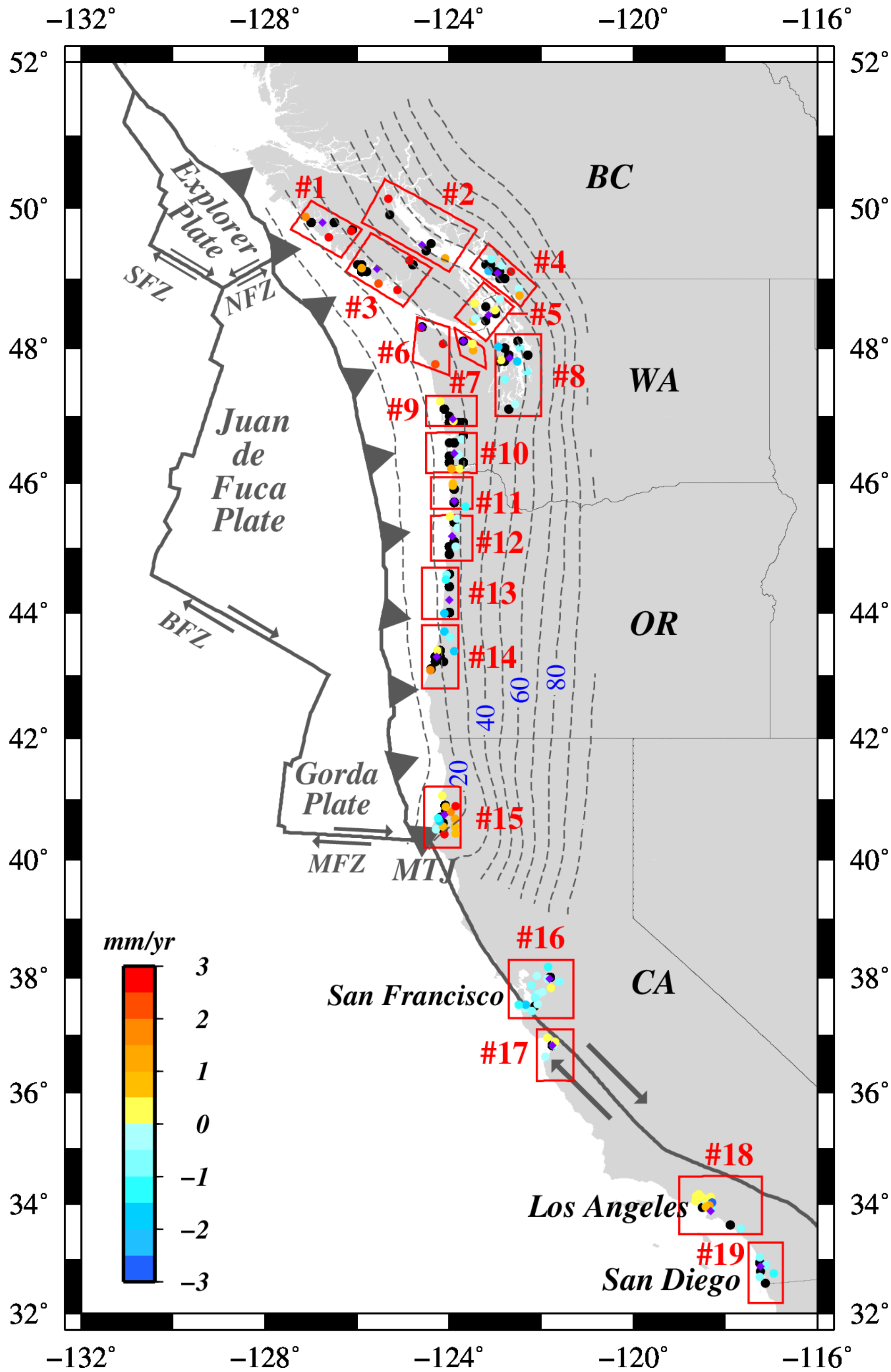

Figure S7. Map showing the spatial distribution of RSL data as well as GPS stations corresponding to the second attempt for subdividing the dataset. All symbols are the same as Figure 4.1.

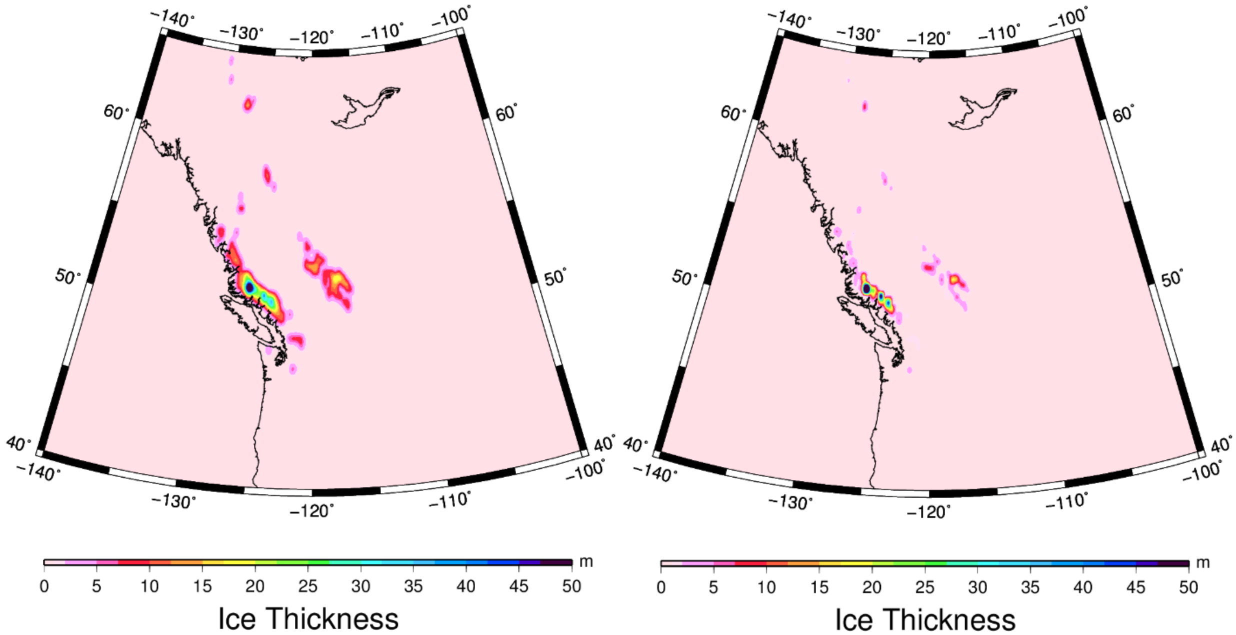

Figure S8. Modelled thickness and extent of the Western Canada and US glaciers before (left panel) and after (right panel) the estimated mass loss.

a)

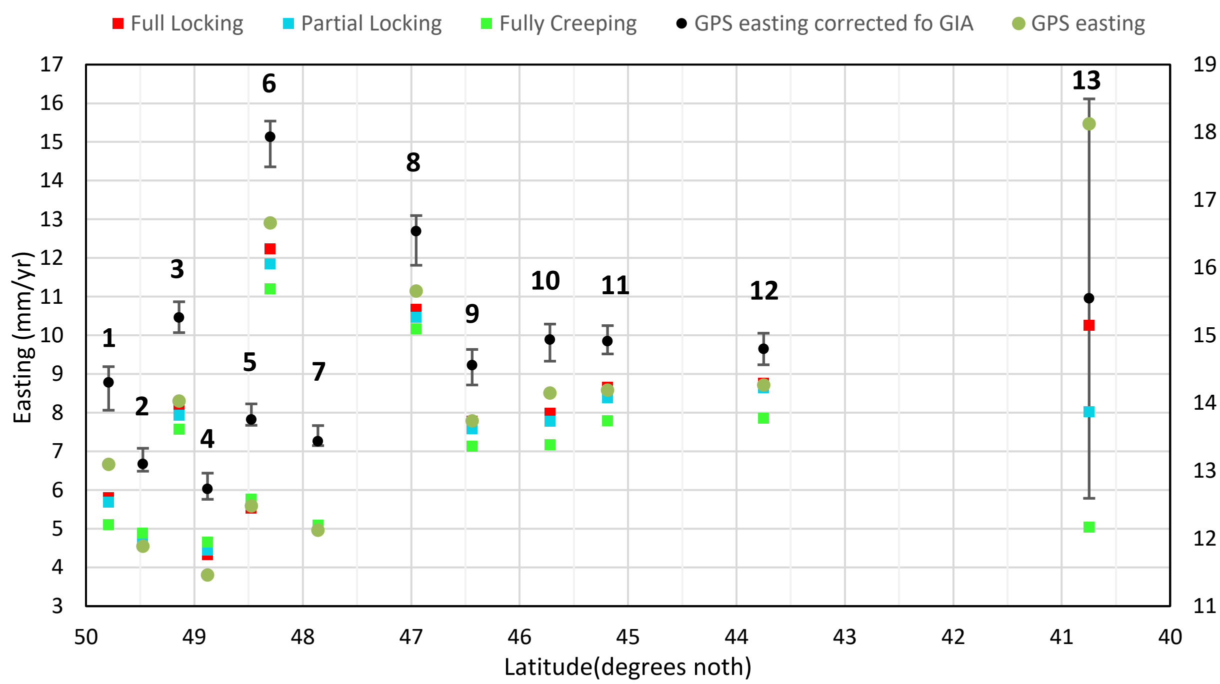

Full Locking
Partial Locking
Fully Creeping
GPS easting corrected fo GIA
GPS easting
Easting (mm/yr)
Latitude(degrees noth)
1
2
3
4
5
6
7
8
9
10
11
12
13

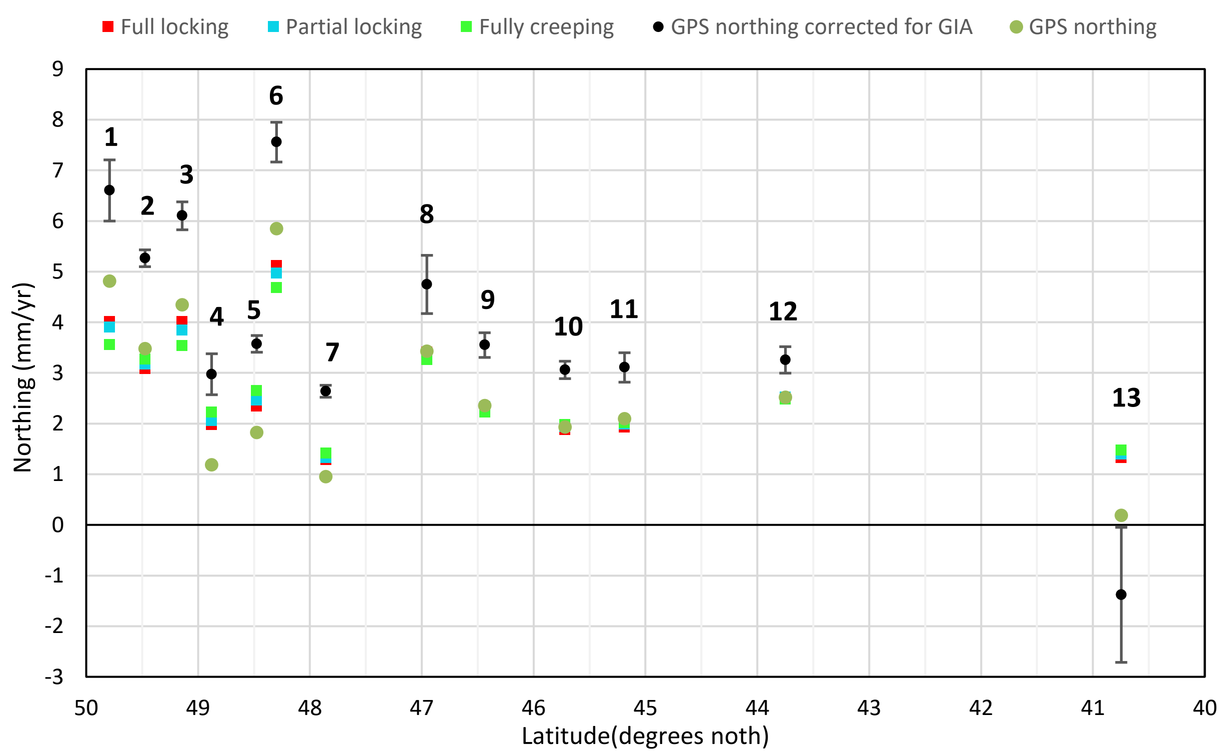

Full locking
Partial locking
Fully creeping
GPS northing corrected for GIA
GPS northing
Northing (mm/yr)
Latitude(degrees noth)
1
2
3
4
5
6
7
8
9
10
11
12
13

b)

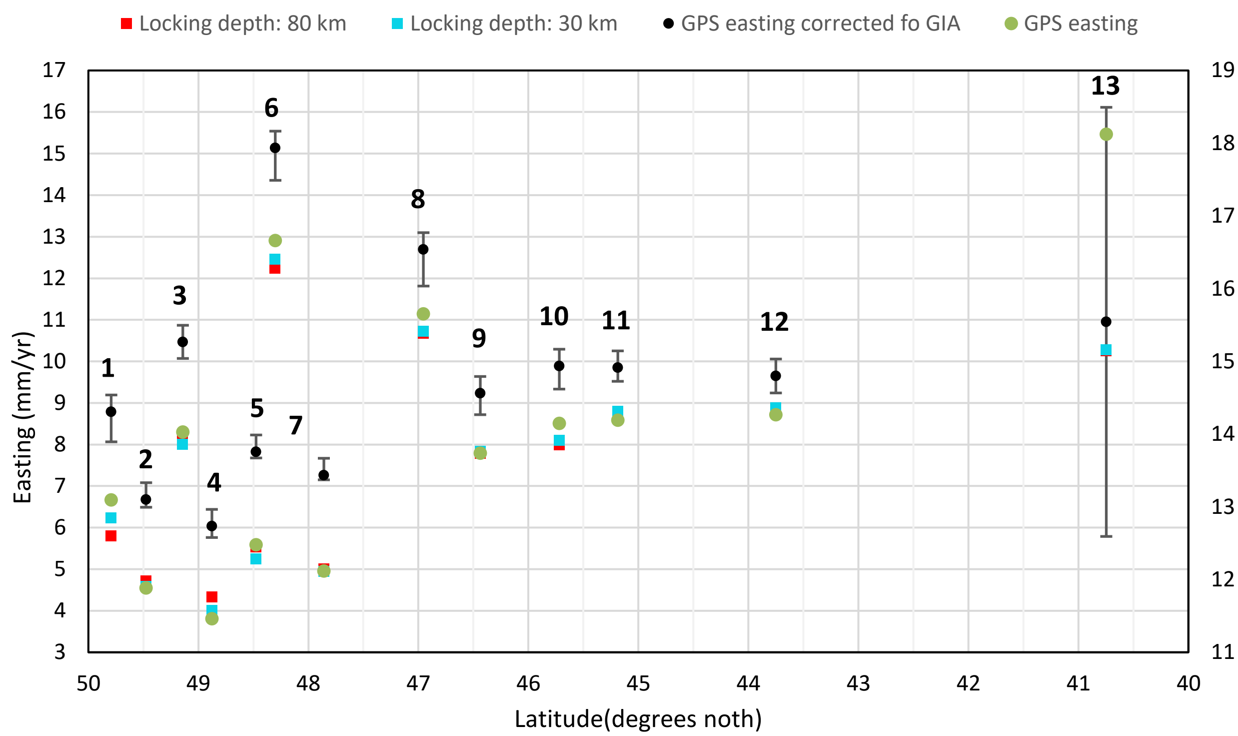
Locking depth: 80 km
Locking depth: 30 km
GPS easting corrected fo GIA
GPS easting
Easting (mm/yr)
Latitude(degrees noth)
17
16
15
14
13
12
11
10
9
8
7
6
5
4
3
19
18
17
16
15
14
13
12
11
50
49
48
47
46
45
44
43
42
41
40
1
2
3
4
5
6
7
8
9
10
11
12
13

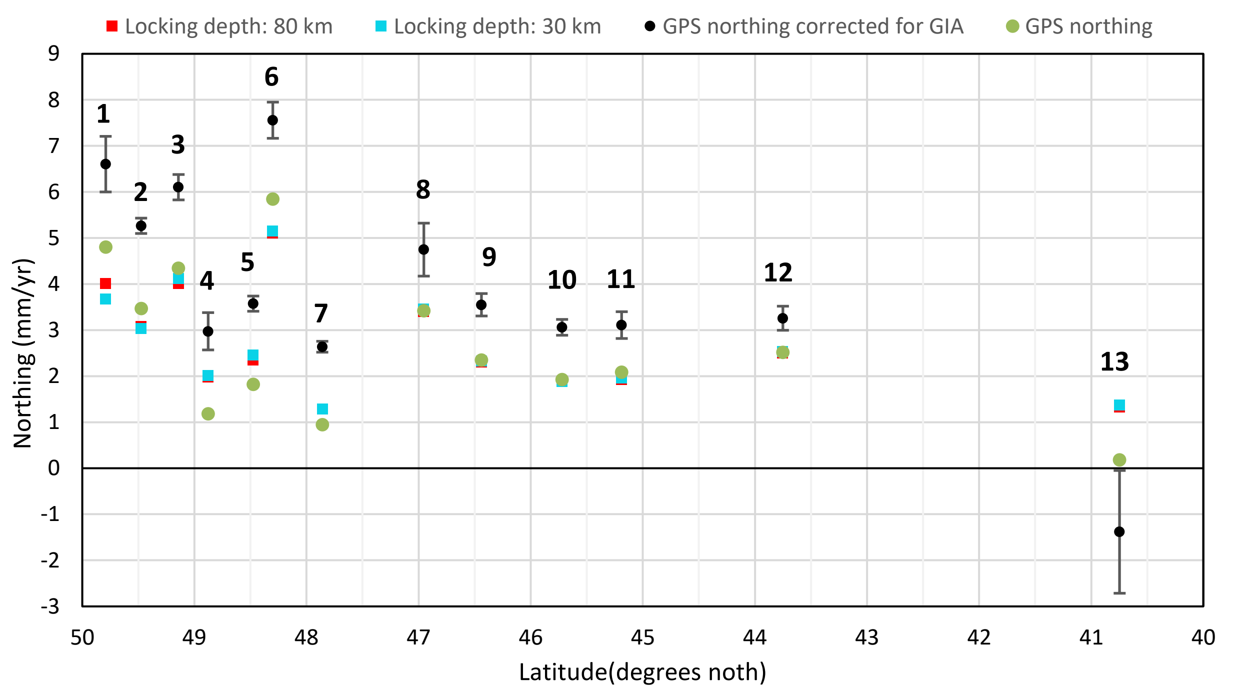
Locking depth: 80 km
Locking depth: 30 km
GPS northing corrected for GIA
GPS northing
Northing (mm/yr)
Latitude(degrees noth)
9
8
7
6
5
4
3
2
1
0
-1
-2
-3
50
49
48
47
46
45
44
43
42
41
40
1
2
3
4
5
6
7
8
9
10
11
12
13

c)

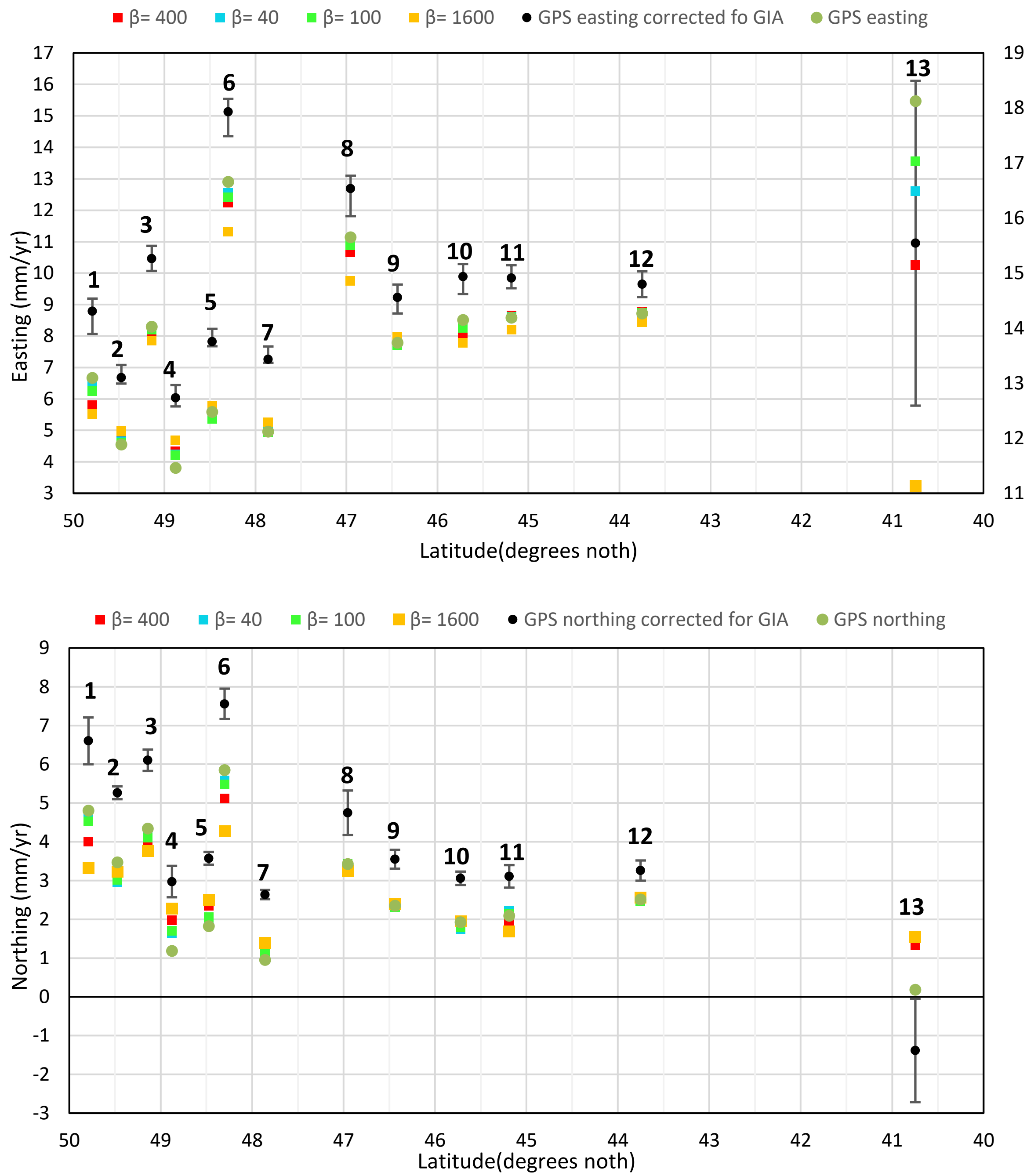

Figure S9. Comparison of horizontal GPS rates (easting and northing components, black circles, corrected for GIA), to interseismic rates estimated from different sets of model parameters (all symbols are the same as Figure 4.6: i.e. panels a, b, and c are corresponding to different fault locking parameters used in panels a, b, and c in Figure 4.6). The horizontal rates that are not corrected for GIA are shown as grey circles. The uncertainty associated with the GIA correction was not estimated. For better visualization, the easting values associated with site 13 are shown using the right vertical axis and those related to the rest of the sites are shown using the left vertical axis.

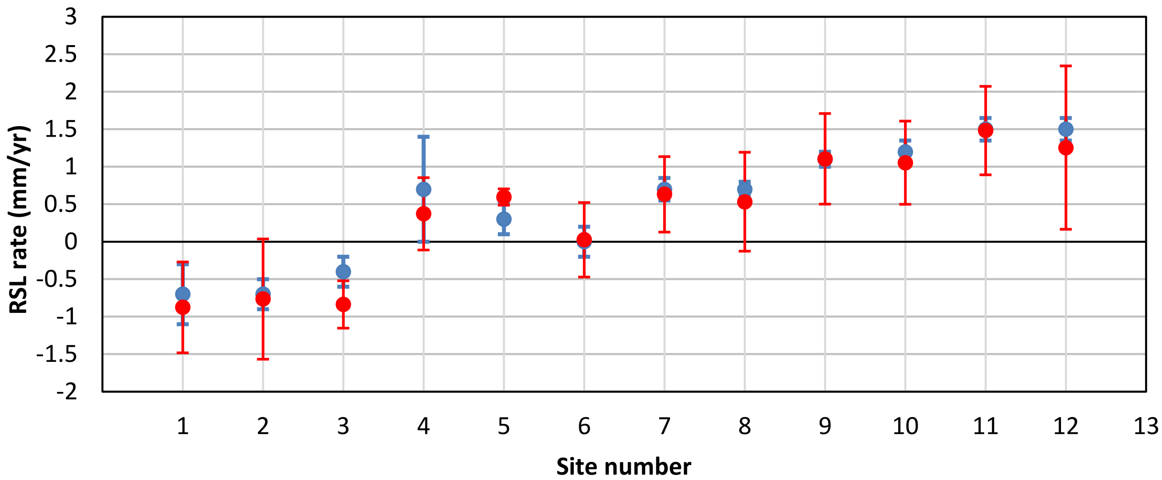

Figure S10. Late Holocene RSL rates from Engelhart et al., 2015 (blue circles) and this study (red circles). The site numbers used as x-axis in this plot are adopted from Figure 1 in Engelhart et al. (2015). Error bars represent 1σ uncertainty.

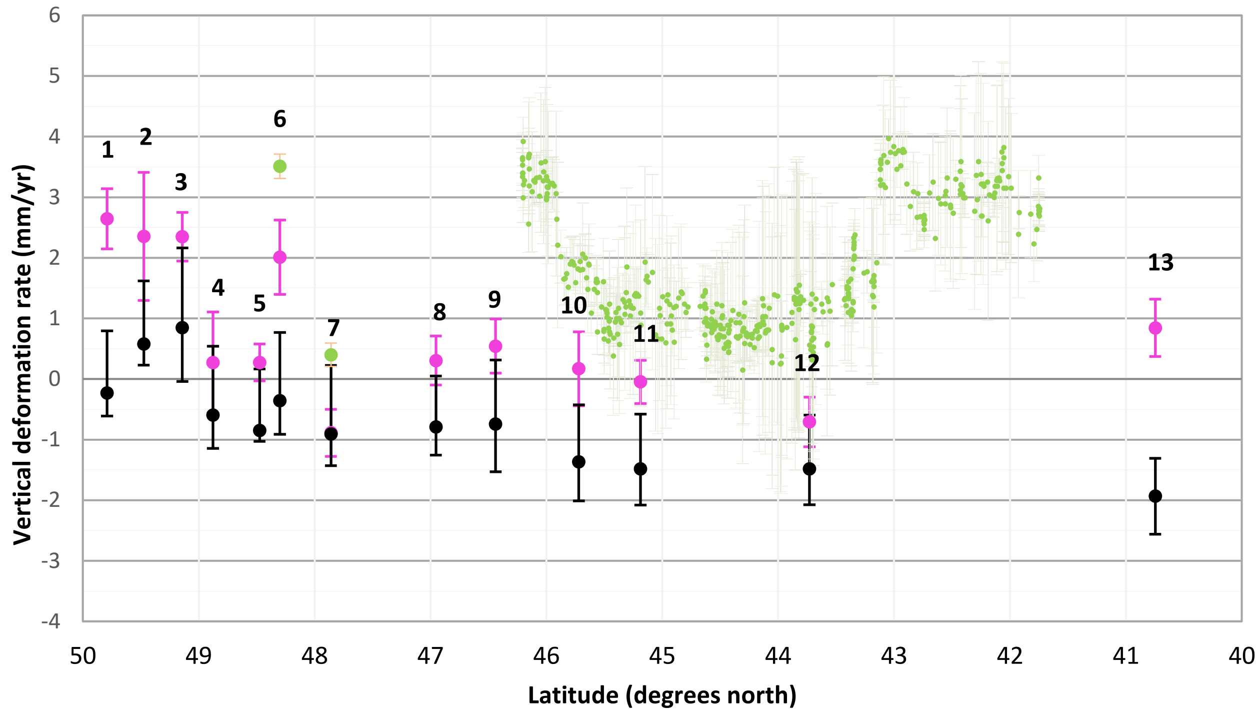

Figure S11. Geodetic VLM rates inferred from GPS (magenta circles) and leveling (green circles) data and geologic VLM rates inferred from RSL data (black circles). The GPS rates are computed using the NA12 reference frame and the leveling rates are referenced to mean sea level at six permanent tide gauge stations (Crescent City, Port Orford, Charleston, South Beach, Garibaldi, and Astoria). All symbols are the same as in Figure 4.2. For more details and discussion about the discrepancy between the two geodetic VLM rates, we refer the reader to section 4.3.2.2.

5

Synthesis and Future Research

During my PhD thesis I have accomplished three research projects, aimed at better understanding active geodynamic processes along the Pacific coast of North America. The methodology and results associated with each research project are detailed in this thesis, Chapters 2, 3, and 4. In this chapter, I summarise some key findings of each chapter within a broader context and discuss the implications for possible future work.

Among the various geodynamic processes operating on different time scales along the west coast of North America, GIA is known to be important on millennial timescales. Quantifying this importance requires estimating two key aspects or model inputs: the Earth viscosity structure and history of past ice loading. In Chapter 2, we constrained the GIA signal (and its associated uncertainty) using Late Glacial/Holocene RSL observations. In this study, we explored a large parameter space of 29 ice sheet reconstructions and more than 700 spherically symmetric (1D) Earth models which enabled more accurate estimates of model parameter uncertainty to be determined. The “noise” introduced by other processes at play, such as tectonics, is an obstacle that complicates the parameter estimation procedure and has deterred GIA modellers from considering this tectonically active region (hence the relative lack of past publications). Given that the observations used to constrain the GIA model parameters have been affected by the tectonic activity of the Cascadia subduction zone, we took a careful approach in order to confirm that our parameter estimates are robust. This approach can be applied in other areas using recently compiled/published RSL observations that are also likely to be contaminated by tectonic processes, such as the Japanese Islands (e.g., Okuno et al., 2014), Caribbean region (e.g., Khan et al., 2017) and Alaska (e.g., Garrett et al., 2015).

The results obtained from our 1D GIA modelling analysis indicate that none of the considered model parameter sets could satisfy the entire RSL data set simultaneously and so the observations were partitioned into three regions to reflect different tectonic settings and proximity to the Cordilleran ice sheet. The need for this partitioning suggests that there are significant lateral variations in viscosity structure from north to south with relatively low viscosity values in the northern region increasing towards higher values in the central and southern areas. The difficulty to fit all data well also reflects changes in viscosity-depth sensitivity of the data with northern sites showing greater sensitivity to relatively shallow upper mantle structure while central and southern regions exhibit greater sensitivity to deeper and more laterally extensive structure (particularly in the direction of the Laurentide ice sheet).

The data-model misfits are largest in northern parts of the study area which were ice covered for several thousands of years beneath the southwestern margin of the Cordilleran ice sheet. Our inferred value of upper mantle viscosity in the north is generally compatible with previous study in this region (e.g., James et al., 2009). The low value obtained is generally consistent (i.e. 2-3 orders of magnitude lower than global mean values) with results obtained in other tectonically active regions such as

Alaska (Hu and Freymueller, 2019), West Antarctica (van der Wal et al., 2015), Antarctic Peninsula (Nield et al., 2014), and Patagonia (Lange et al., 2014). We also performed a sensitivity analysis to examine the influence of a low-viscosity asthenosphere layer (as suggested by James et al., 2009) on RSL model outputs. Our model results did not show a significant improvement in fitting the data compared to models without such a layer. Therefore, the data-model misfits can most likely be attributed to limitations in our ice loading histories and/or other aspects of the Earth model.

One limitation of our Earth model is the assumption of a linear Maxwell rheology throughout the whole mantle. Several studies have suggested non-linear behaviour in some parts of the mantle that varies radially, laterally, and temporally. It has been suggested that the high stress levels induced during and immediately after deglaciation can cause deformation that is accommodated by non-linear (power-law) rheology and low effective viscosities (e.g., Ranalli, 2001; Wu and Wang, 2008; James et al., 2009). During intervals of lower stress, towards the end of the deglaciation, a linear behaviour and higher effective viscosity values are expected. The inclusion of nonlinear rheology into GIA modelling has been considered in a small number of studies that have modelled data in other regions (e.g., Van der Val et al., 2010) and there is evidence of improved fits to the data when non-linear deformation is permitted. However, it is still an open area of investigation and a similar approach can be put into effect in future for our study area to examine the sensitivity of the model results to an Earth model with four-dimensional (effective) viscosity.

Another factor that plays an important role in governing the quality of data-model agreement is the regional ice loading history. As shown in Chapter 2, sensitivity of our results to this model input is particularly high in northern parts of the study area due to proximity to the ice sheet margin. Our results suggest that a 500-1000 year delay in our reconstructed deglaciation history is favoured by the data in this area.

Considering the relatively large uncertainty in the ice margin chronology, one cannot rule out the possibility of this delay in ice retreat. The lower viscosity values estimated in Chapter 2 as well as other previous studies (e.g., James e al., 2009) have likely influenced the ice sheet evolution through interactions between the solid Earth and the ice sheet. For example, a faster Earth response will impact the elevation of the ice sheet surface and thus the surface mass balance of the ice sheet during deglaciation. The implications of this process on the regional ice chronology and whether it can lead to a delayed ice retreat would be an interesting hypothesis to examine in future work.

Regardless of the model limitations, the results in Chapter 2 represent state-of-the-art for this region and so the optimal parameter sets were used to estimate the GIA contribution to present-day crustal movement and future RSL change. Our results suggest that GIA contributes significantly to present-day vertical motion; mostly at those parts of the coastline experiencing forebulge subsidence, with amplitudes of a few mm/year, and future RSL projectionsas large as 15 cm (28%) of the total estimated values. The model estimates of crustal motions and RSL variations at GPS and tide gauge stations, with the corresponding uncertainty, can be used by researchers seeking to use these geodetic observations to study other (non-GIA) processes of interest.

The data-model misfits evident in Chapter 2 motivated us to improve the applied Earth model by incorporating lateral variations in viscosity structure, and this work is presented in Chapter 3. In this chapter, Earth structure with laterally variable viscosity was built upon an optimal 1D viscosity model solution found from the analysis in Chapter 2, henceforth referred to as the reference model. Since lateral structure is generally added to a 1D model, the availability of an optimised 1D viscosity profile is an important prerequisite for the 3D modelling procedure. Three different approaches were used to construct 3D realizations of Earth viscosity structure. For the first approach, lateral variations in viscosity were calculated using four different global seismic tomography models via assumed velocity to viscosity scaling relationships. The lateral variations in lithosphere thickness were also included in modelling but these are determined independently of the sub-lithosphere viscosity structure. As described in Chapter 3, we used two different models of lithosphere thickness, one which was taken from past work and the other developed as part of the original research contributions in Chapter 3 using a combination of published data sets.

The results based on global seismic models indicate that the resolution of these models is not high enough to significantly improve the data-model misfits associated with the 1D model. Specifically, there is no evidence of a clear preference of one of the 3D models over the reference 1D model. The two other approaches resulted in higher resolution models of 3D structure by, in one case, inserting a regional seismic model into two of the global seismic models and, in the other case, explicitly incorporating regional structure of the Cascadia subduction zone (i.e., the subducting slab, the overlying mantle wedge, and the plate boundary interface). The results associated with these higher resolution models do not reveal any clear improvement in satisfying the RSL observations, particularly in the Victoria region where a rapid RSL fall is recorded immediately after deglaciation.

Given that the inclusion of lateral structure did not result in significantly improved data-model fits compared to the 1D model, we can reach the conclusion that, either, our estimates of lateral structure are inaccurate, or, other model limitations must dominate – specifically, the deglacial history or our assumption of linear (Maxwell) deformation. Alternatively, it is possible that tectonic deformation and/or glacially-induced faulting (e.g. Steffen et al., 2020) may have been important during this period. The occurrence of large Holocene earthquakes associated with the Leech River-

Devil's mountain fault system adjacent to Victoria City supports the idea of glacially-triggered fault rupture.

In defining the lateral viscosity structure, we made several assumptions that may have introduced error in our simulations. For example, relating velocity variations to changes in thermal structure when several studies suggest that there is evidence of presence of localized melt/fluids in this region (Bodmer et al., 2018; Audet and Schaeffer, 2018; Delph et al., 2018). Additionally, in the conversion from seismic to viscosity variations we only used a single set of scaling parameters, each of which with its own degree of uncertainty. Complementary observational constraints such as heat flow, gravity anomalies, magnetotelluric data, etc, are needed to reduce ambiguity/uncertainty when converting seismic velocities to viscosity structure. Finally, our assumption of Earth behaviour as a Maxwell material with a linear rheology may differ from reality. The application of power-law or transient Earth rheology is encouraged for future studies to explore this possibility.

Our results in Chapter 3 are disappointing in that the inclusion of lateral structure was unable to produce improved data-model fits. However, the application of these models does provide insight to the spread (and thus uncertainty) of modelled RSL values, which can be as large as 20 meters due to the influence of lateral structure. Future work to further quantify and, ideally, reduce the model uncertainty associated with defining lateral properties – e.g. via joint inversion of different data sets (Afonso et al., 2016) – is an important area of investigation.

In Chapter 4, we applied two different datasets to investigate the observed signals originating from geodynamic processes that act on different timescales along the Pacific coastline of North America. Specifically, we used late Holocene RSL observations (over the past 4 kyr) and GPS data (over the past few decades) to infer the associated vertical land motion (VLM) rates. Both datasets reflect the slow solid-Earth processes that act over millennial scales such as GIA or long-term tectonics, etc.

The Holocene rates, particularly, show good agreement with the modelled GIA rates inferred in Chapter 2. The reason that we did not simply apply our GIA model results was to minimize the uncertainty and error introduced from models, particularly given the relatively poor fits in the northern region. Contemporary GPS rates, in comparison to the longer-term RSL rates, record recently activated processes or transient signals prominent on short timescales in addition to the slower millennial scale signals. Two examples of recently activated processes are the isostatic response of the Earth to melting of mountain glaciers in the northernmost part of the coastline (British Columbia); and -groundwater depletion of the reservoirs in southern parts of the coastline (California). An example of a shorter-term transient signal is that signal associated with deformation during the interseismic period of the Cascadia megathrust earthquake cycle. The calculated residual between the GPS and late Holocene VLM rates is a measure of both the interseismic signal, 20th-century glacier mass loss and ground water depletion. We modelled and removed the signals associated with the two later processes, so that the residual VLM rates is expected to represent the signal due to the Cascadia earthquake cycle. The maximum contribution from melting glaciers and groundwater depletion are on the order of ~1mm/yr at the northern and southern ends of our study region.

The residual (corrected GPS minus Holocene) rates compare well with those predicted using a recent locking model of Cascadia subduction, even though the model was developed using only horizontal land motion observations. These residuals indicate uplift at many of the sites with amplitude of less than ~3mm/yr, which in central and southern Cascadia is comparable (in terms of magnitude) to the GIA signal inferred in Chapter 2. This again emphasizes the importance of considering the influence of geodynamic processes at play, before using the observations to make interpretations or constrain model parameters.

The plate locking model was used to perform a parameter sensitivity test, the results of which suggest that the residual VLM rates are able to provide useful constraints on key subduction model parameters such as the (near-trench) locking state. Surprisingly, in comparing the constraints based on our residual VLM rates to those from horizontal GPS data, we found that the latter have lower sensitivity to model parameter variations and thus lower resolving power. The fault locking simulations in this study are developed based on a relatively limited number of model parameters, e.g., a uniform mantle viscosity (10^{19} Pas beneath the continents and 10^{20} Pas for oceanic mantle). Exploring a larger suite of model parameters and using both vertical and horizontal rates of land motion are two key steps for future analyses. The careful approach taken in this study to isolate the interseismic cycle of Cascadia can be applied in other areas with active subduction zones such as Japan (e.g. the Nankai subduction zone). The capability of the GPS-inferred VLM rates to resolve the along-strike structure promotes the idea of using the data from a dense network of GPS stations extending further inland to provide additional constraints on along-dip variations of the locking parameters. However, since the locked zone is mostly offshore, the application of seafloor geodetic measurements near the deformation front is a key target to better resolve the locking model parameters, specifically the updip extent of the locking zone (Wang and Trehu, 2016).

Bibliography

Adams, J. (1990), Paleoseismicity of the Cascadia subduction zone: Evidence from turbidites off the Oregon-Washington margin, Tectonics, 9, 569–583.

Afonso J.C., Rawlinson N., Yang Y., Schutt D.L., Jones A.G., Fullea J., & Griffin W.L. (2016), 3-D multiobservable probabilistic inversion for the compositional and thermal structure of the lithosphere and upper mantle: III. Thermochemical tomography in the Western-Central US, J. geophys. Res., 121(10), 7337–7370, doi: 10.1002/2016JB013049.

Atwater, B.F. (1987), Evidence for great Holocene earthquakes along the outer coast of Washington State, Science, 236 (4804), 942-944, doi: 10 .1126 /science .236.4804 .942.

Atwater, B. F. & Hemphill-Haley E. (1997), Recurrence intervals for great earthquakes of the past 3,500 years at northeastern Willapa Bay, Washington, U.S. Geol. Surv. Prof. Pap. 1576, 108 pp.

Audet, P., & Schaeffer, A.J. (2018), Fluid pressure and shear zone development over the locked to slow slip region in Cascadia. Science Advances, 4, eaar2982. https://doi.org/10.1126/sciadv.aar2982.

Bostock, M.G., Hyndman, R.D., Rondenay, S., & Peacock S.M. (2002), An inverted continental Moho and serpentinization of the forearc mantle, Nature, 417, 536–538, doi:10.1038/417536a.

Crameri, F., Conrad, C.P., Montési, L., & Lithgow-Bertelloni, C.R. (2018), The dynamic life of an oceanic plate. Tectonophysics. DOI: 10.1016/j.tecto.2018.03.016.

Dalton A.S., Margold M., Stokes C.R., Tarasov L., Dyke A.S., Adams R.S., Allard S., Arends H.E., Atkinson N., Attig J.W., & Barnett P.J. (2020), An updated radiocarbon-based ice margin chronology for the last deglaciation of the North American Ice Sheet Complex. Quaternary Science Reviews 234: 106223, https://doi.org/10.1016/j.quascirev.2020.106223.

Dragert, H., Hyndman, R.D., Rogers, G.C., & Wang, K. (1994), Current deformation and the width of the seismogenic zone of the northern Cascadia subduction thrust. Journal of Geophysical Research, 99, 654-668, doi: 10.1029/93JB02516.

Dyke, A.S., Moore, A., & Robertson, L. (2003), Deglaciation of North America. Tech. Rep. Open File 1574, Geological Survey of Canada, Thirty-Two Maps at 1:7000000 Scale with Accompanying Digital Chronological Database and One Poster (in Two Sheets) with Full Map Series.

Dyke, A.S. (2004), An outline of North American deglaciation with emphasis on central and northern Canada. In: Ehlers, J., Gibbard, P.L. (Eds.), Quaternary Glaciations-Extent and Chronology, Part II, Vol. 2b. Elsevier, pp. 373–424.

Farrell, W.E., & Clark, J.A. (1976), On postglacial sea level, Geophys. J. R. astr. Soc., 46, 647–667, doi: 10.1111/j.1365-246X.1976.tb01252.x.

Garrett, E., Barlow, N.L.M., Cool, H., Kaufman, D.S., Shennan, I., & Zander, P.D. (2015) Constraints on regional drivers of relative sea-level change around Cordova, Alaska, Quat. Sci. Rev., 113, pp. 48-59.

Goldfinger, C., Nelson, C.H., Morey, A.E., Johnson, J.E., Patton, J., Karabanov, E., Gutiérrez–Pastor, J., Eriksson, A.T., Gràcia, E., Dunhill, G., Enkin, R.J., Dallimore, A., & Vallier, T. (2012), Turbidite event history—Methods and implcations for Holocene paleoseismicity of the Cascadia subduction zone, U.S. Geological Survey Professional Paper 1661–F, 170 p, 64 figures, available at http://pubs.usgs.gov/pp/pp1661f/.

Gosselin, J.M., Audet P., Estève C., McLellan M., Mosher S.G., & Schaeffer,A.J. (2020), Seismic evidence for megathrust fault-valve behavior during episodic tremor and slip, Science Advances: Vol. 6, no. 4, eaay5174, doi: 10.1126/sciadv.aay5174.

Gowan, E.J., (2007), Glacio-isostatic adjustment modelling of improved relative sea-level observations in southwestern British Columbia, Canada, MSc. thesis, 148 pp., Univ. of Victoria, Victoria, B. C., Canada.

Han, D. & Wahr, J. (1989) Post-glacial rebound analysis for a rotating Earth, in Slow Deformations and Transmission of Stress in the Earth, eds. S. Cohen and P. Vanicek, ACU Mono. Senes 49, p. 1-6.

Hawley, W. B., & Allen, R.M. (2019), The fragmented death of the Farallon Plate. Geophys. Res. Lett.,2019GL083437, doi: 10.1029/2019GL083437.

Hu, Y., & Freymueller, J.T. (2019), Geodetic observations of time-variable glacial isostatic adjustment in Southeast Alaska and its implications for Earth rheology. Journal of Geophysical Research: Solid Earth, 124, 9870–9889. https://doi.org/10.1130/10.1029/2018JB017028.

James, T.S., Gowan E.J., Wada I., & Wang K. (2009), Viscosity of the asthenosphere from glacial isostatic adjustment and subduction dynamics at the northern Cascadia subduction zone, British Columbia, Canada. J. Geophys. Res., 114, doi: 10.1029/2008JB006077.

Karato, S. (2008), Deformation of Earth Materials: An Introduction to the Rheology of Solid Earth, Cambridge: Cambridge University Press, doi: 10.1017/CBO9780511804892.

Kelsey, H.M., Engebretson, D.C., Mitchell, C.E., & Ticknor, R.L. (1994), Topographic form of the Coast Ranges of the Cascadia margin in relation to coastal uplift rates and plate subduction, J. Geophys. Res., 99, 12,245-12,255.

Khan, N.S., Ashe, E., Shaw, T.A., Vacchi, M., Walker, J., Peltier, W.R., Kopp, R.E., Horton, B.P. (2015), Holocene relative sea-level changes from near-, intermediate-, and far-field locations. Curr Clim Chang Rep.,1:247–62.

Khan, N.S., Ashe, E., Horton, B.P., Dutton, A., Kopp, R.E., Brocard, G., …Scatena, F.N. (2017). Drivers of Holocene sea-level change in the Caribbean. Quaternary Science Reviews, 155, 13–36, https://doi.org/10.1016/j.quascirev.2016.08.032.

Kuchar, J., Milne, G.A., Latychev K. (2019), The importance of lateral Earth structure for North American glacial isostatic adjustment, Earth planet. Sci. Lett., 512, 236–245. 10.1016/j.epsl.2019.01.046.

Lambeck, K., Rouby, H., Purcell, A., Sun, Y., & Sambridge, M. (2014), Sea level and global ice volumes from the Last Glacial Maximum to the Holocene, Proceedings of the National Academy of Sciences, 111.43, pp. 15296–15303, doi: 10.1073/pnas.1411762111.

Lange, H., Casassa, G., Ivins, E. R., Schröder, L., Fritsche, M., Richter, A., et al. (2014). Observed crustal uplift near the Southern Patagonian Icefield constrains improved viscoelastic Earth models. Geophysical Research Letters, 41, 805–812, https://doi.org/10.1002/2013GL058419.

Leonard, L. J., Currie, C.A., Mazzotti, S., & Hyndman R.D. (2010), Rupture area and displacement of past Cascadia great earthquakes from coastal coseismic subsidence, Geol. Soc. Am. Bull., 122, 2079–2096, doi:10.1130/B30108.1.

Li, S., Wang, K., Wang, Y., Jiang, Y., & Dosso, S.E. (2018), Geodetically inferred locking state of the Cascadia megathrust based on a viscoelastic Earth model. Journal of Geophysical Research: Solid Earth, 123, 8056–8072, doi: 10.1029/2018JB015620.

Love, R., Milne, G.A., Tarasov, L., Engelhart, S., Hijma, M., Latychev, K., Horton, B.P., Törnqvist, T. (2016), Projections of sea level change along the east and Gulf coasts of North America. Earth's Future, doi: 10.1002/2016EF000363.

McCaffrey, R., Qamar, A., King, R., Wells, R., Khazaradze, G., Williams, C., Stevens, C., Vollick, J., & Zwick P. (2007), Fault locking, block rotation and crustal deformation in the Pacific Northwest, Geophys. J. Int., 169(3), 1315–1340, doi:10.1111/j.1365-246X.2007.03371.x.

Milne, G.A., & Mitrovica, J.X. (1998), Postglacial sea-level change on a rotating Earth, Geophysical Journal International, 133, 1–19, doi: 10.1046/j.1365-246X.1998.1331455.x.

Milne, G.A., and Shennan, I. (2013), Isostasy: glaciation-induced sea-level change. In Encyclopedia of Quaternary Science, volume 3, Elsevier, Oxford, p. 452–459.

Mitrovica, J.X., & Milne, G.A. (2002), On the origin of late Holocene sea-level highstands within equatorial ocean basins, Quaternary Science Reviews, 21(20-22), 2179–2190, doi: 10.1016/S0277-3791(02)00080-X.

Mitrovica, J.X., & Milne, G.A. (2003), On post-glacial sea level: I. general theory, Geophysical Journal International, 154, 253-267.

Nield, G., Barletta, V.R., Bordoni, A., King, M.A., Whitehouse, P.L., Clarke, P.J., et al. (2014), Rapid bedrock uplift in the Antarctic Peninsula explained by viscoelastic response to recent ice unloading. Earth and Planetary Science Letters, 397, 32–41. https://doi.org/10.1016/j.epsl.2014.04.019.

Okuno, J., Nakada, M., Ishii, M. and Miura, H. (2014), Vertical tectonic crustal movements along the Japanese coastlines inferred from late Quaternary and recent relative sea-level changes. Quatern. Sci. Rev., 91, 42–61. Okutani, T. (2000) Marine Mollusks in Japan. Tokai University Press, Tokyo, 1173 pp.

Peltier, W.R. (1974), The impulse response of a Maxwell Earth, Reviews of Geophysics 12.4, pp. 649–669.

Ranalli, G. (1995), Rheology of the Earth, 2nd ed. Chapman and Hall, pp. 230.

Ranalli, G. (2001), Mantle rheology: Radial and lateral viscosity variations inferred from microphysical creep laws, J. Geodyn., 32(4–5), 425–444, doi:10.1016/S0264-3707(01)00042-4.

Rogers, G., & Dragert, H. (2003), Episodic tremor and slip on the Cascadia subduction zone: The chatter of silent slip, Science, 300, 1942–1943.

Sabadini, R., Yuen, D.A., & Boschi, E. (1982), Polar wander and the forced responses of a rotating, rnultilayered, viscoelastic planet, J. Geophys. Res., 87. 28854903.

Satake, K., K. Wang, & Atwater B.F. (2003), Fault slip and seismic moment of the 1700 Cascadia earthquake inferred from Japanese tsunami descriptions, J. Geophys. Res., 108(B11), 2535, doi:10.1029/2003JB002521.

Sella, G.F., Stein, S., Dixon, T.H., Craymer, M., James, T.S., Mazzotti, S., Dokka, R.K. (2007), Observation of glacial isostatic adjustment in stable North America with GPS. Geophys. Res. Lett. 34, L02306.

Severinghaus, J., & Atwater, T. (1990), Cenozoic geometry and thermalstate of the subducting slabs beneath western North America. In: Wernicke, B.P. (Ed.), Basin and Range Extensional Tectonics Nearthe Latitude of Las Vegas, Nevada. Geological Society of America Memoir, vol. 176. Boulder, Colorado.

Shackleton, N.J., & Opdyke, N.D. (1973), Oxygen isotope and paleomagnetic stratigraphy of Equatorial Pacific Core V28-38: Oxygen isotope temperatures and ice volumes on a 10' year and 1066 year scale, Quat. Res., 3, 39-55.

Shennan. I. (2007), Overview. In: S. Elias (Ed.), Encyclopedia of Quaternary Sciences. Elsevier, London, UK, pp. 3015–3023.

Shennan, I., Long, A.J., & Horton, B.P. (2015), Handbook of Sea-Level Research. John Wiley & Sons.

Steffen, H., & Kaufmann, G. (2005), Glacial isostatic adjustment of Scandinavia and northwestern Europe and the radial viscosity structure of the earth's mantle, Geophys. J. Int., 163(2), 801–812.

Stuiver, M. & Suess, H.E. (1966), On the relationship between radiocarbon dates and true sample ages. Radiocarbon, 8, 534-540.

Tarasov, L., & Peltier W.R. (2004), A geophysically constrained large ensemble analysis of the deglacial history of the North American ice sheet complex, Quat. Sci. Rev., 23, 359–388.

Tarasov, L., Dyke A.S., Neal R.M., Peltier W.R. (2012), A data calibrated distribution of deglacial chronologies for the North American ice complex from glaciological modeling, Earth Planet. Sci. Lett., 315–316, 30–40.

Törnqvist, T.E., Rosenheim, B.E., Hu, P., & Fernandez, A.B. (2015) Radiocarbon dating and calibration, in: Handbook of Sea-Level Research, edited by: Shennan, I., Long, A. J., and Horton, B. P., 349–360, Wiley Blackwell, doi:10.1002/9781118452547.ch23, 2015.

van der Wal, W., Wu, P., Wang, H., Sideris, M.G. (2010), Sea levels and uplift rate from composite rheology in glacial isostatic adjustment modelling, J. Geodyn., vol. 50 1(pg. 38-48).

van der Wal, W., Barnhoorn, A., Stocchi, P., Gradmann, S., Wu, P., Drury, M., Vermeersen, L.L.A. (2013), Glacial isostatic adjustment model with composite 3D earth rheology for Fennoscandia. Geophys. J. Int., http://dx.doi.org/10.1093/gji/ggt099.

van der Wal, W., Whitehouse, P., & Schrama,, E.J.O. (2015), Effect of GIA models with 3D composite mantle viscosity on GRACE mass balance estimates for Antarctica. Earth and Planetary Science Letters, 414, 134-143, doi: 10.1016/j.epsl.2015.01.001.

Wang, K., Wells, R., Mazzotti, S., Hyndman, R.D., & Sagiya, T. (2003), A revised dislocation model of interseismic deformation of the Cascadia subduction zone, J. Geophys. Res., 108(B1), 2026, doi:10.1029/2001JB001227.

Wang, K., & Tréhu, A.M. (2016), Invited review paper: Some outstanding issues in the study of great megathrust earthquakes—The Cascadia example. Journal of Geodynamics, 98, 1–18, doi: 10.1016/j.jog.2016.03.010.

Whitehouse, P.L. (2018), Glacial isostatic adjustment modelling: historical perspectives, recent advances, and future directions. Earth Surface Dynamics 6: 401–429.

Wilson, D.S. (2002), The Juan de Fuca plate and slab: Isochron structure and Cenozoic plate motions, U.S. Geol. Surv. Open-File Rep., 02–328, pp. 9–12.

Wu, P., & Wang H. (2008), Postglacial isostatic adjustment in a selfgravitating spherical earth with power-law rheology, J. Geodyn., 46, 118 – 130, doi:10.1016/j.jog.2008.03.008.